Reliability-based design optimization of composite laminates for aeroelastic applications

Ludovic Coelho

université
PARIS-SACLAY

Reliability-based design optimization of composite laminates for aeroelastic applications

Optimisation de stratifiés composites sous contrainte fiabiliste pour des applications aéroélastiques

Thèse de doctorat de l'université Paris-Saclay

École doctorale n°579 : sciences mécaniques et énergétiques, matériaux et géosciences (SMEMaG)
Spécialité de doctorat: Mécanique des solides
Graduate School : Sciences de l'ingénierie et des systèmes.
Référent : Faculté des sciences d'Orsay

Thèse préparée à **DMAS Matériaux et Structures** (Université Paris-Saclay, ONERA) , sous la direction de **Didier LUCOR**, directeur de recherche CNRS, le co-encadrement de **Cédric JULIEN**, ingénieur de recherche, le co-encadrement de **Christian FAGIANO**, ingénieur de recherche et le co-encadrement de **Nicolò FABBIANE**, chargé de recherche.

Thèse soutenue à ONERA-Châtillon, le 09 mars 2023, par

Ludovic COELHO

THESE DE DOCTORAT

NNT : 2023UPAST039

Composition du jury

Membres du jury avec voix délibérative

Pietro Marco CONGEDO Directeur de recherche, INRIA	Président
Jean-Marc BOURINET Professeur des universités, SIGMA Clermont	Rapporteur & Examinateur
Angela VINCENTI Professeur des universités, Sorbonne Université	Rapporteur & Examinatrice
Jacobo DÍAZ Maître de conférences, Universidade da Coruna	Examinateur
Cécile MATTRAND Maître de conférences, SIGMA Clermont	Examinatrice
Carl SCARTH Docteur, University of Bath	Examinateur

université PARIS-SACLAY

ÉCOLE DOCTORALE
Sciences mécaniques et énergétiques, matériaux et géosciences (SMEMAG)

Titre : Optimisation de stratifiés composites sous contrainte fiabiliste pour des applications aéroélastiques

Mots clés : optimisation sous incertitudes, matériau composite, multi-échelle, paramètres de stratification, métamodèles, flottement

Résumé : L'optimisation de stratifiés composites sous contrainte fiabiliste a été réalisée avec la prise en compte de l'incertitude des orientations de plis. Ce travail propose une nouvelle méthodologie itérative qui lie deux espaces d'analyse. Dans le premier espace est gérée la conception macroscopique à faible dimension (en utilisant les paramètres de stratification) avec des informations de gradient pour effectuer une optimisation rapide. Dans le deuxième espace, mésoscopique à haute dimension, les incertitudes des variables de conception sont modélisées et ensuite transportées à l'échelle macroscopique. Avec cette méthodologie, un problème inverse doit être résolu à chaque itération pour pouvoir propager l'incertitude de l'espace mésoscopique à l'espace de conception macroscopique et calculer la probabilité de défaillance nécessaire. Pour cela, une quantification de l'incertitude est nécessaire pour identifier correctement une séquence d'empilement correspondant à la description statistique des paramètres de stratification. Une base orthonormale de Fourier a donc été développée. L'approche d'optimisation présentée est appliquée à différents problèmes : d'abord, l'optimisation d'une plaque composite favorisant la rigidité de la plaque avec une contrainte analytique de flambage et ensuite une optimisation aéroélastique favorisant la flexibilité de la plaque tout en restant fiable vis-à-vis du phénomène de flottement. En raison de la nature modale de la vitesse de flottement, une stratégie combinant une classification et un modèle de substitution classique est proposée pour approximer la quantité d'intérêt et effectuer une analyse de fiabilité rapide. Les résultats obtenus démontrent une amélioration de la fiabilité par rapport à la conception optimisée déterministe et un gain de calcul significatif par rapport à l'approche consistant à optimiser directement les orientations des plis via un algorithme génétique.

Title: Reliability-based design optimization of composite laminates for aeroelastic applications

Keywords: optimization under uncertainty, composite material, multi-scale, lamination parameters, surrogate models, flutter

Abstract: Reliability-based design optimization of composite laminates was performed with uncertainty in ply orientation. This work proposes a new iterative methodology that links two analysis spaces. In the first space, the low-dimensional macroscopic design is managed (using lamination parameters) with gradient information to perform rapid optimization. In the second, a high-dimensional mesoscopic scale, uncertainties in the design variables are modeled and then propagated to the macroscopic scale. With this methodology, an inverse problem must be solved at each iteration to propagate the uncertainty from the mesoscopic space to the macroscopic design space and calculate the required failure probability. For this purpose, uncertainty quantification is necessary to correctly identify a stacking sequence corresponding to the statistical description of the lamination parameters. To this end, a Fourier orthonormal basis has been developed. The optimization methodology is applied to various problems, including instability constraint: (i) composite plate optimization promoting the plate stiffness with an analytic buckling constraint and (ii) aeroelastic tailoring promoting the plate flexibility while remaining reliable with respect to the flutter phenomenon. Due to the modal nature of the flutter velocity, a strategy combining a classifier and classic surrogate models is proposed to approximate the quantity of interest and perform a fast reliability analysis. The results demonstrate an improvement in the reliability compared to the deterministic optimized design and a significant computational gain compared to the approach of directly optimizing ply orientations via a genetic algorithm.

ACKNOWLEDGEMENTS/REMERCIEMENTS

Le bon déroulement de cette thèse n'aura pas été possible sans de nombreuses personnes... Tout d'abord je veux remercier mon encadrement : Nicoló Fabbiane, Christian Fagiano, Cédric Julien et Didier Lucor pour votre confiance. Sans parler de l'aspect technique, je vous remercie pour votre rigueur exigée tout au long de la thèse mais également pour votre bonne humeur pendant les nombreuses réunions concernant la thèse.

Merci Christian et Cédric pour votre suivi quasi quotidien. Vos bureaux étaient toujours ouverts en cas de problème, également pour discuter sur l'aspect scientifique et technique ou même pour booster ma motivation à certain moment sachant que la première année n'a pas été facile pour moi. Merci Nicolo pour toute ton aide sur la partie code autour de Python et NASTRAN ; sans toi je n'aurai pas avancé aussi vite et merci également pour toute les discussions scientifiques et pas que. Didier, merci, dans un premier temps d'avoir été mon directeur de thèse mais aussi pour les visites au LISN, les points téléphoniques et ta bonne humeur. Le recul que tu avais par rapport à la thèse m'était clairement bénéfique pour prendre les bonnes décisions.

Je voudrais ensuite remercier les membres du jury de la thèse : les rapporteurs Angela Vincenti et Jean-Marc Bourinet, Cécile Mattrand, Jacobo Diaz et Carl Scarth en tant qu'examinateurs et Pietro Congedo en sa qualité de président du jury. La bienveillance dont vous avez fait preuve à mon égard m'a sans doute permis d'être à l'aise et d'exprimer clairement mes idées.

Merci à l'équipe MC2 pour tous les bons souvenirs que j'emporte avec moi : les bonnes pauses café, les courses à pied, les quelques soirées autour d'une bière ; mais aussi les demies journées où les doctorants répètent leur présentation pour des conférences ou autre qui ont été clairement bénéfique pour avoir un avis extérieur et prendre plus de recul sur ses travaux. Un grand merci à François-Henri pour toutes les discussions scientifiques autour des travaux de thèse et les nombreux conseils que tu donnes pour les présentations ou les méthodes à utiliser ou à potentiellement développer. Ce fut un énorme plaisir de partager ces moments avec toi. Merci également à l'équipe MSAE qui m'avait déjà accueilli en stage avant la thèse puis actuellement en CDD, à Yann pour tes conseils avant d'avoir fait le choix de faire une thèse, à Fabien qui avait participé aux entretiens.

Ce fut un plaisir de vivre cette expérience avec les doctorants de MC2, merci pour la bonne ambiance et bienveillance lors de ces trois années. Pensée particulière pour Matthieu, qui m'a

poussé à faire toujours plus de courses à pied, avec un semi-marathon effectué pendant la thèse ; Clément pour les sorties culturelles et les discussions toujours aussi enrichissantes, Salim pour les discussions sur la musique autour d'un bon kebab, Enrico pour ton rayon de soleil venu d'Italie. Et merci à Laurence pour ton aide sur tout l'aspect administratif pour les conférences, les workshops et l'organisation de la soutenance.

Ce travail n'aurait pas pu aller au bout sans le soutien moral de mes proches. Un grand merci au Fascicule, au Menu, à Apero Time et à Gredur. Une pensée à mes amis qui ont également fait une thèse pendant la même période avec qui on pouvait discuter librement des doutes et craintes mais aussi des réussites autour de la thèse. Merci Hector, Yutao, Hugo. Un grand merci Filipa pour tes encouragements et bien sûr à mes parents qui ont fait énormément de sacrifices pendant leur vie pour nous mettre dans les meilleures conditions avec ma sœur. Merci pour votre amour et les repas du dimanche pendant ces trois années. Une pensée particulère à toute la famille au Portugal également. Enfin merci à Julia, qui a été mon plus grand soutien moral depuis le début de la thèse. Elle a su me remotiver ou me faire prendre du recul quand il le fallait et m'a supporté même pendant le confinement. Malheureusement tu ne vas plus entendre parler des uncertainties, des composites ou des laminations parameters... Le destin a fait qu'on se rencontre juste avant le début de la thèse et cela n'aurait pas été si paisible sans toi. Merci !

CONTENTS

ACRONYMS

CDF Cumulative Density Function. 61

CFD Centered Finite Differences. 77, 79, 88, 90, 93

CLPT Classical Laminated Plate Theory. 6, 7, 10, 11, 15, 17, 47, 89

CLT Classical Lamination Theory. 130

CoV Coefficient of Variation. 62, 79

CRN Common Random Numbers. 78, 80

DLM Doublet Lattice Method. 98

DoE Design of Experiments. 68, 69, 72, 74, 83, 107

FCE Fourier Chaos Expansion. 37–39, 45, 47–50, 76, 80–82, 87, 88, 90, 106

FE Finite Element. 97

FORM First Order Reliability Method. 21, 60, 61, 68, 75

GA Genetic Algorithm. 12, 13, 52

GCMMA Globally Convergent Method of Moving Asymptotes. 86

GP Gaussian Process. 64, 71, 72

GPC Gaussian Process Classification. 71–73, 76, 133

GPR Gaussian Process Regression. 73, 76

HL-RF Hasofer-Lind and Rackwitz-Fiessler. 60

IS Importance Sampling. 63

KDE Kernel Density Estimation. 25, 26, 28, 45

KKT Karush-Kuhn-Tucker. 20

LP Lamination Parameter. 9, 15, 17, 18, 23, 24, 29, 35, 36, 43, 47, 49, 50, 52–55, 58, 64, 68–70, 72, 73, 75, 77, 80–83, 86, 87, 91, 93, 101, 102, 104–108, 134

MC Monte Carlo. 37, 45, 47–49, 62–64, 73, 75, 77, 78, 82

MCMC Markov Chain Monte Carlo. 63

MMA Method of Moving Asymptotes. 86, 90, 92, 101, 108

MPFP Most Probable Failure Point. 60, 77

OUU Optimization Under Uncertainty. 1, 3

PCE Polynomial Chaos Expansion. 36, 37, 39, 107

PDF Probability Density Function. 2, 37, 45, 58, 60, 61, 63, 71, 77, 80, 92, 102, 103

PP Polar Parameter. 9, 15, 17, 18

RBDO Reliability-Based Design Optimization. 1–4, 19, 20, 22, 30, 34, 55, 58, 75, 77, 80, 83, 86, 90–93, 97, 101–107, 129, 134, 135

RDO Robust Design Optimization. 1, 2, 129

SA Simulated Annealing. 12, 13

SF Score Function. 77, 79, 93

SLA Single Loop Approach. 20

SORA Sequential Optimization and Reliability Assessment. 20

SORM Second Order Reliability Method. 60, 61, 68

SS Subset Sampling. 63

SST Stacking Sequence Tables. 18, 36, 87

UQ Uncertainty Quantification. 2, 76, 80, 81

INTRODUCTION

Context

One of the main challenges in the field of composite structure optimization is exploiting their full potential. Composite materials allow tailoring the elastic properties of a structure. The composite structural design process often results in an optimization problem where the structural performance is maximized, or the mass is minimized within a set of constraints imposed by the materials and general behavior of the structure.

Due to the complexity of these materials, variability in their performance arises mainly from the variability coming from the manufacturing process, such as mechanical properties, fiber orientation, and structural geometry, but even from loading conditions. Such uncertainties can affect the mechanical response of a structure (Petit, 2004; Chiachio et al., 2012; Beran et al., 2017), and lead to a catastrophic failure.

For deterministic optimization, such uncertainties are often dealt with by simplifying hypotheses, such as using safety factors and considering only average or extreme values. However, such approaches can lead to conservative and inefficient designs or optimistic designs with poor reliability (Beck and Gomes, 2012). To better exploit composite materials, the ambition is to extend these strategies in a stochastic framework taking into account uncertainties in composite materials. The research topic of optimization under uncertainty (OUU) is vast and presents significant computational challenges in implementing efficient numerical procedures. A crucial initial step is the formulation of the OUU problem, conditioned by the evolution of the system from a deterministic design problem to a design under uncertain conditions.

Motivation: reliability-based design optimization under design variables uncertainty

Stochastic formulations of the objective(s) and constraint(s) must be carefully described. The two principal methodologies for OUU are Robust Design Optimization (RDO) and Reliability-Based Design Optimization (RBDO). Uncertainties are usually taken into account in the objective function foe RDO, thereby minimizing a mean response value and the sensitivity to random parameters via the variance. RBDO optimizes a design by introducing uncertainties in the constraint functions having a particular target of risk via a probability computation. It is possible to mix both approaches (António and Hoffbauer, 2009; Doh et al., 2018; Lobato et al., 2020). In this work, the focus is made on RBDO. Taking into account

the uncertainty relies on repeated evaluations of the mechanical model. This optimization's time-consuming computation may limit the range of applications. Surrogate models have been used in order to alleviate the computational time. For the RBDO task, surrogate models relying, for instance, on Polynomial Chaos Expansion were considered in Suryawanshi and Ghosh (2016); López et al. (2017), or Kriging in Dubourg et al. (2011); Li et al. (2016). Rivier and Congedo (2022) proposed a Surrogate-Assisted Bounding-Box approach that handles robustness and reliability measures for RDO or RBDO. Gaussian Process is also exploited with an adaptative refinement strategy. Another interesting approach is the one of Moustapha et al. (2016), where a new quantile-based formulation is proposed, motivated by the relatively high target failure probabilities that can be accepted in the automotive design field.

The review made by Chiachio et al. (2012) on reliability in composites sums up the works performing reliability analyses of composite structures. On the one hand, most of the works consider uncertainty on loads or strength. On the other hand, uncertainties on the geometry, such as the thickness and the ply angle, are less present in the literature. However, Conceição António and Hoffbauer (2017) perform a RBDO with the minimization of the mass of a simple composite structure while remaining reliable with respect to buckling instability with uncertainty on the loads imposed. Subsequently, a sensitivity analysis was performed on the optimal structure to study the influence of random design parameters and variables on the structural response. This analysis revealed that the longitudinal elastic modulus and ply orientations were the most influential parameters. Other works show the detrimental influence of the ply orientation on buckling instability (Wang et al., 2017; Pagani and Sanchez-Majano, 2022). The uncertainty of ply orientations has some effect on flutter instability in the aeroelastic field.

Aeroelasticity is the study of the interaction between inertial, elastic, and aerodynamic forces on bodies subject to a flow. The study of aeroelasticity may be extensively classified into two categories: *static aeroelasticity* dealing with the static or steady-state response of an elastic body to a fluid flow; and *dynamic aeroelasticity* dealing with the body vibration response. In the latter category, phenomena like flutter or limit cycle oscillations are present. Concerning the aeroelastic application, this work will focus on the flutter dynamic instability. Regarding the composite material, it allows to optimize locally the stiffness of the structure in order to adapt the overall aero-structural behavior and possibly delay instabilities. The complex interactions between the structure and the fluid that lead to flutter are highly sensitive to uncertainties Beran et al. (2017). The review in Beran et al. (2017) illustrates some reasons why there is particular interest in uncertainty quantification (UQ) in this area, and one of the most important reasons is the classical 15% safety factor margin on the flutter airspeed, which is required for the qualification of aircraft (Administration, 2014). Therefore, taking into account the uncertainties in the design process may reduce this margin in the future, leading to less conservative designs. Scarth et al. (2014); Nitschke et al. (2019) studied the UQ of the flutter velocity considering uncertainty on ply orientations. These works show the possible important variation in the critical flutter velocity in some parts of the composite laminate design space. An example is shown in Figure 1 where the probability density function (PDF) has a bimodal behavior while taking into account ply orientation uncertainty. The deterministic quantity could respect the constraint, but considering the uncertainty on ply angles could lead to poor reliability with respect to the flutter. Therefore, taking into account the uncertainty on ply orientations is of interest for the aeroelastic design process.

Scarth and Cooper (2018) investigated the minimization of the probability of the flutter occurring on a composite plate wing with uncertain design variables, i.e., the ply orientations. However, even if the resulting design is, in some sense, an *optimized* solution concerning the

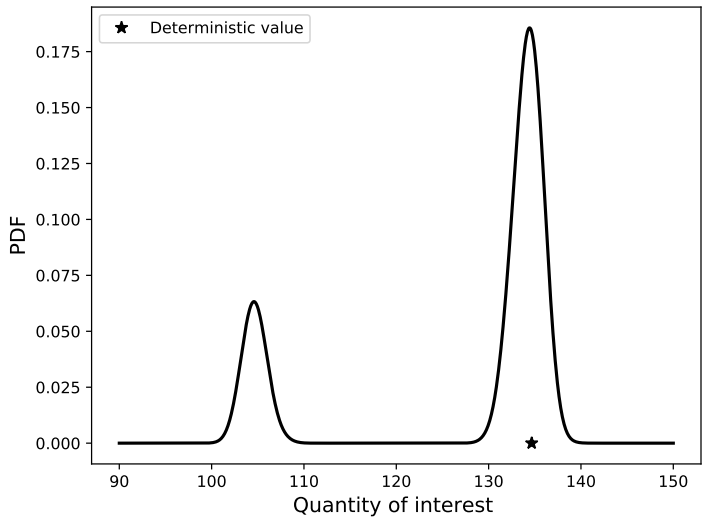

Figure 1: Example of a probability density function of a composite plate flutter velocity with ply angle uncertainty.

onset of the flutter instability, their proposed formulation could be improved for the aircraft design process since the aeroelastic stability has to be taken into account as a constraint instead of an *improvable* objective. Moreover, a genetic algorithm is used to solve the optimization, which can be limited to complex high-dimensional problems.

To conclude, this overview shows the interest in taking into account uncertainties on the ply orientations, especially on mechanical instability, such as buckling or flutter phenomenon. However, a limited number of studies take into account these uncertainties in a OUU framework and more especially for RBDO. Recently, a strategy, solving a mono-objective optimization taking into account the uncertainty of the ply orientations, has yielded reliable designs with respect to the flutter phenomenon (Scarth and Cooper, 2018). Nevertheless, the proposed formulation could be more evolved if a more realistic application is considered.

Objectives and thesis layout

In this context, this work aims to develop a strategy for composite laminate RBDO under uncertainty of design variables through the most realistic formulation for aeroelastic applications.

The research work is around a few axes of development: composite laminate optimization, surrogate modeling, and reliability-based design optimization. Each chapter of the manuscript includes one or two coupled axes of development with a state of the art review of each domain.

The primary goal was to formulate the optimization problem to perform efficiently and the most quickly the RBDO. An outline of the existing strategies and methods for composite structure optimization, under uncertainty or not, is introduced in Chapter 1. The idea is to explore the possibility of quantifying the uncertainty of homogeneous parameters to perform gradient-based optimization in the homogeneous space. Therefore, a strategy is presented in this chapter exploiting two design spaces at different scales of the material during the optimization process to use a gradient-based algorithm. Nevertheless, even if the formulation is presented and explained, some steps need technical development to carry out the strategy.

One of the steps is an inverse problem resolution to retrieve a composite layup from the homogenized design variables. In a variability framework, the statistics of the linked variables of each scale need to be matched. In Chapter 2, a metamodel, based on the Polynomial Chaos Expansion family, that efficiently and quickly computes the statistics of homogenized design variables is developed. Different formulations of the inverse problem are investigated and compared via the surrogate model developed.

Chapter 3 focuses on the reliability analysis of a multimodal response and its sensitivity. The objective is to set up a strategy for the failure probability computation and its sensitivity in a convenient computational time. Indeed, aeroelastic models are often expensive, so it is necessary to use metamodeling methods for this step. Kriging is exploited in this step with a strategy using classification to handle the discontinuity of the mechanical response coming from the physics. Concerning the probability sensitivity, different methods are tested, and a hybrid approach is proposed, which seems adapted to the design variables of the optimization problem.

Chapter 4 aims to validate the global strategy exploiting different scales of the material in a variability framework and to compare the RBDO with a deterministic optimization. The validation is made on a simple test case of a composite plate under compression load. Then an aeroelastic optimization is performed still on a composite plate. Multiple studies on the computational time, the initial guess, and the reliability analysis are presented.

The last chapter will present the conclusions drawn from this work and discuss its perspectives.

CHAPTER 1

MULTI-SCALE COMPOSITE DESIGN OPTIMIZATION FRAMEWORK

Contents

1.1 Introduction

In the literature, many works can be found on laminated composite structure optimization, but fewer works take into account uncertainties on design variables, such as ply orientation. An overview of the composite structure design methods is given in this chapter through the existing literature. The objective of this chapter is to show the limits of the existing strategies for composite laminate optimization under design variable uncertainty and to present the principal steps of the new methodology of composite laminate reliability-based design optimization that will be detailed in the remainder of the manuscript. The chapter starts with the description of composite laminates and the hypotheses made for composite modeling. The existing approaches for optimizing composite laminate structure in a deterministic framework are covered in Section 1.3. Then, reliability-based design optimization is introduced with a literature review applied to composite and the introduction of the new multi-scale reliability-based design optimization formulation is made.

1.2 Laminates stiffness modeling

1.2.1 Material basis concept

Composite laminates are a sub-class of composite materials obtained by stacking thin plies, called lamina, made of two basic constituents: high-stiffness fibers aligned in a common direction, bonded by a polymer matrix (Figure. 1.1c). The laminae are held together by a polymeric resin, forming a laminate. The use of composite laminates is motivated by their high stiffness-to-mass and strength-to-mass ratios. Moreover, composite materials introduce new degrees of freedom in the design of structures by tailoring the stacking sequence of the laminate.

1.2.2 Mechanics of composite laminates

In this thesis, composite laminates are treated as plate elements. Analyses of composite plates could be based on different approaches, such as the classical laminated plate theory (CLPT), the shear deformation laminated plate theories, the traditional 3D elasticity formulations, or the layerwise theories. All these approaches are presented in Reddy (2003).

The classical laminated plate theory (CLPT) is considered here. This theory follows some assumptions concerning the kinematics of the deformation and the stress state through the thickness of the laminate. This is based on the Kirchhoff-Love plate kinematics and plane stress assumption.

Kirchhoff-Love hypotheses hold:

1. Straight lines normal to the mid-surface remain straight after deformation.
2. Straight lines normal to the mid-surface rotate such that they remain normal to the mid-surface after deformation.
3. Thickness does not change during deformation.

These assumptions lead to zero transverse normal strain ϵ_{zz} and zero transverse shear strains ϵ_{xz}, ϵ_{yz}. Moreover, the plane stress assumptions lead to neglect the stress components in the out-of-plane direction. Finally, the deformations are constant through the thickness and equal to those of the mid plane; this is the consequence of the combination of Kirchhoff-Love and the perfect adhesion of the layers.

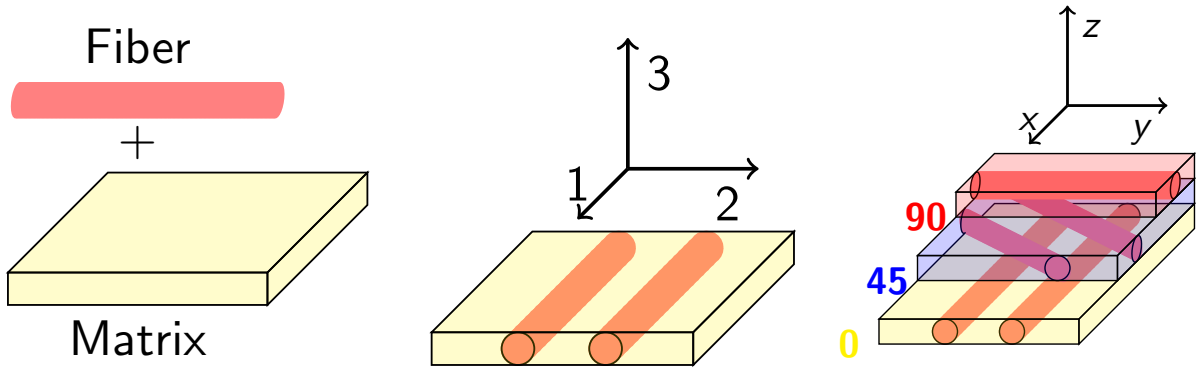

(a) Constituents. (b) Unidirectionnal ply. (c) Stacking sequence.

Figure 1.1: Different scales of the composite material.

With all these assumptions, the constitutive relations (strain-stress) for an orthotropic lamina in the principal material coordinates of the lamina (Figure 1.1b) are:

$$\begin{pmatrix} \sigma_1 \\ \sigma_2 \\ \tau_{12} \end{pmatrix} = \begin{bmatrix} Q_{11} & Q_{12} & 0 \\ Q_{12} & Q_{22} & 0 \\ 0 & 0 & Q_{66} \end{bmatrix} \begin{pmatrix} \epsilon_1 \\ \epsilon_2 \\ \gamma_{12} \end{pmatrix}, \tag{1.1}$$

where ϵ_1, ϵ_2 and γ_{12} are the strain components referred to the material coordinate system, the Q_{ij}'s are the reduced laminate stiffness components, defined in terms of the material's longitudinal modulus (E_1), transverse modulus (E_2), shear modulus (G_{12}) and Poisson ratio (ν_{12}) as:

$$Q_{11} = \frac{E_1}{1-\nu_{12}\nu_{21}}, \quad Q_{12} = \frac{\nu_{12}E_2}{1-\nu_{12}\nu_{21}}, Q_{22} = \frac{E_2}{1-\nu_{12}\nu_{21}}, \quad Q_{66} = G_{12}. \tag{1.2}$$

In the CLPT framework, the laminate is made of orthotropic layers with their material axes oriented with respect to the laminate coordinates. A laminate is constructed by stacking multiple plies with a given thickness t_k and orientation angle θ_k with respect to the laminate axes (Figure 1.1c). The constitutive equations of each layer must be transformed to the laminate coordinates as follows:

$$\begin{pmatrix} \sigma_{xx} \\ \sigma_{yy} \\ \tau_{xy} \end{pmatrix} = \begin{bmatrix} \overline{Q}_{11} & \overline{Q}_{12} & \overline{Q}_{16} \\ \overline{Q}_{12} & \overline{Q}_{22} & \overline{Q}_{26} \\ \overline{Q}_{16} & \overline{Q}_{26} & \overline{Q}_{66} \end{bmatrix} \begin{pmatrix} \epsilon^\circ_{xx} + z\kappa_{xx} \\ \epsilon^\circ_{yy} + z\kappa_{yy} \\ \gamma^\circ_{xy} + z\kappa_{xy} \end{pmatrix} \quad \text{with} \quad z_{k-1} < z < z_k, \tag{1.3}$$

where z_k and z_{k-1} are the positions of the k^{th} skin layer (see Figure 1.2) such as $z_{k-1} - z_k = t_k$, $\boldsymbol{\epsilon}^\circ$ denote the strains at the midplane, $\boldsymbol{\kappa}$ the curvature, $\overline{Q}_{ij}$'s are the lamina stiffness components in the laminate coordinate system of the k^{th} layer and are given by:

$$\begin{aligned} \overline{Q}_{11} &= U_1 + U_2\cos 2\theta_k + U_3\cos 4\theta_k, \\ \overline{Q}_{12} &= U_4 - U_3\cos 4\theta_k, \\ \overline{Q}_{22} &= U_1 - U_2\cos 2\theta_k + U_3\cos 4\theta_k, \\ \overline{Q}_{66} &= U_5 + U_3\cos 4\theta_k, \\ \overline{Q}_{16} &= (U_2\sin 2\theta_k + 2U_3\sin 4\theta_k)/2, \\ \overline{Q}_{26} &= (U_2\sin 2\theta_k - 2U_3\sin 4\theta_k)/2, \end{aligned} \tag{1.4}$$

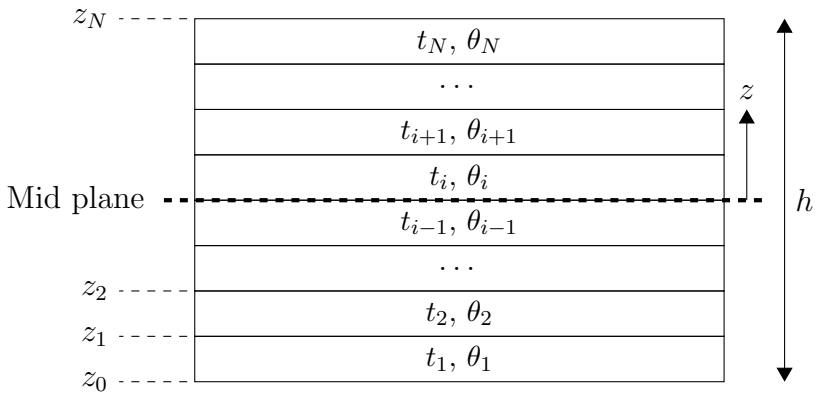

Figure 1.2: Schematic view of a composite laminate consisting of N laminae with orientation θ_k, thickness t_k and coordinate z_k from the mid-plane.

where the U_i's are material parameters derived from the material properties of the lamina as follows:

$$\begin{pmatrix} U_1 \\ U_2 \\ U_3 \\ U_4 \\ U_5 \end{pmatrix} = \frac{1}{8} \begin{bmatrix} 3 & 3 & 2 & 4 \\ 4 & -4 & 0 & 0 \\ 1 & 1 & -2 & -4 \\ 1 & 1 & -6 & -4 \\ 1 & 1 & -2 & 4 \end{bmatrix} \begin{pmatrix} Q_{11} \\ Q_{22} \\ Q_{12} \\ Q_{66} \end{pmatrix}. \tag{1.5}$$

The stresses evolve continuously piecewise through the thickness of the laminate. Hence, stress and moment resultants are expressed as the integration of laminate in-plane stresses throughout the thickness of the laminate:

$$N_x = \int_{-h/2}^{h/2} \sigma_x dz, \qquad N_y = \int_{-h/2}^{h/2} \sigma_y dz, \qquad N_{xy} = \int_{-h/2}^{h/2} \tau_{xy} dz, \tag{1.6}$$

$$M_x = \int_{-h/2}^{h/2} \sigma_x z dz, \quad M_y = \int_{-h/2}^{h/2} \sigma_y z dz, \quad M_{xy} = \int_{-h/2}^{h/2} \tau_{xy} z dz. \tag{1.7}$$

Substituting layer stresses from Eq.(1.3) into the above equations, we obtain the constitutive relations for the laminate:

$$\begin{Bmatrix} N_x \\ N_y \\ N_{xy} \end{Bmatrix} = \begin{bmatrix} A_{11} & A_{12} & A_{16} \\ A_{12} & A_{22} & A_{26} \\ A_{16} & A_{26} & A_{66} \end{bmatrix} \begin{Bmatrix} \epsilon_x^\circ \\ \epsilon_y^\circ \\ \gamma_{xy}^\circ \end{Bmatrix} + \begin{bmatrix} B_{11} & B_{12} & B_{16} \\ B_{12} & B_{22} & B_{26} \\ B_{16} & B_{26} & B_{66} \end{bmatrix} \begin{Bmatrix} \kappa_x \\ \kappa_y \\ \kappa_{xy} \end{Bmatrix}, \tag{1.8}$$

$$\begin{Bmatrix} M_x \\ M_y \\ M_{xy} \end{Bmatrix} = \begin{bmatrix} B_{11} & B_{12} & B_{16} \\ B_{12} & B_{22} & B_{26} \\ B_{16} & B_{26} & B_{66} \end{bmatrix} \begin{Bmatrix} \epsilon_x^\circ \\ \epsilon_y^\circ \\ \gamma_{xy}^\circ \end{Bmatrix} + \begin{bmatrix} D_{11} & D_{12} & D_{16} \\ D_{12} & D_{22} & D_{26} \\ D_{16} & D_{26} & D_{66} \end{bmatrix} \begin{Bmatrix} \kappa_x \\ \kappa_y \\ \kappa_{xy} \end{Bmatrix}, \tag{1.9}$$

where:

$$\begin{aligned} A_{ij} &= \sum_{k=1}^{N} (Q_{ij})_k \left(z_k - z_{k-1}\right), \\ B_{ij} &= \sum_{k=1}^{N} (Q_{ij})_k \left(z_k^2 - z_{k-1}^2\right), \\ D_{ij} &= \sum_{k=1}^{N} (Q_{ij})_k \left(z_k^3 - z_{k-1}^3\right). \end{aligned} \tag{1.10}$$

The $\boldsymbol{A}$ and $\boldsymbol{D}$ matrices are, respectively, the membrane and bending stiffness matrices, which relate the in-plane stress resultants to the mid-plane strains and the moment resultants to the curvatures of the mid-plane of a laminate. The $\boldsymbol{B}$ matrix is the bending-membrane coupling matrix that relates the in-plane stress resultants to the curvatures and the moment resultants to the mid-plain strains of a laminate. This coupling can be beneficial for particular structural applications.

1.2.3 Modeling using lamination parameters

The constitutive relations presented in the previous section include the design variables in the $\overline{Q}_{ij}$ terms, which include the layer orientation angles via Eq.(1.4) and the thicknesses of the layers. Another form of representing the $\boldsymbol{A}$, $\boldsymbol{B}$ and $\boldsymbol{D}$ matrices is based on the use of lamination parameters (LPs) introduced by Tsai and Hahn (1980). Considering a laminate with a total thickness h and identical plies, i.e., with the same material parameters and thickness, laminate stiffness matrices can be expressed as:

$$\begin{aligned}
\boldsymbol{A} &= h(\boldsymbol{\Gamma}_0 + \boldsymbol{\Gamma}_1 \mathrm{v}_1^A + \boldsymbol{\Gamma}_2 \mathrm{v}_2^A + \boldsymbol{\Gamma}_3 \mathrm{v}_3^A + \boldsymbol{\Gamma}_4 \mathrm{v}_4^A), \\
\boldsymbol{B} &= \frac{h^2}{4}(\boldsymbol{\Gamma}_1 \mathrm{v}_1^B + \boldsymbol{\Gamma}_2 \mathrm{v}_2^B + \boldsymbol{\Gamma}_3 \mathrm{v}_3^B + \boldsymbol{\Gamma}_4 \mathrm{v}_4^B), \\
\boldsymbol{D} &= \frac{h^3}{12}(\boldsymbol{\Gamma}_0 + \boldsymbol{\Gamma}_1 \mathrm{v}_1^D + \boldsymbol{\Gamma}_2 \mathrm{v}_2^D + \boldsymbol{\Gamma}_3 \mathrm{v}_3^D + \boldsymbol{\Gamma}_4 \mathrm{v}_4^D),
\end{aligned} \tag{1.11}$$

where $\boldsymbol{\Gamma}_i$ are fully defined by material parameters of Eq.(1.5) as follows:

$$\begin{gathered}
\boldsymbol{\Gamma}_0 = \begin{bmatrix} U_1 & U_4 & 0 \\ U_4 & U_1 & 0 \\ 0 & 0 & U_5 \end{bmatrix}, \quad \boldsymbol{\Gamma}_1 = \begin{bmatrix} U_2 & 0 & 0 \\ 0 & -U_2 & 0 \\ 0 & 0 & 0 \end{bmatrix}, \quad \boldsymbol{\Gamma}_2 = \begin{bmatrix} 0 & 0 & U_2/2 \\ 0 & 0 & U_2/2 \\ U_2/2 & U_2/2 & 0 \end{bmatrix}, \\
\boldsymbol{\Gamma}_3 = \begin{bmatrix} U_3 & -U_3 & 0 \\ -U_3 & U_3 & 0 \\ 0 & 0 & -U_3 \end{bmatrix}, \quad \boldsymbol{\Gamma}_4 = \begin{bmatrix} 0 & 0 & U_3 \\ 0 & 0 & -U_3 \\ U_3 & -U_3 & 0 \end{bmatrix}.
\end{gathered} \tag{1.12}$$

The lamination parameters are defined as follows:

$$v_{[1,2,3,4]}^{A,B,D} = H(\boldsymbol{\theta}) = \frac{1}{\int_{-h/2}^{h/2} z^p \, dz} \int_{-h/2}^{h/2} z^p \left[\cos(2\theta), \sin(2\theta), \cos(4\theta), \sin(4\theta)\right] \, dz, \tag{1.13}$$

where p depends on which matrix is considered: $p = 0$ for $\boldsymbol{A}$, $p = 1$ for $\boldsymbol{B}$ and $p = 2$ for $\boldsymbol{D}$ and we call H the mapping of the stacking sequence to the lamination parameters. Each laminate stiffness matrices ($\boldsymbol{A}$, $\boldsymbol{B}$ or $\boldsymbol{D}$) can be expressed as a linear combination of Tsai-Pagano material parameters (Eq. 1.5) and the LPs. Then, the influence of the laminate thickness, material parameters, and the stacking sequence is decoupled. Each tensor is represented by four different LPs, and the stiffness response of a laminate is thus represented by up to twelve LPs.

1.2.4 Modeling using polar parameters

Polar parameters (PPs) are issued from the extension of the polar representation to the case of fourth-order elastic tensors (Verchery, 1982). This operation leads to the definition of six polar components for a fourth-order tensor of the elastic type $\mathbb{Q}$. These are the scalars T_0 and T_1, the moduli R_0 and R_1, and the polar angles Φ_0 and Φ_1. The first four are invariants by rotation of the reference frame, while the angular difference $\Phi_0 - \Phi_1$ constitutes the fifth and last polar invariant.

Once these parameters are defined, it is possible to write the link between the Cartesian components Q_{ijkl} in a $1-2$ axis system and the polar components of $\mathbb{Q}$:

$$\begin{array}{rcccccccccc}
Q_{1111} = & & T_0 & + & 2T_1 & + & R_0\cos 4\Phi_0 & + & 4R_1\cos 2\Phi_1, \\
Q_{1122} = & - & T_0 & + & 2T_1 & - & R_0\cos 4\Phi_0, & & \\
Q_{1112} = & & & & & & R_0\sin 4\Phi_0 & + & 2R_1\sin 2\Phi_1, \\
Q_{2222} = & & T_0 & + & 2T_1 & + & R_0\cos 4\Phi_0 & - & 4R_1\cos 2\Phi_1, \\
Q_{2212} = & & & & & - & R_0\sin 4\Phi_0 & + & 2R_1\sin 2\Phi_1, \\
Q_{1212} = & & T_0 & & & - & R_0\cos 4\Phi_0, & &
\end{array} \tag{1.14}$$

and vice-versa:

$$\begin{array}{rcccccccccc}
8T_0 = & Q_{1111} & & & - & 2Q_{1122} & + & 4Q_{1212} & & & + & Q_{2222}, \\
8T_1 = & Q_{1111} & & & + & 2Q_{1122} & & & & & + & Q_{2222}, \\
8R_0e^{4i\Phi_0} = & Q_{1111} & + & 4iQ_{1112} & - & 2Q_{1122} & - & 4Q_{1212} & - & 4iQ_{1222} & + & Q_{2222}, \\
8R_1e^{2i\Phi_1} = & Q_{1111} & + & 2iQ_{1112} & & & & & + & 2iQ_{1222} & - & Q_{2222}.
\end{array} \tag{1.15}$$

The rotation transformation laws of the reference frame are greatly simplified in the polar representation. Thus, when we change from the $1-2$ reference frame to the $x-y$ reference frame rotated by an angle θ, only the polar angles Φ_0 and Φ_1 vary and become, respectively, $\Phi_0-\theta$ and $\Phi_1-\theta$. The relations show that the Cartesian components of a fourth-order tensor are sums of an invariant quantity which is a function of the polar moduli T_0 and T_1, and of two quantities which depend on trigonometric functions of the angle θ. Thus, it is possible to distinguish the parameters T_0 and T_1, related to the isotropic part, from the quantities $R_0e^{4i\Phi_0}$ and $R_1e^{2i\Phi_1}$, related to the anisotropic part of the tensor $\boldsymbol{Q}$.

This polar representation is generic to any material with in-plane anisotropy, and is not necessarily committed for composite materials and the CLPT. However, the polar representation method can be applied to the membrane, bending and coupling between the membrane and bending stiffness tensors $\boldsymbol{A}$, $\boldsymbol{D}$ and $\boldsymbol{B}$ just as it is applied to tensor $\boldsymbol{Q}$. The polar invariants are then denoted as $(T_0^A, T_1^A, R_0^A, R_1^A, \Phi_0^A - \Phi_1^A)$ for the membrane behavior, $(T_0^B, T_1^B, R_0^B, R_1^B, \Phi_0^B - \Phi_1^B)$ for the coupling behavior, and $(T_0^D, T_1^D, R_0^D, R_1^D, R_0^D, \Phi_0^D - \Phi_1^D)$ for the bending behavior. All polar angles are expressed in the $x-y$ laminate reference frame.

In the case of identical plies in a laminate, the membrane, coupling, and bending components are then expressed in terms of the polar parameters of the single base layer $(\overline{T_0}, \overline{T_1}, \overline{R_0}, \overline{R_1}, \overline{\Phi_0}, \overline{\Phi_1})$ (Vincenti, 2002)[↗]:

$$\begin{aligned}
T_0^A &= h\overline{T_0}, \quad R_0^A e^{4i\Phi_0^A} = \frac{h}{N}\overline{R_0}e^{4i\overline{\Phi}_0}\sum_{k=1}^{N} e^{4i\theta_k}, \\
T_1^A &= h\overline{T_1}, \quad R_1^A e^{2i\Phi_1^A} = \frac{h}{N}\overline{R_1}e^{2i\overline{\Phi_1}}\sum_{k=1}^{N} e^{2i\theta_k},
\end{aligned} \tag{1.16}$$

$$\begin{aligned}
T_0^B &= \frac{1}{2}\left(\frac{h}{N}\right)^2 \overline{T_0}\sum_{k=1}^{N} b_k, \quad R_0^B e^{4i\Phi_0^B} = \frac{1}{2}\left(\frac{h}{N}\right)^2 \overline{R_0}e^{4i\overline{\Phi_0}}\sum_{k=1}^{N} b_k e^{4i\theta_k}, \\
T_1^B &= \frac{1}{2}\left(\frac{h}{N}\right)^2 \overline{T_1}\sum_{k=1}^{N} b_k, \quad R_1^B e^{2i\Phi_1^B} = \frac{1}{2}\left(\frac{h}{N}\right)^2 \overline{R_1}e^{2i\overline{\Phi_1}}\sum_{k=1}^{N} b_k e^{2i\theta_k},
\end{aligned} \tag{1.17}$$

$$\begin{aligned}
T_0^D &= \frac{1}{12}\left(\frac{h}{N}\right)^3 \overline{T_0}\sum_{k=1}^{N} d_k, \quad R_0^D e^{4i\Phi_0^D} = \frac{1}{12}\left(\frac{h}{N}\right)^3 \overline{R_0}e^{4i\overline{\Phi_0}}\sum_{k=1}^{N} d_k e^{4i\theta_k}, \\
T_1^D &= \frac{1}{12}\left(\frac{h}{N}\right)^3 \overline{T_1}\sum_{k=1}^{N} d_k, \quad R_1^D e^{2i\Phi_1^D} = \frac{1}{12}\left(\frac{h}{N}\right)^3 \overline{R_1}e^{2i\overline{\Phi_1}}\sum_{k=1}^{N} d_k e^{2i\theta_k}.
\end{aligned} \tag{1.18}$$

In (1.17) and (1.18), the coefficients b_k and d_k are relative integers which represent the influence of the plies position k on the behavior considered, respectively coupling and bending (Vincenti, 2002). Their expression depends on the parity of the total number of layers N in the following form:

$$N \text{ pair} : \quad b_k = 2k - \frac{|k|}{k} \quad ; \quad d_k = 12k^2 - 12|k| + 4 \tag{1.19a}$$

$$N \text{ impair} : \quad b_k = 2k \ , \ b_0 = 0 \quad ; \quad d_k = 12k^2 + 1 \ , \ d_0 = 0. \tag{1.19b}$$

In the CLPT framework, the polar parameters are then similar to lamination parameters. It is possible to switch from lamination parameters to polar invariants as follows:

$$\begin{aligned} \frac{R_0^{(.)}}{R_0} e^{4i\phi^{(.)}} &= \mathrm{v}_3^{(.)} + i\mathrm{v}_4^{(.)}, \\ \frac{R_1^{(.)}}{R_1} e^{2i\phi^{(.)}} &= \mathrm{v}_1^{(.)} + i\mathrm{v}_2^{(.)}, \end{aligned} \tag{1.20}$$

where (.) denotes the behavior studied, i.e., A for membrane, D for bending or B for membrane/bending coupling. For the sake of synthesis, a deeper scientific discussion about polar parameters is not given here. The reader may refer to the book of Vannucci (2018) for a more in-depth discussion around the polar parameters and their link with the lamination parameters.

1.2.5 Conclusion

Composite laminates have three main design variables: the number of layers, the orientation of each layer with respect to a fixed reference frame, and the through-the-thickness order in which the layers are placed in the laminate, which is known as the stacking sequence. These new degrees of freedom in the composite design can change the in-plane and bending stiffness of the laminate. The orientation of each ply in the laminate directly affects the in-plane stiffness properties of the laminate. The bending stiffness of a laminate is affected by the stacking sequence. Such a design problem can be formulated as an optimization aiming at improving structural performances, e.g., stiffness, strength, bucking resistance, natural frequency, etc., or decrease the mass.

1.3 Optimization of composite laminates

The general problem of a stacking sequence optimization with respect to an objective f and n_g constraints g_i can be formulated as follows:

$$\min_{\{\boldsymbol{\theta}, N\}} f \quad \text{subject to: } g_j \leqslant 0 \quad j = 1, \ldots, n_g, \tag{1.21}$$

where $\boldsymbol{\theta} = [\theta_1, \ldots, \theta_N]$ is the stacking sequence of the laminate with N plies. The number of plies can be a variable of the optimization in order to minimize the mass of a structure, for example. Therefore the number of design variables may vary over the optimization process. Moreover, some restrictions on the ply orientations may exist. As a result, the problem is highly non-linear and non-convex.

To solve this kind of optimization problem, two types of algorithms may usually be adopted: meta-heuristics and gradient-based methods. The former are employed to find a global optimum

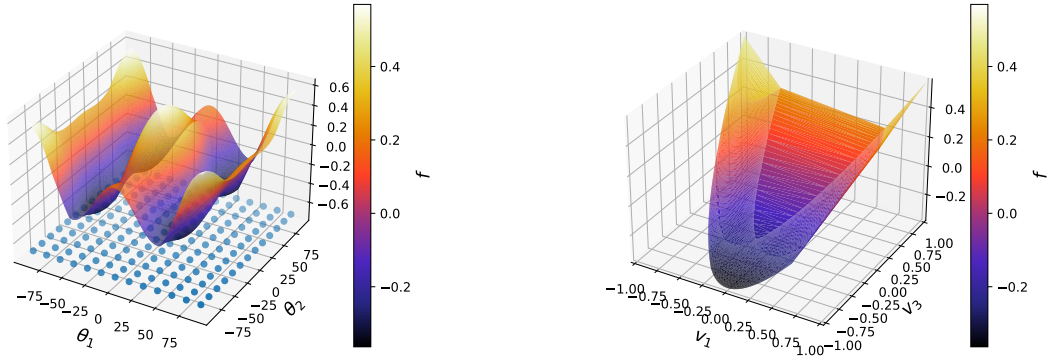

(a) 2D mesoscopic space.

(b) 2D macroscopic space.

Figure 1.3: Response example of a function in both spaces.

with the capability to explore the highly non-convex domain and handle the problem's combinatorial nature. The latter are selected to obtain a fast convergence to a solution, minimizing the number of evaluations of structural analyses and handling large numbers of variables and constraints, but can be trapped by local optima.

The fastest way to optimize a structure is to assign the same laminate to the entire structure. This is called the *constant stiffness design* Ghiasi et al. (2009). It is quite a mature formalism and is well suited for structures subject to uniform loading without particular geometrical singularities. However, it does not significantly improve the structure performances for more complex applications compared to metallic design. To overcome this, another design family exists where variations of thickness, ply orientations, or fiber volume fraction are applied. This optimization formalism is called *variable-stiffness design*. It can provide a wider range of possible designs and improved performance useful for aeroelastic applications, for example. However, the higher number of design variables and the manufacturability conditions for the continuity between the zones of the structure lead to a more complex problem. General strategies have been developed for optimizing composite laminates, depending on how the composite laminates are parametrized. An extensive review of algorithms used for the optimization of composite laminates is found in Ghiasi et al. (2009, 2010); Xu et al. (2018). Strategies found in the literature can be split into two families: direct methods and bi-level approaches.

1.3.1 Direct methods

When composite laminate optimization is parametrized in terms of the explicit characteristics of a stacking sequence, i.e., ply thickness and ply orientations, direct methods are used to handle the combinatorial characteristic of the problem and is formulated as shown in the Eq.(1.21). The thickness is a discrete variable corresponding to an integer number of plies, and the ply orientations can be discrete depending on the manufacturing aspect. Furthermore, the multimodal and non-convex nature of the function of interest (see Figure 1.3a) do not allow the use of gradient-based methods. Direct search methods have the advantage of requiring no gradient information of the objective functions and the constraints. It can be advantageous since derivative calculations are often costly or impossible to obtain. This type of problem can be solved using metaheuristic algorithms like genetic algorithm (GA) (Conceição António, 2001; Riche and Haftka, 1993) or simulated annealing (SA) (Erdal and Sonmez, 2005), which are

suited for discrete problems and are the most popular direct methods for composite laminate optimization.

Simulated annealing mimics the annealing process in metallurgy (Kirkpatrick, 1984). The SA conducts a global search by permitting unfavorable solutions to be accepted with a probability related to a parameter called "temperature". The temperature is initially set to a high value, which corresponds to a higher probability of accepting a wrong move, and then, a user-defined cooling schedule gradually reduces this value. Rao et al. (2002) conducted an optimization of the laminate composite plate to maximize its natural frequency. The results indicated that the SA effectively deals with design problems concerning layup optimization. However, one of the problems in SA is the generation of a sequence of points that converges to a non-optimal solution. Therefore, Romeijn et al. (1999) propose to increase the occurence rate of sampling points far from the current point. To increase the convergence rate, Genovese et al. (2005) proposed a two-level SA including a *global annealing* where all design variables were perturbed simultaneously and a *local annealing* where only one design variable was perturbed after each iteration of the *global annealing* in order to improve the trial point locally.

Simulated annealing is a good choice for the general case of optimal layup selection; however, it has some convergence issues. Genetic algorithm is more robust although it is often computationally more time consuming (Sargent et al., 1995; Di Sciuva et al., 2003).

A genetic algorithm is an evolutionary optimization technique using Darwin's principle of "survival of the fittest" to improve a population of solutions. GA tries to imitate biological evolution, creating a random design population at first and choosing over the options with a better fitness to continue the genetic evolution, creating a new further evolved population. The main operations of the GA consist of selection, i.e, determining which individuals are more likely to achieve the best results; crossover, i.e., crossing two parents to create one alternate offspring; and mutation, i.e., creating new individuals by modifying the existing ones randomly. The population size of GA must be suitably large in order to find a global solution. Despite the high computation cost, its simple coding and flexibility in handling problems with various variables and objective functions make GA useful for problems with multimodal functions, discrete variables, and functions with costly derivatives. That is why GA has been the most popular method used for optimizing a laminated composite (Venkataraman and Haftka, 1999).

Callahan and Weeks (1992), Nagendra et al. (1992) and Riche and Haftka (1993) firstly used GA to design the stacking sequence of laminated composite structures. Since then, GA has been applied to the design of laminated composite structures with various objectives and constraints, such as weight (Gantovnik and Gu, 2002; Walker and Smith, 2003; Narayana Naik et al., 2008) , buckling loads (Kogiso et al., 1994; Todoroki and Ishikawa, 2004; Abouhamze and Shakeri, 2007), stiffness Potgieter and Stander (1998), deflection Walker and Smith (2003). Moreover, GA has been used for the design of a variety of composite structures ranging from simple rectangular plates to complex geometries such as sandwich plates Lin and Lee (2004), stiffened plates Nagendra et al. (1996), bolted composite lap joints Kradinov et al. (2007).

Although GA has been widely used for designing composite structures, an obvious disadvantage is its convergence rate. Like all the population-based evolutionary algorithms, GA requires many generations before converging to the final solution Potgieter and Stander (1998). A large number of computations are involved in each generation, which results in time-consuming and expensive computations.

Other less popular heuristic methods have been used, such as tabu search (Pai et al., 2003), scatter search (Rama Mohan Rao and Arvind, 2005) or particle swarm (Suresh et al., 2007).

In the framework of variable-stiffness design, design variables are locally defined over different zones of a structure, and it is complex for the Finite Element Method to handle the possible huge number of plies. Therefore, the idea is to express the composite as a homogeneous material, and this will regularize the function of interest responses. This is achieved by using continuous variables to linearize the structural response. This conduct to another type of optimization: the bi-level framework.

1.3.2 Bi-level approach

The bi-level framework constitutes an efficient way of solving composite laminate structures. It is based on the different representations of a laminate either by its stacking sequence or by its homogeneous material properties in membrane, bending, and membrane-bending coupling. The process consists in dividing the optimization of the stacking sequence into two distinct problems, solved one after the other.

1.3.2.1 Problem formulation

The first level problem optimizes the homogeneous material properties and the thickness h of a laminate with respect to the same objective and constraints of the global optimization problem of Eq.1.21:

$$\min_{\{\boldsymbol{A},\boldsymbol{B},\boldsymbol{D},h\}} f \quad \text{subject to:} \begin{cases} g_j \leqslant 0 & j = 1,\dots,n_g, \\ \{\boldsymbol{A},\boldsymbol{B},\boldsymbol{D}\} \in \mathcal{D}_{\text{lam}}, & \\ h \in \mathcal{D}_{\text{thick}}, & \end{cases} \tag{1.22}$$

where $\mathcal{D}_{\text{lam}}$ and $\mathcal{D}_{\text{thick}}$ are the design domains of the laminate and of its thickness. The stiffness matrices can be parametrized by lamination parameters or polar parameters. The solution of the optimization problem of Eq.(1.22) constitutes target material properties $\boldsymbol{A}^{\text{des}}$, $\boldsymbol{B}^{\text{des}}$ and $\boldsymbol{D}^{\text{des}}$ and thickness h^{des} for the second-level problem.

The second level problem aims at retrieving the stacking sequence that has the target material properties and thickness obtained from the first-level problem of Eq.(1.22):

$$\min_{\boldsymbol{\theta}=[\theta_1,\dots,\theta_N]} \|[\boldsymbol{A}^{\text{des}},\boldsymbol{B}^{\text{des}},\boldsymbol{D}^{\text{des}}] - [\boldsymbol{A}(\boldsymbol{\theta}),\boldsymbol{B}(\boldsymbol{\theta}),\boldsymbol{D}(\boldsymbol{\theta})]\| \quad \text{subject to: } N = \lceil h^{\text{des}}/t_{\text{ply}} \rceil, \tag{1.23}$$

where $\lceil . \rceil$ denotes a rounding operation to the integer number of plies and t_{ply} the ply thickness.

The advantage of the first level formulation is that the domain of homogenized material properties is convex, and the functions of interest (objective and constraints) are more regular than in the ply orientations design space, in which the responses are highly non-linear and non-convex (see Figure 1.3). Hence, the first level optimization can be solved with gradient-based algorithms, thus limiting the computational cost. Moreover, the number of design variables is independent of the number of plies, and that simplifies the optimization process when dealing with thickness variations. The number of design variables can also decrease when some hypotheses are made. For example, the coupling between bending and in-plane extension can be useful for some applications, but it is commonly considered undesirable, which reduces the tensor $\boldsymbol{B}$ to zero. In some industrial applications, the orthotropic hypothesis is made where the tension-shear and bending-twist couplings are avoided, meaning that the coupling terms A_{16}, A_{26}, D_{16} and D_{26} are zeros.

This approach, however, shifts the challenge to the second level - i.e., the inverse mapping problem from the homogenized space to the stacking sequence - which is highly multimodal and complex. This step only requires the evaluation of the CLPT, a low computational calculation, in order to match a stacking sequence to target stiffness properties. Hence, it is solved mostly via meta-heuristics algorithms. This bi-level framework represents one of the most effective methods to optimize composite laminate structures Albazzan et al. (2019).

One difficulty in directly using tensor components is that their cartesian representation is quite complex when the reference frame is rotated. Nevertheless, these difficulties can be reduced with the use of the *lamination parameters* or the *polar parameters* to parametrize the stiffness in the first-level optimization. Moreover, instead of using the component of the tensors in Eq.(1.23), LPs or PPs could be the target for the second level problem.

Lamination parameters, introduced in Section 1.2.3 were first used by Miki and Sugiyama (1991) to parametrize an optimization with the LPs. Yamazaki (1996) apply them in a bi-level framework, assuming ply orientations of 0°, ±45° or 90°. Bloomfield et al. (2008) applied the bi-level approach to minimizing the mass of a supported composite plate under different loading conditions. At the first level, a gradient-based method is used, and then, at the second level, a particle swarm optimization algorithm is used to determine the stacking sequence with a possible 30° increment for ply orientation. Other notable developments are the formulation of strength-based failure criteria directly in the first-level optimization (IJsselmuiden et al., 2008). Moreover, the LPs formulation has been extended to higher-order shear deformation theories in order to handle thick laminates and sandwich structures (Balabanov et al., 2012; Irisarri et al., 2021).

The **polar parameters**, introduced in Section 1.2.4, were first used in order to find laminates with particular properties without making any assumptions on the stacking sequence, such as uncoupling or homogeneity of the membrane and bending behaviors Vannucci and Verchery (2001). Then Vincenti et al. (2001) add the assumptions of uncoupling and quasi-homogeneity of the laminate elastic tensors. The PPs were also used for composite laminate optimization with the bi-level framework (Jibawy et al., 2011; Montemurro et al., 2012b,a). No restrictions are imposed on the stacking sequence during the second optimization level. The multi-scale two-level (MS2L) optimization framework has been applied to realistic engineering problems in a constant stiffness framework. Montemurro et al. conducted design optimization of stiffened panels Montemurro et al. (2018) or sandwich panels Montemurro et al. (2016) with manufacturing constraints. This methodology is also applied to variable stiffness design Catapano et al. (2015).

1.3.2.2 Feasible region for the first-level optimization

The lamination and polar parameters, presented in Section 1.2.3 and Section 1.2.4, allow to represent each of the three stiffness tensors $\boldsymbol{A}$, $\boldsymbol{B}$ and $\boldsymbol{D}$ characterizing the plane anisotropic behavior of an anisotropic material. However, the material properties need to be realizable by composite laminates. The aim is now to restrict the parametrization. Indeed, the terms of the stiffness tensors $\boldsymbol{A}$, $\boldsymbol{B}$ and $\boldsymbol{D}$ become intrinsically related by compatibility conditions that are complex to derive in a general case. One of the primary difficulties faced is the development of direct relations to define the feasible region of the lamination parameters or the polar parameters. Researchers have tackled this problem in the literature where an analytical expression of the feasible region combining all variables is still unavailable. Therefore, the

laminates are usually restricted to particular families of stacking sequences (mainly restricting the search to a small set of ply orientations). Uncoupled laminates are considered, which verify $\boldsymbol{B} = 0$.

In the **lamination parameters** framework, Miki and Sugiyama (1991) determined the feasible regions to describe both the in-plane or out-of-plane stiffnesses of an orthotropic laminate using two in-plane or two out-of-plane lamination parameters as follow:

$$2\left(\mathrm{v}_1^{A,D}\right)^2 - 1 - \mathrm{v}_3^{A,D} \leq 0. \tag{1.24}$$

The domain $\mathcal{D}_{\text{lam}}$ with this compatibility constraint is shown in Figure 1.4a. Fukunaga and Sekine (1992) derived the feasible regions of the four in-plane and four out-of-plane lamination parameters separately. Next, Grenestedt and Gudmundson (1993) derived explicit expressions between certain sets of the in-plane and out-of-plane lamination parameters. Later, Diaconu and Sekine (2004) derived explicitly the feasible regions of lamination parameters that related the in-plane, coupling, and out-of-plane lamination parameters to each other for 0°, ±45° or 90° plies. After that, Setoodeh et al. (2006) established a method based on successive convex hull approximations to approximate the boundary of the general feasible region of lamination parameters in the form of a huge number of linear inequalities that could be included explicitly as constraints. By contrast, Bloomfield et al. (2009) presented a method to derive constraints on the feasible region for any predefined ply angles. Even if these constraints appear as promising, it is still an approximation. More recently, an explicit feasible region combining four coupled lamination parameters of orthotropic laminates was finally derived by Wu et al. (2015).

In the **polar parameters** framework, an alternative, adopted in most of the works using the polar representation, is to assume that the laminates have a homogeneous membrane and bending behaviors (Montemurro et al., 2012b; Vannucci, 2013) which verify:

$$\boldsymbol{A}^* = \boldsymbol{D}^*, \tag{1.25}$$

where $\boldsymbol{A}^* = \dfrac{1}{h}\boldsymbol{A}$ and $\boldsymbol{D}^* = \dfrac{12}{h^3}\boldsymbol{D}$ are the stiffness tensors normalized by the total thickness h of the laminate. This assumption has the advantage of further reducing the total number of variables to parametrize the properties of the laminate to only four for either the membrane or the bending tensors: R_0, R_1, ϕ_0 and ϕ_1. The orthotropy is also considered, and it is simply expressed, with the polar formalism, by:

$$\phi_0 - \phi_1 = K\frac{\pi}{4}, \quad K \in 0, 1. \tag{1.26}$$

The parameter ϕ_0 is now a function of ϕ_1 hence simplifying the relations of Eq.(1.14):

$$\begin{aligned} R_0 \cos 4\phi_0 &= (-1)^K R_0 \cos 4\phi_1, \\ R_0 \sin 4\phi_0 &= (-1)^K R_0 \sin 4\phi_1. \end{aligned} \tag{1.27}$$

For the sake of simplicity, the quantity $R_{0k} = (-1)^K R_0$ is introduced, where the sign of the real R_{0k} determines the value of K ($K = 0$ or $K = 1$). This reduces the total number of design variables to only three parameters: R_{0k}, R_1, and ϕ_1, where ϕ_1 is interpreted as the principal axis of orthotropy. We can introduce the dimensionless quantities:

$$\rho_{0k} = \frac{R_{0k}}{R_0}, \quad \rho_1 = \frac{R_1}{R_1}, \tag{1.28}$$

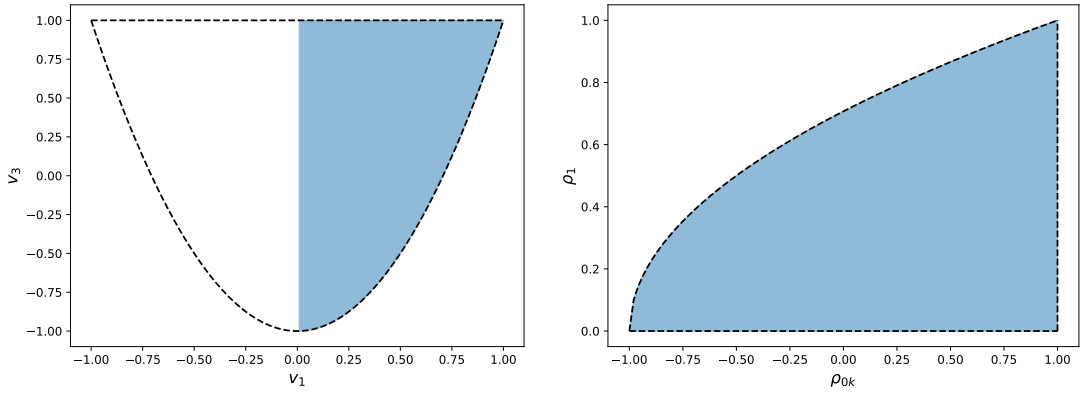

(a) Lamination parameters.

(b) Polar parameters.

Figure 1.4: Feasible domains with the assumption of orthotropic laminates.

and now the compatibility constraint is expressed as:

$$2\rho_1^2 - 1 - \rho_{0k} \leq 0, \tag{1.29}$$

which is similar to the lamination parameters compatibility constraint found in Eq.(1.24) with the assumption of orthotropic laminates.

Figure 1.4b illustrates the domain in the polar parameters space, which corresponds to the right side of the lamination parameters space. To project the polar invariant space on the left-hand side of the lamination parameters space, it is necessary to apply a $n\frac{\pi}{2}$ rotation of ϕ_1 with $n \in \mathbb{Z}$, the set of all integers.

1.3.2.3 Conclusion

Both stiffness parametrizations are available with the LP and PP. They are quite similar when applied to CLPT. At ONERA, the bi-level approach using lamination parameters has been applied to a buckling optimization of a composite plate (Irisarri et al., 2011) and in a variable stiffness framework, to sandwich structures (Irisarri et al., 2021) and to the aeroelastic optimization of a wing (Bordogna et al., 2020; Fabbiane et al., 2022). This is the reason why, in the following sections, this work will focus on a bi-level optimization strategy making use of the lamination parameters.

1.3.3 Laminate design rules

Usually, stacking sequences must verify general design rules to obtain certain mechanical and manufacturability properties. Moreover, in the variable stiffness framework, ensuring the continuity between the different zones along composite structures is an important issue (Lozano et al., 2016) that introduces additional design constraints.

Constraints issued from industrial practices are generally applied to the design of composite laminates and are brought from experience Bailie et al. (1997); MIL-HDBK-17 (2002). The most common design constraints are the following:

- **Symmetric laminates:** sufficient (though not necessary) condition to ensure that the coupling membrane-bending tensor vanishes.

- **Balanced laminates:** it avoids tension-shear and bending-twist coupling and ensures the orthotropy of the membrane properties but not those in bending in the general case. Further restraining ply orientations to only $0°, \pm 45°, 90°$ allows to limit bending orthotropy, even if not strictly enforced.

- **Continuity rule:** it constrains the maximum number of successive layers of the same orientation in order to avoid thick layers which favor transverse crack initiation. Generally, no more than four of the same layers are accepted.

- **Disorientation rule:** it constrains the maximum orientation change between two consecutive plies. It reduces interlaminar shear, which can cause delamination and crack propagation. Generally, no more than a $45°$ angle difference between two successive layers is accepted.

- **10% rule:** it corresponds to the minimum proportion of orientations plies in each of the $0°, \pm 45°, 90°$ directions. This rule prevents crack propagation.

- **Damage tolerance rule:** it consists in placing $\pm 45°$ plies on the outer faces of the laminate in order to protect the more stressed layers from small impacts and scratches.

In a variable-stiffness design framework, continuity rules ensure the manufacturability of the structure. Continuity constraints are used to force the continuity of fibers at the interfaces of contiguous zones. In literature, the commonly used methods are blending rules and curvilinear definitions.

When thickness varies, the orientations of the thinnest region must be included within the stacking sequence of any contiguous thicker laminate in order to blend panels of different thickness Kristinsdottir et al. (2001). First, blending has been implemented during stacking sequence retrieval. Van Campen and Gürdal (2009) proposed a corresponding point (CP) procedure using the constrained relation between in-plane and flexural LPs for balanced symmetric laminates without any restriction on orientations. Adams et al. (2004) proposed to use a guide-based approach where plies are dropped from a guide sequence. This method was extended to consider industrial laminate design guidelines by Irisarri et al. (2014) with Stacking Sequence Tables (SST) formulation, which allows ply drops anywhere in the sequence. Other strategies consist in patch-based approaches proposed by Zehnder and Ermanni (2006, 2007), which were brought to an industrially usable strategy by Irisarri et al. (2021). Consequently, two sets of constraints are used in the two subsequent optimizations. This reduces the chance of retrieving the stacking sequence design close to the optimal continuous solution. Hence, Macquart et al. (2016) proposed employing lamination parameters combined with a set of blending constraints to be used in the first-level optimization, i.e., the continuous optimization, to achieve more realistic and manufacturable continuous designs. They applied it in aeroelastic optimization of a wing model (Macquart et al., 2017), and the results demonstrate that applying the blending constraints significantly increases the chance of retrieving the stacking sequences that closely match the lamination parameter distribution. Panettieri et al. (2019) and Picchi Scardaoni et al. (2021) extended the derivation of these constraints to PPs.

The second type of blending condition concerns the design with variable-angle-tow plies, i.e. where the fiber orientations vary continuously within a ply. This type of laminate is manufactured by fiber placement processes and entails design rules that are reviewed by Lozano et al. (2016). The curvilinear definition uses a curvilinear function to model the fiber path and the laminate thickness variation. It can decrease design variable numbers significantly and guarantee structural continuity.

1.4 Extension to a reliability framework

While composite laminate optimization in a deterministic framework is something that has been studied for decades and is now mature, composite optimization under uncertainty has comparatively only been studied recently. Reliability analysis associated with the optimal design of composite structures has been a topic of interest since the end of the 1990s (Boyer, 1997; Conceição António, 2001; Adali et al., 2003)[][][] and reliability-based design optimization of composite structures is currently an important area of research. A review of ongoing developments on reliability analysis and RBDO applied to composite structures can be found in Chiachio et al. (2012)[].

In this section, the classical RBDO formulation is presented, followed by a state of the art of composite lamination optimization in a RBDO framework. Then the RBDO multi-scale formulation and the global approach proposed on this thesis are explained.

1.4.1 RBDO formulation

In general RBDO problems, both design variables and other system parameters can contain deterministic and/or random quantities. According to that, $\boldsymbol{\theta}$ is defined as the vector of design variables, and $\mathbf{p}$ describes the environmental parameters. In the following, subscripts r and d refer to random and deterministic quantities, respectively. These vectors can be written as follows:

$$\boldsymbol{\theta} = \begin{Bmatrix} \boldsymbol{\Theta}_r \\ \boldsymbol{\theta}_d \end{Bmatrix}, \quad \mathbf{p} = \begin{Bmatrix} \boldsymbol{P}_r \\ \boldsymbol{p}_d \end{Bmatrix}, \quad \mathbf{R} = \begin{Bmatrix} \boldsymbol{\Theta}_r \\ \boldsymbol{P}_r \end{Bmatrix}, \quad \mathbf{d} = \begin{Bmatrix} \boldsymbol{\theta}_d \\ \boldsymbol{p}_d \end{Bmatrix}. \tag{1.30}$$

Reliability analysis evaluates structural safety considering the random nature of all phenomena affecting a structural system. The performance function $g(\mathbf{R}, \mathbf{p})$ characterizes the response of the system. The design region is divided into two domains:

$$\text{Failure domain: } F = \{\mathbf{R}, \mathbf{p} \mid g(\mathbf{R}, \mathbf{d}) \geqslant 0\}. \tag{1.31}$$

$$\text{Safety domain: } S = \{\mathbf{R}, \mathbf{p} \mid g(\mathbf{R}, \mathbf{d}) < 0\}. \tag{1.32}$$

The boundary between failure and safety domains is the limit state surface, which generally is a hypersurface in the n-dimensional space of random variables $\mathbf{R}$. According to this, the failure probability $\mathbb{P}$ is formulated as:

$$\mathbb{P}\left(g(\mathbf{R}, \mathbf{p}) \geqslant 0\right) = \int \cdots \int_F \pi_{\mathbf{R}} d\mathbf{R}, \tag{1.33}$$

where $\pi_{\mathbf{R}}$ is the joint probability density function of the random variables. An example in two dimensions is shown in Figure 1.5 with both domain and the probability density function. Except in some cases, the integral expression cannot be resolved analytically because of the nonlinearity of $\pi_{\mathbf{R}}$ and also due to the number of random variables that can be large. Two approximate methods are often applied: stochastic simulations (e.g., crude Monte Carlo, importance sampling, subset sampling) using sometimes surrogate models or moment methods (e.g., first and second order reliability FORM/SORM) (Hasofer Abraham M. and Lind Niels C., 1974)[]. Some of these methods are detailed in Chapter 3.

The RBDO formulation can be set out in different ways. The two-level approaches consider the reliability constraints within the optimization loop (Nikolaidis and Burdisso, 1988; Tu

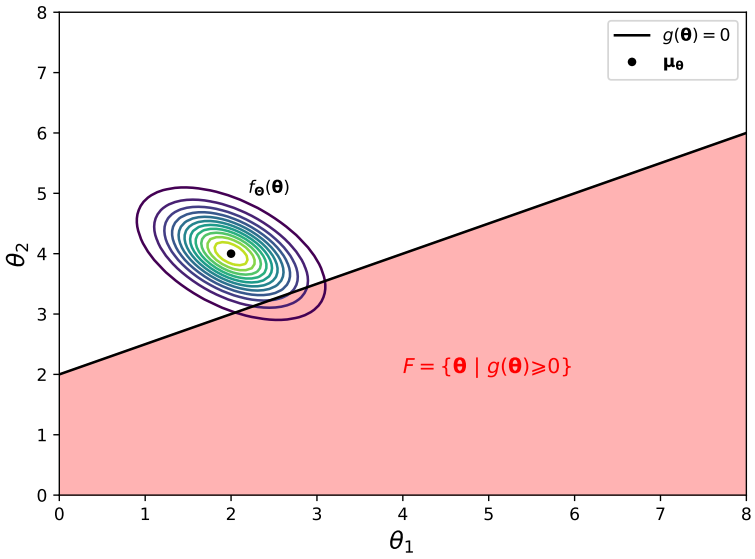

Figure 1.5: Physical space for the basic structural reliability problem.

et al., 1999). Mono-level approaches exist, such as Karush-Kuhn-Tucker (KKT) (Kuschel and Rackwitz, 1997) or single loop approach (SLA) (Chen et al., 1997) where the probabilistic constraint is approximated with deterministic values, converting the double loop into a single loop. Finally, uncoupled approaches, such as sequential optimization and reliability assessment (SORA) (Du and Chen, 2004) solve sequentially deterministic optimization procedures with a reliability analysis at the end of each optimization. The result of the reliability analysis allows to shift the constraint in the deterministic optimization. For further details on each formulation, the reader can refer to some reviews on optimization under uncertainty (Aoues and Chateauneuf, 2010; Yao et al., 2011; Lelièvre et al., 2016; Acar et al., 2021).

Remark 1.4.1. The **two-level approach** from the RBDO framework and the **bi-level approach** from the composite optimization framework are different and must not be confused with one another. They can however be complementary.

Mono-level or decoupled formulation seems to perform faster RBDO than the two-level approach (Aoues and Chateauneuf, 2010). However, in the mono-level approaches, KKT method shows weak stability on different test cases, and SLA could have some difficulties with nonlinear limit state function (Aoues and Chateauneuf, 2010). Decoupled approaches are interesting since they are able to deal with complex structures. However, they are based on approximation methods to compute the failure probability which can lead to inaccurate estimation with nonlinear limit state function Aoues and Chateauneuf (2010). In this thesis, mechanical instabilities are considered for the reliability constraint of the RBDO. These instabilities encourage doing the reliability analysis at each iteration, with the possibility of having different regions of convergence between the deterministic and the reliability-based optimization. Consequently, the two-level approach is preferred.

This approach is the most global one, where the uncertainties are controlled during the optimization process. The formulation of the problem is written in the following:

$$\min_{\boldsymbol{\mu}_{\boldsymbol{\Theta}_r}, \boldsymbol{\theta}_d} f\left(\boldsymbol{\mu}_{\mathbf{R}}, \mathbf{d}\right) \quad \text{subject to:} \begin{cases} h_i\left(\boldsymbol{\mu}_{\mathbf{R}}, \mathbf{d}\right) \leq 0 & i = 1, ..., n_d, \\ \mathbb{P}\left(g_j\left(\mathbf{R}, \mathbf{d}\right) \geqslant 0\right) \leq \mathbb{P}_j^{\max} & j = 1, ..., n_p, \end{cases} \tag{1.34}$$

where f is the deterministic cost function to be minimized, $\boldsymbol{\mu}_{\mathbf{R}}$ is the vector gathering the random variables mean values, $\mathbf{d}$ the deterministic parameters, $\boldsymbol{\mu}_{\boldsymbol{\Theta}_r}$ the mean of random design variables, $\boldsymbol{\theta}_d$ the deterministic design variables, h_i are the n_d deterministic constraints, and $\mathbb{P}$ are the n_p failure probabilities of the limit state functions g_j, which have to be below the maximum failure probabilities $\mathbb{P}_j^{\max}$.

1.4.2 State of the art in composite optimization

António et al. (1996) were one of the first to apply reliability analysis in laminate composite optimization. They considered uncertainties on transversal tensile strength, shear strength, longitudinal and transversal modulus to keep the reliability of the laminate composite in terms of the ultimate failure state. Reliability analysis in the optimization process is applied for various responses such as displacement or stresses of bonded steel-concrete composite beams (Luo et al., 2011), buckling criteria of composite stiffened panels (Díaz et al., 2016; López et al., 2017), or aeroelastic instability (e.g., flutter) for a composite plate (Scarth and Cooper, 2018).

Remark 1.4.2. Failure probability is related to the reliability analysis, i.e., the probability that a constraint is not respected. It is different than the failure state of a composite layer.

António et al. (1996) approximate the failure probability with the First Order Reliability Method (FORM) of the ultimate failure state, which is widely used due to its simplicity and efficiency. For this kind of constraint, this method is efficient. However, for highly non-linear limit-state functions, this type of approximation could lead to inaccurate results on the failure probability due to its low-order approximation of the limit state function. Therefore, simulation methods are used, such as the Monte Carlo method, importance sampling, or subset sampling. For example, some aeroelastic responses lead to a limit-state function that is highly non-linear and multimodal. Many techniques have been used to model uncertainty of composite structures in aeroelasticity. The Monte Carlo method is a commonly used technique and is applied in the work of Murugan et al. (2008) to model the aeroelastic response of a composite rotor blade with uncertain elastic moduli and Poisson's ratio. Indeed, the Monte Carlo method is one of the most robust methods; however, it is disadvantageous in terms of computational time.

Due to the time-consuming computation of some mechanical models and taking into account the uncertainty, which relies on repeated evaluations of the model, surrogate models have been used in order to alleviate the computation time. Manan and Cooper (2009) used polynomial chaos to model the flutter of composite plate wings with uncertain ply orientation, ply thickness, and longitudinal and shear moduli. Díaz et al. (2016) compare several types of surrogate models and several reliability analysis methods for reliability-based design optimization of composite panels with probabilistic constraints on the buckling factor of the first mode and the Tsai-Wu first ply failure. For the most complex case, with nine random variables (including four design variables), the choice of the multivariate adaptive regression splines (MARS) surrogate model is made to replace the finite element analysis. This may be feasible for a small number of total variables, but creating surrogate models for a large number of random variables can be computationally expensive, as a large number of training points are often needed for accuracy (Moustapha and Sudret, 2019). Another approach is to use multiple surrogate models. For example, Rais-Rohani and Singh (2004) compared global surrogate modeling with an approach

using a series of local models, each focusing on a region around the current design point. It was concluded that the local approach is more computationally efficient than the global approach.

In order to take into account the multiscale nature of composite materials, Ghasemi et al. (2014) created a kriging metamodel for the multi-scale uncertainty propagation model of CNT/polymer structure. Based on a similar concept, Omairey et al. (2019) used a surrogate model to establish the relationship between micro-scale uncertainties and macro-scale material property uncertainties, thereby reducing computational costs and improving computational efficiency. This is applied to RBDO of unidirectional fiber-reinforced polymer (FRP) composite laminates in Omairey et al. (2021) where uncertainties are taken into account at different scales of the composite. The optimization is solved via a metaheuristic method because there are only four design variables to optimize.

Little work takes into account the uncertainty in ply orientation which could badly affect some mechanical responses. For instance, Conceição António and Hoffbauer (2017) proposed a new methodology of reliability-based design optimization using a genetic algorithm. The loads imposed on the structure are sources of uncertainties. Subsequently, a sensitivity analysis was performed on the optimal structure to study the influence of parameters and design variables on the structural response. The most influential parameters were found to be the modulus of longitudinal elasticity and the ply orientations. However, this work did not consider these uncertainties during the RBDO. Salas and Venkataraman (2009) investigates the effect of modeling uncertainties of various parameters, including ply orientation, on the predictability of progressive failure in optimized composites. The study highlights the importance of including uncertainties in the model and in design variables to achieve a robust and predictable progressive failure response. The ply orientation uncertainty effect is studied on mechanical instability, such as the flutter phenomenon (aeroelastic instability). Scarth et al. (2014) shows a significant spread of the critical flutter velocity in some part of the design space, considering the uncertainty in orientations. This work uses lamination parameters to represent the uncertainty in ply orientation to reduce the number of random variables. A similar analysis was conducted by Chassaing et al. (2018), in which the polar formalism is used. Therefore, Scarth and Cooper (2018) investigated the minimization of the probability of the flutter instability, modeled as Gaussian processes, in a simple, composite-plate wing, with random design variables, i.e., the ply orientations. Even if the resulting design is, in some sense, an optimized solution with respect to the onset of the flutter instability, their proposed procedure is far from being representative of the real aircraft design process since it is a mono-objective optimization where the aeroelastic stability is taken into account as an objective instead of a constraint. Moreover, a genetic algorithm was used to solve the optimization, which can be limited to complex high-dimensional problems.

In the following, a new methodology is proposed to take into account the uncertainty of ply orientations where the lamination parameters and orientation spaces are exploited.

1.4.3 Multi-scale RBDO strategy for composite

The goal here is to develop a strategy that could be applied to composite structures. Therefore the bi-level approach, introduced in Section 1.3.2, is suitable for this. The uncertain design variables that must be optimized for manufacturing and to provide reliable performance are the ply orientations. We assume we have a good model for these uncertainties. However, is it the case for the lamination parameters? In the following, an uncertain quantification study is presented for these parameters in Section 1.4.3.1. This study will justify the multi-scale strategy

proposed in Section 1.4.3.2, which is inspired by the bi-level approach.

1.4.3.1 Uncertainty quantification of lamination parameters

The ply orientation errors are assumed to come from manufacturing and are considered Gaussian, as the manufacturer is assumed to make the best effort to fulfill the request. They are expressed as:

$$\boldsymbol{\Theta} = \boldsymbol{\mu}_{\boldsymbol{\Theta}} + \boldsymbol{\sigma}_{\boldsymbol{\Theta}}\mathbf{X}, \tag{1.35}$$

where $\boldsymbol{\mu}_{\boldsymbol{\Theta}}$ are the deterministic orientations of each ply, which represent the mean of $\boldsymbol{\Theta}$, $\boldsymbol{\sigma}_{\boldsymbol{\Theta}}$ is the known standard deviations of the ply orientations, and $\mathbf{X}$ is the error, which is modeled as an independent joint Gaussian distribution $\pi_{\mathbf{X}}$ with zero mean and unit variance.

The uncertainty analysis is done on three laminates composed of eight plies and two quasi-trivial laminates (Vannucci and Verchery, 2001)[↗] composed of 10 plies with the same stiffness properties. The laminates and the corresponding lamination parameters are found in Table 1.1. The shapes of the composites anisotropy are presented in Figure 1.6 via the polar-plot of the engineering modulus:

$$E_{\boldsymbol{A},ij}(\theta) = \frac{1}{\left(\boldsymbol{T}(\theta)^T \boldsymbol{A}^{-1} \boldsymbol{T}(\theta)\right)_{ij}}, \tag{1.36}$$

where θ is the polar angle, $\boldsymbol{A}$ is the membrane tensor and $\boldsymbol{T}(\theta)$ is the rotation operator. The corresponding quantity computed for the flexion tensor $\boldsymbol{D}$ is also shown.

Firstly, the idea is to observe the impact on uncertainties in different areas of the lamination parameters design space and, secondly, the impact on two laminates that have the same lamination parameter nominal values. In the following, we assume a variance σ^2_{Θ} of 2°.

Laminate	Stacking Sequence	Membrane and bending LPs
L1	$[0, 45, 90, -45]_s$	$\mathbf{v}^A = (0, 0, 0, 0)$ $\mathbf{v}^D = (0.47, 0.28, 0.37, 0)$
L2	$[45, 90, -45, 0]_s$	$\mathbf{v}^A = (0, 0, 0, 0)$ $\mathbf{v}^D = (-0.28, 0.47, -0.37, 0)$
L3	$[0_2, 90_2]_s$	$\mathbf{v}^A = (0, 0, 1, 0)$ $\mathbf{v}^D = (0.75, 0, 1, 0)$
L4	$[-89, 27, 84, -89, 27, 84, -89, 84, 27, 84]$	$\mathbf{v}^A = (-0.51, 0.31, 0.57, 0.14)$ $\mathbf{v}^D = (-0.51, 0.31, 0.57, 0.14)$
L5	$[27, 83, 90, 27, 83, 90, 27, 90, 83, 90]$	Same as L4

Table 1.1: List of laminates for the uncertainty quantification study. The subscript s refers to a symmetric laminate.

1.4.3.1.1 Lamination parameters domain exploration The objective of this study is to show that depending on the stacking sequence and where it is in the LP domain, the variability of these parameters could be highly different. Three laminates (L1, L2, and L3) are investigated at different places of the lamination parameters domain. The analysis of the influence of the ply angles uncertainty on the lamination parameters and the material stiffnesses

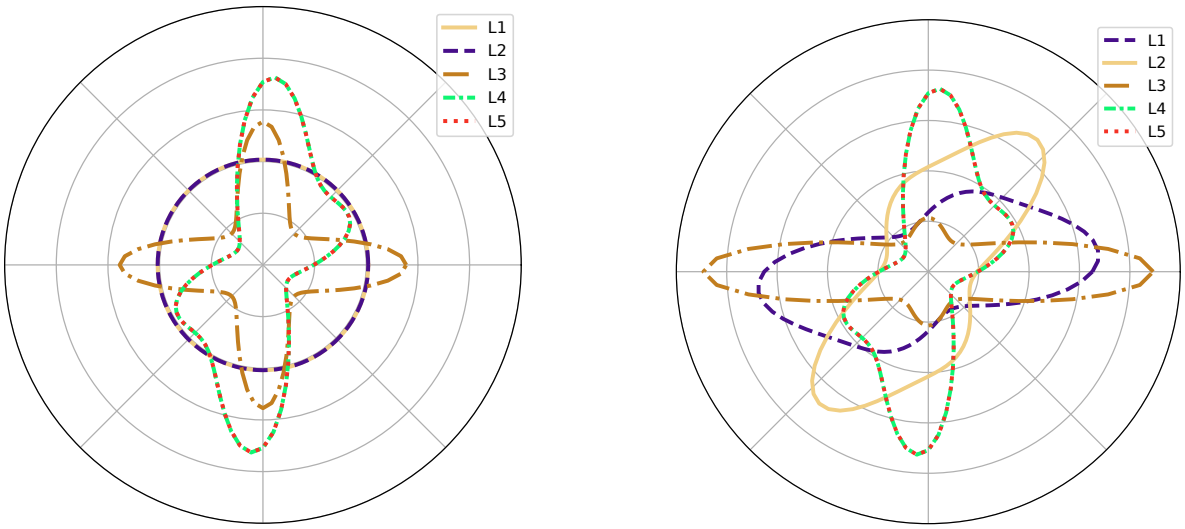

(a) $E_{\boldsymbol{A},11}$ (Membrane-stiffness). (b) $E_{\boldsymbol{D},11}$ (Flexion-stiffness).

Figure 1.6: Polar plot of the engineering modulus evolution of the laminates in Table 1.1.

is presented. The distributions are obtained using 10^5 samples.

The first two laminates, L1 and L2, are compared in Figure 1.7. Both laminates are quasi-isotropic, which means that the vector $\mathbf{v}^{\mathbf{A}}$ and v_4^D are zeros. Concerning the LP domain, they are far from the feasible limit. For these five parameters, the dispersion is similar and shows gaussian-shaped curves because the same ply orientations are used. However, dispersion is quite different for the $\mathrm{v}_{1,2,3}^D$ parameters. The variances are pretty different even if the distributions for v_1^D and v_2^D tend to a Gaussian behavior. The variance in v_1^D is higher for the L2 laminate. It means that L1 laminate has less variability on the bending stiffness D_{11} and D_{22} of both principal axes. However, it is the opposite for bending-twisting coefficients D_{16} and D_{26}, which are influenced by v_2^D. The L1 laminate has more variability in this behavior. Concerning the last parameter v_3^D for both laminates, the distributions are not symmetric and do not follow a Gaussian tendency.

In the following, the lamination parameters distributions of laminate L1 and L3 are compared in Figure 1.8. The L3 stacking sequence is only composed of 0° and 90° orientations. Firstly, the nominal value and the variability for $\mathrm{v}_4^{A,D}$ are the same due to the classical ply orientations used (i.e., 0°, 90°, or ±45°) in both stacking sequences. Both $\mathrm{v}_2^{A,D}$ distributions of the L3 laminate show bell-shaped curves with slightly lower variances than the L1 laminate. For the $\mathrm{v}_1^{A,D}$ parameters, the distributions are highly contrasting in terms of shape and variance. Finally, the feasible domain limit is shown on $\mathrm{v}_3^{A,D}$ for the L3 laminate as the lamination parameters cannot exceed 1.

Scatter plot of each couple of out-of-plane lamination parameters of the L1 laminate are plotted in Figure 1.9. The correlations between each parameter are quite different. Parameters $\mathrm{v}_{1,2}^D$ seem to be uncorrelated. The couples $\mathrm{v}_{1,4}^D$ and $\mathrm{v}_{2,4}^D$ tend to have a gaussian correlation. However, the rest of the couples do not seem to follow a parametric copula.

In the following, the same study is done for two laminates that have the same LPs value.

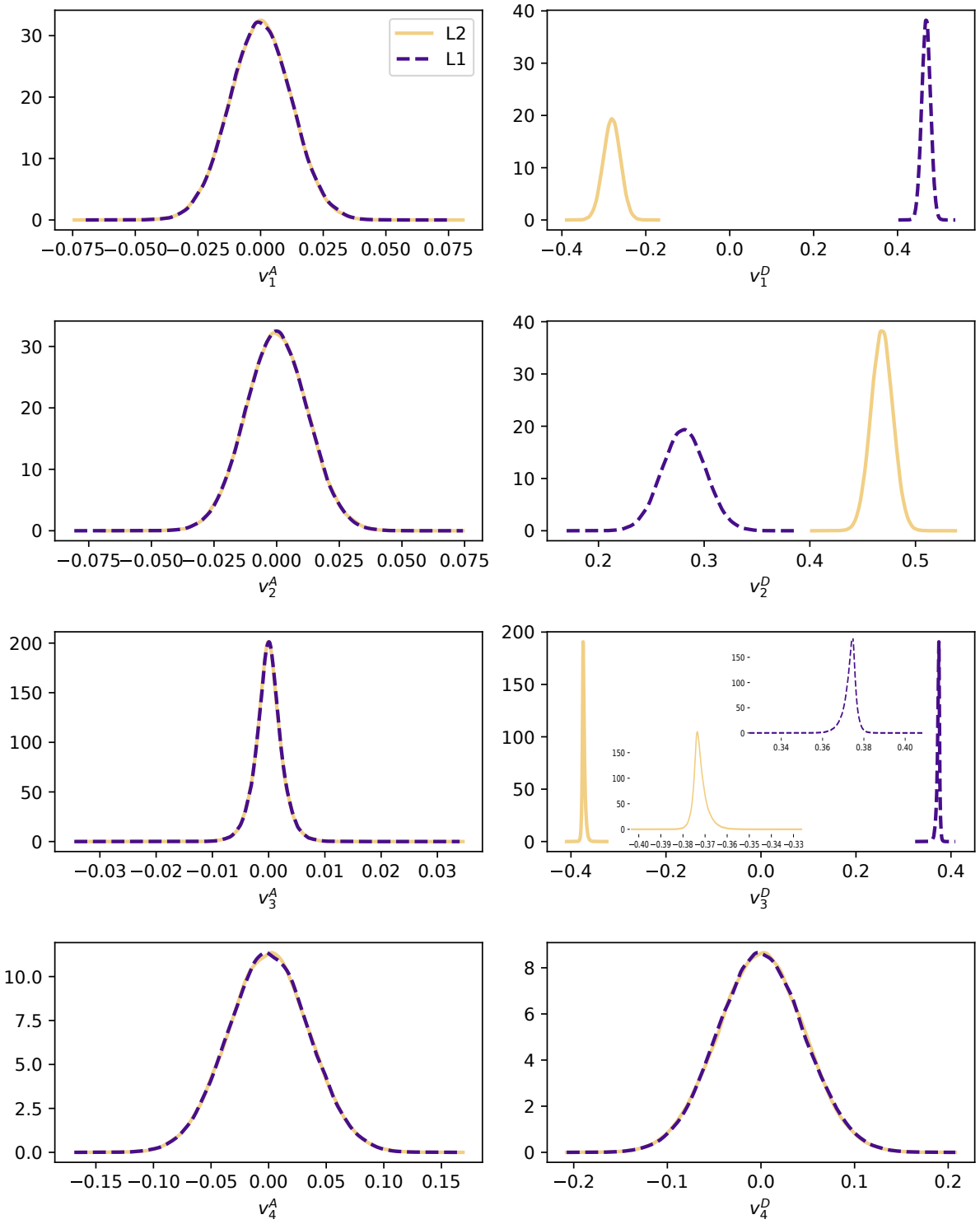

Figure 1.7: Gaussian Kernel Density Estimations (KDEs) of lamination parameters coming from laminates L1 and L2 with ply orientation uncertainty and Monte Carlo Simulation using 10^5 samples.

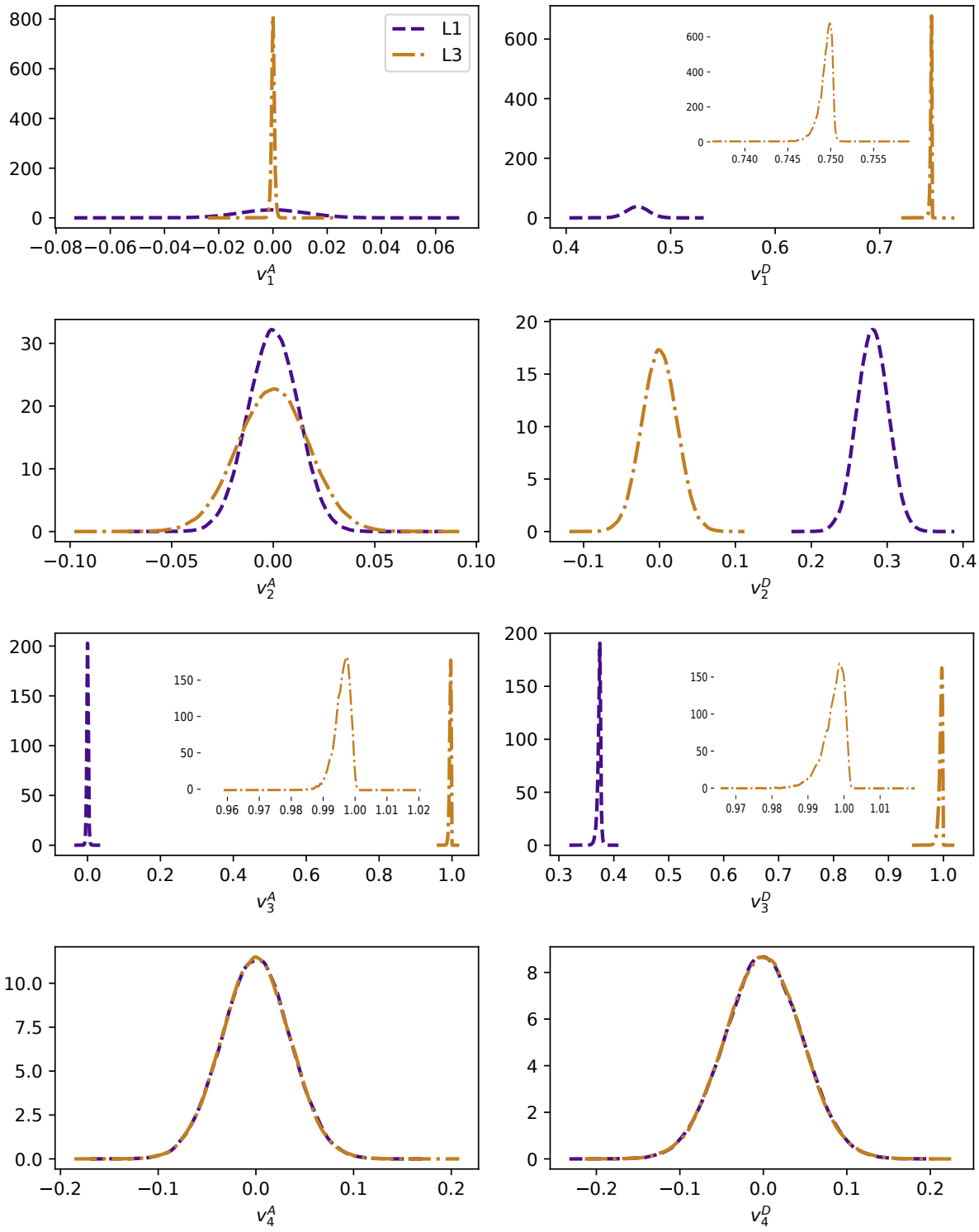

Figure 1.8: Gaussian KDEs of lamination parameters coming from laminates L1 and L3 with ply orientation uncertainty and Monte Carlo Simulation using 10^5 samples.

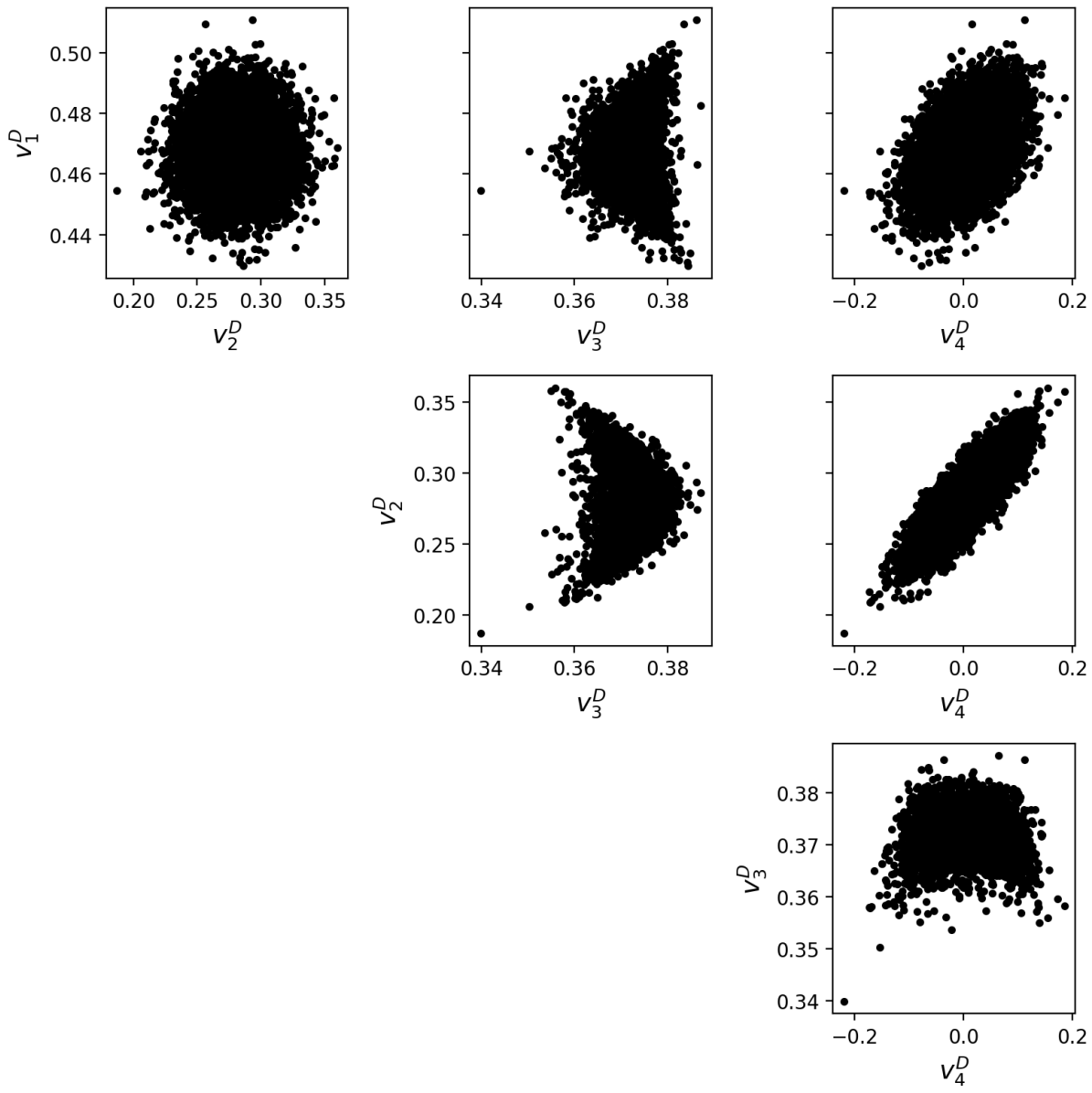

Figure 1.9: Scatter plot of each $\mathrm{v}_{i,j}^D$ couple of the L1 laminate.

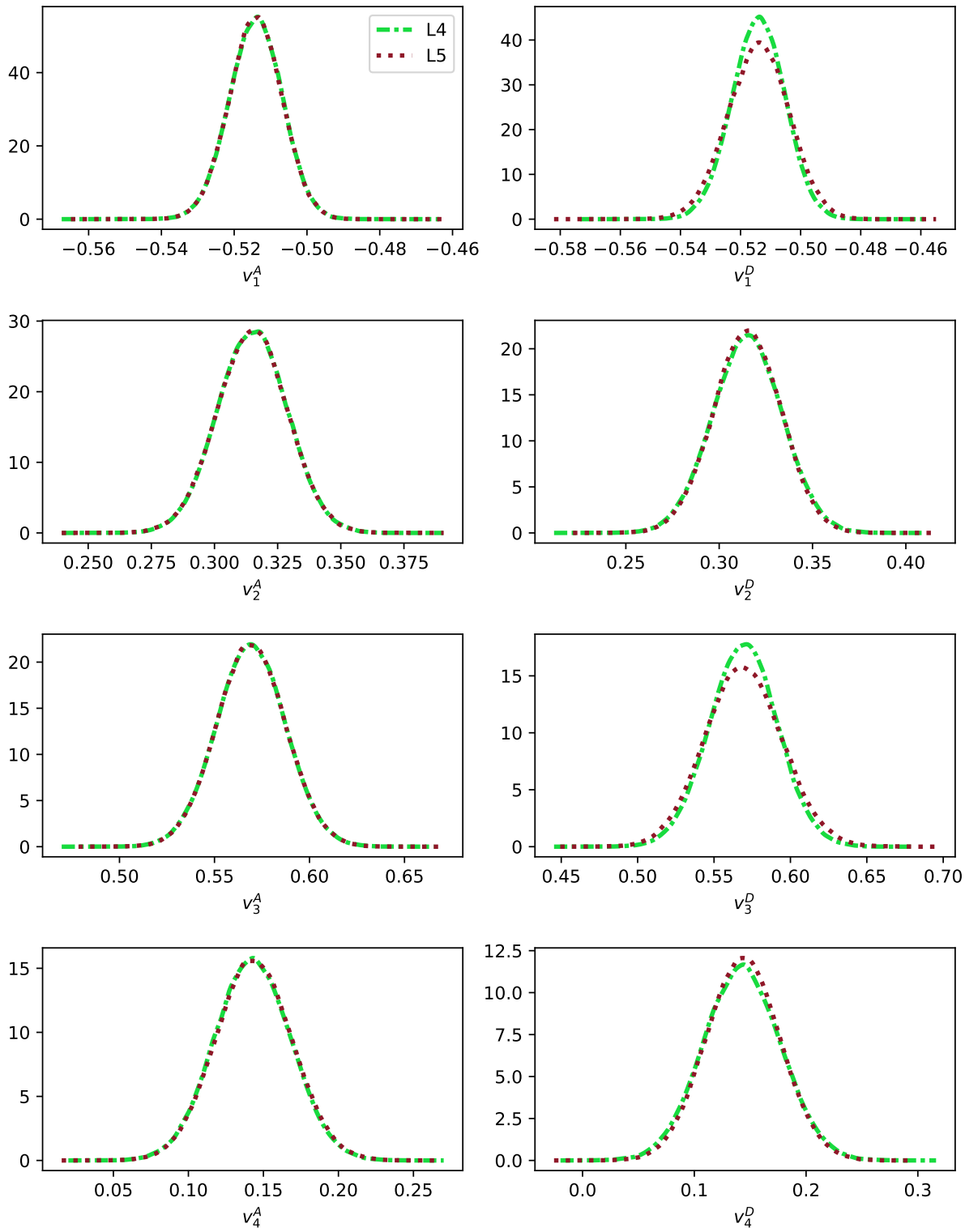

Figure 1.10: Gaussian KKDEs of lamination parameters coming from laminates L4 and L5 with ply orientation uncertainty and Monte Carlo Simulation using 10^5 samples.

1.4.3.1.2 Identical lamination parameters with different stacking sequences

In table 1.1, L4 and L5 are two quasi-trivial laminates. This family of laminates provides exact solutions to either uncoupling, homogeneity, or both, namely quasi-homogeneity (Vannucci and Verchery, 2001). We recall that uncoupling means that membrane and bending are not linked (i.e., the $\boldsymbol{B}$ coupling tensor is zero), and homogeneity means that normalized membrane and bending behaviors are equal (i.e., $\boldsymbol{A}^* = \boldsymbol{D}^*$). These properties are obtained by particular arrangements of the plies within the stacking sequence: plies that share the same orientation are clustered into groups, and the positions of layers associated to different groups are defined within the stack in order to satisfy the properties. The value of the orientation angle can be set freely within each group.

Within this family of laminates, it is easier to find two different stacking sequences with the same properties on the membrane and bending behavior. Indeed, L4 and L5 laminates have the same $\mathbf{A}$ and $\mathbf{D}$ tensors, even though the orientations in the stacking sequence are drastically different. The same study is performed by taking into account the ply orientation uncertainty. The lamination parameters distributions of these two laminates are shown in Figure 1.10. Overall the distributions are similar and have the same shape for all $\mathbf{v}^{A,D}$. However, the variances could vary a little, as, for instance, for $\mathrm{v}^{D}_{1,2,3}$ parameters. Therefore, two stacking sequences with the same lamination parameters can have slightly different variability, showing the complexity of these parameters.

With this study, we show that modeling the LPs uncertainty is complex. It is the same with polar parameters as shown in Nitschke et al. (2019). Therefore, it is not possible to apply a two-level approach since the uncertainty of design variables of the first level is unknown. Nevertheless, a new methodology is proposed to take into account the uncertainty of ply orientations within a multi-scale RBDO formulation where the lamination parameters and orientation spaces are exploited.

1.4.3.2 Formulation

We consider two scales of the material, the mesoscale and the macroscale. The mesoscale concerns the ply scale where the material properties and the ply orientations are defined. In this work, the design variables for composite laminate optimization are the ply orientations $\boldsymbol{\theta}$ as introduced in Section 1.3. The macroscale concerns the homogenized representation of the composite laminate using lamination parameters $\mathbf{v}$ as design variables. We know a nonlinear homogenization process mapping the mesoscale to the macroscale description of the material in Eq.(1.13). The uncertain design variables that must be optimized for manufacturing to provide reliable performance are the orientation variables, called $\boldsymbol{\Theta}$, modeled as in Eq.(1.35). Therefore, the uncertainty of the ply orientations is known and modeled with a probability density function $\pi_{\boldsymbol{\Theta}}$. On the other hand, the uncertainties associated with the lamination parameters variables are unknown and complex to model, in addition to various correlations. Therefore, the calculation of the failure probability in the lamination parameters space is not possible. Despite this complication, it remains more efficient to take advantage of the homogenized space where gradient-based algorithms can accelerate the convergence of the optimization problem.

Our idea is to take an iterative approach, repeatedly moving from one scale to the other during the optimization in order to take advantage of each scale and deal with the uncertainty quantification upscaling. This strategy, exploiting both spaces for the calculation of the failure probability, is illustrated in Figure 1.11.

The macroscopic space relies on a gradient algorithm for the global optimization process.

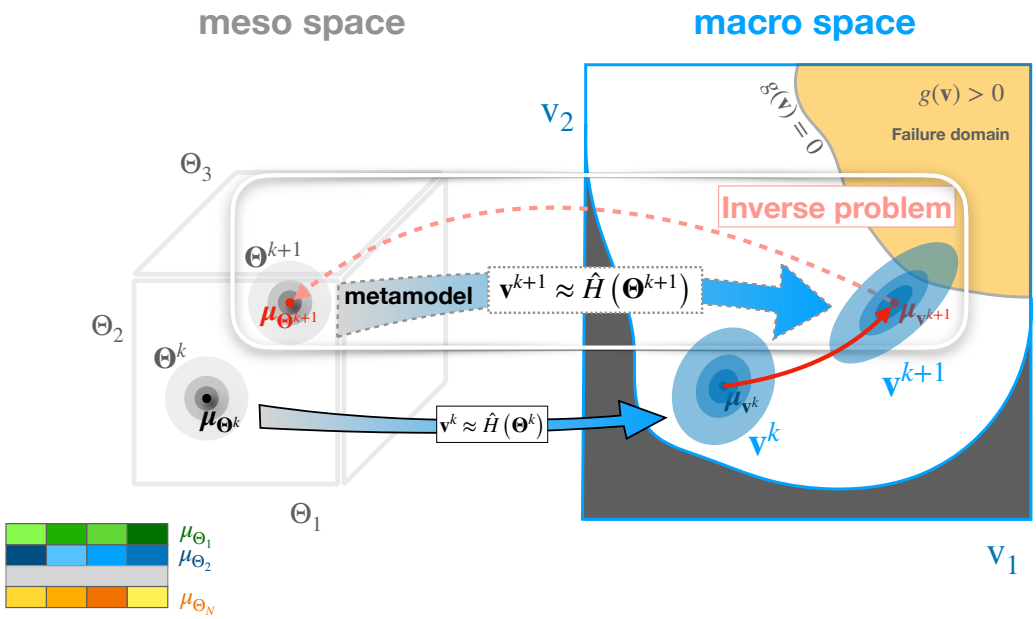

Figure 1.11: The proposed sequential multi-scale RBDO approach.

The principal steps of the methodology are detailed below with a schematic flowchart in Figure 1.12:

1. The objective function and the constraints are defined in the macroscopic space. Assuming that f, h_i and $\mathbb{P}_j$ are known, gradient RBDO optimization is then carried out on the mean value - see the red arrow in Figure 1.11 - to improve lamination parameters design variables.

2. Ply orientations design variables bear some uncertainties in the mesoscopic space. This design space is going to be used to help in evaluating the failure probability of the next iteration since the distribution of the ply orientations is known. Therefore an inverse problem is solved to identify the best corresponding mesoscale design - see the dashed pink arrow in Figure 1.11. This involves a metaheuristic optimization with a genetic algorithm.

3. Once the genetic algorithm identifies a potent set of stacking sequences, it is conceptually straightforward to propagate the uncertainty to the lamination parameters space with Eq.(1.13) - see the large blue arrow in Figure 1.11. Then the lamination parameters sample is propagated to the mechanical model in order to calculate the failure probability with the help of surrogate models.

4. Then, the gradient optimizer can propose another design point and repeat the process until convergence is reached.

However each step exhibits some difficulties. Computational burdens will remain at each iteration of the optimization process, such as the evaluation of the failure probability and its gradient. Then, the inverse mapping from the continuous design variables to the discrete ones is far from being trivial. It is a highly multimodal optimization problem where it is necessary to use metaheuristic optimization methods. Then, depending on the mechanical model, the reliability analysis could be time-consuming.

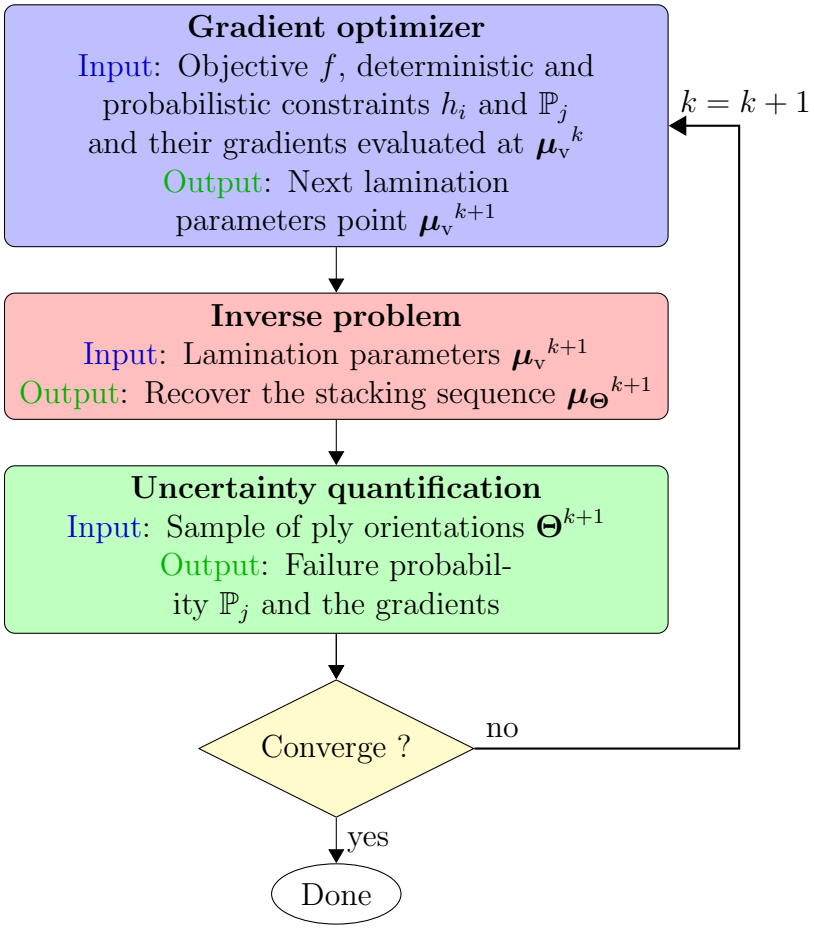

Figure 1.12: Schematic flowchart of the principal steps of the methodology.

Finally, the formulation of our multi-scale reliability-based design optimization, taking into account design variables uncertainties, is described as follows:

$$\min_{\boldsymbol{\mu}_{\boldsymbol{\Theta}}} f\left(\boldsymbol{\mu}_{\mathbf{v}(\boldsymbol{\Theta}|\boldsymbol{\mu}_{\boldsymbol{\Theta}})}\right) \quad \text{subject to:} \quad \begin{cases} h_i\left(\boldsymbol{\mu}_{\mathbf{v}(\boldsymbol{\Theta}|\boldsymbol{\mu}_{\boldsymbol{\Theta}})}\right) \leq 0, & i = 1, \ldots, n_d \\ \mathbb{P}_j\left(g_j(\mathbf{v} = H(\boldsymbol{\Theta})) \geqslant 0\right) \leq \mathbb{P}_j^{\max}, & j = 1, \ldots, n_p \end{cases} \tag{1.37}$$

where:

- $\mu_{\boldsymbol{\Theta}}$ are the ply orientation mean values to optimize,
- h_i are the deterministic nonlinear constraints emerging from the homogenization process,
- g_j are the limit state functions subject to reliability analysis,
- H is the nonlinear mapping of Eq.(1.13), from the mesoscopic space to the macroscopic space used to obtain the lamination parameters $\mathbf{v}$ for a given $\boldsymbol{\mu}_{\boldsymbol{\Theta}}$,
- $\mathbb{P}_j$ are the failure probabilities evaluated in the macrospace.

Remark 1.4.3. While this work uses lamination parameters for the homogenized space, note that the same methodology could apply to polar parameters indifferently.

1.5 Conclusion

Composite structure optimization is a vast research field. In this chapter, various methods have been overviewed in a deterministic framework. However, it is quite challenging to optimize complex geometry under uncertainties while taking reasonable computational time. It is even trickier when the uncertainty is taken on design variables such as the ply orientations. That is why most of the applications concerned simpler geometries. Almost all previous work uses the direct method with a metaheuristic algorithm to optimize the stacking sequences. Here, a new methodology is inspired by the bi-level approach used in the deterministic framework where a macroscopic design space is used, and then the stacking sequence is retrieved via an inverse problem resolution. We proposed to perform this approach at each iteration of the optimization. This strategy is justified by the uncertainty quantification study of the lamination parameters: modeling these macroscopic design variables is complex and forces us to use the ply orientation design space where the uncertainty is known and modeled. Therefore, the strategy proposed optimizes a stacking sequence under ply orientation uncertainty in a reliability framework. However, the computational burden is binding. Indeed, the time to perform the inverse problem under uncertainty and the uncertainty quantification could be significant.

Because of the design variables uncertainties in both spaces, it is important to efficiently propagate uncertainties from the stacking sequence to the lamination parameters to solve an inverse mapping that satisfies certain statistical constraints. Therefore, we propose to build a surrogate mapping that is constructed to rapidly access needed statistics of the lamination parameters for a given population of stacking sequences. This is the second step in the flowchart in Figure 1.12, and the technical details are presented in Chapter 2. Moreover, the mechanical constraints, subject to reliability analysis, could be expensive; therefore, a strategy is proposed to efficiently approximate the quantity of interest using a surrogate model strategy to compute efficiently and quickly the failure probability and its gradient. Technical details are presented in Chapter 3.

CHAPTER 2

PROBABILISTIC METAMODELING FOR LAYUP RETRIEVAL IN A VARIABILITY FRAMEWORK

Contents

2.1 Introduction

The previous chapter presented the multi-scale RBDO formulation, where the idea is to jump between two scales during the optimization. An inverse problem has to be solved at each iteration to propagate the uncertainty from the mesoscopic scale to the macroscopic scale to compute the failure probability needed during the optimization. The proper way to do this is to match the statistics. Instead of matching the nominal values of lamination parameters using Eq.(1.13), an uncertainty quantification from the stacking sequence to the lamination parameters is necessary to correctly identify an optimized stacking sequence set in terms of the statistical description of the lamination parameters. This step must be quick and efficient. With the uncertainty taken into account in the ply orientations at the mesoscale, it is straightforward to propagate the uncertainty into the lamination parameters with Eq.(1.13). However, even if the formulation is analytic, it could be costly to use simulation methods such as Monte Carlo at each iteration of the global optimization process. In the literature, some works have been done in the composite framework building surrogate model to propagate the microscopic properties of fibers to the macroscopic stiffness of the composite laminate (Omairey et al., 2019). Kriegesmann (2017) provides a closed-form solution for the mean values, variances, and covariances of lamination parameters. Scarth and Adhikari (2017) proposed to use lamination parameters to model random fields, in which the ply orientation uncertainty is defined using Karhunen-Loève expansion, and the lamination parameters are approximated using an intrusive polynomial chaos expansion.

In this chapter, we propose to build a non-intrusive surrogate model to quickly access the needed statistics of the lamination parameters using a particular Fourier basis which gives a closed-form solution for the mean values, variances, and covariances of lamination parameters. The technical details are presented in Section 2.3 with a validation. Before that, the optimization-based inverse problem is presented in Section 2.2 with an overview of existing formulations. Once the formulations used are chosen, the contribution of the metamodel to the inverse problem is shown in Section 2.4.

2.2 Optimization-based stacking sequence retrieval

2.2.1 Classical formulations for the deterministic case

To retrieve a stacking sequence, the objective is to minimize a cost function f measuring the difference between the properties of the target (superscript 'des') and those of a given stacking sequence $\boldsymbol{\theta}$:

$$\min_{\boldsymbol{\theta}} f(\boldsymbol{A}^{\text{des}}, \boldsymbol{B}^{\text{des}}, \boldsymbol{D}^{\text{des}}, \boldsymbol{A}(\boldsymbol{\theta}), \boldsymbol{B}(\boldsymbol{\theta}), \boldsymbol{D}(\boldsymbol{\theta})). \tag{2.1}$$

The cost function can be formulated in different ways to represent the laminate stiffness properties. The most common formulation is based on the lamination parameters formalism. It is found in various stacking retrieval algorithms (Herencia et al., 2007; Macquart et al., 2016). The second family of formulations is based on the polar parameters (Vincenti et al., 2010; Picchi Scardaoni et al., 2021). These two groups have already been introduced in Section 1.3.2. A final formulation based on the stiffness tensors $\boldsymbol{A}$, $\boldsymbol{B}$ and $\boldsymbol{D}$ has been proposed by Irisarri et al. (2011).

Savine (2022) proposed a benchmark study of these formulations. A method is suggested to establish a relative comparison between the different cost functions. Indeed, the different cost functions do not have the same scale. The results are presented for a limited study with

three different targets and five runs of optimization. However, the formulation with the stiffness properties is privileged, but it is closely followed by the formulation using LPs.

In this study, we keep using the most common formulation with lamination parameters expressed as:

$$f_{LP} = \sum_{i=1}^{j} \sqrt{(\mathrm{v}_j^{\mathrm{des}} - \mathrm{v}_j(\boldsymbol{\theta}))^2}, \tag{2.2}$$

where j is the number of lamination parameters taken into account. For the most general case, j is equal to 12. We can reformulate this cost function with the euclidean norm $\|\cdot\|$. To retrieve a stacking sequence for a given state $\mathbf{v}$ in the homogeneous lamination parameters space, the inverse problem is written as:

$$\begin{aligned} \mathbf{v}^{\mathrm{des}} &\leftarrow \mathbf{v}, \\ \min_{\boldsymbol{\theta}} \|\mathbf{v}^{\mathrm{des}} - \boldsymbol{H}(\boldsymbol{\theta})\|, & \end{aligned} \tag{2.3}$$

where H is the mapping between the stacking sequence and the LPs - see Eq.(1.13). The orthotropy or the decoupling hypothesis can be forced either by restricting the search of symmetrical or balanced stacking sequences or by forcing some target LP values:

- uncoupling is obtained by canceling $\mathrm{v}^B_{1,\dots,4} = 0$,
- if the orthotropy direction is aligned with the reference frame, the target $\mathrm{v}^{A,D}_{2,4}$ can be forced to zero.

2.2.2 Formulations for the variability case

In the variability framework, the proper way to solve the inverse problem is to match the statistics between the LPs target and the ply orientations. But which statistics should be taken into account? The average is one of the first statistical indicators. Therefore, the first idea is trying to match the mean values between the LPs of a given stacking sequence and the target LPs. The cost function of the inverse problem optimization can be written as:

$$\begin{aligned} \boldsymbol{\mu}_{\mathbf{v}}^{\mathrm{des}} &\leftarrow \boldsymbol{\mu}_{\mathbf{v}}, \\ \min_{\boldsymbol{\mu}_{\boldsymbol{\Theta}}} \|\boldsymbol{\mu}_{\mathbf{v}}^{\mathrm{des}} - \boldsymbol{\mu}_{H(\boldsymbol{\Theta}|\boldsymbol{\mu}_{\boldsymbol{\Theta}})}\|, & \end{aligned} \tag{2.4}$$

where $\boldsymbol{\mu}_{H(\boldsymbol{\Theta}|\boldsymbol{\mu}_{\boldsymbol{\Theta}})}$ is the mean of the random quantity of the mapping from the stacking sequence to the lamination parameters.

The standard deviation could also be used for several reasons. With the standard deviation, we could try to limit the variability of lamination parameters in presence of uncertainty. Moreover, the use of standard deviation could limit the non-respect of some hypotheses, such as orthotropy for example. Indeed, if you apply a ply orientation uncertainty on an orthotropic stacking sequence, this property is not fully respected. An idea could be to minimize the standard deviation of the $\mathrm{v}^{A,D}_{2,4}$ parameters in addition to the objective of Eq.(2.4). This multi-objective can be formulated as a mono-objective cost function with partial objectives:

$$\min_{\boldsymbol{\mu}_{\boldsymbol{\Theta}}} \left(\|\boldsymbol{\mu}_{\mathbf{v}}^{\mathrm{des}} - \boldsymbol{\mu}_{H(\boldsymbol{\Theta}|\boldsymbol{\mu}_{\boldsymbol{\Theta}})}\| + \rho \|\boldsymbol{\sigma}_{\mathbf{v}}^{\mathrm{des}} - \boldsymbol{\sigma}_{H(\boldsymbol{\Theta}|\boldsymbol{\mu}_{\boldsymbol{\Theta}})}\| \right), \tag{2.5}$$

where $\boldsymbol{\sigma}_{\mathbf{v}}^{\mathrm{des}} = 0$ if we want to minimize the variability of each parameter and ρ is the weight given to the second objective.

Parameters	Value
Initial population size	160
Population size per generation	40
Probability of crossover	0.75
Probability of mutation	0.5

Table 2.1: Parameters of the genetic algorithm.

2.2.3 Solving the inverse problem

The inverse problem is non-convex, non-linear, and is most of the time parametrized with discrete ply orientations. The computation of the cost function presented in Eq.(2.3) is relatively cheap as it corresponds to analytic evaluations of the LPs with Eq.(1.13). Therefore, this is generally solved by meta-heuristic algorithms, which can handle the complexity of the combinatorial problem. Different meta-heuristic algorithms have been used to solve the problem, with a majority of genetic algorithms (Wang and Sobey, 2020). Some algorithms have been designed especially for stacking sequences optimization. This type of algorithm is thus privileged in the present work to retrieve a stacking sequence; and the optimizer developed by Vicente (2019), which followed the formulation proposed by Irisarri et al. (2014) known as stacking sequence tables SST, is preferred. The parameters used throughout the manuscript for the genetic algorithm are shown in Table 2.1.

However, to solve the optimization of Eq.(2.4) or Eq.(2.5), it requires a greater number of calls to the mapping function H. The computational cost of the Monte Carlo method to compute $\boldsymbol{\mu}_{H(\boldsymbol{\Theta}|\boldsymbol{\mu}_{\boldsymbol{\Theta}})}$ or $\boldsymbol{\sigma}_{H(\boldsymbol{\Theta}|\boldsymbol{\mu}_{\boldsymbol{\Theta}})}$ for each inverse problem resolution can be particularly high. Therefore, a surrogate model could accelerate the propagation from the ply orientation uncertainty to the LPs to quickly access their statistics.

2.3 Statistics computation via Fourier Chaos Expansion

The main concern is the selection of the technique for this particular problem. A well-known family of surrogate models is the polynomial one, and especially, the polynomial chaos expansion (PCE) (Xiu and Karniadakis, 2002). This is an effective tool that guarantees exponential convergence with increasing expansion order. Moreover, once the projection is set, access to the statistics of the parameters is direct with the expansion coefficients. Nevertheless, this method is inaccurate for models which are highly non-linear or are of high dimensionality. Another family is the Gaussian processes - like Kriging (Rasmussen and Williams, 2006) - which is employed for larger experimental areas such as Bayesian optimization, approximating deterministic function, and machine learning. It combines a regression model with a stationary Gaussian process error model. The advantage is that it provides a stochastic error bound. However, it is again imprecise for models which are highly non-linear or are of high dimensionality. Other methods, such as the least-square approximation, radial basis function, or neural network-based method, could be used as well.

This work requires the mean of the mapping H to solve the inverse problem. Depending on the application, the variance could be used as well, which motivates the choice to use the polynomial

method, which is accurate for these statistical moments at a low cost. However, this method will be extended to a particular basis involving trigonometric functions. This method is called Fourier Chaos Expansion (FCE) and was briefly sketched in Millman et al. (2005). It is analogous to the PCE, and that is why a little overview of PCE is presented below.

2.3.1 Overview of the Polynomial Chaos Expansion

We assume that the model response is a scalar random variable $Y = H(\mathbf{X})$. However, the following derivations hold in the case of a vector-valued response. We can expand Y into a series of polynomials:

$$Y(\mathbf{X}) = \sum_{i}^{\infty} \xi_i \phi_i(\mathbf{X}), \tag{2.6}$$

where ϕ_i are orthonormal polynomials with respect to the joint PDF $f_{\boldsymbol{X}}(\mathbf{x})$:

$$\begin{aligned} \mathbb{E}\left[\phi_i(\mathbf{X})\phi_j(\mathbf{X})\right] &= < \phi_i(\mathbf{X}), \phi_j(\mathbf{X}) > \\ &= \int_{\mathbb{R}} \phi_i(\mathbf{x})\phi_j(\mathbf{x}) f_{\boldsymbol{X}}(\mathbf{x}) \mathrm{d}\mathbf{x} \\ &= \delta_{ij}, \ \forall i, j \in \mathbb{N}, \text{ with } \delta \text{ the Kronecker delta,} \end{aligned} \tag{2.7}$$

and ξ_i are the expansion coefficients. Thanks to the orthonormality of the approximation space, the deterministic coefficients are obtained as projections of the function of interest onto each member of the approximation basis:

$$\xi_i = \mathbb{E}\left[Y(\mathbf{X})\phi_i(\mathbf{X})\right]. \tag{2.8}$$

Therefore, the choice of an orthonormal base and a technique to evaluate the coefficients has to be made. With the Gaussian distribution hypothesis on random variable $\mathbf{X}$, Hermite polynomials can be used (Wiener, 1938). Afterward, other families of orthogonal polynomials (Hermite, Legendre, Laguerre, Jacobi,...) are regrouped in the Askey scheme (Xiu and Karniadakis, 2002) based on underlying random variables which are not restricted to gaussian random variables.

Concerning the ξ_i coefficients computation, we focus on the non-intrusive techniques, which means that the model is used as a black box. The Eq.(2.8) is written as:

$$\xi_i = \int_{\mathbb{R}} Y(\mathbf{x})\phi_i(\mathbf{x}) f_{\boldsymbol{X}}(\mathbf{x}) \mathrm{d}\mathbf{x}. \tag{2.9}$$

Most of the time, these integrals cannot be computed analytically. Therefore numerical quadrature methods can be used. There are two types of numerical quadrature: stochastic ones or deterministic ones. One of the stochastic approaches is based on Monte Carlo, where integration points are chosen randomly. Be $\mathcal{X}_{\boldsymbol{X}} = \left\{\mathbf{x}^{(1)}, \mathbf{x}^{(2)}, \ldots, \mathbf{x}^{(N)}\right\}$ a Monte Carlo sample and $\mathcal{Y}_Y = \left\{y^{(1)}, y^{(2)}, \ldots, y^{(N)}\right\}$ the corresponding set of the model response. The integral is approximated as follows:

$$Q = \mathbb{E}\left[Y(\mathbf{X})\phi_i(\mathbf{X})\right] = \frac{1}{N}\sum_{i=1}^{N} y^{(i)}. \tag{2.10}$$

The law of large numbers ensures the convergence of this quantity to the real integral. However, the quadrature by MC method converges slowly.

Another option is the Gauss quadrature. With this technique, the quadrature points and the corresponding weights are deterministic quantities that inherit the properties of one-dimensional quadrature rules chosen to suit the probability measure. The quadrature points $\mathbf{x}^{(i)}$ are roots

of orthogonal polynomials with respect to the probability measure. Then, the weights of the quadrature are defined in terms of the quadrature points and the associated orthogonal polynomials. Examples can be found in Gautschi (2004). If we consider a quadrature Q based on a number of points N along each dimension j, with $(j = 1, \ldots, N_d)$, and which integrates with respect to the measure $f_{\boldsymbol{X}}(\mathbf{x})$, it can be approximated as follows:

$$Q_j = \sum_{i=1}^{N} w_j^{(i)} y(x_j^{(i)}). \tag{2.11}$$

The multidimensional quadrature with respect to the measure $f_{\boldsymbol{X}}(\mathbf{x})$ is written as:

$$Q_{N_d} = Q_1 \otimes \cdots \otimes Q_{N_d}, \tag{2.12}$$

and the integral becomes:

$$Q_{N_d} = \sum_{i_1=1}^{N} \cdots \sum_{i_1=N_d}^{N} w_1^{(i_1)} \ldots w_{N_d}^{(i_{N_d})} y\left(x_1^{(i_1)}, \ldots, x_{N_d}^{(i_{N_d})}\right). \tag{2.13}$$

Then, another way to compute the coefficients ξ_i is based on the least square approximation, which is based on a random sample $\mathcal{X}_{\boldsymbol{X}}$, and the corresponding set of the solution $\mathcal{Y}_Y$. The quantity of interest is written as:

$$Y(\mathbf{X}) = \sum_{i}^{\infty} \xi_i \phi_i(\mathbf{X}) + r(\mathbf{X}). \tag{2.14}$$

A least square approach consists in minimizing the residual between the observed and estimated values $r \equiv (\mathbf{y} - \boldsymbol{\phi}\boldsymbol{\xi})$ in L_2 norm and can be rewritten as an optimization problem:

$$\min_{\boldsymbol{\xi}} \|\mathbf{y} - \boldsymbol{\phi}\boldsymbol{\xi}\|. \tag{2.15}$$

The solution is obtained by computing the following relation, written in matrix form:

$$\boldsymbol{\xi} = \left(\boldsymbol{\phi}^T \boldsymbol{\phi}\right)^{-1} \boldsymbol{\phi}^T \boldsymbol{y}, \tag{2.16}$$

where $\boldsymbol{y}$ is the vector of observations, $\boldsymbol{\phi}$ is the measurement matrix with $\phi_{ij} = \phi_j(\boldsymbol{x}^{(i)})$ and $\boldsymbol{\xi}$ is the vector of coefficients.

Once the coefficients ξ_i are computed, access to the statistics of the output Y is direct with the expansion coefficients as follows:

$$\mu_Y = \xi_0, \quad \mathrm{Var}(Y) = \sum_{i=1}^{p} \xi_i^2. \tag{2.17}$$

In this work, even if the random parameters are modeled with Gaussian distribution, Hermite polynomials are not used. Another basis is constructed, which is efficient for the lamination parameters. We propose to use the Fourier chaos expansion (FCE) because it naturally involves trigonometric polynomials and simplifies the expansion coefficients computation, as shown in the following.

2.3.2 Orthonormal Fourier basis construction

The development of the FCE is analogous to the standard PCE basis. Nevertheless, the bases to be orthogonalized are not classical polynomials basis, e.g., $u_i = \{1, x, x^2, ...\}$; instead, the development begins with the Fourier basis for trigonometric functions, that is, the set $u_i = \{1, \sin(nx), \cos(nx)\}$, where $n = 1, ..., \infty$. An FCE representation was introduced in Millman et al. (2005) to obtain the probability distribution of an airfoil pitch angle where oscillatory motion was involved. The orthonormal basis is numerically constructed thanks to the Gram–Schmidt orthogonalization method. The latter has, for instance, been used in Navarro et al. (2014) to construct arbitrary polynomial chaos and applied in aeroelasticity for the critical flutter velocity uncertainty quantification Nitschke et al. (2019).

In our case, we have formalized the approach to extend it to an arbitrary order of accuracy and to random variables with different wavenumbers. Since the ply orientation uncertainty in Eq.(1.35) is modeled with a Gaussian random variable $\mathbf{X}$ and scaled by a standard deviation $\boldsymbol{\sigma_\Theta}$ in radian, the trigonometric polynomials are functions of scaled random variables $\psi_i(\hat{\mathbf{X}} = \boldsymbol{\sigma_\Theta}\mathbf{X})$. Then, the mapping from the stacking sequence to the lamination parameters H is expanded into a series of polynomials:

$$H(\mathbf{X}) = \sum_{i}^{\infty} e_i \psi_i(\boldsymbol{\sigma_\Theta}\mathbf{X}), \tag{2.18}$$

where ψ_i are Fourier orthonormal polynomials which depend on the standard deviation $\boldsymbol{\sigma_\Theta}$ and e_i are the expansion coefficients.

In order to orthogonalize the polynomials with respect to the distribution $\pi_{\boldsymbol{X}}$, the Gram-Schmidt algorithm calculates the coefficients of the polynomials using the inner product to ensure that each polynomial is orthogonal to all of its predecessors:

$$\begin{aligned} \psi_0(\hat{\mathbf{X}}) &= 1, \\ \psi_i(\hat{\mathbf{X}}) &= u_i(\hat{\mathbf{X}}) - \sum_{k=0}^{i-1} C_{ik}\psi_k(\hat{\mathbf{X}}), \end{aligned} \tag{2.19}$$

where u_i are the set of Fourier polynomials $(\cos(n\hat{\mathbf{X}}),\ \sin(n\hat{\mathbf{X}}))$ with $n \in \mathbb{N}$ and deterministic quantities C_{ik} must be computed as:

$$C_{ik} = \frac{\mathbb{E}\left[u_i(\hat{\mathbf{X}})\psi_k(\hat{\mathbf{X}})\right]}{\mathbb{E}\left[\psi_k(\hat{\mathbf{X}})\psi_k(\hat{\mathbf{X}})\right]}. \tag{2.20}$$

Remark 2.3.1. Expectations of useful random trigonometric functions Some useful expectations of random trigonometric functions are presented below. Using the symbolic computation of Mathematica, the expectation of $\sin(aX)$ and $\cos(aX)$ can be computed as follows:

$$\mathbb{E}\left[\cos(aX)\right] = \cos(a\mu)w, \tag{2.21}$$
$$\mathbb{E}\left[\sin(aX)\right] = \sin(a\mu)w, \tag{2.22}$$

with $a \in \mathbb{R}$ and $w = \exp(-0.5a^2\sigma^2)$. The product of the trigonometric functions $\cos(kx)$ and $\sin(lx)$ can be expressed as:

$$\cos(kx)\sin(lx) = \frac{1}{4}\left(ie^{i(k-l)x} + ie^{-i(k+l)x} - ie^{i(k+l)x} - ie^{i(l-k)x}\right). \tag{2.23}$$

u_0	1
u_1	$\sin(\hat{X})$
u_2	$\cos(\hat{X})$
u_3	$\sin(2\hat{X})$
u_4	$\cos(2\hat{X})$
u_5	$\sin(3\hat{X})$
u_6	$\cos(3\hat{X})$

Table 2.2: Set of Fourier polynomials to be orthogonalized with $\hat{X} = \sigma_\Theta X$.

Since the part of interest is only on the real part, the Eq.(2.23) can be written as the Eq.(A.4), and its expected value as the Eq.(2.25) using the Eq.(2.22) and Eq.(2.21).

$$\cos(kx)\sin(lx) = -0.5\ \sin((k-l)x) + 0.5\ \sin((k+l)x), \tag{2.24}$$
$$\mathbb{E}[\cos(kX)\sin(lX)] = -0.5\ \mathbb{E}[\sin((k-l)X)] + 0.5\ \mathbb{E}[\sin((k+l)X)]. \tag{2.25}$$

With the same idea:

$$\mathbb{E}[\cos(kX)\cos(lX)] = 0.5\ \mathbb{E}[\cos((l-k)X)] + 0.5\ \mathbb{E}[\cos((k+l)X)], \tag{2.26}$$
$$\mathbb{E}[\sin(kX)\sin(lX)] = 0.5\ \mathbb{E}[\cos((l-k)X)] - 0.5\ \mathbb{E}[\cos((k+l)X)]. \tag{2.27}$$

Moreover, given $\sin^2(x) = \frac{1-\cos(2x)}{2}$, $\cos^2(x) = \frac{1+\cos(2x)}{2}$, we can write:

$$\mathbb{E}\left[\sin^2(aX)\right] = 0.5 - 0.5\ \mathbb{E}\left[\cos(2aX)\right], \tag{2.28}$$
$$\mathbb{E}\left[\cos^2(aX)\right] = 0.5 + 0.5\ \mathbb{E}\left[\cos(2aX)\right]. \tag{2.29}$$

In the following, the one-dimensional Fourier chaos basis is constructed with a single random variable X following a normal distribution $X \sim \pi_X = \mathcal{N}(0, 2)$. Now the orthonormal basis can be constructed using Eq.(2.19) and Eq.(2.20) with the set of Fourier polynomials $\boldsymbol{u}$ in Table 2.2. Here is an example of the first polynomials construction:
The Fourier basis function $\psi_0^{\mathrm{n}}(X)$ is equal to:

$$\begin{aligned} \psi_0 &= u_0 = 1, \\ \psi_0^n &= 1. \end{aligned} \tag{2.30}$$

The Fourier basis function $\psi_1^{\mathrm{n}}(X)$ is computed as follows:

$$\psi_1(X) = u_1 - \frac{\mathbb{E}\left[u_1\psi_0\right]}{\mathbb{E}\left[\psi_0^2\right]}\psi_0 = \sin(\hat{X}) - \mathbb{E}\left[\sin(\hat{X})\right]. \tag{2.31}$$

The expected value can be computed with Eq.(2.22). With a zero mean in the random variable, the expected value of the sinus function is equal to zero. Therefore:

$$\psi_1 = \sin(\hat{X}), \tag{2.32}$$

and ψ_1 can be normalized as:

$$\psi_1^n = Z_{11}\sin(\hat{X}), \quad \text{with} \quad Z_{11} = \frac{1}{\sqrt{\mathbb{E}\left[\sin(\hat{X})^2\right]}}, \tag{2.33}$$

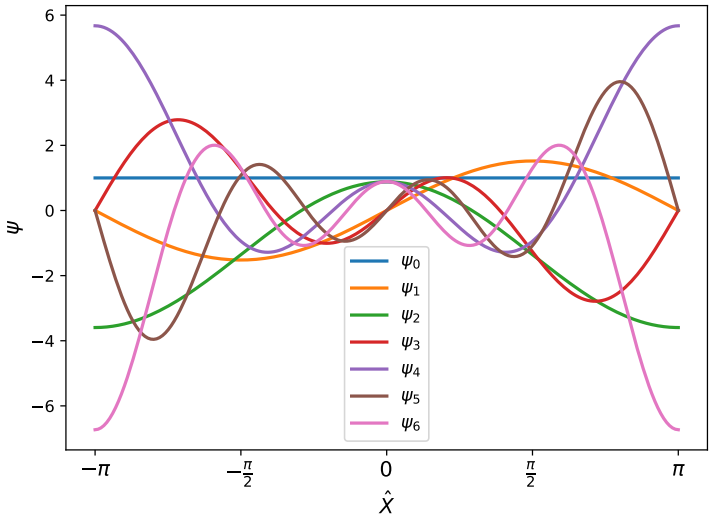

Figure 2.1: Orthonormal Fourier basis

which can be computed with the Eq.(2.28).
The Fourier basis function $\psi_2^{\mathrm{n}}(X)$ is computed as follows:

$$\begin{aligned}\psi_2 &= u_2 - \frac{\mathbb{E}\left[u_2\psi_0\right]}{\mathbb{E}\left[\psi_0^2\right]}\psi_0 - \frac{\mathbb{E}\left[u_2\psi_1\right]}{\mathbb{E}\left[\psi_1^2\right]}\psi_1 \\ &= \cos(\hat{X}) - \mathbb{E}\left[\cos(\hat{X})\right] - \frac{\mathbb{E}\left[\cos(\hat{X})\sin(\hat{X})\right]}{\mathbb{E}\left[\sin(\hat{X})^2\right]}\psi_1 \\ &= \cos(\hat{X}) - C_{20} - C_{21}\psi_1.\end{aligned} \tag{2.34}$$

The expected values can be computed with Eq.(2.21), Eq.(2.25), and Eq.(2.22). With a zero mean in the random variable, the expected value of the product between sinus and cosinus functions is equal to 0. Therefore:

$$\psi_2 = \cos(\hat{X}) - C_{20}, \tag{2.35}$$

and ψ_2 can be normalized as:

$$\psi_2^{\mathrm{n}} = Z_{21}(\cos(\hat{X}) - C_{20}), \quad \text{with} \quad Z_{21} = \frac{1}{\sqrt{\mathbb{E}\left[(\cos(\hat{X}) - C_{20})^2\right]}}, \tag{2.36}$$

which can be computed with Eq.(2.29) and Eq.(2.21).

The generic form of the obtained orthonormal polynomials are written in Table 2.3 and shown in Figure 2.1 between $-\pi$ and π. A more details derivation of the basis is shown in Appendix A. Once the orthonormal basis is constructed, it could be used to compute the statistics of the lamination parameters.

2.3.3 Stochastic moments of lamination parameters

In this work, the statistics of the lamination parameters are sources of interest, especially for the inverse problem resolution in Eq.(2.4) and Eq.(2.5). The expected values of the lamination

Basis number	Fourier chaos polynomials $\psi_i^{\mathrm{n}}(\hat{X} = \sigma_\Theta X)$
0	1
1	$Z_{11}\sin(\hat{X})$
2	$Z_{21}\cos(\hat{X}) - Z_{22}$
3	$Z_{31}\sin(2\hat{X}) - Z_{32}\sin(\hat{X})$
4	$Z_{41}\cos(2\hat{X}) - Z_{42}\cos(\hat{X}) - Z_{43}$
5	$Z_{51}\sin(3\hat{X}) - Z_{52}\sin(2\hat{X}) - Z_{53}\sin(\hat{X})$
6	$Z_{61}\cos(3\hat{X}) - Z_{62}\cos(2\hat{X}) - Z_{63}\cos(\hat{X}) - Z_{64}$

Table 2.3: Example of generic orthonormal Fourier basis first terms.

parameters are expressed as:

$$\begin{aligned}
\mathbb{E}[\mathbf{v^A}] &= \alpha^{\mathbf{A}} \sum_k^N \tau_k^{\mathbf{A}} [\mathbb{E}\left(\cos(2\Theta_k)\right), \mathbb{E}\left(\sin(2\Theta_k)\right), \mathbb{E}\left(\cos(4\Theta_k)\right), \mathbb{E}\left(\sin(4\Theta_k)\right)], \\
\mathbb{E}[\mathbf{v^B}] &= \alpha^{\mathbf{B}} \sum_k^N \tau_k^{\mathbf{B}} [\mathbb{E}\left(\cos(2\Theta_k)\right), \mathbb{E}\left(\sin(2\Theta_k)\right), \mathbb{E}\left(\cos(4\Theta_k)\right), \mathbb{E}\left(\sin(4\Theta_k)\right)], \\
\mathbb{E}[\mathbf{v^D}] &= \alpha^{\mathbf{D}} \sum_k^N \tau_k^{\mathbf{D}} [\mathbb{E}\left(\cos(2\Theta_k)\right), \mathbb{E}\left(\sin(2\Theta_k)\right), \mathbb{E}\left(\cos(4\Theta_k)\right), \mathbb{E}\left(\sin(4\Theta_k)\right)],
\end{aligned} \tag{2.37}$$

with α and τ detailed in Table 2.4, N the number of plies, h the thickness of the laminate, and z_k the coordinate of the k^{th} ply.

i	α^i	τ_k^i
A	$\frac{1}{h}$	$(z_k - z_{k-1})$
B	$\frac{4}{h^2}$	$\frac{(z_k^2 - z_{k-1}^2)}{2}$
D	$\frac{12}{h^3}$	$\frac{(z_k^3 - z_{k-1}^3)}{3}$

Table 2.4: Some parameterization for the lamination parameters formulation.

Now, the trigonometric functions could be approximated as Fourier polynomial functions:

$$\cos\left(a\left(\Theta_k(X)\right)\right) \approx \sum_i^p e_{i,ca}\psi_i(\sigma_{\Theta_k}X), \qquad \sin\left(a\left(\Theta_k(X)\right)\right) \approx \sum_i^p e_{i,sa}\psi_i(\sigma_{\Theta_k}X), \tag{2.38}$$

with p the order of the expansion, where a can take the value of 2 or 4 and the subscripts ca and sa refer to, respectively, $\cos(a\Theta)$ and $\sin(a\Theta)$. Using the Fourier chaos expansion, the expected values of out-of-plane lamination parameters can be expressed as:

$$\mathbb{E}[\mathbf{v^D}] = \alpha^{\mathbf{D}} \sum_k^N \tau_k^{\mathbf{D}} [e_{0,c2}^k(\mu_{\Theta_k}), e_{0,s2}^k(\mu_{\Theta_k}), e_{0,c4}^k(\mu_{\Theta_k}), e_{0,s4}^k(\mu_{\Theta_k})], \tag{2.39}$$

with $e_{0,ca}$ and $e_{0,sa}$ the first coefficient of Eq.(2.38) who have to be computed. $E[\mathbf{v^A}]$ and $E[\mathbf{v^B}]$ are computed in the same manner. As random variables are independent, the variances are expressed as:

$$\begin{aligned}
\mathrm{Var}[\mathbf{v^D}] &= \left(\alpha^{\mathbf{D}}\right)^2 \sum_k^N \left(\tau_k^{\mathbf{D}}\right)^2 \left[\mathrm{Var}\left(\cos(2\Theta_k)\right), \mathrm{Var}\left(\sin(2\Theta_k)\right), \mathrm{Var}\left(\cos(4\Theta_k)\right), \mathrm{Var}\left(\sin(4\Theta_k)\right)\right], \\
\mathrm{Var}[\mathbf{v^D}] &= \left(\alpha^{\mathbf{D}}\right)^2 \sum_k^N \left(\tau_k^{\mathbf{D}}\right)^2 \left[\sum_{i=1}^p e_{i,c2}^k (\mu_{\Theta_k})^2, \sum_{i=1}^p e_{i,s2}^k (\mu_{\Theta_k})^2, \sum_{i=1}^p e_{i,c4}^k (\mu_{\Theta_k})^2, \sum_{i=1}^p e_{i,s4}^k (\mu_{\Theta_k})^2\right].
\end{aligned} \tag{2.40}$$

Since some lamination parameters can be strongly correlated, it is essential to consider their correlation in probabilistic analysis. The covariance between the lamination parameters can be computed with the product of, respectively, each coefficient. An example is shown considering the covariance of two LP v_1^A and v_2^A:

$$\mathrm{Cov}\left(\mathrm{v}_1^A, \mathrm{v}_2^A\right) = \left(\alpha^{\mathbf{A}}\right)^2 \sum_k^N \left(\tau_k^{\mathbf{A}}\right)^2 \sum_{i=1}^p e_{ic2}^k (\mu_{\Theta_k}) e_{is2}^k (\mu_{\Theta_k}). \tag{2.41}$$

In the same manner, the covariances of all combinations are generalized. To obtain a condensed format, the subscripts f and g of the coefficients are expressed as:

$$\begin{aligned}
f = 1 \Rightarrow e_{i,f} = e_{i,c2} \quad f = 2 \Rightarrow e_{i,f} = e_{i,s2}, f = 3 \Rightarrow e_{i,f} = e_{i,c4} \quad f = 4 \Rightarrow e_{i,f} = e_{i,s4}, \\
g = 1 \Rightarrow e_{i,g} = e_{i,c2} \quad g = 2 \Rightarrow e_{i,g} = e_{i,s2}, g = 3 \Rightarrow e_{i,g} = e_{i,c4} \quad g = 4 \Rightarrow e_{i,g} = e_{i,s4},
\end{aligned} \tag{2.42}$$

and the superscript F and G refers to the stiffness matrix studied ($\boldsymbol{A}$,$\boldsymbol{B}$ or $\boldsymbol{D}$). Then, the covariances are expressed as:

$$\mathrm{Cov}\left(\mathrm{v}_f^F, \mathrm{v}_g^G\right) = \alpha^{\mathbf{F}} \alpha^{\mathbf{G}} \sum_k^N \tau_k^{\mathbf{F}} \tau_k^{\mathbf{G}} \sum_{i=1}^p e_{i,f}^k (\mu_{\Theta_k}) e_{i,g}^k (\mu_{\Theta_k}). \tag{2.43}$$

To compute all of these statistics, the coefficients e_i need to be computed through the projection of the function of interest on the orthonormal basis.

2.3.4 Coefficients computation

The advantage of using a Fourier basis for the lamination parameters is that a closed-form formulation of the coefficients e_i in Eqs.(2.38) is available. An example can be shown using $\cos\left(a\left(\Theta_k(X)\right)\right) = \sum_i^p e_{i,ca} \psi_i(\sigma_{\Theta_k} X)$ with a taking the value of 2 or 4. We can write the function:

$$\begin{aligned}
e &= \cos\left(a(\mu_\Theta + \sigma_\Theta X)\right) \\
&= c_1 \cos(a\hat{X}) - s_1 \sin(a\hat{X}),
\end{aligned} \tag{2.44}$$

with $c_1 = \cos(a\mu_\Theta)$, $s_1 = \sin(a\mu_\Theta)$ and $\hat{X} = \sigma_\Theta X$.

The coefficients $e_{i,ca}$ are obtained as projections of the function of interest (e.g., e) onto each member of the Fourier basis. For example, the first two coefficients can be written as:

$$\begin{aligned}
e_{0,ca} &= \mathbb{E}[e \times \phi_0] = \mathbb{E}[e \times 1] \\
&= c_1 \mathbb{E}\left[\cos(a\hat{X})\right] - s_1 \mathbb{E}\left[\sin(a\hat{X})\right],
\end{aligned} \tag{2.45}$$

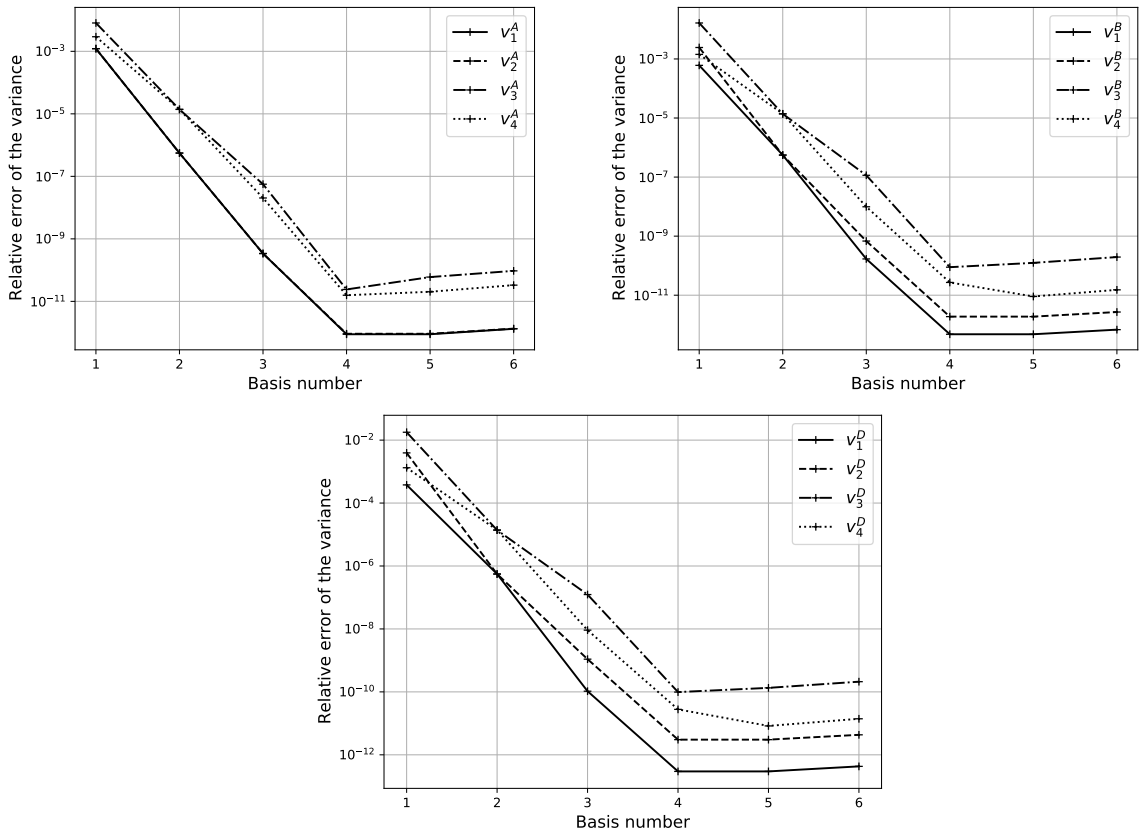

Figure 2.2: Relative error of the variances obtained from Fourier Chaos Expansion of in-plane, out-of-plane, and coupling lamination parameters of a stacking sequence.

and

$$\begin{aligned} e_{1,ca} &= \mathbb{E}[e \times \phi_1] = \mathbb{E}[e \times C_{11} \sin(\hat{X})] \\ &= C_{11} \left(c_1 \mathbb{E}\left[\cos(a\hat{X}) \sin(\hat{X})\right] - s_1 \mathbb{E}\left[\sin(a\hat{X}) \sin(\hat{X})\right] \right), \end{aligned} \tag{2.46}$$

where the expected values are computed with the Eqs.(2.25,2.27,2.22,2.21) and Eq.(2.22). The coefficients are obtained up to the order p, in the same manner, using the equations in Section 2.3.2.

The procedure is the same with the function $\sin\left(a\left(\Theta(X)\right)\right) = \sum_i^p e_{i,sa}\psi_i(X)$. Then a database is created for every orientation μ_Θ needed. Once this database is created, the means and covariances of lamination parameters of any stacking sequence are computed directly with Eq.(2.39) and Eq.(2.40).

2.3.5 Validation of the metamodel upscaling

The Fourier Chaos Expansion approach is numerically validated by computing the statistics associated with a simple case of lamination parameters. Increasing the size of the approximation basis, the variances of the bending lamination parameters $\mathbf{v^D}$ are compared to the variances computed with a numerical quadrature applied to the first equation of Eq.(2.40). For each ply, the variance of the trigonometric function, $\cos(a\Theta_k)$ for example, is written as:

$$\mathrm{Var}\left(\cos(a\Theta_k)\right) = \mathbb{E}[\cos(a(\mu_\Theta + \sigma_\Theta X))^2] - \mathbb{E}[\cos(a(\mu_\Theta + \sigma_\Theta X))]. \tag{2.47}$$

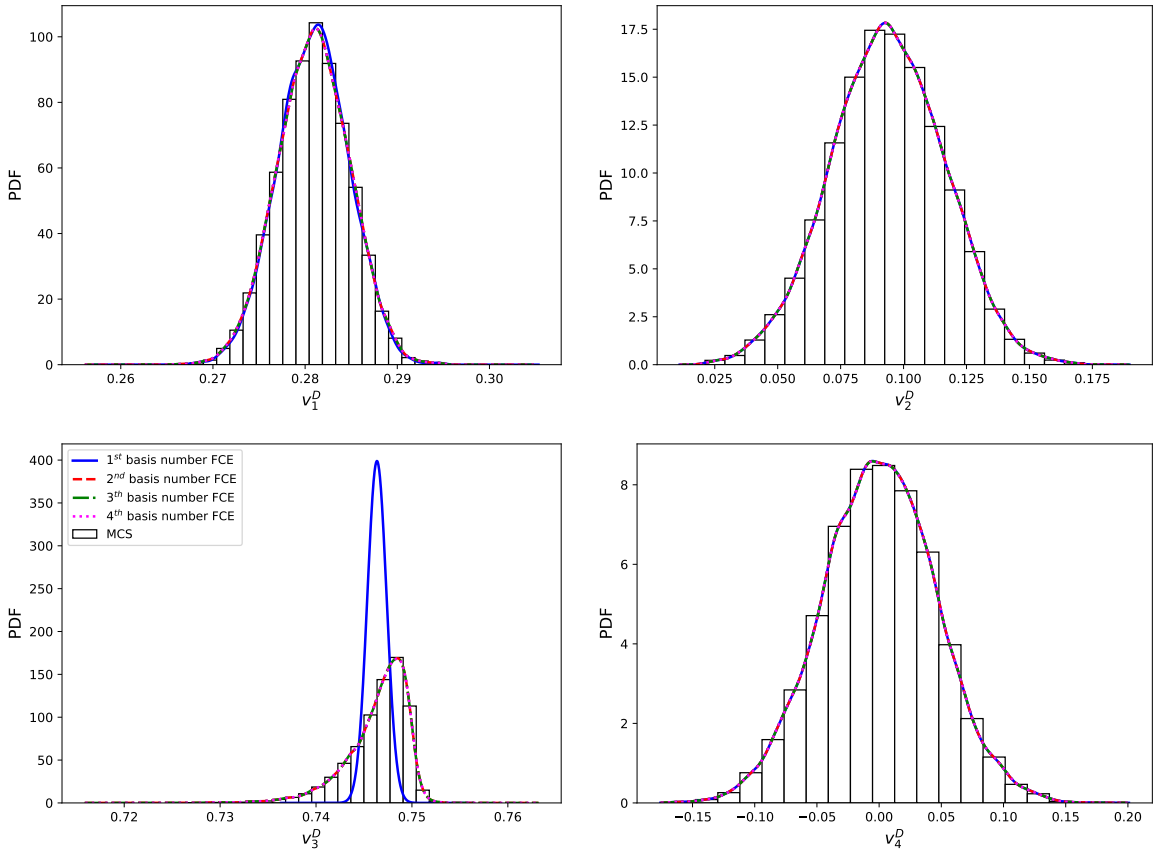

Figure 2.3: Convergence of out-of-plane lamination parameter PDFs for a $[0, 90, \pm 45]_s$ laminate.

The reference expected values are expressed as:

$$\mathbb{E}[\cos(a(\mu_\Theta + \sigma_\Theta X))] = \int_{-\infty}^{\infty} \cos(a(\mu_\Theta + \sigma_\Theta X)) f_X dX, \tag{2.48}$$

and can be computed with the integration sub-package of *SciPy* with f_X the normal distribution. The integration function of *SciPy* is able to integrate on infinite support $(-\infty, \infty)$ of functions. The metamodel is validated for a stacking sequence of 16 plies ([45°,30°,0°,-45°,90°,-30,-15°,15°]$_s$), and the relative error is plotted in Figure 2.2. We notice, as expected in this case, the spectral convergence of the error to very small values for 4-term Fourier-Chaos expansion.

Additionally, scatter plots of different sets of out-of-plane lamination parameters are shown in Figure 2.5 for the "fourth-order" FCE of a $[0, 90, \pm 45]_s$ laminate. They are compared with MC simulation using the real lamination parameters equation. It is shown that FCE for lamination parameters is accurate enough. This approach is used to estimate lamination parameters PDFs that are compared with the Monte Carlo simulation. Gaussian KDEs for the out-of-plane lamination parameters of a $[0, 90, \pm 45]_s$ laminate are shown in Figure 2.3. The distributions for each order of the FCE are plotted to study the convergence.
The PDFs of $v_{2,4}^D$ are approximately Gaussian, and a first-order expansion is sufficient to model these parameters. Increasing order is most evident for $v_{1,3}^D$. For v_1^D, a small improvement is achieved in using a second-order expansion in comparison with a first-order expansion, whereas for v_3^D, the difference is tremendous because of the non-symmetric PDF. It seems that "second-order" FCE is enough. However, if we focus on the details, we observe that the "fourth-order"

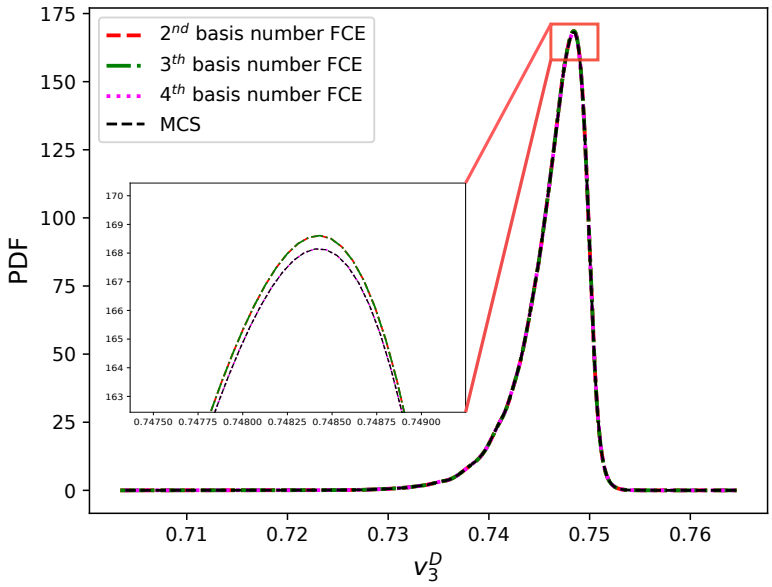

Figure 2.4: Zoom of the convergence of out-of-plane lamination parameter v_3^D for a $[0, 90, \pm 45]_s$ laminate.

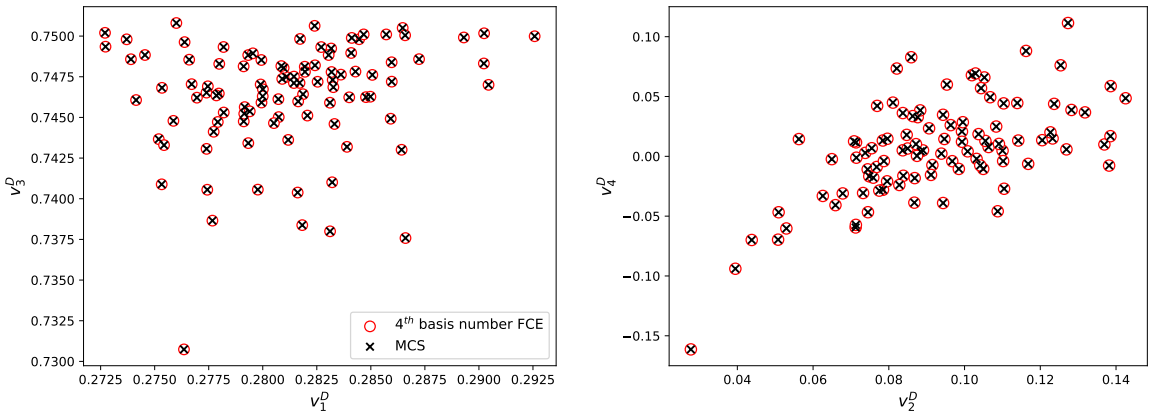

Figure 2.5: Comparison of scatter plots for the out-of-plane lamination parameters of a $[0, 90, \pm 45]_s$ laminate.

	Cost function	Type	Computation Method of $\mathbf{v^D}$ or $\boldsymbol{\mu}_{\mathbf{v^D}}$ and $\sigma_{\mathbf{v^D}}$
F1	$\min_{\boldsymbol{\theta}} \|\mathbf{v^{D,des}} - \mathbf{v^D}(\boldsymbol{\theta})\|$	Deterministic	Analytical CLPT
F2	$\min_{\boldsymbol{\mu_\Theta}} \|\boldsymbol{\mu}^{\text{des}}_{\mathbf{v^D}} - \boldsymbol{\mu}_{\mathbf{v^D}(\boldsymbol{\Theta}\|\boldsymbol{\mu_\Theta})}\|$	Stochastic	Monte Carlo
F3	$\min_{\boldsymbol{\mu_\Theta}} \|\boldsymbol{\mu}^{\text{des}}_{\mathbf{v^D}} - \boldsymbol{\mu}_{\widehat{\mathbf{v^D}}(\boldsymbol{\Theta}\|\boldsymbol{\mu_\Theta})}\|$	Stochastic	FCE
F4	$\min_{\boldsymbol{\mu_\Theta}} \Big(\|\boldsymbol{\mu}^{\text{des}}_{\mathbf{v^D}} - \boldsymbol{\mu}_{\widehat{\mathbf{v^D}}(\boldsymbol{\Theta}\|\boldsymbol{\mu_\Theta})}\| + \rho\sqrt{\Big(\sigma_{\widehat{\mathrm{v}^D_2}}(\boldsymbol{\Theta}\|\boldsymbol{\mu_\Theta})\Big)^2 + \Big(\sigma_{\widehat{\mathrm{v}^D_4}}(\boldsymbol{\Theta}\|\boldsymbol{\mu_\Theta})\Big)^2} \Big)$	Stochastic	FCE

Table 2.5: Different formulations studied of the inverse problem cost function.

	Lamination Parameters
Target 1 (T1)	$\mathbf{v^{D,des}} = (0.603, 0, -0.273, 0)$
Target 2 (T2)	$\mathbf{v^{D,des}} = (-0.25, 0, 0.25, 0)$

Table 2.6: Values of the target lamination parameters studied.

is exactly the same as MC simulation in Figure 2.4.

2.4 Inverse problem resolution via Fourier Chaos Expansion

From now on, the Fourier Chaos Expansion can be used for the inverse problem to match the statistics of both scale parameters. Several optimization formulations of the inverse problem will be tested. We will focus on matching only the bending LPs $\mathbf{v}^D$. Firstly, the resolution of the inverse problem in a variability framework can be compared between the use of the Monte Carlo and the FCE for the computation of the lamination parameters mean. Then, a comparison between the deterministic (i.e., using the *nominal* values) and the stochastic (i.e., using the *mean* statistic) inverse problem is performed to show in which case different results are possible. Finally, the variance could be used to limit some variability or limit the non-respect of some hypotheses. In this case, we will try to minimize the standard deviations of $\mathrm{v}^D_{2,4}$, which means trying to enforce planar orthotropy even in the presence of uncertainty.

The formulations tested in this section are summed up in Table 2.5. The "type" column indicates if the uncertainty of ply orientations is taken into account or not. The computation method refers to which method is used to compute the LPs or their statistics. The target points studied are shown in Table 2.6.

2.4.1 Matching the mean statistics

The inverse problem is solved by matching the mean between the lamination parameters given a stacking sequence and the target lamination parameters. The methods to compute the LPs average are compared. Both cost functions F2 and F3 are studied, where the first uses the Monte Carlo method to compute the mean of the LPs and the second uses FCE presented earlier in Section 2.3.

Target	n_{plies}	$\Delta_\theta^{\text{inc}}$	Cost function formulation	Cost function value	Computation time
T1	24	5	F1	0.0109	$\approx$ 1.5s
			F2	0.01282	$\approx$ 190s
			F3	0.0086	$\approx$ 5.6s
		15	F1	0.0119	$\approx$ 1.4s
			F2	0.01374	$\approx$ 173s
			F3	0.0142	$\approx$ 5.3s
	16	5	F1	0.009	$\approx$ 1.4s
			F2	0.0131	$\approx$ 140s
			F3	0.0111	$\approx$ 3.9s
		15	F1	0.0217	$\approx$ 1.3s
			F2	0.0131	$\approx$ 133s
			F3	0.0161	$\approx$ 3.8s
T2	24	5	F1	0.0016	$\approx$ 1.5s
			F2	0.0011	$\approx$ 190s
			F3	0.0016	$\approx$ 5.6s
		15	F1	0.0021	$\approx$ 1.4s
			F2	0.0015	$\approx$ 173s
			F3	0.0013	$\approx$ 5.3s
	16	5	F1	0.0037	$\approx$ 1.4s
			F2	0.0022	$\approx$ 140s
			F3	0.0035	$\approx$ 3.9s
		15	F1	0.0083	$\approx$ 1.3s
			F2	0.0008	$\approx$ 133s
			F3	0.0006	$\approx$ 3.8s

Table 2.7: Results of the inverse problem depending according to the different formulations presented in Table 2.5.

Available orientations to be chosen from are uniformly distributed over $]-90^{\text{o}} : \Delta_\theta^{\text{inc}} : 90^{\text{o}}]$, with $\Delta_\theta^{\text{inc}}$ the angular increment. Two angular increments are tested: 5° and 15°. Moreover, two amounts of plies n_{plies} are also tested (i.e., 16 and 24 plies). Since the problem is non-convex with discrete ply orientations, the optimization is run 10 times. Then, the stacking sequence with the lowest cost function of the 10 optimization runs is chosen as the best candidate. For the Monte Carlo method, the size of the sample is 10000 to compute the mean of lamination parameters following the distribution in Eq.(1.35).

The results presented in Table 2.7 show that retrieved stacking sequences are a bit different between the use of MC and FCE. Indeed, the sample size for MC is not large enough to be as accurate as FCE to compute the statistics. It could explain the differences in the stacking sequences. However, the cost function has the same order of magnitude for each case. Concerning the computational time, the interest of FCE is shown. The time presented is the average time over the 10 optimizations made for each case. A huge difference in the computational time is found between the use of MC or FCE. Moreover, a detailed result is presented in Figure 2.6 with the vision of the results in the lamination parameters space and the impact on the macroscopic

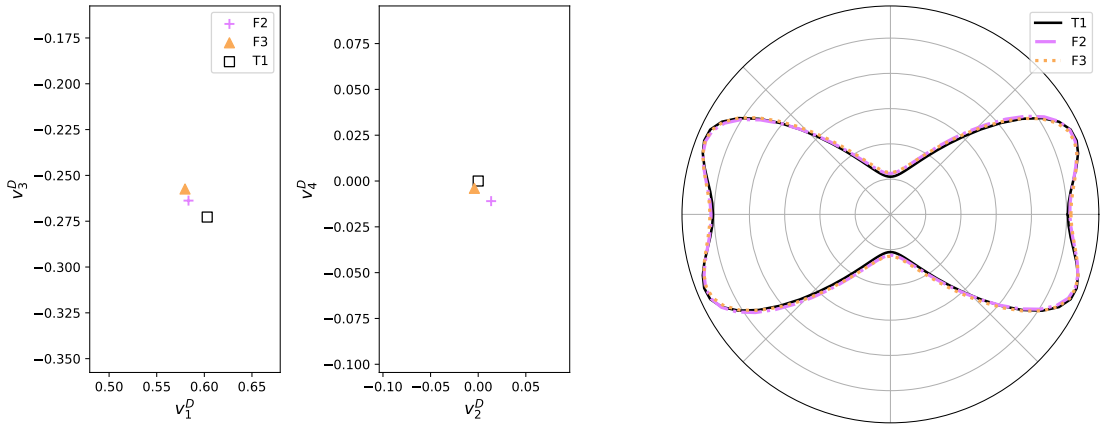

(a) Scatter plot in 2D projection.

(b) Polar plot of the engineering modulus evolution $E_{\boldsymbol{D},11}$.

Figure 2.6: Detailed results of the inverse problem of Target 1 using MC (F2) and FCE (F3) with $n_{\text{plies}} = 24$ and $\Delta_\theta^{\text{inc}} = 15°$.

response of the composite laminate with the polar plot. In Figure 2.6a, the mean of v_2^D and v_4^D is closest to the target using FCE. The difference on the engineering modulus evolution in Figure 4.12b between both results is small.

2.4.2 Comparison between deterministic and stochastic formulations

The inverse problem solutions, performed in a deterministic and stochastic framework following the formulation F1 and F3 of Table 2.5, are compared. The objective is to observe if discrepancies appear in the macroscopic response of the stacking sequence designs using both formulations. The genetic algorithm is run 10 times for each case.

The results are also found in Table 2.7. The cost function values for each design for the first target know some differences. An example is shown in Figure 2.7, where the mean of the retrieve stacking sequence coming from the formulation F3 matching the mean is closer to the target than the one matching the nominal values. The results for the second target are quite similar except for the case where $n_{\text{plies}} = 16$ and $\Delta_\theta^{\text{inc}} = 15$ (see Figure 2.8). However the macroscopic response via the polar plot are quite similar with both formulations (see Figure 2.7b).

Nevertheless, it could be interesting to study the variance of these two parameters to observe the impact on orthotropy. Therefore the variability is studied for the Target 2 with $n_{\text{plies}} = 16$ and $\Delta_\theta^{\text{inc}} = 15°$. The variability is shown in Figure 2.9 in the 2D projection $(\mathrm{v}_1^D, \mathrm{v}_3^D)$ and $(\mathrm{v}_2^D, \mathrm{v}_4^D)$. Even if the mean and nominal values of LPs are close to the target for both stacking sequences, the variability is quite different. The correlation between $(\mathrm{v}_1^D, \mathrm{v}_3^D)$ and $(\mathrm{v}_2^D, \mathrm{v}_4^D)$ is at its highest for the stacking sequence coming from the F3 cost function. Moreover, the orientation of the correlation is different between both stacking sequences in the $(\mathrm{v}_1^D, \mathrm{v}_3^D)$ plan.

Therefore, in a variability framework, it opens the question of taking into account the variance or the correlation in the inverse problem resolution. In the end, the variances of lamination parameters could be exploited for trying to respect some hypothesis (e.g., the orthotropy) or

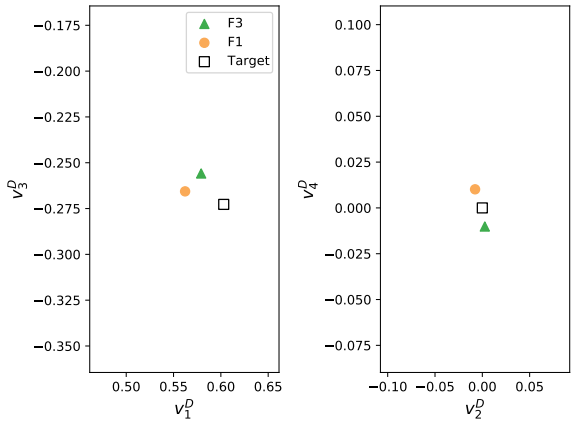

(a) Scatter plot in 2D projection.

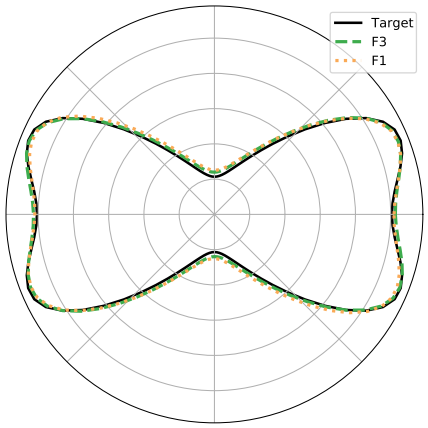

(b) Polar plot of the engineering modulus evolution $E_{\boldsymbol{D},11}$.

Figure 2.7: Detailed results of the inverse problem of Target 1 with $n_{\text{plies}} = 16$ and $\Delta_\theta^{\text{inc}} = 15°$ for the nominal formulation (F1) and the stochastic formulation using FCE (F3).

maybe to regularize the inverse problem resolution.

2.4.3 Multi-objective formulation with variability reduction for orthotropy

The objective is to retrieve a stacking sequence with the target T2 of Table 2.6 while taking into account the minimization of the variance of v_2^D and v_4^D as in formulation F4 of Table 2.5. We recall the cost function formulation below:

$$\min_{\boldsymbol{\mu_\Theta}} \|\boldsymbol{\mu}_{\mathbf{v^D}}^{\text{des}} - \boldsymbol{\mu}_{\widehat{\mathbf{v^D}}(\boldsymbol{\Theta}|\boldsymbol{\mu_\Theta})}\| + \rho\sqrt{\left(\sigma_{\widehat{\mathrm{v}_2^D}}(\boldsymbol{\Theta}|\boldsymbol{\mu_\Theta})\right)^2 + \left(\sigma_{\widehat{\mathrm{v}_4^D}}(\boldsymbol{\Theta}|\boldsymbol{\mu_\Theta})\right)^2}. \tag{2.49}$$

A choice on the value of ρ has to be made. It depends on the order of magnitude of each objective and the weight that the user wants to give to the standard deviation minimization objective in comparison to the mean matching objective. In this study, we will study the influence of this parameter in optimization-based stacking sequence retrieval. Moreover, we consider stacking sequence with 24 plies.

First, the inverse problem was solved with a $\rho = 0$ corresponding to the F3 formulation of Table 2.5. The average LPs of the three best laminates are plotted in Figure 2.10a. The three best solutions are very close to the target. However, the dispersion for each stacking sequence can be quite different. It has already been shown in Section 1.4.3.1. For each stacking sequence, the ply orientation uncertainty is modeled as in Eq.(1.35) and can be propagated with the FCE. The dispersion in the (v_1^D,v_3^D) frame are all different (see Figure 2.10b). The second stacking sequence shows limited variability in this projection plane, whereas, in the (v_2^D,v_4^D) frame, variability is at its highest.

Furthermore, the possibility to reduce $\|\sigma_{\mathrm{v}_{2,4}^D}\|$ during the stacking sequence retrieval, without impacting the objective $\|\boldsymbol{\mu}_{\mathbf{v^D}}^{\text{des}} - \boldsymbol{\mu}_{\widehat{\mathbf{v^D}}(\boldsymbol{\Theta}|\boldsymbol{\mu_\Theta})}\|$ is investigated. The values of the weight ρ in the Eq.(2.49) have been gradually augmented. For each case, thirty optimizations have been

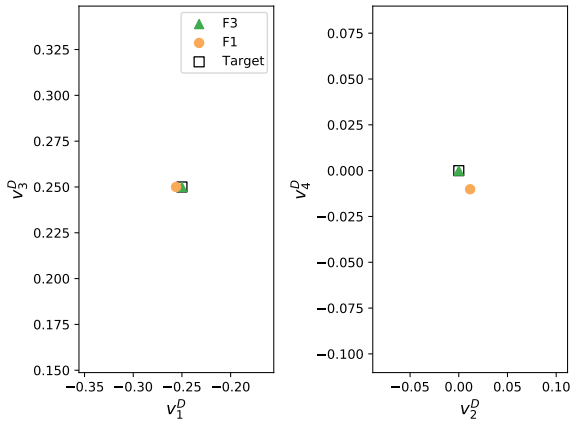

(a) Scatter plot in 2D projection.

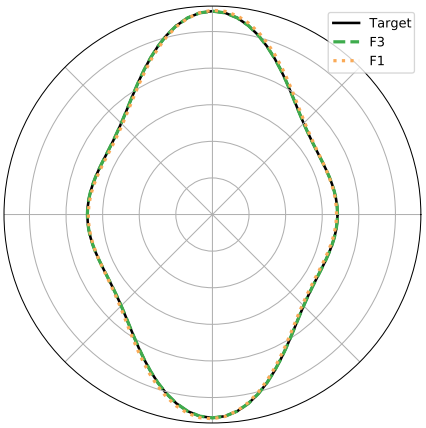

(b) Polar plot of the engineering modulus evolution $E_{\boldsymbol{D},11}$.

Figure 2.8: Detailed results of the inverse problem of Target 2 with $n_{\text{plies}} = 16$ and $\Delta_\theta^{\text{inc}} = 15°$ for formulation F1 and F3.

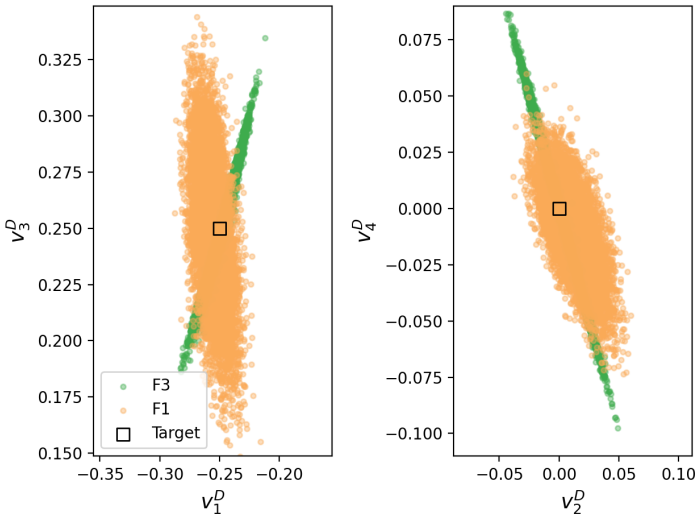

Figure 2.9: Sample in the 2D projection $(\mathrm{v}_1^D, \mathrm{v}_3^D)$ and $(\mathrm{v}_2^D, \mathrm{v}_4^D)$ coming from the ply orientations uncertainty of the results presented in Figure 2.8.

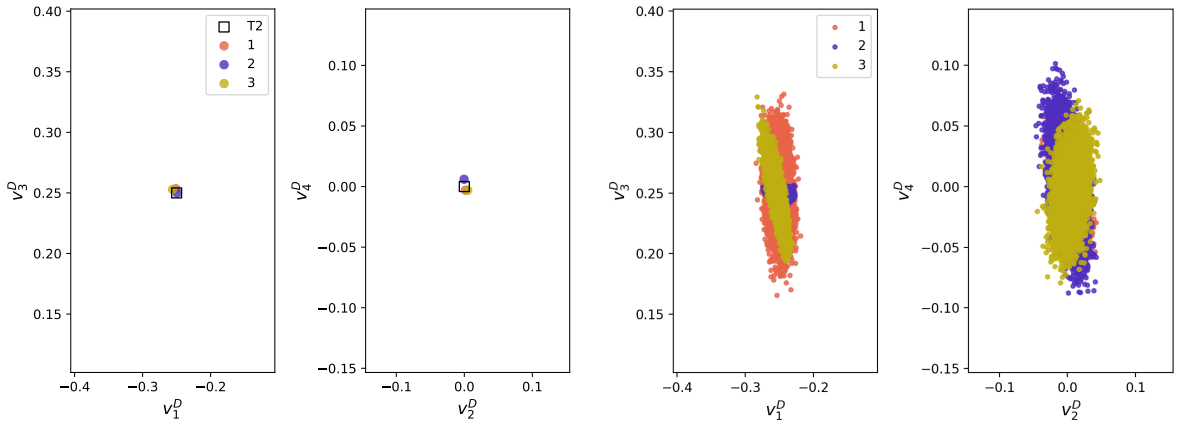

(a) Mean of LPs in the 2D projection. (b) Corresponding sample of the solutions.

Figure 2.10: Three best solutions of the inverse problem with $\rho = 0$.

run with the GA. For each ρ, we observe on Figure 2.11 a cluster of solutions. The average values of both objectives are plotted with a line on each axis with the corresponding color. These results are logical with respect to the weight given to the second objective. For $\rho = 0$, we have the smallest average on the objective $\|\boldsymbol{\mu}^{\text{des}}_{\mathbf{v^D}} - \boldsymbol{\mu}_{\widehat{\mathbf{v^D}}(\boldsymbol{\Theta}|\boldsymbol{\mu}_{\boldsymbol{\Theta}})}\|$ and the highest in the second one. The opposite is found out for $\rho = 25$. Moreover, it appears clear that there is a limit value for the variable $\|\sigma_{\mathrm{v}^D_{2,4}}\|$ at approximately 0.017. A higher value of ρ does not further reduce the standard deviation norm of $\mathrm{v}^D_{2,4}$ parameters. Therefore, any value of ρ bigger than 25 will only contribute to possibly deteriorate the solution within the objective on the mean target $\|\boldsymbol{\mu}^{\text{des}}_{\mathbf{v^D}} - \boldsymbol{\mu}_{\widehat{\mathbf{v^D}}(\boldsymbol{\Theta}|\boldsymbol{\mu}_{\boldsymbol{\Theta}})}\|$. This argument is reinforced when we compare with the solutions using $\rho = 10$. These latest solutions reach, most of the time, the minimum level of standard deviation norm; however, the first objective of matching the mean statistics has a lower range than the solution using $\rho = 25$. Moreover, the results with $\rho = 10$ may achieve lower values of the first objective than with $\rho = 25$. Based on these results, it appears that choosing ρ between 5 or 10 is a good compromise between both objectives of Eq.(2.49).

Now, the three best results with $\rho = 0$ and $\rho = 25$ are compared in terms of the mean objective and the dispersion in the LPs space. The results are shown in Figure 2.12. Firstly, we observe that the LPs average coming from the solutions with $\rho = 25$ the solutions are slightly off the target. Nevertheless, even if the stacking sequences are different, the dispersions in the 2D projection are similar for all the solutions with $\rho = 25$ (see Figure 2.12d). The variability of $\mathrm{v}^D_{2,4}$ parameters are effectively reduced in comparison to the solutions with $\rho = 0$. They seem even less correlated. However, a correlation exists in the Figure 2.12d between v^D_1 and v^D_3 for all the solutions. Moreover, while you reduce the variability for v^D_2 and v^D_4 parameters, it seems to affect v^D_1 and v^D_3.

The impact of the $\mathbf{v^D}$ variability on the engineering modulus $E_{\boldsymbol{D},11}$ is shown in Figure 2.13 via a polar plot. In addition to mean, the standard deviation is displayed. In this figure the focus is made on the solution 2 of Figure 2.12 for both ρ. The uncertainty has, most of the time, a bigger impact on the stacking sequence coming from the $\rho = 25$ solution, especially in the 90° axis.

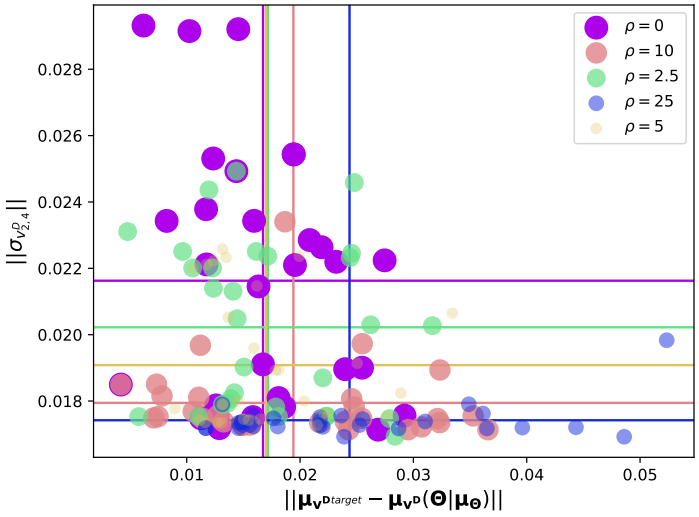

Figure 2.11: Multi-objective graph of the standard deviation norm $\|\sigma_{\mathrm{v}^D_{2,4}}\|$ and $\|\boldsymbol{\mu}^{\mathrm{des}}_{\mathbf{v^D}} - \boldsymbol{\mu}_{\widehat{\mathbf{v^D}}(\boldsymbol{\Theta}|\boldsymbol{\mu}_{\boldsymbol{\Theta}})}\|$ for different ρ values. For each ρ, the inverse problem has been solved thirty times. The lines correspond to the average value for each objective over the 30 runs.

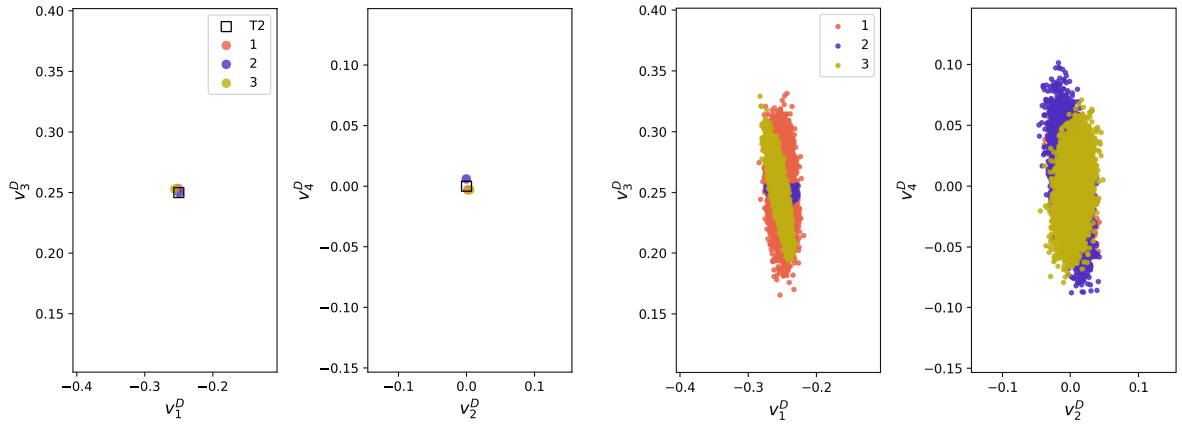

(a) Mean of LPs in the 2D projection ($\rho = 0$).

(b) Corresponding sample ($\rho = 0$).

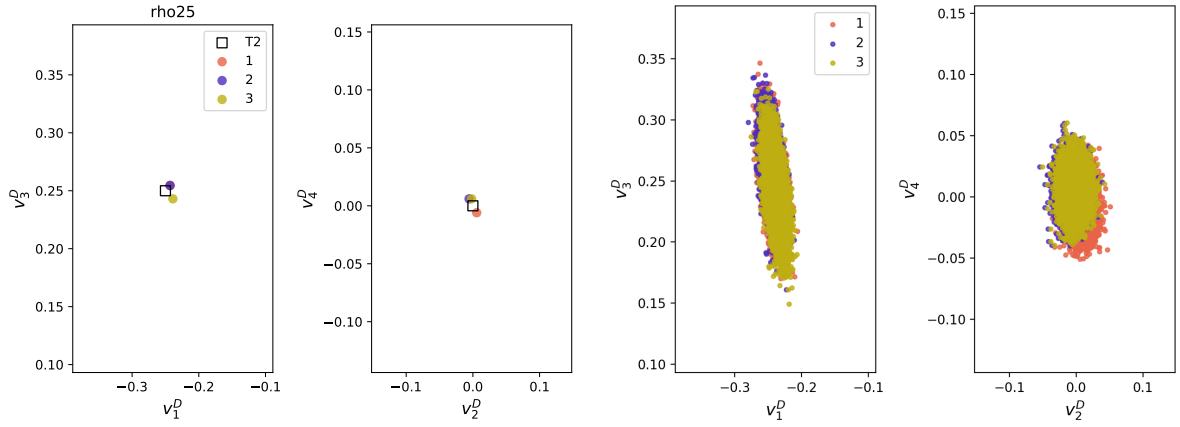

(c) Mean of LPs in the 2D projection ($\rho = 25$).

(d) Corresponding sample ($\rho = 25$).

Figure 2.12: Three best solutions of the inverse problem for different values of ρ.

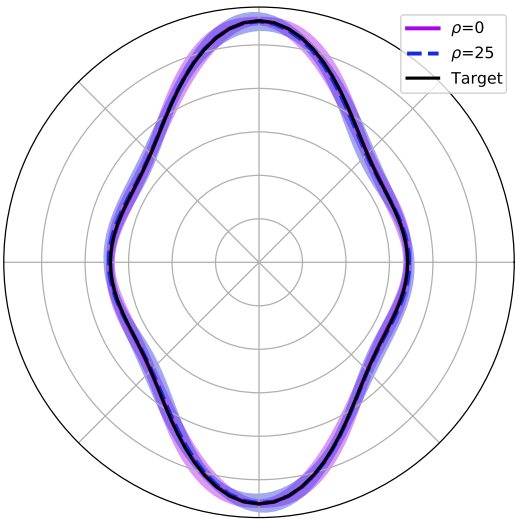

Figure 2.13: Polar plot of the evolution of the engineering modulus $E_{\boldsymbol{D},11} \pm 3$ standard deviation for one solution of two different ρ values.

2.5 Conclusion

In a variability framework, the inverse problem needs to match the statistics between the orientations of a stacking sequence and the target lamination parameters. Therefore a non-intrusive surrogate model has been developed to achieve this step. A Fourier Chaos Expansion approximates the trigonometric functions found in the lamination parameters formulation. The particular orthonormal Fourier basis constructed enables a closed-form formulation of the deterministic coefficients of the expansion. This surrogate model has been validated with numerical integration and Monte Carlo Simulation, showing its efficiency for the inverse problem resolution in terms of computational time compared to the Monte Carlo method. Moreover, different formulation types were proposed, i.e. taking into account only the mean statistic or also the standard deviation. The presented results show that solving the inverse problem with or without the mean statistics may lead to slightly different results in terms of the cost function but very different variability in the lamination parameters space. Then, the idea was to minimize as well the standard deviations of two parameters to limit the deviation from bending orthotropy. For the case where the weight of the standard deviation is important, the variability is similar for the best solutions: it could maybe constrain the inverse problem optimization and regularize it. Moreover, limiting the variability on those parameters appears to have a more significant impact on the other LPs, and maybe later on the reliability analysis, depending on the physics and the mechanical model used. It opens up an issue on the choice between enforcing strictly the hypotheses on which a given mechanical model is based, or favoring a reliability analysis that is more suitable to this model, but where the aforementioned hypotheses may not be valid in the variability framework. Therefore, depending on the laminate composite problem and the hypotheses made, the inverse problem formulation could take into account different statistical information. However, it is important to note that the present study has been carried out on a very limited set of target points, and that these conclusions may not hold when the analysis is extended to a broader set of points over the domain.

This chapter describes one step of the multi-scale reliability-based design optimization approach: given a set of lamination parameters, a stacking sequence is retrieved matching the

statistics. Thanks to this, the orientation uncertainty can be appropriately modeled and propagated through the lamination parameters design space. Once a LPs sample is available, the reliability analysis needed for the RBDO can be performed. However, the mechanical model used in this thesis is costly, and a strategy needs to be set up to perform reliability analysis in an acceptable computation time through another surrogate model strategy. This will be the focus of the next chapter.

CHAPTER 3

METAMODELING STRATEGY FOR RBDO WITH MULTI-MODAL CONSTRAINT

Contents

3.1 Introduction

Considering continuous optimization processes subject to a set of constraints, the optimum solution tends to activate at least one constraint. Therefore, it is essential to effectively quantify the probability of a laminate having unsafe configurations when the ply orientation errors are introduced. Such a probability is conveniently defined as follows:

$$\begin{aligned} \mathbb{P} &= \mathrm{P}[g(\mathbf{X}) \geq 0] \\ \mathbb{P} &= \int_{\mathcal{F}=\{\mathbf{x}\in\mathcal{X} \mid g(\mathbf{X})\geq 0\}} f_{\mathbf{X}}(\mathbf{x}) d\mathbf{x}, \end{aligned} \tag{3.1}$$

where $\mathcal{F} = \{\mathbf{x} \in \mathcal{X} : g(\mathbf{X}) \geq 0\}$ is the domain of failure and $\mathbf{X}$ is the random vector.

This chapter concerns the estimation of the failure probability in a context where the constraint g is costly to evaluate, and the target probability is around 10^{-2}. This means that the probability estimation should be possible within a reasonable number of calls to the model. The quantities of interest for the reliability analysis of this work are mechanical instabilities, such as buckling or flutter. Their computation comes from modal analysis. Subsequently, discontinuity of their response can occur in the design space if mode switching occurs. Jonsson et al. (2019) and Stanford et al. (2014) show the different types of discontinuity possibly present in the design space for the flutter phenomenon. In addition to mode switching (see Figure 3.1a), there is a special mode that can become abruptly the critical mode between two designs: it is called the *hump mode* (see Figure 3.1b). An example of constraint studied in this work is shown in Figure 3.2. In this case, both types of discontinuities are present. The response of mode 3 is a *hump mode*, and the global response (i.e., the minimum value) in Figure 3.2d shows mode switching.

Since a gradient-based algorithm is preferred, the sensitivity of the failure probability is of interest. Some methods, detailed later, allows computing the sensitivity without increasing the number of calls to the model. To do so, a parametric PDF of the random variables is needed. However, our random input variables are the lamination parameters. Indeed, in Chapter 1, we observed that modeling the LPs uncertainty is not always straightforward and sometimes impossible to model with parametric function.

Therefore the strategy proposed in this chapter has to deal with:

1. the expensive cost of the models used,
2. the possible different multi-modal behavior of the quantity of interest in the design space,
3. and the computation of the failure probability sensitivities, adapted for lamination parameters, most efficiently.

Section 3.2 introduces some techniques existing in the literature for estimating failure probability. Section 3.3 details a surrogate model strategy dealing with discontinuity in the design space to compute the failure probability and its sensitivity. Finally, a hybrid strategy is implemented to compute the sensitivity of failure probability needed during the RBDO process.

3.2 Probability estimation methods

This section reviews the state-of-the-art for estimating the failure probability defined in Eq. (3.1). Approximation methods are first reviewed, then simulation methods such as Monte Carlo are presented. Finally, the focus is on surrogate-based methods with an active learning strategy.

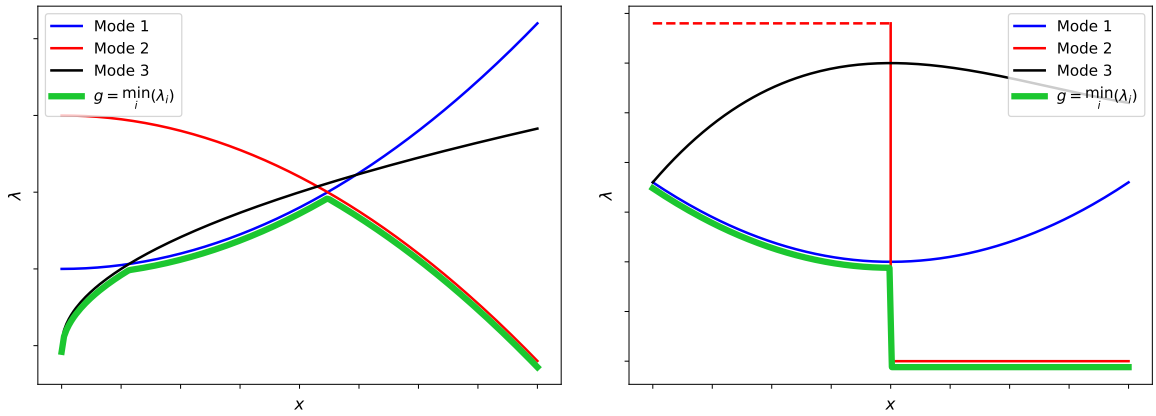

(a) Mode switching.

(b) Mode 2 is a *hump mode*. The dashed line represents the stability zone of the second mode, represented by a bearing value.

Figure 3.1: Example of possible discontinuities in an 1D design space. Three modes are represented. The quantity of interest is the minimum eigenvalue.

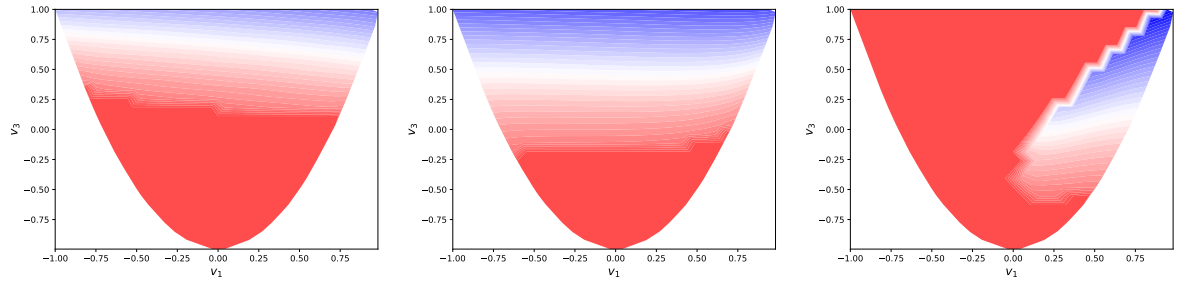

(a) First mode

(b) Second mode

(c) Third mode

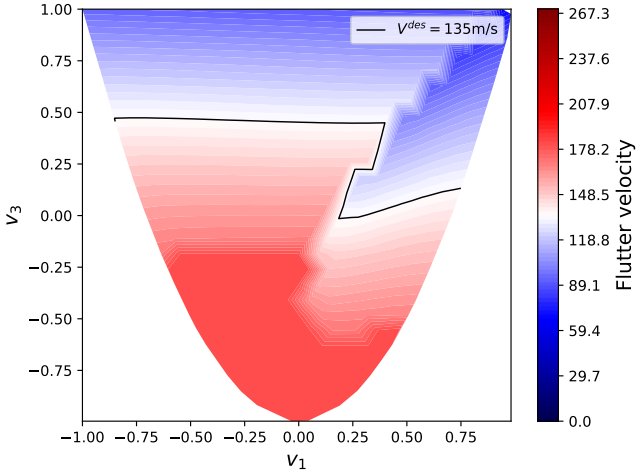

(d) Minimum critical velocity of the three first modes

Figure 3.2: Flutter instability response in a 2D design space in the presence of a discontinuity. The black line represent the design velocity, which is the limit-state function.

3.2.1 Most-probable-failure-point-based techniques

The general term 'Most-Probable-Failure-Point-based techniques', or (MPFP), refers specifically to the first-order reliability method (FORM) and the second-order reliability method (SORM). The following only covers FORM theoretical details. For a more comprehensive understanding of this topic, please refer to general textbooks on the subject (Ditlevsen and Madsen, 2007; Lemaire, 2009) .

FORM is one of the more practical approaches to approximate a failure probability. A transformation is performed from the *original space* (i.e., physical space), denoted the "x-space", to the so-called *standard normal space*. All the random components $\mathbf{X}$ become independent standard Gaussian PDF. To this end, a mapping from the space of original random variables $\mathbf{X}$ to the standard Gaussian space is performed:

$$\begin{aligned} \mathbf{u} &= T(\mathbf{x}), \\ g_u(\mathbf{u}) &= g(T^{-1}(\mathbf{u})), \end{aligned} \tag{3.2}$$

where T is the mapping application which varies according to the method used. Isoprobabilistc transformation can be performed for non-normally distributed and independent random variables. In the general case, the Nataf (Nataf, 1962) and Rosenblatt (Murray Rosenblatt, 1952) transformations are used (Lebrun and Dutfoy, 2009). Both spaces are represented in Figure 3.3 with a limit-state function represented with a black line on the physical and standard spaces.

FORM replaces the sampling strategy by finding the point over the limit-state surface, which is the closest to the origin of the standard space. In other words, the point corresponds to the maximum probability of occurrence of the failure event, and it is called the *most probable failure point* (MPFP). This point is found with a constrained optimization problem:

$$\mathbf{u}^* = \arg\min \frac{1}{2}\mathbf{u}^T\mathbf{u} \quad \text{subject to} : g_u(\mathbf{u}) = 0. \tag{3.3}$$

Thus, one can define a new safety measure, called the *Hasofer-Lind reliability index* (HL-RF) (Hasofer Abraham M. and Lind Niels C., 1974), denoted by β_{HL} and defined such that:

$$\beta_{HL} = \beta = \alpha^T\mathbf{u}^*, \tag{3.4}$$

where α is a unit vector of the axis between the origin O of the standard normal space and the MPFP; providing a *most probable failure direction*:

$$\alpha = \frac{\nabla g_u(\mathbf{u}^*)}{\|\nabla g_u(\mathbf{u}^*)\|}, \tag{3.5}$$

for the less usual convention where $g \geq 0$. The safety measure β represents the Euclidean distance from the MPFP to the origin O of the standard normal space (i.e, the dotted black line in Figure 3.3b). In general, the origin of the standard normal space belongs to the safe domain; consequently, β is positive. Assuming that the limit-state function is continuous, smooth, and differentiable around the MPFP, the first-order Taylor series expansion is applied such that:

$$g_u(\mathbf{u}) \approx g_u(\mathbf{u}^*) + \nabla_u^T g_u(\mathbf{u}^*)\,(\mathbf{u} - \mathbf{u}^*) \tag{3.6}$$

Since $g_u(\mathbf{u}^*) = 0$ by definition and combining with Eq.(3.6), the approximation of the limit state function can be written:

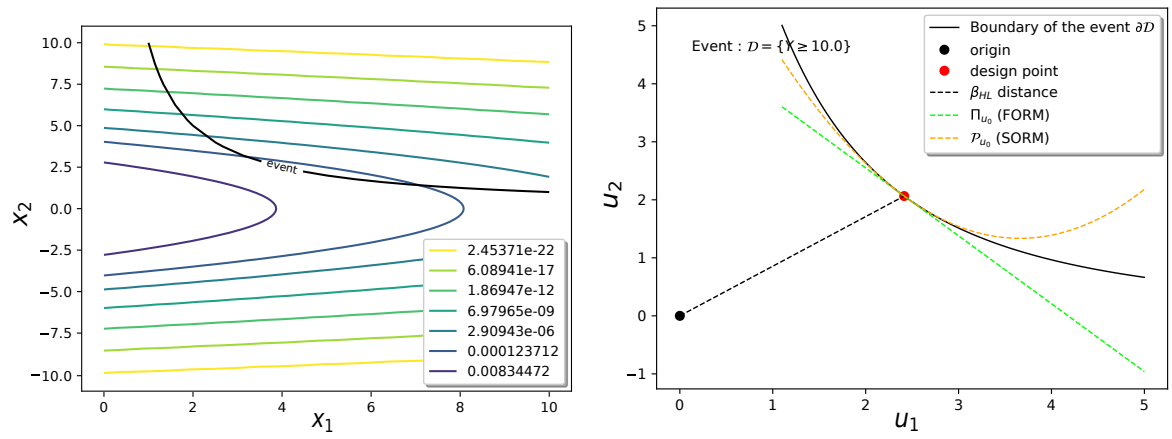

(a) PDF in the 2D physical space.

(b) Standard space.

Figure 3.3: Schematic representation of FORM and SORM approximations with the mapping from the physical to the standard space.

$$g_u(\mathbf{u}) = \|\nabla_u^T g_u(\mathbf{u}^*)\| \left(\alpha^T \mathbf{u} - \alpha^T \mathbf{u}^*\right) = \|\nabla_u^T g_u(\mathbf{u}^*)\| \left(\alpha^T \mathbf{u} - \beta\right). \tag{3.7}$$

Thus, FORM consists in approximating the failure probability by the following Equation:

$$\mathbb{P}_{\text{FORM}} = \int_{\mathcal{F}_\mathbf{u} = \{\mathbf{u} \in \mathbb{R} \mid g_u(\mathbf{U}) \geq 0\}} f_\mathbf{U}(\mathbf{u}) d\mathbf{u}, \tag{3.8}$$

where $\mathcal{F}_\mathbf{u} = \{\mathbf{u} \in \mathbb{R} \mid g_u(\mathbf{U}) \geq 0\} = \left\{\mathbf{u} \in \mathbb{R} \mid \alpha^T \mathbf{u} - \beta \geq 0\right\}$ is the domain of failure in the standard space. The integral is now written as follows:

$$\mathbb{P}_{\text{FORM}} = \mathbb{P}\left(g_u(\mathbf{u}) \geq 0\right) = \mathbb{P}\left(-\alpha^T \mathbf{u} \leq -\beta\right). \tag{3.9}$$

Since the quantity $-\alpha^T \mathbf{u}$ turns out to be a standard Gaussian random vector, the failure probability can be evaluated in a closed form:

$$\mathbb{P}_{\text{FORM}} = \phi\left(-\beta\right), \tag{3.10}$$

where ϕ denotes the one-dimensional standard normal cumulative density function (CDF).

This estimation is exact when the limit state surface is linear. However, the FORM approximation may become too inaccurate when facing nonlinearity. Then an extension that uses second-order polynomial approximation has been proposed by Breitung (1989). Indeed, the second-order reliability method (SORM) uses the previous Taylor series expansion up to the quadratic term and requires computing the Hessian of the limit state function. Figure 3.3b shows an example of both approximations.

Conclusion The FORM and SORM approximation methods provide reasonably good results for engineering problems, but they assume that there is only one point of failure. If there are multiple potential failure points, these methods may not be accurate (Der Kiureghian and Dakessian, 1998). To address this limitation, several multi-FORM algorithms have been proposed by (Der Kiureghian and Dakessian, 1998; Dubourg, 2011) to discover the multiple failure points. In addition, these approaches may perform poorly in the presence of a discontinuity. Therefore our interest could be turned to simulation methods with sampling techniques.

3.2.2 Sampling methods

Sampling methods do not approximate the limit state function. Instead, these approaches generate samples from a random variable distribution that can then be used to approximate a failure probability by calling the mechanical model. The Monte Carlo (MC) sampling method was the first one used for uncertainty propagation in the field of nuclear and particle physics in the 1950s Metropolis and Ulam (1949).

Monte Carlo sampling is the most common method and one of the more robust to approximate a probability. Monte Carlo sampling generates random or pseudo-random samples from a specified probability distribution (Gentle, 2003). It has been widely used to estimate rare events, as evidenced by many scientific studies. For further reading on the subject, the reader may refer to the books by Rubinstein and Kroese (2004); Zio (2013).

Let us define the failure indicator $\mathbb{I}_{\mathcal{F}}$ defined as:

$$\mathbb{I}_{\mathcal{F}}(\mathbf{x}) = \begin{cases} 1 & \text{if } g(\mathbf{x}) \geq 0 \\ 0 & \text{otherwise.} \end{cases} \tag{3.11}$$

By introducing the failure indicator in Eq. (3.1), the failure probability can be written as:

$$\mathbb{P} = \int_{\mathcal{X}} \mathbb{I}_{\mathcal{F}}(\mathbf{x}) \pi_{\mathbf{X}}(\mathbf{x}) d\mathbf{x} \equiv \mathbb{E}[\mathbb{I}_{\mathcal{F}}(\mathbf{X})], \tag{3.12}$$

where $\pi_{\mathbf{X}}$ is the probability density function of random variable $\mathbf{X}$. Therefore, this quantity can be estimated as follows:

$$\mathbb{P}_{\mathrm{MC}} = \frac{1}{n_{\mathrm{MC}}} \sum_{i=1}^{n_{\mathrm{MC}}} \mathbb{I}_{\mathcal{F}}\left(X^{(i)}\right), \tag{3.13}$$

where $\mathcal{X} = \left\{X^{(i)},\ i = 1, ..., n_{\mathrm{MC}}\right\}$ is a sample of n_{MC} independent copies of the random vector $\mathbf{X}$.

The value of this estimator, which is calculated as the sum of n_{MC} independently and identically distributed random variables, is itself a random variable. According to the central limit theorem, the Monte Carlo estimator is unbiased and normally distributed around zero mean with a specific variance σ^2_{MC} with n_{MC} sufficiently large. The variance of the Monte Carlo estimator is easily proved in Lemaire (2009) to read as follows:

$$\sigma^2_{\mathrm{MC}} = \frac{1}{n_{\mathrm{MC}}} \mathbb{P}_{\mathrm{MC}}(1 - \mathbb{P}_{\mathrm{MC}}). \tag{3.14}$$

The variance in the estimation decreases with the number of samples used to calculate the failure probability, which indicates that the uncertainty in the estimation is only due to statistical error and can be reduced through the use of additional samples.
To evaluate the precision of a sampling run, the coefficient of variation is typically used. It is defined as follows:

$$\mathrm{CoV} = \frac{\sigma_{\mathrm{MC}}}{\mathbb{P}_{\mathrm{MC}}} = \sqrt{\frac{1 - \mathbb{P}_{\mathrm{MC}}}{n_{\mathrm{MC}} \mathbb{P}_{\mathrm{MC}}}}. \tag{3.15}$$

From this relationship, we can estimate how many samples are needed to compute a given probability of failure within some prescribed accuracy. The problem with the Monte Carlo estimator is that the required sample size n_{MC} can drastically increase when the probability gets low to ensure that the probability is estimated with a given coefficient of variation. For instance, the required sample size, for a probability of 10^{-2} with a 5% coefficient of variation (CoV), is almost 40000. If 1% coefficient of variation is required, the call number is up to 10^6.

Despite its computational cost, the Monte Carlo method is robust with respect to probabilistic model dimension since the convergence speed depends only on n_{MC} and $\mathbb{P}$. Moreover, this approach converges regardless of the regularity of the function of interest g. Therefore, the Monte Carlo method could handle discontinuity. Finally, another feature is that independent calls to the function of interest can be parallelized to decrease the computational cost.

Other simulation techniques have been developed specifically for reducing the simulation cost associated with a rare event probability. They are known as *variance reduction techniques* and implement various strategies to produce an equally accurate estimator as Monte Carlo but with fewer samples. Well-known examples are importance sampling, stratified sampling, splitting, control variates, or conditional Monte Carlo. For further reading on the subject, the reader may refer to Zuniga (2011) for a more detailed comparison. Most of them are general-purpose algorithms, but two techniques are more commonly used in the reliability field: *importance sampling* (IS) and *subset sampling (SS)*. Giving a precise development of each technique is beyond the scope of this thesis. However, the basic concepts are presented below.

Importance sampling aims to solve the problem associated with drawing samples in the failure domain for rare events. IS is a method that seeks to estimate the expected value of a function by using an *auxiliary* (or *instrumental*) distribution denoted by $h_{\mathbf{X}}$ instead of the original PDF. In other words, IS involves substituting the original distribution of the random variable with a different distribution in order to increase the number of samples drawn from the failure domain.

The choice of the instrumental PDF is difficult and crucial to generate samples in the failure zone. There are non-adaptive IS techniques and adaptive strategies with parametric and nonparametric techniques. Examples of appropriate choices can be found in Asmussen and Glynn (2007); Chabridon (2018). To resume, IS techniques may be more efficient in terms of computational time than Monte Carlo. However, the major difficulty is constructing an efficient quasi-optimal auxiliary density. Despite their drawbacks, adaptive techniques are more effective at finding an appropriate auxiliary density compared to non-adaptive methods (Chabridon, 2018).

Subset sampling relies on the idea of considering the rare event as the combination of several, more likely events, each corresponding to a subset containing the set of true failures. Since the probability associated with each subset will be larger and thus easier to estimate, then the probability of the overall event is readily computed as the product of conditional probabilities, applying chain rules.

This estimator can be accurate when the thresholds are appropriately set. Another possible issue is the computation of conditional probabilities. This step relies mostly on the Markov Chain Monte Carlo (MCMC) algorithms (Metropolis et al., 1953; Andrieu and Andrieu, 2003). One major advantage of SS is the ability to handle complex functions that are highly nonlinear and may have multiple failure regions. Additionally, SS tends to perform better than other techniques when dealing with high-dimensional input. The method presents some drawbacks as well. In some cases, the number of samples required to achieve convergence is larger than that required using IS techniques. Moreover, in contrast to MC and IS, the estimation error for SS is not calculated using an analytical formula. Instead, it is estimated using bounds provided by Au and Beck (2001) or by repetition. Then a wrong tuning of parameters in the MCMC algorithm could lead to an inefficient algorithm. Finally, Au and Beck (2001) proved that the SS formulation leads to a biased estimator of the failure probability.

For any further information about subset techniques for rare event simulation, the interested reader could refer to Morio et al. (2014).

Conclusion

Regarding our objective introduced in Section 3.1, the simulation methods could possibly compute the failure probability over a discontinuous quantity of interest. However, with the costly mechanical model, the slow convergence and the significant simulation budget, relying MC seems impractical. The variance reduction technique could reduce this computation time, but it is still insufficient. It is worth mentioning that these simulation methods can be effectively used in conjunction with surrogate models (Balesdent et al., 2013; Bourinet, 2016).

3.2.3 Surrogate-based methods

3.2.3.1 Overview of existing methods

Before going through the specific metamodel studied in this work, a brief overview of those previously used in reliability analysis will be provided. There has been a significant amount of research in the field of meta-model-based reliability analysis. There are a wide variety of meta-model-based strategies available in the literature, making it difficult to provide an exhaustive overview of the state-of-the-art. However, several notable examples include the use of *quadratic response surfaces*, as studied by (Bucher and Bourgund, 1990; Gayton et al., 2003).

Bourinet et al. (2011); Kang et al. (2016) have resorted to support vector machines. The radial basis function is also an option Li et al. (2018). Additionally, sparse polynomial chaos expansions have been shown to provide promising results in reliability analysis, as demonstrated by (Blatman et al., 2008; Blatman and Sudret, 2010). Another widely used family is artificial neural networks (ANN). An exhaustive review of techniques based on ANN can be found in Saraygord Afshari et al. (2022).

Moreover, the use of Gaussian process (or Kriging) predictors has been explored. The benefits of Kriging is the development of active learning algorithms for realibility analysis (Bichon et al., 2008; Picheny et al., 2010; Echard et al., 2011; Huang et al., 2016; Lelièvre et al., 2018; Wang et al., 2020; Razaaly and Congedo, 2020). Recently, a metamodel, called PC-Kriging, which merges Kriging and Polynomial chaos expansion has been proposed by Schöbi and Sudret (2014) and has been applied to reliability analyses coupled with an active learning algorithm (Schöbi et al., 2017).

In the end, the choice of a surrogate model is most of the time problem-dependent. In our case, since the input vector is the LPs and a precise distribution is not known in every part of the design space, GP is an excellent alternative to approximate our quantity of interest in the LP design space. In the following, some theoretical elements of Kriging are detailed.

3.2.3.2 Kriging

This paragraph describes the surrogate modeling technique used in this work. This method was originally developed by Krige (1951) in the geostatistics framework and later formalized by Matheron (1962) with the name of Kriging (also known as Gaussian process modeling). The basic idea is to model some function known only at a finite number of sampling points (two or three-dimensional space) as the realization of a Gaussian random field. Later Sacks et al. (1989) extend the application to computer experiments where the number of inputs could be larger than 2 or 3. In contrast to polynomial chaos expansions, Kriging provides a surrogate

model that does not depend on the probabilistic model for the random input vector.

In the following, it is assumed we aim at creating a surrogate model of a scalar-value model $\mathcal{M} : \mathbf{x} \to y$. The set of observations is obtained with the model over a design of experiments gathered in the following dataset $\left((\mathbf{x}^{(i)}, y^{(i)}),\ i = 1, \ldots, m\right)$. In this case, Kriging catches two levels of variability, global and local. The model is considered to be a realization of a stochastic process:

$$Y(\mathbf{x}) = \mu(\mathbf{x}) + Z(\mathbf{x}), \tag{3.16}$$

where $\mu(\mathbf{x})$ is a deterministic function approximating the mean trend of the model and $Z(\mathbf{x})$ is a zero-mean stationary Gaussian process whose covariance function reads:

$$\mathrm{Cov}[Z(\mathbf{x}), Z(\mathbf{x}')] = \sigma^2 R(\mathbf{x} - \mathbf{x}', \boldsymbol{\zeta}), \tag{3.17}$$

where $\sigma^2 > 0$ is the variance of the Gaussian process and R is the correlation function that depends on the difference between input points $\mathbf{x} - \mathbf{x}'$ and its so-called hyperparameters grouped in $\boldsymbol{\zeta}$.

This representation is known as a two-stage Gaussian prior model. It is characterized by its ability to capture both large and small scale variability.

Different types of Kriging exist, determined by the nature of the deterministic part:

Simple Kriging assumes a known and constant deterministic component.

Ordinary Kriging assumes an unknown but constant deterministic value. It is usually considered as the mean value of the observations.

Universal Kriging considers the deterministic component as a linear combination of basis functions and depends on $\mathbf{x}$:

$$\mu(\mathbf{x}) = \sum_{j=1}^{p} \beta_j f_j(\mathbf{x}), \tag{3.18}$$

where $\boldsymbol{\beta} = \{\beta_j,\ j = 1, \ldots, p\}$ is a weight vector and $\boldsymbol{f} = \{f_j,\ j = 1, \ldots, p\}$ is a function basis with a collection of regression functions.

For multi-dimensional case, the auto-correlation functions is written as a product of univariate ones:

$$R(\mathbf{x} - \mathbf{x}', \boldsymbol{\zeta}) = \prod_{i=1}^{d} R(x_i - x_i', \zeta_i). \tag{3.19}$$

Examples of widely used auto-correlation functions are listed below (Rasmussen and Williams, 2006)[↗]. For the sake of simplicity, we consider one-dimensional cases:

- Linear:

$$R(x, x', l) = \max\left(0, 1 - \frac{|x - x'|}{l}\right), \tag{3.20}$$

where $l > 0$ is the so-called *characteristic length-scale*.

- Generalized exponential:

$$R(x, x', \boldsymbol{\zeta}) = \exp\left(-\left(\frac{x - x'}{l}\right)^{\gamma}\right), \quad \text{for} \quad 0 < \gamma \leq 2 \quad \text{and} \quad l > 0, \tag{3.21}$$

  where $\boldsymbol{\zeta} = \{l, \gamma\}$. The smoothness of the associated process is determined by the parameter γ. The higher the value, the smoother the sample path. When $\gamma = 2$, it corresponds to the Gaussian auto-correlation function introduced below and is the only value that leads to a mean-square differentiable generated process.

- Squared exponential (also called Gaussian):

$$R(x, x', l) = \exp\left(-\left(\frac{x - x'}{l}\right)^{2}\right). \tag{3.22}$$

  It is the most used auto-correlation function for learning problems. The generated processes are infinitely differentiable and thus very smooth.

- Matérn:

$$R(x, x', \zeta) = \frac{1}{2^{\nu-1}\Gamma(\nu)}\left(\sqrt{2\nu}\frac{|x - x'|}{l}\right)^{\nu}\kappa_{\nu}\left(\sqrt{2\nu}\frac{|x - x'|}{l}\right), \tag{3.23}$$

  where $\boldsymbol{\zeta} = \{l, \nu\}$, $\nu \geq 0.5$ is the so-called shape parameter, Γ the Euler Gamma function and κ_{ν} the modified Bessel function of the second kind. The smoothness of the auto-correlation is controlled by ν. An interesting feature is that the sample paths from the Gaussian process are k-times differentiable for any positive integer k such that $\nu > k$. Moreover, if ν is chosen as a half-integer, as $\nu = k + 0.5$, an analytical expression of the auto-correlation can be derived. Finally, as ν tends to infinity, the Matérn autocorrelation function tends toward the squared exponential autocorrelation function, which has infinitely differentiable sample paths. The most practical cases correspond to $\nu = 3/2$ and $\nu = 5/2$, which are respectively once and two times differentiable.

In the following, we focus on the most general case using universal Kriging and a generalized exponential auto-correlation for the smoothest of the generated process. The first step is to estimate the parameters $\boldsymbol{\beta}$ and σ of the regression model. The departure of the linear regression from the observation is assumed to be a Gaussian random noise. Minimizing this noise means searching the parameters so that the noise is most likely Gaussian as assumed a priori. This is called the *maximum likelihood estimates*. The likelihood function is obtained by inverting the role of the observations and the parameters in the multivariate normal probability function:

$$L(\boldsymbol{\beta}, \sigma^2|\mathbf{y}) = \frac{1}{((2\pi\sigma^2)^n \det\mathbf{R})^{\frac{1}{2}}}\exp\left(-\frac{1}{2\sigma^2}(\mathbf{y} - \mathbf{F}\boldsymbol{\beta})^T\mathbf{R}^{-1}(\mathbf{y} - \mathbf{F}\boldsymbol{\beta})\right), \tag{3.24}$$

where $\mathbf{F} = \{f_j(\mathbf{x}^{(i)}),\ i = 1, \ldots, m,\ j = 1, \ldots, p\}$ is the regression matrix. Maximizing Eq.(3.24) is equivalent to minimizing its opposite logarithm:

$$\min_{\boldsymbol{\beta}, \sigma} -\log\, L(\boldsymbol{\beta}, \sigma^2|\mathbf{y}). \tag{3.25}$$

This leads to the following estimates of $\boldsymbol{\beta}$ and σ

$$\hat{\boldsymbol{\beta}} = \left(\mathbf{F}^T\mathbf{R}^{-1}\mathbf{F}\right)^{-1}\mathbf{F}^T\mathbf{R}^{-1}\mathbf{y}, \tag{3.26}$$

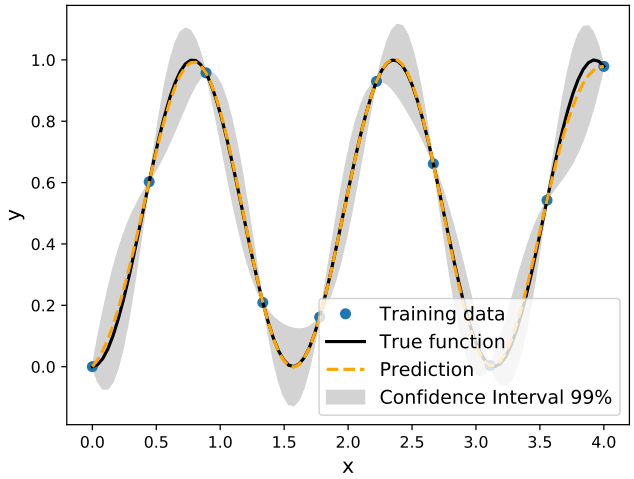

Figure 3.4: Krigging approximation using an exponential auto-correlation function with the 99% confidence interval.

$$\hat{\sigma}^2 = \frac{1}{m}(\mathbf{y} - \mathbf{F}\boldsymbol{\beta})^T \mathbf{R}^{-1}(\mathbf{y} - \mathbf{F}\boldsymbol{\beta}). \tag{3.27}$$

Finally, the best linear unbiased predictor of the unobserved quantity of interest $y_0 \equiv \mathcal{M}(\mathbf{x}_0)$ gives the mean and variance of the Gaussian random variate $\hat{Y}_0$:

$$\mu_{\hat{Y}_0} = f_0^T \hat{\boldsymbol{\beta}} + \mathbf{r}_0^T \mathbf{R}^{-1} \left(\mathbf{y} - \mathbf{F}\boldsymbol{\beta}\right), \tag{3.28}$$

$$\sigma^2_{\hat{Y}_0} = \sigma^2 \left(1 - r_0^T \mathbf{R}^{-1} \mathbf{r}_0 + \mathbf{u}^T \left(\mathbf{F}^T \mathbf{R}^{-1} \mathbf{F}\right)^{-1} \mathbf{u}\right), \tag{3.29}$$

where $\hat{\boldsymbol{\beta}}$ is the maximum likelihood estimation from Eq.(3.26) and $\mathbf{u} = \mathbf{F}^T \mathbf{R}^{-1} \mathbf{r}_0 - f(\mathbf{x}^{(0)})$ and $\mathbf{r}_0 = R(\mathbf{x}^{(0)} - \mathbf{x}^{(i)}, \boldsymbol{\zeta})$ is the vector of cross-correlations between the point prediction $\mathbf{x}^{(0)}$ and the observations. An example is shown in Figure 3.4 with the Kriging approximation of a 1D-function and the 99% confidence interval computed with the variance $\sigma^2_{\hat{Y}_0}$. Calculating the conditional mean and variance involves the inverse of the covariance matrix of the observations. Depending on the size of the problem, the number of points in the database, and the choice of the correlation kernel, this matrix can be ill-conditioned and numerical difficulties may occur.

Once the family of parametric auto-correlation functions is chosen, the parameters need to be specified, either empirically, or through the use of various techniques, such as cross-validation or maximum likelihood. Cross-validation consists in searching for the parameters' values that minimize the generalization error through re-sampling. As the brute force approach is expensive, Bompard (2011) proposes a technique of leave-one-out (LOO) to reduce the computational cost. Maximum likelihood is the same idea as in Eq.(3.24) while highlighting its dependency in $\boldsymbol{\zeta}$. However, it is not easy to minimize because of the poorly conditioned auto-correlation function, for some values of $\boldsymbol{\zeta}$, and the numerous local minima.

In this manuscript, the Kriging applications are run using *OpenTURNS* (Baudin et al., 2016) and *scikit-learn* (Pedregosa et al., 2011).

3.2.4 Conclusion

The reliability analysis and its sensitivity are performed on instability phenomena such as buckling or flutter. A modal analysis is achieved to study the stability of the system. Indeed, multimodal behavior exists in the design space. Moreover, performing a simulation method, such as Monte Carlo or Importance Sampling, on a finite element method or an aeroelastic model demands a high computation time. Therefore a suitable strategy needs to be introduced. Since discontinuity occurs in the design space, approximation methods, such as FORM or SORM, could be ineffective in some parts of the design space and still computationally costly. The most practical strategy could be based on a surrogate method coupled with Monte Carlo simulation with a strategy handling the discontinuity. Kriging is preferred here because it is suitable with the lack of knowledge of the LP variability in the design space. Moreover, the Kriging is advantageous for reliability analysis, where the Kriging error can be exploited with active learning criteria for reliability.Note however that we will not be using an active learning criterion in this work.

3.3 Surrogate-based reliability analysis strategy to handle discontinuity responses

An optimized design of experiment needs to be constructed on the lamination parameters space to build an efficient surrogate model. Then, a classification strategy is applied to identify a possible hump mode within the structural modes considered. Finally, a strategy with Kriging surrogate model, which handles the possible switch mode, is presented. In addition, the coupling with the classification holds both types of discontinuities simultaneously.

3.3.1 Lamination Parameters design of experiments

Firstly, a design of experiments (DoE), which is well distributed over the dimension, must be constructed. In this study, the focus is made on the out-of-plane lamination parameters $\mathrm{v}^{\mathbf{D}}$. It is a four-dimension space with compatibility constraints between those four parameters. Moreover, the orthotropic hypothesis made in the LPs average reduces the space to only two dimensions with $\mu_{\mathrm{v}_2^D} = \mu_{\mathrm{v}_4^D} = 0$. However, with the ply orientation uncertainty, these two parameters will not be zero and, therefore, will be considered in the surrogate models.

The strategy to construct the design of experiments focuses first on the $(\mathrm{v}_1^D, \mathrm{v}_3^D)$ projection. The idea is to create a grid inside the 2D space respecting the orthotropic laminate compatibility constraint (Miki and Sugiyama, 1991) between these two parameters (i.e., the red line in Figure 3.5):

$$2(\mathrm{v}_1^D)^2 - 1 - \mathrm{v}_3^D \leq 0. \tag{3.30}$$

A regular step is chosen for the v_3^D axis with 12 points. For each value of v_3^D, the point in the v_1^D axis are distributed between $-\sqrt{\frac{\mathrm{v}_3^D+1}{2}}$ and $\sqrt{\frac{\mathrm{v}_3^D+1}{2}}$. However, for the v_1^D axis, variable step size is applied with 2 points for $\mathrm{v}_3^D = -1$ up to 12 points for $\mathrm{v}_3^D = 1$. The details of the distribution number N_{sub} of v_1^D points along the v_3^D are given by:

$$N_{\text{sub}} = [2, 4, 6, 6, 8, 8, 9, 10, 10, 10, 12, 12]. \tag{3.31}$$

It gives a DoE of 97 points, shown in Figure 3.5a. It is a quite dense grid and can be reduced by decreasing the number of points in the v_3^D direction and the size of N_{sub}.

Value	Count		Percent	
	v_2^D	v_4^D	v_2^D	v_4^D
-0.05	29	36	29.90 %	37.11 %
0.00	41	37	42.27 %	38.14 %
0.05	27	24	27.84 %	24.74 %

Table 3.1: Distribution of the v_2^D and v_4^D values in the LP design of experiment.

Once this step is made, the values of v_2^D and v_4^D need to be sampled. We chose three possible values for these parameters: -0.05, 0, or 0.05. The draw is made equiprobable for both parameters and is allocated to the grid points in 2D (v_1^D, v_3^D) space. However, two other compatibility constraints exists between the four parameters:

$$\begin{aligned} \left(v_1^D\right)^2 + \left(v_2^D\right)^2 - 1 \leq 0, \\ 2\left(v_1^D\right)^2\left(1 - v_3^D\right) + 2\left(v_2^D\right)^2\left(1 + v_3^D\right) + \left(v_3^D\right)^2 + \left(v_4^D\right)^2 - 4v_1^D v_2^D v_4^D - 1 \leq 0. \end{aligned} \tag{3.32}$$

For each point, these constraints are checked; and it appears that some points do not respect the constraints and are unfeasible. These unfeasible points are represented with circle points in the 2D projections in Figure 3.5a and 3.5c. From now on, the strategy for the unfeasible points at the frontier is to take the closest point feasible. To do so, an extensive database of feasible LPs is created where v_2^D and v_4^D are equal only to -0.05, 0. or 0.05. Firstly, a 60000-size random sample is generated over a 2-dimensional space, representing v_1^D and v_3^D, with a $[-1, 1]$ range for each dimension. Then, a draw is made equiprobable between -0.05, 0. and 0.05 for v_2^D and v_4^D parameters and is concatenated to the sample generated at first. From this database, we keep only the $\mathbf{v^D}$ that respect the compatibility functions in Eq.(3.30) and Eq.(3.32). Afterward, the distance of v_1^D and v_3^D between the unfeasible points present in the 97 points DoE and the database points are compared:

$$d = \sqrt{\left(v_{\mathbf{1}}^{\mathbf{D^{db}}} - v_{\mathbf{1}}^{\mathbf{D^{db}}}\right)^2 + \left(v_{\mathbf{3}}^{\mathbf{D^u}} - v_{\mathbf{3}}^{\mathbf{D^{db}}}\right)^2}, \tag{3.33}$$

where $v^{\mathbf{D^u}}$ are the unfeasible lamination parameters of the DoE and $v^{\mathbf{D^{db}}}$ are the feasible LPs from the database generated. Each database point $v^{\mathbf{D^{db}}}$ minimizing the distance with $v^{\mathbf{D^{db}}}$ replace the old unfeasible points. The points in Figure 3.5b and Figure 3.5d respect now all the compatibility constraints. We observe the densification of points with $v_2^D = 0$ in Figure 3.5d. The distribution between -0.5, 0, and 0.5 values of v_2^D and v_4^D parameters are not equal anymore. Table 3.1 shows the percentage of each value allocated to v_2^D and v_4^D parameters. We observe an important percentage of 0 values for v_2^D. However, we consider that it is well scattered in the v_2^D and v_4^D directions.

3.3.2 Discontinuity issues

Now that the design of experiments is built, the surrogate model of the aeroelastic quantity of interest shown in Figure 3.2d can be constructed. The details of the model will be explained later in Chapter 4. However, the aeroelastic stability is studied via an eigenvalues problem to identify the critical flutter velocity. Hence, the global critical velocity is the minimum of the computed modes. The stability study is made between a velocity range prescribed. Therefore, a mode can stay stable for the velocity range studied. In Figure 3.2d, the response of the critical flutter

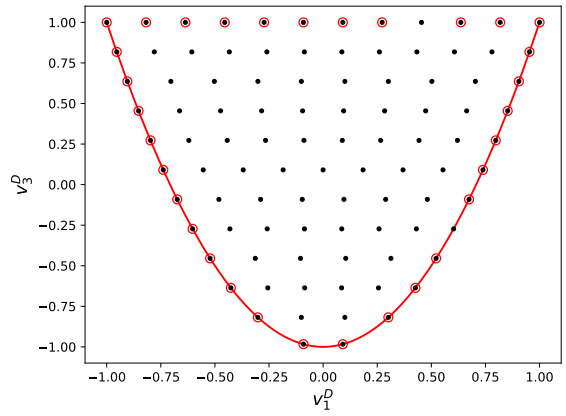

(a) $(\mathrm{v}_1^D, \mathrm{v}_3^D)$ projection before the check of the compatibility constraints.

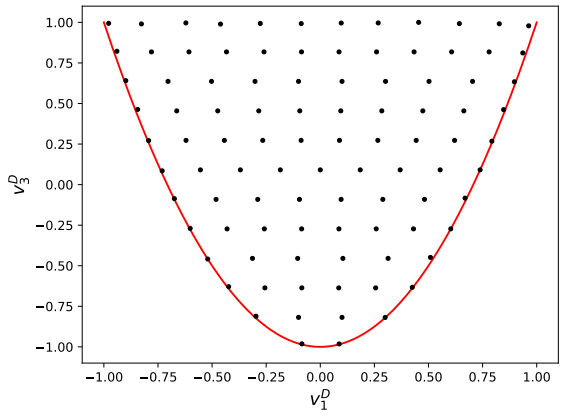

(b) $(\mathrm{v}_1^D, \mathrm{v}_3^D)$ projection after changing the previous unfeasible points thanks to the database.

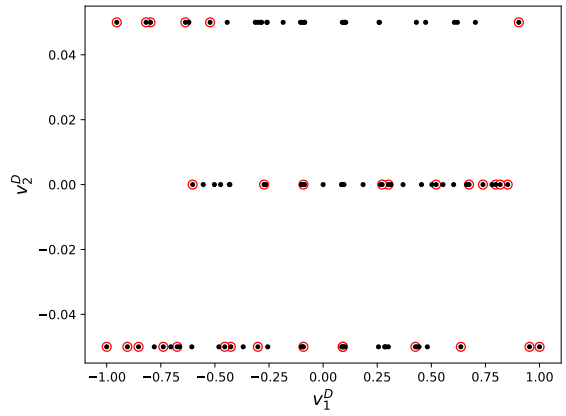

(c) $(\mathrm{v}_1^D, \mathrm{v}_2^D)$ projection before the check of the compatibility constraints.

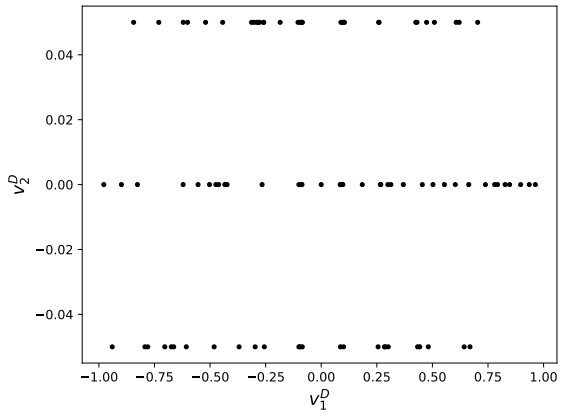

(d) $(\mathrm{v}_1^D, \mathrm{v}_2^D)$ projection after changing the previous unfeasible points thanks to the database.

Figure 3.5: Design of experiments in different 2D projections. The circle points are unfeasible LPs before using the database.

velocity is shown and exhibits a discontinuity in the design space where the critical velocity switches from the second mode to the third one.

In the aeroelastic field, some work focused on this discontinuity problem. A multi-element surrogate model strategy is used to handle sharp and sudden flutter onset for the uncertainty quantification in limit-cycle oscillations (Chassaing et al., 2012). The quantity of interest is expanded on a piecewise generalized polynomial chaos basis. Since we do not have a PDF of the lamination parameters, the Askey scheme cannot be applied in our work to choose the right orthogonal polynomials. More recently, some clustering techniques were applied for the flutter velocity Chassaing et al. (2018) to identify the different modal regimes. Scarth and Cooper (2018) construct a Gaussian process for each mode; however, their model does not guarantee that eigenvalues will be output in the same order from one sample to another. Therefore, they sort the eigenvalues comparing the mode-shape using Modal Assurance Criterion (MAC) Allemang (2003) and the surrogate model is now accurate to approximate the flutter velocity. Therefore, the Kriging looks to be a good compromise to our need.

Assuming that our model gives the eigenvalues in the same order, we could build a simple surrogate model per mode. Nevertheless, the third mode exhibits a discontinuity (see Figure 3.2c). It behaves as a *hump mode* that can abruptly switch its stability status within a small perturbation of the lamination parameters, as illustrated in Figure 3.1b. This phenomenon is well summarized in Jonsson et al. (2019); Stanford et al. (2014), which mentions some techniques to handle hump modes in the optimization process, as the one proposed by Stanford et al. (2015) which enforce the real part of each eigenvalue to remain below a preset bounding curve. Although the above approach alleviates the discontinuity issues, it abruptly increases the number of constraints. In our procedure, we aim to minimize the number of constraints.

In the following, a strategy is proposed to handle a possible discontinuity of a *hump mode* using classification and to handle possible mode switching on the global quantity of interest using the coupling of classical surrogate models and the classification.

3.3.3 Classifier assistance to handle hump mode

The proposed strategy to deal with a possible hump mode is to train a classifier to know whether the design point is unstable or not in the design space. With the design of experiments shown in Figure 3.5b, the aeroelastic model is run to compute the critical flutter velocity. We wish to assign an input parameter $\mathbf{v^D}$ to one of C classes, $\mathcal{C}_1, \ldots, \mathcal{C}_C$. As previously said, two stability statuses are possible: unstable when flutter occurs or stable when instability does not occur. Therefore we consider a binary classification problem with $C = 2$. Different techniques are available such as Nearest Neighbors, Support Vector Machines, Gaussian Process, Decision Tree, and others. In this work, a classifier is trained with Gaussian Process Classification (GPC) to identify a boundary between both regions of stability.

In GPC, a Gaussian Process is used as a nonparametric Bayesian model for the relationship between the input variables and the class labels. The goal is to predict the class label (i.e., the output) for a given input based on the training data. The key idea behind GPC is to use a GP to model the distribution over possible functions that could generate the training data. This is done by specifying a mean function and a covariance function (also known as a kernel) already detailed in Section 3.2.3. To predict a new input, we can use the GP to obtain a distribution over the possible functions that could generate that input and then use this distribution to compute the probability of each class label. However, in classification, the target values are

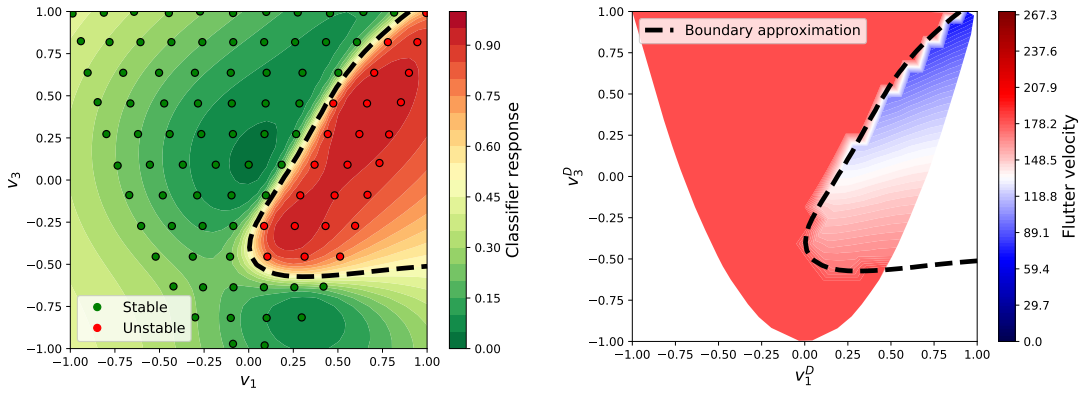

(a) Classifier response with the stability status of the DoE.

(b) True response of the flutter velocity.

Figure 3.6: Representation of the classifier for the third mode in the 2D space $(\mathrm{v}_1^D, \mathrm{v}_3^D)$ projection with $\mathrm{v}_2^D = \mathrm{v}_4^D = 0$. The dashed line represents the delimitation between the stable and unstable regions computed by the GPC.

discrete class labels, and the Gaussian likelihood is inappropriate. Therefore the resulting posterior distribution is not automatically Gaussian. That is the main difference that the Gaussian Process Regression presented at the end of Section 3.2.3. In Rasmussen and Williams (2006), two analytic approximations which both approximate the non-Gaussian joint posterior with a Gaussian one are presented: the first is the straightforward *Laplace approximation method* (C. K. I. Williams and D. Barber, 1998), and the second is the more sophisticated *expectation propagation* (EP) method (Minka, 2001).

The gaussian process module of *scikit-learn* is used Pedregosa et al. (2011). The GPC is implemented with Algorithms 3.1, 3.2, and 5.1 from Rasmussen and Williams (2006) and uses the Laplace approximation for the non-Gaussian posterior approximation. The GP is trained with a linear model and a squared exponential covariance kernel.

The GPC is applied to separate the stable and unstable region of the third mode. The delimitation computed by the classifier approximates the boundary correctly (see Figure 3.6). This classification presents a 97% accuracy with three hundred points tested around this boundary.

In conclusion, with a quantity of interest, such as the flutter, two stability classes are possible in each structural mode studied. Therefore, if needed, the GPC efficiently delimitates both regions. This will be incorporated into the procedure to perform a reliability analysis of the instability. Before that, surrogate models are constructed to efficiently approximate the quantity of interest.

3.3.4 Classic surrogate model to handle mode switching

Now, the idea is to create a metamodel of the quantity of interest for each mode using Gaussian Processes. Kriging provides a surrogate model that does not depend on the probabilistic model of the random input vector. Since the input vector are the LPs and a precise distribution is not known in every part of the design space, GP is a good alternative to approximate our quantity of interest in the LPs design space. Moreover, Kriging provides a value for the error made on the interpolation, which could be useful for the reliability analysis using active learning criteria.

Mode	Mean model	Covariance kernel
1	Quadratic	Square exponential
2	Quadratic	Square exponential
3	Linear	Square exponential

Table 3.2: Model of the Gaussian processes of the critical flutter velocity for each mode.

Some comments on a strategy with active learning are given in the perspectives at the end of the manuscript.

The models used for the Kriging of each mode are detailed in Table 3.2. With this strategy, it is easy to prevent mode switching in the global response if the response of each mode is well approximated. But the question of how to construct the surrogate model of a potential *hump mode* remains. In this case, only the design points that present instability are used to build the surrogate model. A flowchart describes the principal steps to construct the surrogate models and the classifier in Figure 3.7.

Gaussian processes of the quantities of interest of each mode are reported in Figure 3.8 with $v_2^D = v_4^D = 0$. Each surrogate model is validated with true versus prediction graphs in Figure 3.9. Three hundred points were used for it. The validation of the hump mode was made only with input parameters in the unstable part (i.e., the blue part between 0.5 and 1 of Figure 3.6a). For the third mode, we can see the difference between the gaussian process in Figure 3.8c and the true function in Figure 3.6b.

3.3.5 Coupling classic surrogate models with the classifier to perform reliability analysis

The surrogate model of the hump mode could lead to the wrong estimation of the critical flutter velocity if the input parameters are in the stable region of the third mode (i.e., the green part between 0 and 0.5 of Figure 3.6a). The global critical velocity is defined as the minimum of the computed modes. Therefore, the classification is exploited to know which flutter surrogate model to use. In our example, the metamodel of the third mode is only used when the design point studied is in the unstable part thanks to the classifier (i.e., the blue part of Figure 3.6a). The global critical velocity is compared between the real model and the kriging response in Figure 3.10 with the associated predicted vs. actual graph in Figure 3.10c. The approximated response coupling the classifier with the classical surrogate model leads to some error around a little part of the discontinuity. Within the set of samples used for the validation, the flutter velocity estimations of five design points are completely inaccurate. This comes from the classification that do not have a 100% accuracy to delimitate the stable and unstable regions of the third mode. Therefore, the strategy could be improved.

Now, with the surrogate models and the classifier constructed, it is possible to perform the reliability analysis. In this work, the surrogate models are coupled with the MC method to compute the reliability. The global critical velocity is defined as the minimum of the computed modes. The process to compute the failure probability is presented in Figure 3.11. The input parameters are the mean ply orientations of a stacking sequence. The uncertainty propagation is propagated until the LPs, which are the input parameters of the classifier and surrogate models. Then, in the presence of hump mode, the GPC and the GPR are coupled to estimate

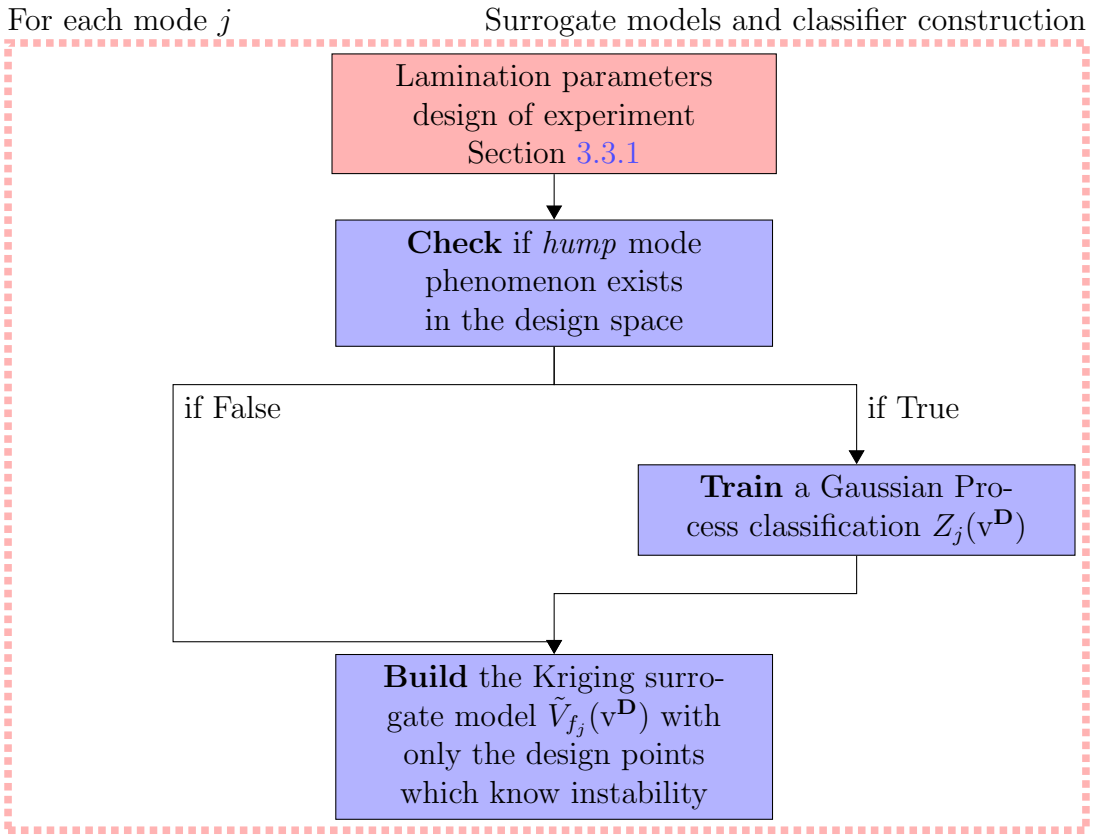

Figure 3.7: Flowchart of the surrogate models construction for each mode. A classifier is constructed in the presence of *hump mode*.

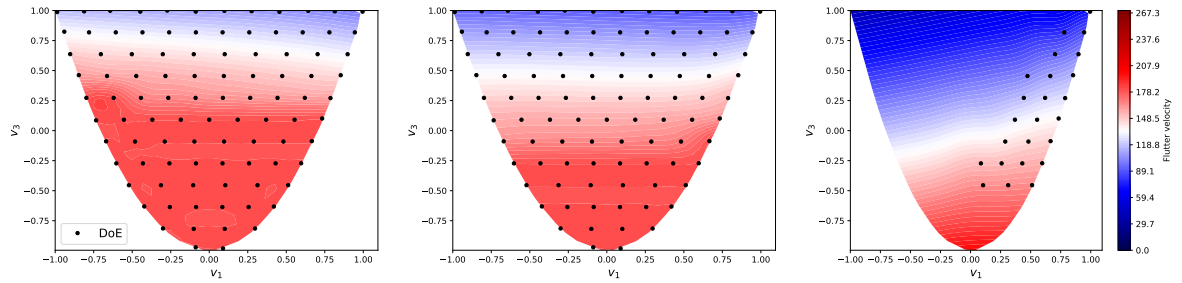

(a) First mode. (b) Second mode. (c) Third mode.

Figure 3.8: Gaussian processes of the flutter critical velocity for the first three modes in the 2D design space with $\mathrm{v}_2^D = \mathrm{v}_4^D = 0$ with the corresponding DoE used.

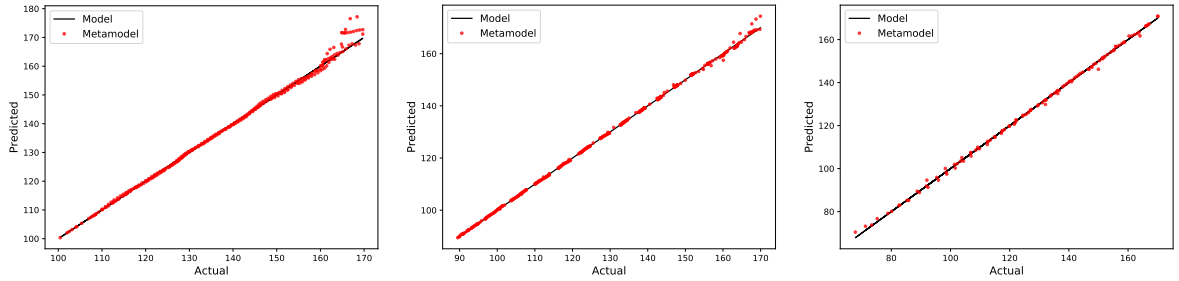

(a) First mode. (b) Second mode. (c) Third mode.

Figure 3.9: Predicted vs actual graph of each Kriging surrogate model. Three hundred realizations were computed.

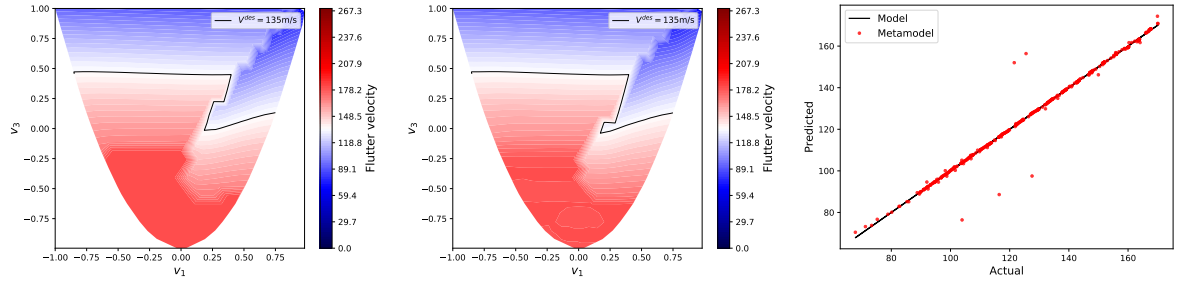

(a) True model response. (b) Surrogate model response using the classifier. (c) Predicted vs. actual graph.

Figure 3.10: Validation of the flutter velocity V_f in the 2D design space.

the value of the critical velocity to perform, in the end, the reliability analysis.

3.3.6 Conclusion

In conclusion, building a surrogate model of instability such as flutter should handle discontinuities coming from hump mode or mode switching in the design space. The strategy proposed to couple surrogate models with a classifier shows some interest in efficiently approximating the quantity of interest, such as flutter velocity. It can handle the two types of discontinuities. Now the reliability analysis can be performed with MC. However, since we are in a gradient-based framework for the RBDO, the gradients of the failure probability with respect to the LPs design variables are needed. The surrogate model will still be exploited to compute the quantity of interest, which leaves open the question of how to compute the local sensitivity with respect to LPs.

3.4 Strategy for the failure probability sensitivity computation

The challenging part of the gradient-based approach for RBDO resides in the computation of the failure probability gradient. The sensitivity computation is not trivial since the constraints are stochastic. Bjerager Peter and Krenk Steen (1989) developed a local derivative-based approach based on FORM to evaluate the effect of changes in the input distribution parameters

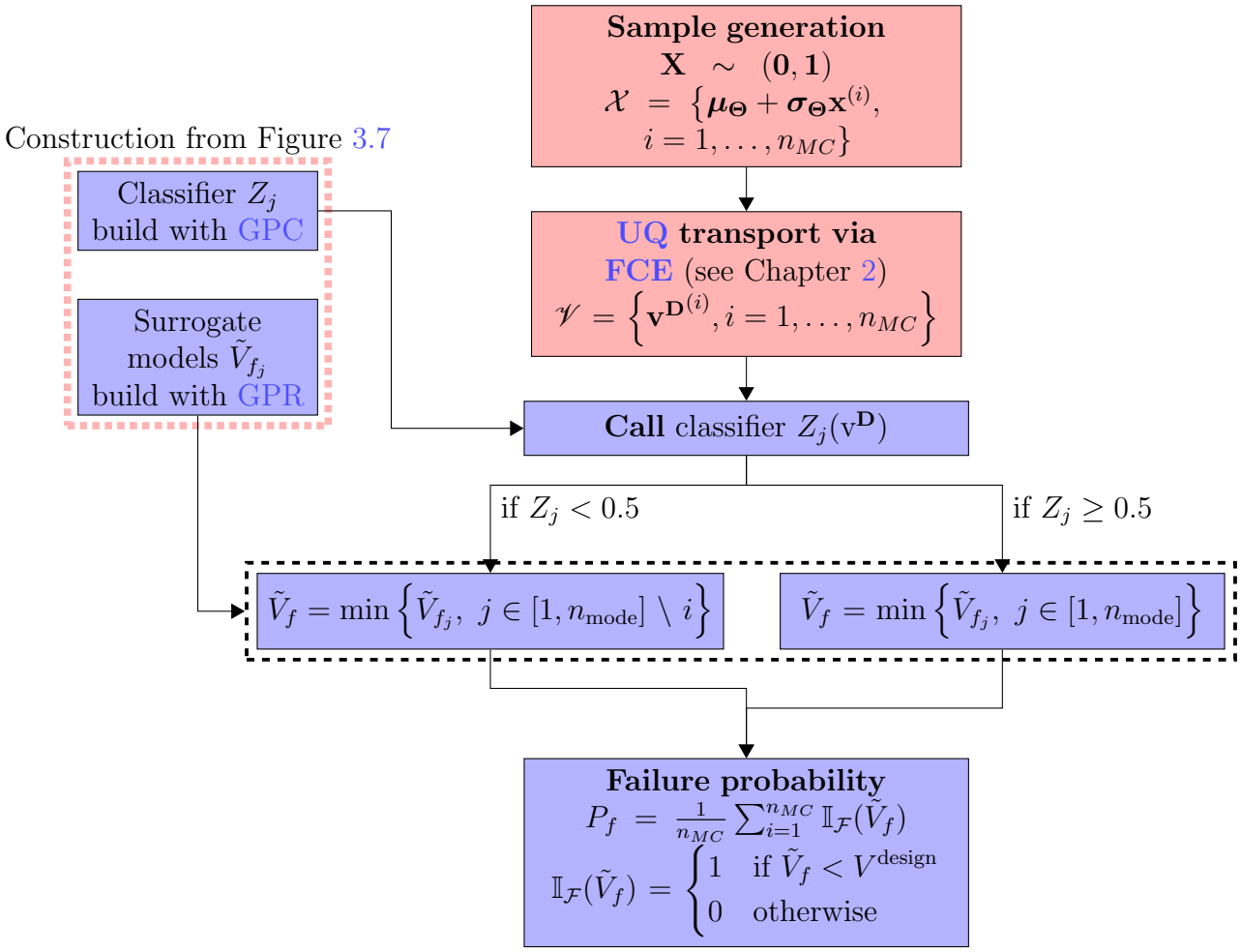

Figure 3.11: Flowchart to run reliability analysis with, as input parameters a stacking sequence.

on the reliability index. This was applied in a RBDO framework in Chun (2021) for example. However, computing sensitivities through MPFP-based techniques are not adapted to our reliability analysis strategy.

Sampling-based techniques can be used to determine local reliability sensitivity. It is possible to derive the gradient of the failure probability with respect to a distribution parameter with MC using the score function (Rubinstein, 1986). This function is well summarized in Mohamed et al. (2020) for Monte-Carlo approaches in machine learning. Wu (1994) brought the score function approach to the structural reliability community. Nevertheless, a parametric distribution is needed. In our case, the input parameters are LPs. We observe the impact of the orientation uncertainty on the lamination parameters in Chapter 1, and some marginals tend to have a Gaussian shape. In addition, the number of plies in the stacking sequence could influence the shape of the lamination parameters PDF. Indeed Kriegesmann (2017) shows that the distribution of lamination parameters tends asymptotically to Gaussian distribution increasing the number of plies in the stacking sequence. He believes it is reasonable to assume a normal distribution for laminates with more than 20 plies. However, we will not necessarily use a high number of plies. This means that SF approach cannot be employed in the general case with LPs.

In the most general case, finite differences are an alternative when the LPs sample does not tend to parametric distribution. Since the failure probability is a stochastic quantity, it is more robust to use centered finite differences (CFD).

In the following, the different methods used to compute the probability sensitivity are detailed.

3.4.1 Score function

The goal of the following is to explain the underlying principle of the score function (SF). The partial derivative of the failure probability with respect to the k^{th} distribution parameter d_k reads:

$$\frac{\partial \mathbb{P}}{\partial d_k} = \frac{\partial}{\partial d_k} \int_{\mathbb{X}} \mathbb{I}_{\mathcal{F}}(\mathbf{x}) \pi_{\mathbf{X}}(\mathbf{x}, \boldsymbol{d}) \mathrm{d}\mathbf{x}, \tag{3.34}$$

where $\mathbb{I}_{\mathcal{F}}$ is the indicator function defined in Eq.(3.11), and $\pi_{\mathbf{X}}$ is the probability density function of random variable $\mathbf{X}$. Assuming that the joint PDF $\pi_{\mathbf{X}}$ is continuously differentiable with respect to d_k and that the integration domain $\mathbb{X}$ does not depend on d_k, the partial derivative of the failure probability recasts as follows:

$$\frac{\partial \mathbb{P}}{\partial d_k} = \int_{\mathbb{X}} \mathbb{I}_{\mathcal{F}}(\mathbf{x}) \frac{\partial \pi_{\mathbf{X}}(\mathbf{x}, \boldsymbol{d})}{\partial d_k} \mathrm{d}\mathbf{x}. \tag{3.35}$$

Then, in order to compute this integral as an expectation, it is proposed to use an importance sampling trick:

$$\begin{aligned} \frac{\partial \mathbb{P}}{\partial d_k} &= \int_{\mathbb{X}} \mathbb{I}_{\mathcal{F}}(\mathbf{x}) \frac{\partial \pi_{\mathbf{X}}(\mathbf{x}, \boldsymbol{d})}{\partial d_k} \frac{1}{\pi_{\mathbf{X}}(\mathbf{x}, \boldsymbol{d})} \pi_{\mathbf{X}}(\mathbf{x}, \boldsymbol{d}) \mathrm{d}\mathbf{x} \\ &= \int_{\mathbb{X}} \mathbb{I}_{\mathcal{F}}(\mathbf{x}) \frac{\partial \ln \pi_{\mathbf{X}}(\mathbf{x}, \boldsymbol{d})}{\partial d_k} \pi_{\mathbf{X}}(\mathbf{x}, \boldsymbol{d}) \mathrm{d}\mathbf{x} \\ &= \mathbb{E}\left[\mathbb{I}_{\mathcal{F}}(\mathbf{X}) \mathcal{K}_{d_k}(\mathbf{X})\right], \end{aligned} \tag{3.36}$$

where $\mathcal{K}_{d_k}(\mathbf{X}) = \dfrac{\partial \ln \pi_{\mathbf{X}}(\mathbf{x}, \boldsymbol{d})}{\partial d_k}$ is called the *score function*. Thus, given a sample $\mathscr{X} = \left\{\mathbf{x}^{(i)}, i = 1, \ldots, n_{MC}\right\}$, the MC following estimator:

$$\frac{\partial \mathbb{P}}{\partial d_k}_{\text{MC}} \equiv \frac{1}{n_{\text{MC}}} \sum_{i=1}^{n_{\text{MC}}} \mathbb{I}_{\mathcal{F}}(\mathbf{x}^{(i)}) \mathcal{K}_{d_k}(\mathbf{x}^{(i)}), \tag{3.37}$$

is unbiased and asymptotically convergent according to the central limit theorem. The advantage is that the failure probability gradient is estimated using the same sample used for the failure probability estimation and do not increase the computational time. However, the estimator variance of the score approach is sensitive to the probability function (Mohamed et al., 2020). To improve the accuracy and decrease the variance of the score function, a reweighting scheme proposed by Zhu et al. (2015) could be used.

3.4.2 Centered finite differences

In the most general case, when a parametric distribution is not available, the gradient of the failure probability with respect to the distribution parameter d_k may be approximated with centered finite differences:

$$\frac{\partial \mathbb{P}}{\partial d_k} \approx \frac{\mathbb{P}\left(d_k + c\right) - \mathbb{P}\left(d_k - c\right)}{2c}, \tag{3.38}$$

where c is the step size along the particular dimension taken in the design space. One of the drawbacks is the number of simulations of $\mathcal{O}(2n_v n_s)$ order for a distribution parameters vector of size n_v and n_s the number of simulations for a probability estimation by MC.

Since the numerator of the partial derivative is estimated using Monte Carlo sampling, the variance of its estimator is proportional to:

$$\begin{aligned} \operatorname{Var}\left[\mathbb{P}\left(d_k + c\right) - \mathbb{P}\left(d_k - c\right)\right] = \operatorname{Var}\left[\mathbb{P}\left(d_k + c\right)\right] + \operatorname{Var}\left[\mathbb{P}\left(d_k - c\right)\right] \\ -2\operatorname{Cov}\left[\mathbb{P}\left(d_k + c\right), \mathbb{P}\left(d_k - c\right)\right], \end{aligned} \tag{3.39}$$

where $\mathbb{P}\left(d_k + c\right)$ ((resp. $\mathbb{P}\left(d_k - c\right)$) denotes an unbiased Monte Carlo estimator computed from an sample $\mathscr{X}^{[1]}$ (resp. sample $\mathscr{X}^{[2]}$) of independent copies of the random vector $\mathbf{X}$. The variances simply add up in the most standard case where the two terms are estimated independently.

One of the issues with this approach is the stochasticity in the failure probability. Indeed, the noise intrinsic to each estimation of $\mathbb{P}$ could bias the gradient's estimation without differentiating the information given by the perturbation of the design or the random noise. A straightforward way to reduce the estimator's variance is to have a positive covariance between the two estimated probabilities. This is why Royset and Polak (2004b,a); Taflanidis (2007) propose to use common random numbers (CRN). This strategy essentially consists in using the same seed for generating both samples $\mathscr{X}^{[1]}$ and $\mathscr{X}^{[2]}$. Indeed, CRN introduces dependence in estimating the two probabilities so that the covariance term in Eq.(3.39) reduces the variance of the gradient estimation. Therefore when finite differences are evaluated, it is recommended that samples are generated from the same seed.

The finite differences method is straightforward for computing failure probability gradients. However, it may produce inaccurate sensitivities for a too small sample size due to the statistical noise or because of the step size (or perturbation size). Normally if c tends to zero, the failure

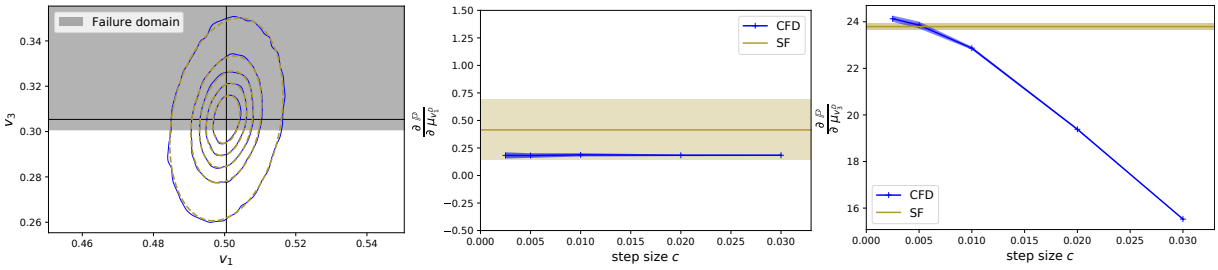

Figure 3.12: Comparison of the failure probability gradients obtained from score function (SF) or centered finite differences (CFD) approach. On the left figure: the yellow dashed contour represents the fitted Gaussian law, and the blue contour is the non-parametric law obtained from a kernel-density estimate using Gaussian kernels.

probability sensitivity tends to the real value. Nevertheless, we treat stochastic quantities. The choice of the step size c is tough because it intrinsically depends on the coefficient of variation of the estimated probabilities. If the CoV of the probabilities in Eq.(3.38) is pretty high, the sensitivity will be biased for a small step size. . Therefore, the smaller the target probabilities CoV, the smaller the step size c can be, and the more precise the sensitivity estimation will be. Nevertheless, the choice of this step size is often arbitrary, but a compromise has to be found between computational cost (coming from the estimation of a probability with small CoV) and accuracy in the estimation of the gradient via CFD with a small step size.

3.4.3 Comparison of reliability sensitivity methods for a simple limit state function

A study is made to compare the computation of failure probability gradients with the score function approach and the centered finite differences for two different samples $\mathcal{V}^1$ and $\mathcal{V}^2$ with different levels of Gaussianity in 2 dimensions $(\mathrm{v}_1^D, \mathrm{v}_3^D)$. The sensitivity analysis will be computed with respect to the mean of each direction for each sample. When the score function is employed, a gaussian distribution is modeled with the means and variances of each sample. Then, the sensitivity is computed using Eq.(3.37). Concerning the centered finite differences, at each perturbation made, a sample is generated with the same seed, as explained in Section 3.4.2, and the sensitivity is then computed with Eq.(3.38) with different step size c.

All sensitivities computations were repeated twenty times with a sample size of 200000 to compute the mean and standard deviation for each sensitivity approach. In Figure 3.12, the score function approach is validated for a set of lamination parameters well modeled by a Gaussian law. In this case, the sample (not represented) seems to follow a Gaussian distribution. In Figure 3.13, the chosen sample does not follow a Gaussian trend. In this case, the Gaussian hypothesis of the score function is misleading, and there is a huge discrepancy for the v_3^D direction. More generally, we also notice that the score function approach is quite sensitive along the v_1^D direction, for both cases, with a higher standard deviation than the centered finite differences method. This is most likely because, in this example, the limit-state function of the constraint is parallel to the v_1^D direction, and the gradient value is close to null.

In the following, when centered finite difference is used the step size c is set to 0.01.

This study shows the limits of using the SF approach if the variability does not follow the right parametric distribution. However, in terms of computational time, it would be a pity to overlook this method when the sample follows a Gaussian tendency, for example. Therefore, the

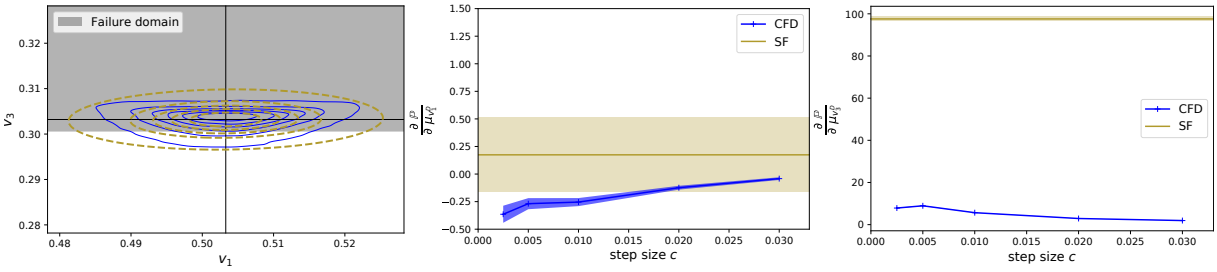

Figure 3.13: Same caption as Figure 3.12 but this time, the sample clearly does not follow a Gaussian distribution (cf. left figure). We notice that the shape places much more weight under the unfeasible region. In this case, failure probability gradients differ depending on the approaches.

strategy proposed is to perform a statistical test of the sample studied to know when to use the score function or centered finite differences.

3.4.4 Hybrid strategy via statistical test

In the multi-scale RBDO framework, once the inverse problem is solved via the FCE (see Chapter 2), we can generate a sample in the orientation space, which is propagated in the lamination parameters space. With this last sample, the failure probability and its sensitivity are computed. The UQ study of lamination parameters made in Chapter 1 shows that, in some cases, a multivariate Gaussian PDF tendency can be modeled. But how to know more precisely if the uncertainty follows a parametric distribution function in the lamination parameters space? Statistical tests exist, such as the Lilliefors (Lilliefors, 1967), the Anderson-Darling (Stephens, 1974), or the Shapiro-Wilk test (Shapiro and Wilk, 1965) that are available in one dimension. For multidimensional distribution, the tests are different. The Henze-Zirkler multivariate normality test is used in this work from the *pingouin* library (Vallat, 2018) available in Python. Some works tried to compare different statistical tests, such as generalized Shapiro-Wilk, Henze-Zirkler, multivariate skewness, multivariate kurtosis, and Royston. Except for some tests, such as multivariate skewness and kurtosis, which present lousy performance in some cases, the results illustrate that none of the tests is universally superior (Székely and Rizzo, 2005; Alpu and Yuksek, 2016).

Therefore, the hybrid strategy is to use the score function whenever the statistical test is true. With the Fourier Chaos Expansion (FCE), the mean and covariance of the LPs sample are directly available. Then, the PDF of the lamination parameters is modeled as $\pi_{\mathbf{v}} \sim \mathcal{N}(\boldsymbol{\mu}_{\mathrm{v}}^{\mathrm{FCE}}, \boldsymbol{\sigma}_{\mathrm{v}}^{\mathrm{FCE}})$. In this case, the gradient is computed with respect to the LPs mean μ_{v_k} using the same sample that computes the failure probability $\mathcal{V} = \left\{\mathbf{v}^{(i)},\ i = 1, ..., n_{\mathrm{MC}}\right\}$:

$$\frac{\partial \mathbb{P}}{\partial \mu_{\mathrm{v}_k}} = \frac{1}{n_{\mathrm{MC}}} \sum_{i=1}^{n_{\mathrm{MC}}} \mathbb{I}_{\mathcal{F}}(\mathbf{v}^{(i)}) \mathcal{K}_{\mu_{\mathrm{v}_k}}(\mathbf{v}^{(i)}), \tag{3.40}$$

In the other case, when the LPs sample does not follow a Gaussian distribution, centered finite differences using CRN are applied as follows:

$$\frac{\partial \mathbb{P}}{\partial \mu_{\mathrm{v}_k}} \approx \frac{\mathbb{P}\left(\boldsymbol{\mu}_{\mathbf{v}} + \boldsymbol{\epsilon}_k\right) - \mathbb{P}\left(\boldsymbol{\mu}_{\mathbf{v}} - \boldsymbol{\epsilon}_k\right)}{2c}, \tag{3.41}$$

where:

- $c = 0.01$ is the value of the step size,

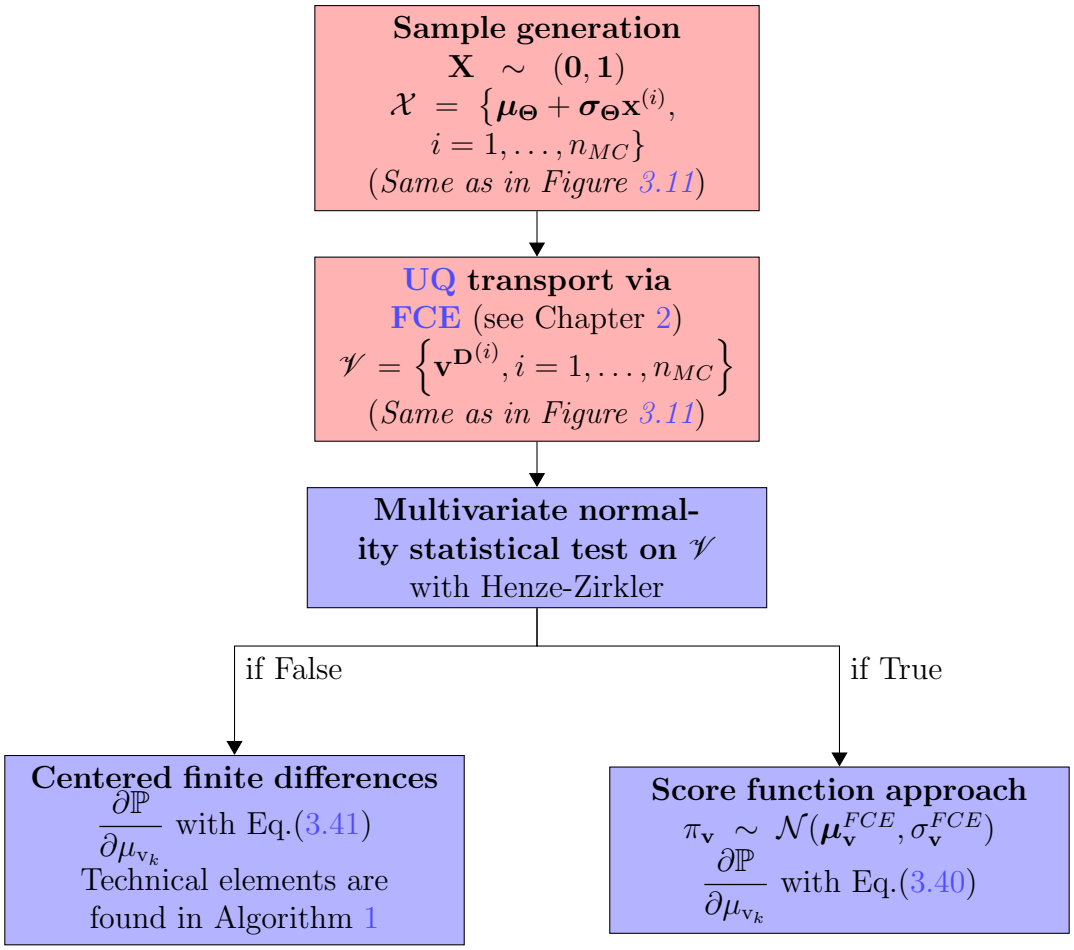

Figure 3.14: Hybrid strategy for failure probability sensitivity.

- $k = \{1, \ldots, n_{\text{dim}}\}$,
- n_{dim} the dimension of the LPs design space,
- $\boldsymbol{\epsilon}$ is the vector of dimension size n_{dim} with zero values,
- $\boldsymbol{\epsilon}_k = \boldsymbol{\epsilon} + c\,\{\boldsymbol{\delta}_{kj}\}$, with δ_{kj} the Kronecker delta. This idea is to set the j^{th} component of $\boldsymbol{\epsilon}$ to the step size. When the index j is equal to the k^{th} direction studied $\delta_{ij} = 1$.

How is the sample generated at each perturbation? For a mean $\boldsymbol{\mu}_{\mathrm{v}}$, we have a stacking sequence associated $\boldsymbol{\mu}_{\boldsymbol{\Theta}}$. The idea to generate a sample for perturbed LPs $\boldsymbol{\mu}_{\mathbf{v}} \pm \boldsymbol{\epsilon}_k$ is to use the original stacking sequence $\boldsymbol{\mu}_{\boldsymbol{\Theta}}$ to find out another close stacking sequence that matches the perturbed LPs perfectly. To do so, a gradient optimization is solved without any rules on the stacking sequence and with the original stacking sequence $\boldsymbol{\mu}_{\boldsymbol{\Theta}}$ as an initial guess. Therefore the stacking sequence $\boldsymbol{\mu}_{\boldsymbol{\Theta},\pm c}$ associated with the perturbed parameters $\boldsymbol{\mu}_{\mathbf{v}} + \boldsymbol{\epsilon}_k$ have almost the same ply orientations than $\boldsymbol{\mu}_{\boldsymbol{\Theta}}$ but with real values and not integers. The overall hybrid strategy is illustrated in Figure 3.14 with the main steps. The details to compute the failure probability sensitivity are found in Algorithm 1.

Algorithm 1 Hybrid strategy for the failure probability sensitivity computation

$n_{MC} = 10000$, $j = 0$, $c = 0.005$

$\boldsymbol{\mu_\Theta}$, $\boldsymbol{\sigma_\Theta}$ ▷ $\boldsymbol{\mu_\Theta}$ and $\boldsymbol{\sigma_\Theta}$ are known

n_{dim} ▷ Dimension of the LP design space

$\boldsymbol{\epsilon} = \text{zeros}(n_{\text{dim}})$

$\mathbf{X} \sim (\mathbf{0}, \mathbf{1})$

$\mathcal{X} = \left\{ \boldsymbol{\mu_\Theta} + \boldsymbol{\sigma_\Theta} \mathbf{x}^{(i)}, i = 1, \ldots, n_{MC} \right\}$

$\mathcal{Y} = \left\{ \mathbf{v} = \hat{H}\left(\mathcal{X}\right) \right\}$ ▷ via FCE

Test := Henze-Zirkler($\mathcal{Y}$) ▷ Multivariate Normality Test

if Test = True **then**

  $\boldsymbol{\mu_\mathbf{v}}, \sigma_\mathbf{v} :=$ FCE($\boldsymbol{\mu_\Theta}, \boldsymbol{\sigma_\Theta}$) ▷ Section 2.3.3

  $\pi_\mathbf{v} \sim \mathcal{N}(\boldsymbol{\mu_\mathbf{v}}, \sigma_\mathbf{v})$

  for $k \leftarrow 1$ to n_{dim} **do**

    $\frac{\partial \mathbb{P}}{\partial \mu_{\mathbf{v}_k}} = \frac{1}{N} \sum_{i=1}^{N} \mathbb{I}_\mathcal{F}(\mathbf{v}^{(i)}) \mathcal{K}_{\mu_{\mathbf{v}_k}}(\mathbf{v}^{(i)})$ ▷ Score Function Eq.(3.40)

  end for

else

  for $k \leftarrow 1$ to n_{dim} **do**

    $\boldsymbol{\epsilon_k} = \boldsymbol{\epsilon} + c\{\delta_{kj}\}$ ▷ j is the index of the vector $\boldsymbol{\epsilon}$

    $\boldsymbol{\mu}_{\boldsymbol{\Theta},-c} := \min \| (\boldsymbol{\mu_\mathbf{v}} - \boldsymbol{\epsilon_k}) - \mathbf{v}(\boldsymbol{\mu}_{\boldsymbol{\Theta},-c}) \|$ ▷ via gradient optimizer with $\boldsymbol{\mu_\Theta}$ as the initial guest

    $\boldsymbol{\mu}_{\boldsymbol{\Theta},+c} := \min \| (\boldsymbol{\mu_\mathbf{v}} + \boldsymbol{\epsilon_k}) - \mathbf{v}(\boldsymbol{\mu}_{\boldsymbol{\Theta},+c}) \|$ ▷ via gradient optimizer with $\boldsymbol{\mu_\Theta}$ as the initial guest

    $\mathcal{X}_{-c} = \left\{ \boldsymbol{\mu}_{\boldsymbol{\Theta},-c} + \boldsymbol{\sigma_\Theta} \mathbf{x}^{(i)}, i = 1, \ldots, n_{MC} \right\}$

    $\mathcal{X}_{+c} = \left\{ \boldsymbol{\mu}_{\boldsymbol{\Theta},+c} + \boldsymbol{\sigma_\Theta} \mathbf{x}^{(i)}, i = 1, \ldots, n_{MC} \right\}$

    $\mathcal{Y}_{-c} = \left\{ \mathbf{v} = \hat{H}\left(\mathcal{X}_{-c}\right) \right\}$

    $\mathcal{Y}_{+c} = \left\{ \mathbf{v} = \hat{H}\left(\mathcal{X}_{+c}\right) \right\}$

    $\mathbb{P}_{-c} = \frac{1}{n_{MC}} \sum_{i=1}^{n_{MC}} \mathbb{I}_\mathcal{F}\left(\mathbf{v}_{-c}^{(i)}\right)$ ▷ via MC

    $\mathbb{P}_{+c} = \frac{1}{n_{MC}} \sum_{i=1}^{n_{MC}} \mathbb{I}_\mathcal{F}\left(\mathbf{v}_{+c}^{(i)}\right)$ ▷ via MC

    $\frac{\partial \mathbb{P}}{\partial \mu_{\mathbf{v}_k}} = \frac{\mathbb{P}_{+c} - \mathbb{P}_{-c}}{2c}$

  end for

end if

3.5 Conclusion

The goal of this chapter was to implement a metamodeling strategy for the reliability analysis, and its sensitivity, of a multimodal quantity of interest without having a parametric distribution of the LP random variables in all the design space. Indeed, the quantities of interest are instabilities and could know different types of discontinuities in the design space (in our case, mode switching on the global response or *hump mode* on a mode response). Furthermore, the costly mechanical models used justify the need of surrogate modeling. The surrogate-based strategy built to approximate the quantity of interest in the design space can handle different types of discontinuity:

- the *hump mode* via Gaussian Process Classification to distinguish instability and stability zones in the design space for each mode,
- the mode switching via Gaussian Process Regression to approximate each mode with a DoE taking design points in the instability zone only.

To perform the reliability analysis, it is possible to exploit both tools when both discontinuity types exist. Before that, a design of experiments of bending lamination parameters in the quasi-orthotropic space was constructed. The strategy allows building a regular design of experiments in the LP space that is governed by geometrical constraints and without using any stacking sequences. An aeroelastic response, used later in the RBDO process, has been approximated in the design space with the DoE and the strategy presented. The surrogate model of the global response has been validated. This surrogate model will be used to compute the probability sensitivity as well. Several techniques were presented to compute the local sensitivity of failure probability. In addition, an hybrid strategy was proposed which limits the computational time in the case where the LPs sample tends to a Gaussian tendency. Hence, the score function or the centered finite differences perform the local sensitivity of the failure probability coupled with the surrogate model. To this end, we have all the tools needed to perform RBDO of composite laminate with instability constraints.

CHAPTER 4

APPLICATION OF THE PROPOSED MULTI-SCALE COMPOSITE RBDO

Contents

4.1 Introduction

The detailed procedure of RBDO under uncertainties of the design variables for a composite laminate optimization is here applied. Firstly, the global methodology is summed up in Section 4.2. The proposed multi-scale methodology is applied in Section 4.3 to the buckling optimization of a composite laminate with uncertainties of ply orientations. Analytical models are used in order to validate the optimization process against a genetic algorithm. The different gains in terms of reliability and computational time are presented. Once the complete procedure is presented and tested on a "simple" case, the aeroelastic optimization under uncertainty can be performed.

4.2 Global RBDO methodology

The aim of this section is to synthesize the global process of optimization. In Chapter 1, we motivated the choice of performing a two-level approach for the RBDO. A multi-scale strategy was proposed to apply the RBDO to composite laminate. Therefore, the optimization process is detailed with the tools that have been developed in Chapter 2 and Chapter 3 for the smooth running of the optimization. In this section, we recall the multi-scale formalism proposed in Chapter 1, which follows the two-level formulation:

$$\min_{\boldsymbol{\mu}_{\boldsymbol{\Theta}}} f\left(\boldsymbol{\mu}_{\mathbf{v}(\boldsymbol{\Theta})}\right) \quad \text{subject to:} \begin{cases} h_i\left(\boldsymbol{\mu}_{\mathbf{v}(\boldsymbol{\Theta})}\right) \leq 0, & i = 1, \ldots, n_d, \\ \mathbb{P}_j\left(g_j(\mathbf{v} = H(\boldsymbol{\Theta})) \geq 0\right) \leq \mathbb{P}_j^{max}, & j = 1, \ldots, n_p, \end{cases} \tag{4.1}$$

where $\boldsymbol{\mu}_{\boldsymbol{\Theta}}$ are the ply orientation mean values to optimize, $\boldsymbol{\mu}_{\mathrm{v}}$ are the lamination parameters mean values, h_i are deterministic nonlinear constraints (emerging from the homogenization process), g_j are limit state functions, H is the nonlinear mapping, from the stacking sequence to the LPs, $\mathbb{P}_j$ are the failure probabilities.

The global reliability-based optimization methodology is presented in Figure 4.1. The initialization is made with a stacking sequence $\boldsymbol{\mu}_{\boldsymbol{\Theta}}$ in the mesoscopic space. Then the mean of lamination parameters is computed with the corresponding objective, reliability, and deterministic constraints for the first iteration. All this information is given to the gradient-based optimizer. In this work, the Method of Moving Asymptotes (MMA) (Svanberg, 1987) is used in the lamination parameter space with the non-monotonic approximation of the GCMMA (Svanberg, 2002). With the MMA, the solution of the original problem is approached by solving a series of convex subproblems which are constructed based on function values and their gradients at current iteration point, and the solution of the subproblem will be used as the starting point of the next iteration. Usually, MMA is used in topology optimization because this optimizer can handle a huge number of constraints. In our case, we need a optimizer that stay in the LP feasible domain in order to avoid too much error in the inverse problem resolution. With the open-source code[1], the tuning of the MMA parameters is possible and allows the optimizer to be conservative with respect to the deterministic constraint (in our case the LP compatibility constraint). It means that the subproblem created at each iteration tends to stay in the LP feasible domain. The MMA parameters used in this work are presented in Table 4.1.

The inverse problem step, which retrieves the stacking sequence, is solved at each iteration by the genetic algorithm optimizer developed by Vicente (2019), which followed the formulation

[1] https://github.com/arjendeetman/GCMMA-MMA-Python

albefa	move	asyinit	asydecr	asyincr
0.3	0.5	0.25	1.1	0.5

Table 4.1: MMA parameters used for optimization.

devised by Irisarri et al. (2014) known as Stacking Sequence Table (SST). The parameters used for the genetic algorithm are detailed in Table 2.1. The Fourier Chaos Expansion, developed in Chapter 2, is used to match the statistics between the stacking sequence and the LPs. Then, a sample can be generated and propagated until the lamination parameters space. Finally, the objective and the deterministic and probabilistic constraints are computed for the gradient optimizer. The statistics are available via the FCE in the case when LPs variability is modeled as Gaussian distribution, and the failure probability sensitivities are computed via the score function approach or the centered finite differences, as explained in Section 3.4.

The procedure is iterated until convergence. The convergence criterion is defined as the change in the LP design variables and is given by Eq.(4.2). In addition, the constraints have to be respected.

$$\epsilon = \frac{\|\boldsymbol{\mu}_{\mathrm{v}}{}^{[j]} - \boldsymbol{\mu}_{\mathrm{v}}{}^{[j-1]}\|}{\boldsymbol{\mu}_{\mathrm{v}}{}^{[j]}}. \tag{4.2}$$

Moreover, the maximum iteration number is set to 50 throughout the manuscript.

4.3 Application of the RBDO to the buckling of a laminate plate

First, the methodology is applied to a test case where an analytical model of the physics is available. This allows to use the Monte Carlo method for the reliability analysis and to compare the methodology with an optimization that uses only a genetic algorithm in order to validate the proposed optimization process.

We consider a simplified composite wing, represented as a flat rectangular plate. The plate dimensions and the applied load direction are shown in Figure 4.2 and detailed in Table 4.2. The composite laminate is 2-mm-thick, which accounts for a total of 16 plies, each stacked at a specific θ_i orientation with respect to the global coordinate system. Available orientations to be chosen from are, in general, uniformly distributed over $[-90^{\mathrm{o}} : \Delta_\theta^{\mathrm{inc}} : 90^{\mathrm{o}}]$, where $\Delta_\theta^{\mathrm{inc}}$ is the angular increment (e.g., 15^{o}). We consider a symmetric and balanced laminate.

The bending stiffness is studied in this case. In classical lamination theory (Tsai and Hahn, 1980), the macroscale constitutive equation relating applied bending moments to the curvature of a symmetrically laminated plate may be written as:

$$\mathbf{M} = \mathbf{D}\boldsymbol{\kappa}, \tag{4.3}$$

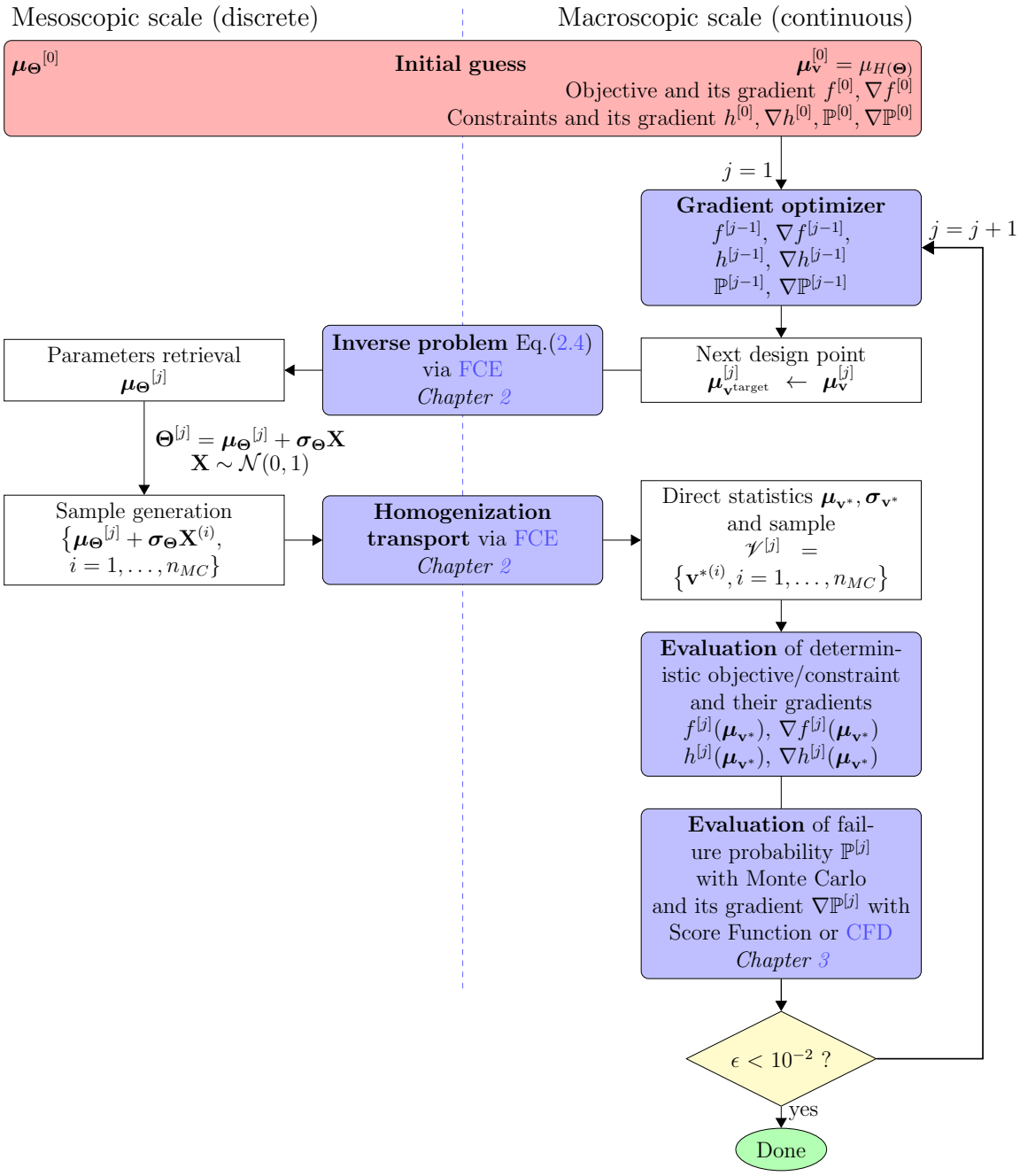

Figure 4.1: Flowchart of the methodology.

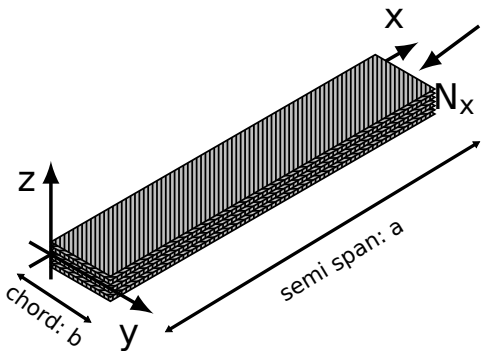

Figure 4.2: Geometry of the wing.

Parameters	Value
a(m)	0.3048
b(m)	0.0762
E_{11}(GPa)	140
E_{22}(GPa)	10
G_{12}(GPa)	5
ν_{12}	0.3
ρ(kg/m^3)	1600
N_{x}(N/mm)	100
Boundary condition	Clamped at $x = 0$

Table 4.2: Dimensions of the plate and material properties.

with:

$$\begin{pmatrix} D_{11} \\ D_{22} \\ D_{12} \\ D_{66} \\ D_{16} \\ D_{26} \end{pmatrix} = \frac{t^3}{12} \begin{bmatrix} 1 & \mathrm{v}_1^D & \mathrm{v}_3^D & 0 & 0 \\ 1 & -\mathrm{v}_1^D & \mathrm{v}_3^D & 0 & 0 \\ 0 & 0 & -\mathrm{v}_3^D & 1 & 0 \\ 0 & 0 & -\mathrm{v}_3^D & 0 & 1 \\ 0 & \mathrm{v}_2^D/2 & \mathrm{v}_4^D & 0 & 0 \\ 0 & \mathrm{v}_2^D/2 & -\mathrm{v}_4^D & 0 & 0 \end{bmatrix} \begin{pmatrix} U_1 \\ U_2 \\ U_3 \\ U_4 \\ U_5 \end{pmatrix}, \tag{4.4}$$

which comes from the CLPT introduced in Section 1.2.

4.3.1 Problem formulation

The plate is under compressive load N_x. An orthotropic hypothesis is made on the stiffness properties of the composite, i.e. the bending-twist coupling is avoided and reduces the coupling terms D_{16} and D_{26} to zero. Therefore, the lamination parameters $\mu_{\mathrm{v}_2^D}$ and $\mu_{\mathrm{v}_4^D}$ are set to zero during the optimization process.

The objective is to maximize the bending stiffness D_{11}:

$$D_{11}(\boldsymbol{\mu}_{\mathbf{v}}) = U_1 + \mu_{\mathrm{v}_1^D} U_2 + \mu_{\mathrm{v}_3^D} U_3, \tag{4.5}$$

while remaining reliable with respect to the buckling phenomenon g:

$$g(\mathbf{v^D}) = \lambda_{crit} - \min_{m,n}(\lambda), \tag{4.6}$$

with:

$$\lambda = \pi^2 \frac{D_{11}\frac{m^4}{a^4} + (D_{12} + 2D_{66})\frac{m^2}{a^2}\frac{n^2}{b^2} + D_{22}\frac{n^4}{b^4}}{\frac{m^2}{a^2}N_x},$$

where λ_{crit} is the limit buckling criterion, λ is the buckling value of a orthotropic laminate, N_x is the compressive load, a and b are the plate dimensions, $\mathbf{D}$ is the bending stiffness matrix, m and n are the number of half-wavelengths in the x and y directions.

Regarding the ply orientation uncertainty, the standard deviation $\sigma_{\boldsymbol{\Theta}}$ is set to 2°. The formulation of the gradient RBDO problem is written in the following form:

$$\min_{\boldsymbol{\mu}_{\boldsymbol{\Theta}}} -D_{11}\left(\boldsymbol{\mu}_{\mathbf{v^D}(\boldsymbol{\Theta}|\boldsymbol{\mu}_{\boldsymbol{\Theta}})}\right) \quad \text{subject to:} \begin{cases} h_{LP}(\boldsymbol{\mu}_{\mathbf{v^D}(\boldsymbol{\Theta}|\boldsymbol{\mu}_{\boldsymbol{\Theta}})}) \leq 0 \\ \mathbb{P}\left(g(\mathbf{v^D} = H(\boldsymbol{\Theta})) \geqslant 0\right) \leq \mathbb{P}^{\max} \end{cases}, \tag{4.7}$$

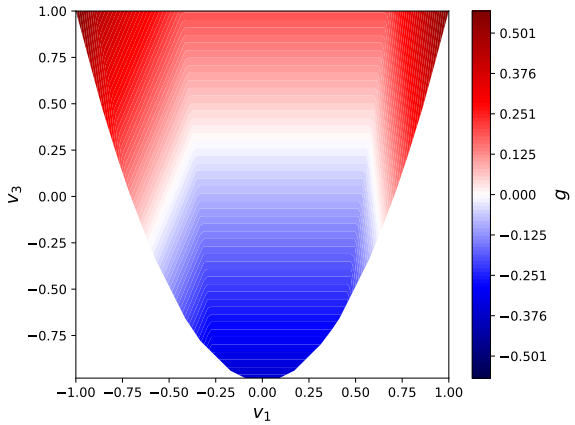

(a) Normalized buckling constraint g.

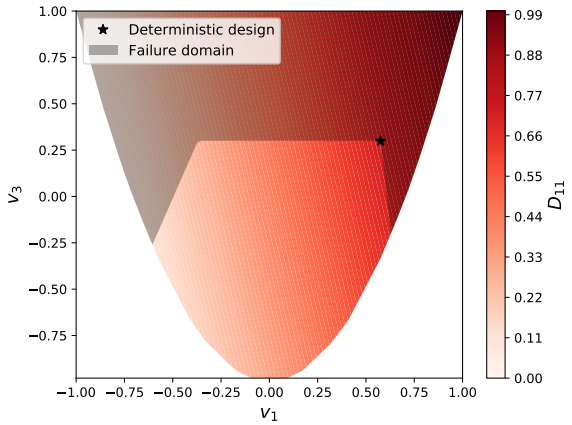

(b) Normalized objective D_{11} with the deterministic design solution. The failure has been shaded to reveal the boundary between failure and safety domains.

Figure 4.3: Reponses of the quantity of interest of the optimization in the 2D lamination parameters macroscopic design space.

where $\boldsymbol{\mu}_{\boldsymbol{\Theta}}$ are the mean ply orientation design variables, $\mathbf{v}^{\mathbf{D}}$ are the macroscopic lamination parameters with their mean $\boldsymbol{\mu}_{\mathbf{v}^{\mathbf{D}}}$, h_{LP} is the compatibility constraint defined by Miki and Sugiyama (1991) for an orthotropic laminate, H is the mapping between ply orientations and lamination parameters found in Eq.(1.13) and $\mathbb{P}^{\max} = 1\%$ is the maximum failure probability. The failure probability $\mathbb{P}$ is approximated via the Monte Carlo method with a sample size $n_{MC} = 200000$. With this sample size, we targeted a 2% coefficient of variation in the probability estimation, which help, in addition, the right estimation of the probability sensitivity when CFD is used.

The normalized objective D_{11}, the constraints h_{LP} and g are illustrated in Fig. 4.3, with the obtained deterministic optimization solution in the lamination parameters space, represented by a small black star.

4.3.2 Results of the RBDO

The first results were obtained with the hypothesis that the lamination parameters followed Gaussian distributions modeled at each iteration, thanks to the accurate statistics provided by the FCE. With this setup, the score function approach is performed for the gradient failure probability computation at each iteration. In Fig. 4.4, the optimization path (4.4a) and the close-up (4.4b) around the final design (cyan star) are shown with the shaded area corresponding to the failure domain. The green points show the designs proposed by the MMA algorithm during the iterative process, and the blue ones are the design points retrieved from the inverse problem solutions. In the close-up, the probability density function around the final design point is shown. The final RBDO solution is more reliable and, as expected, not at the same location as the deterministic optimal.

The convergence of the optimization is shown in Fig. 4.4c with the objective D_{11} and the probability reported through the 19 iterations. Fig. 4.4d shows the design evolution in the lamination parameter and orientation spaces. The convergence is rather slow toward the end, but it is consistent with the general behavior of the MMA algorithm. We notice that while the

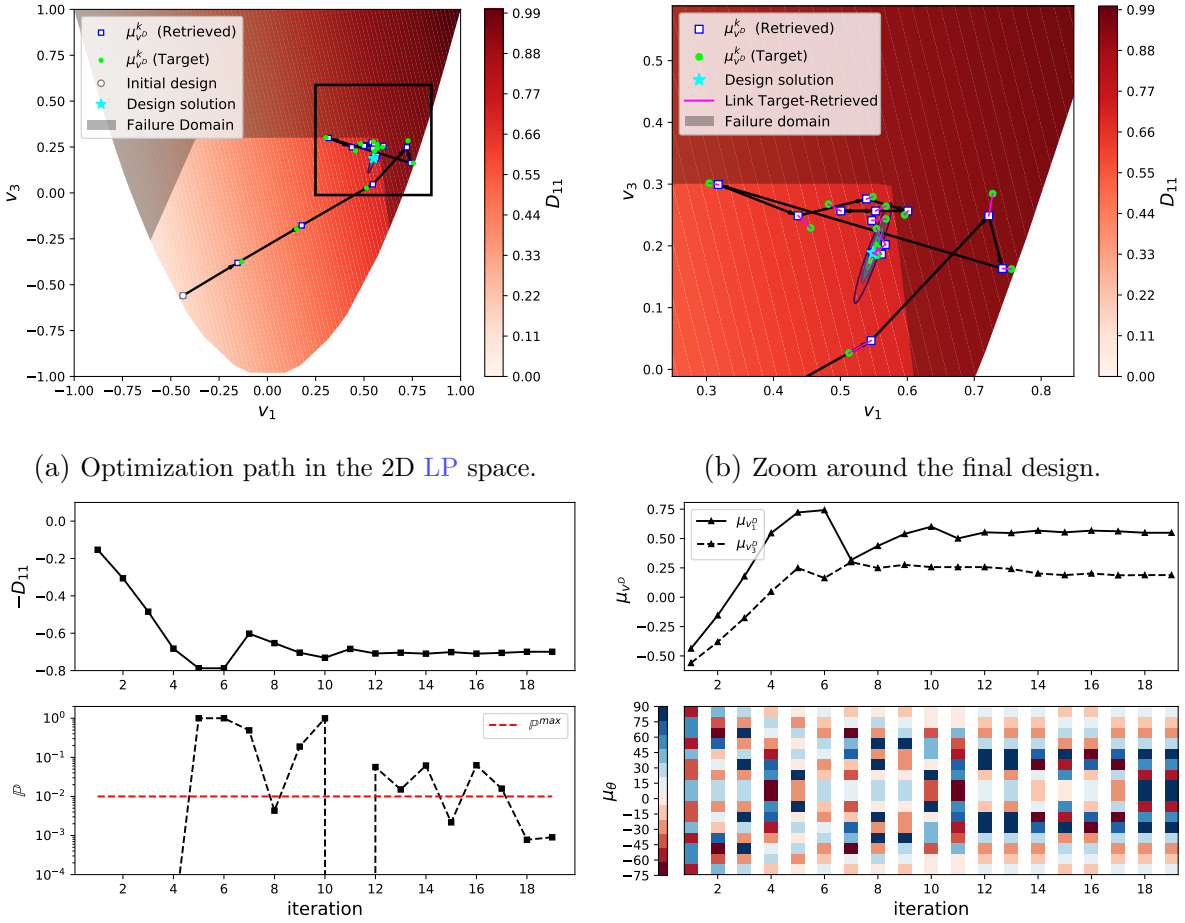

(a) Optimization path in the 2D LP space.

(b) Zoom around the final design.

(c) Convergence of the objective f and the failure probability $\mathbb{P}$.

(d) Convergence of the design variables represented in both design spaces.

Figure 4.4: RBDO result where the probability sensitivity is computed with the score function approach.

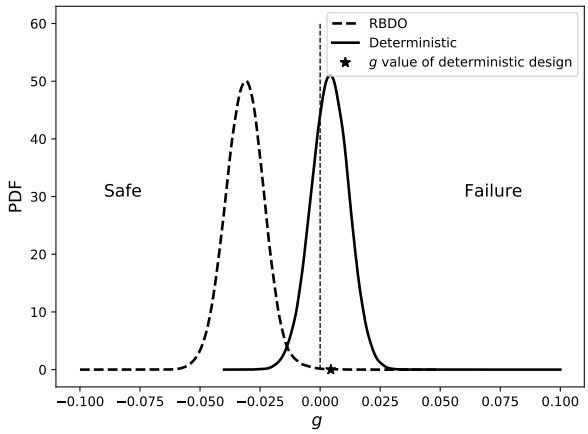

Figure 4.5: Buckling PDFs for the deterministic and reliability-based optimized designs.

maximum probability constraint is not violated by the final design, the obtained value is lower than the threshold. This is, in fact, due to the discrete nature of the ply orientations. Despite the fact that the MMA optimizer is designed to propose a solution closer to the probability threshold, in practice, the resolution of the inverse problem nudges the solution a bit, inducing small deviations (cf. pink segments in Fig. 4.4b). Therefore, the final result at convergence could remain conservative due to the nature of the application.

Additionally, the buckling PDFs corresponding to each of the RBDO and deterministic optimized designs are shown in Fig. 4.5 for the sake of comparison. The PDF for the deterministic case is obtained by uncertainty quantification around the stacking sequence design found after an inverse problem resolution. The deterministic design leads to poor reliability with a failure probability over 0.5. Then, reliability improvement is made with the RBDO design.

4.3.2.1 Gradient probability comparaison

In the following, we test the robustness of the proposed numerical approach. In particular, we are interested in the sensitivity of the method to the choice of different methods to evaluate the failure probability gradients. In the optimization using only the score function for probability gradients computation in Section 4.3.2, the Gaussian hypothesis for the lamination parameters is made, which can lead to an error in the failure probability gradient evaluation. The idea is to compare the optimization with different methods to compute probability sensitivity: score function (results of Figure 4.4), centered finite difference and the hybrid approach.

Firstly, the optimization is run again with the failure probability gradients computed via centered finite differences without assuming Gaussianity. The optimization path is different (see Figure 4.6a), but the convergence is quite similar (see Figure 4.6c and 4.6d) at the end with almost the same number of iterations and the same lamination parameters, as shown in Table 4.3. The variability, shown with the joint PDF in Figure 4.6b, is similar to the design variability of the optimization made with the score function only in Figure 4.4b.

Finally, the hybrid approach detailed in Section 3.4.4 is used to know if the sample can be approximated with a Gaussian law or not to know if the score function approach or the finite differences are used for the gradient analysis (see Algorithm 1). With this approach, the optimization converges with fewer iterations and almost the same design of lamination parameters. In this case, the Gaussian statistical test is positive for half of the iterations.

The details of the results are shown in Table 4.3. Therefore, for this application, the Gaussian

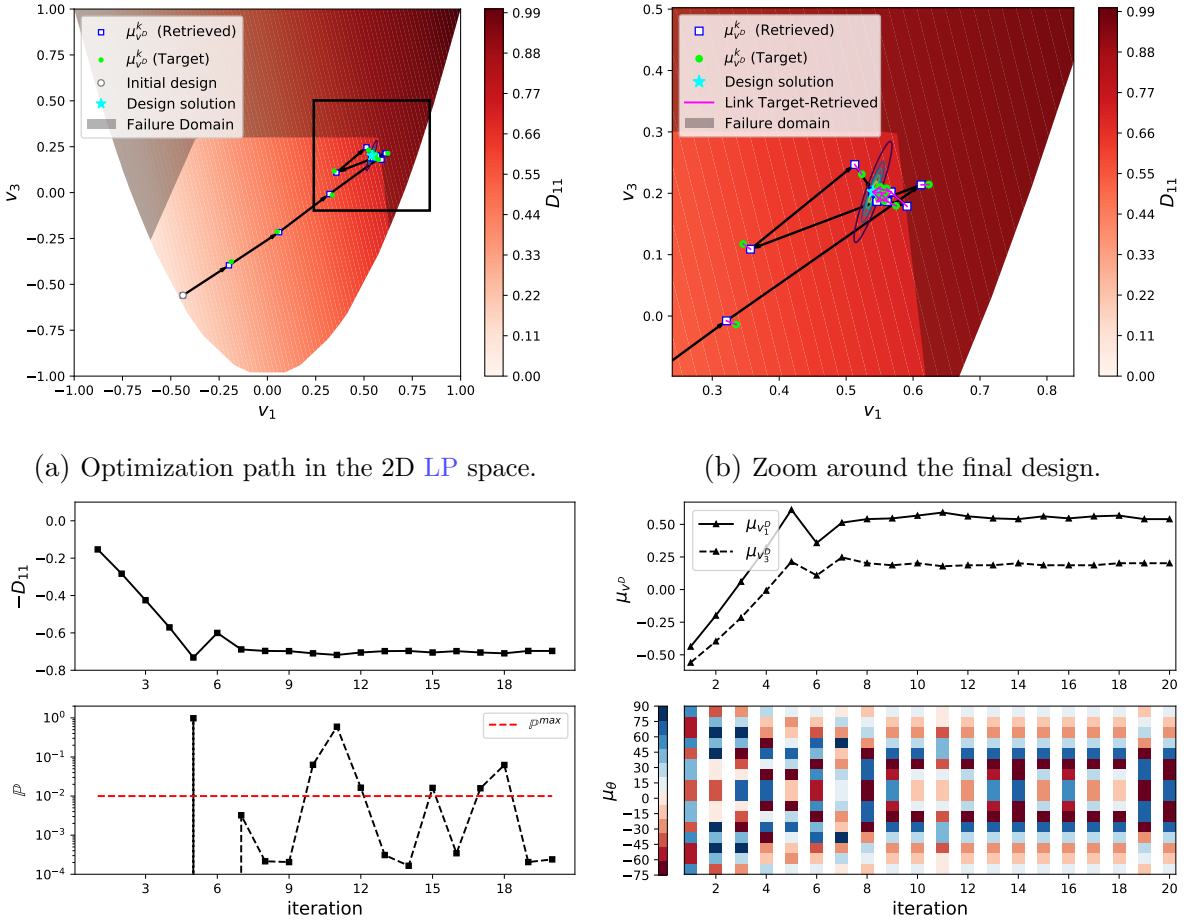

(a) Optimization path in the 2D LP space.

(b) Zoom around the final design.

(c) Convergence of the objective f and the failure probability $\mathbb{P}$.

(d) Convergence of the design variables represented in both design spaces.

Figure 4.6: RBDO result where the probability sensitivity is computed with the centered finite differences.

hypothesis made on LPs, to use SF for probability gradients, leads to the same results as the optimization using CFD.

4.3.2.2 Comparison with evolutionary optimization algorithm

The proposed method has to be compared to a standard method regarding the composite laminate's RBDO. Indeed, various multi-scale approaches rely on direct methods, such as evolutionary algorithms, to optimize directly ply angles in the mesoscopic design space. In the following, a genetic algorithm is used as the reference approach to solve the optimization problem in the mesoscopic space (i.e., the ply orientation space in this case). Therefore, the macroscopic space is not exploited and no convergence path can be identified. Hence the comparison will rely on the final design and computational time.

Results for the here-presented multi-scale RBDO approach combined with different methods for the failure probability sensitivity are now compared with the result obtained by the genetic algorithm in Table 4.3. The final designs in the lamination parameters space are similar for all optimization, but the computational times are quite different. The reference optimization with the genetic algorithm took three times longer than the proposed method with the hybrid approach for failure probability sensitivity. Overall, the multi-scale approach, exploiting the

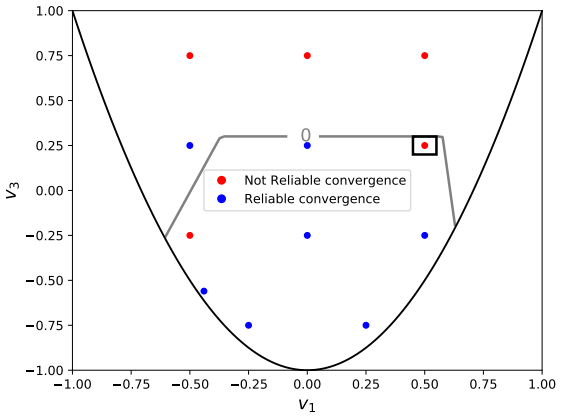

(a) Sensitivity study to initial design guess: regular lattice in the macroscopic space + the reference optimization.

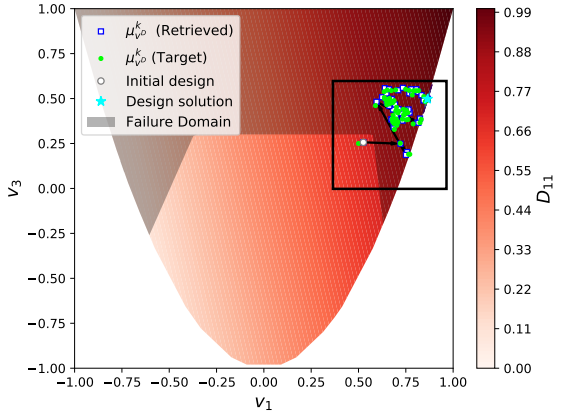

(b) Optimization path of the squared initial design from Figure 4.7a.

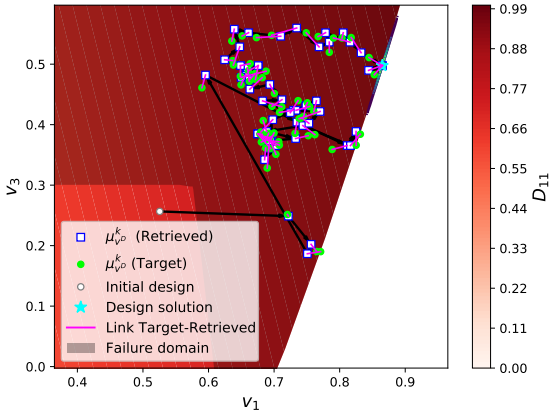

(c) Zoom of the optimization path.

Figure 4.7: Convergence study with different initializations.

lamination parameters, is much more efficient regarding the computational time. Nevertheless, if the macroscopic parameters (i.e., the lamination parameters in this case) cannot be modeled with a parametric distribution (i.e., the Gaussian one), using only finite differences lead to higher computational time. The difference in computational time between the full score function approach and the full centered finite difference could increase with the design variable dimension.

4.3.2.3 Study of the impact of the initial design

In the following, we are interested in the sensitivity of the method to the choice of the initial guess (to determine whether or not there is a correlation between the initial design point and the convergence of the optimization). The study is made with the use of the score function approach for probability sensibility. Optimizations were made with different initial points in the design space to check the robustness of the convergence. In Figure 4.7a, the initial points are spread over the macroscopic design space. Some of these initializations do not converge to a reliable solution. These initializations are mainly close to the limit-state function or in the failure domain. In Figure 4.7b, the optimization paths are shown for the case that did not converge, i.e. for the initial point surrounded by a square in Figure 4.7a.

When the optimizer travels too deep into the failure zone, it could present some difficulties in returning to the safety domain. In fact, in this case, the failure probability is equal to 1, and

Method			Iterations	Objective $-D_{11}$	Lamination parameters $(\mu_{\mathrm{v}_1^D}, \mu_{\mathrm{v}_3^D})$	Stacking sequence $\boldsymbol{\mu_\Theta}$	Failure probability	Computation time
Approach	RBDO	Gradient						
Deterministic	✗	✓	9	-0.73	(0.58, 0.30)	$[-15, 15, 30, 90, -30, -15, 0, 15]_s$	0.64	3 s
Score function	✓	✓	19	-0.70	(0.55, 0.19)	$[15, -30, -15, 30, -15, 30, 15, -30]_s$	0.001	14 min
Centered finite differences	✓	✓	20	-0.68	(0.54, 0.20)	$[0, -30, 30, 30, -30, 30, -30, 0]_s$	0.00024	39 min
Hybrid	✓	✓	12	-0.67	(0.55, 0.18)	$[0, 0, -45, 45, 45, -60, 60, -45]_s$	0.00015	24 min
Genetic algorithm	✓	✗	100	-0.70	(0.54, 0.20)	$[-15, 15, -30, 30, 75, -75, 75, -75]_s$	0.00018	80 min

Table 4.3: Comparison of the deterministic and the various RBDO approaches: the proposed multi-scale RBDOs with various ways of computing the failure probability gradients, a direct RBDO with genetic algorithm and the deterministic optimization is followed by uncertainty quantification at the final design to compute the failure probability.

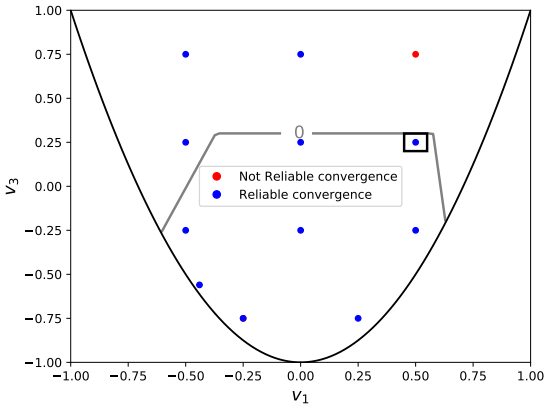

(a) Sensitivity study to initial design guess: regular lattice in the macroscopic space + the reference optimization.

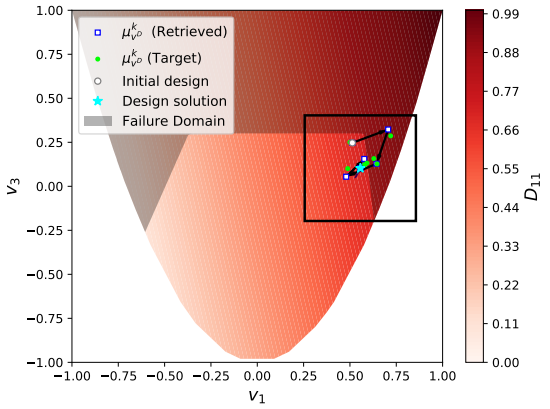

(b) Optimization path of the squared initial design from Figure 4.8a.

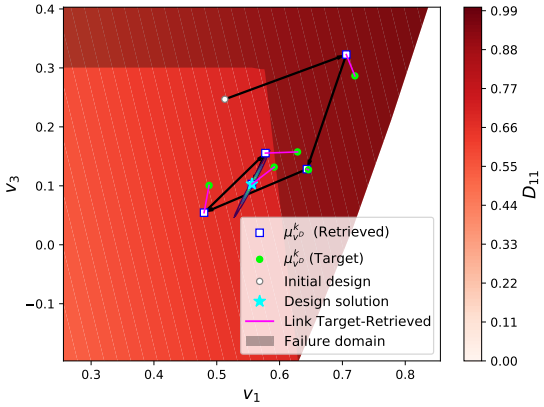

(c) Zoom of the optimization path .

Figure 4.8: Convergence study with different initializations with the addition of the deterministic constraint.

perturbing the design to compute the local sensitivity will not change the failure probability. Hence the failure probability gradients are equal to zero, and the gradient optimizer does not feel that the design is in the failure domain. A first solution to prevent this problem is to do a multi-start optimization, which means running several optimizations with different initial guesses placed mainly in the safety domain. A further approach also tested here is to add the deterministic version of the reliability constraint in the optimization formulation in order to regularize the optimization in the unfeasible region:

$$\min_{\boldsymbol{\mu}_{\boldsymbol{\Theta}}} -D_{11}\left(\boldsymbol{\mu}_{\mathbf{v^D}}\left(\boldsymbol{\Theta}\right)\right) \quad \text{subject to:} \begin{cases} h_{LP}(\boldsymbol{\mu}_{\mathbf{v^D}}) \leq 0 \\ g(\boldsymbol{\mu}_{\mathbf{v^D}}) \leq 0 \\ \mathbb{P}_g = \mathbb{P}\left(g(\mathbf{v^D} = H(\boldsymbol{\Theta})) > 0\right) \leq \mathbb{P}^{max} \end{cases}, \tag{4.8}$$

The same convergence study has been done with this formulation. In Fig. 4.8a, except for one initialization, the RBDOs converge to a reliable design. Therefore, the potential to add the deterministic constraint in a gradient-based method is demonstrated for this case.

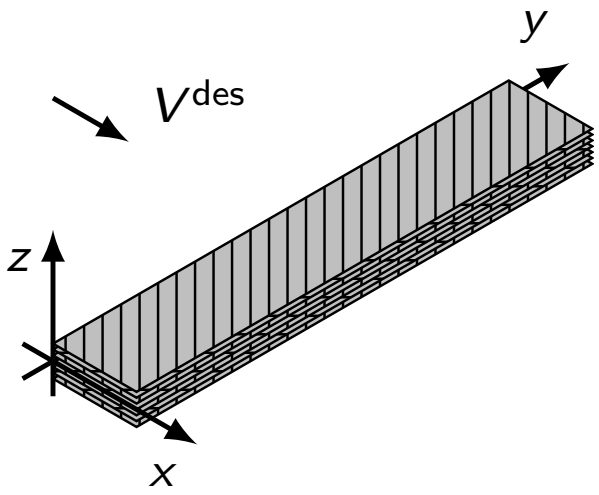

Figure 4.9: Composite plate under airflow.

4.3.3 Conclusion

The strength of the RBDO approach is shown for composite laminate optimization under compressive load, when the ply orientation design variables are considered uncertain. The proposed RBDO method is validated compared to the reference composite RBDO using a genetic algorithm. Regarding the computational time, the multi-scale RBDO methodology performs better for this application. Nevertheless, a critical point concerns the initial guess. If the latter is in the failure domain or the optimizer leads the design to the failure domain during the optimization, it could have some drawbacks in convergence. However, we show the potential of adding the deterministic constraint to counter this problem.

4.4 Toward an aeroelastic application

Reliability-based design optimization is applied to the aeroelastic optimization of a composite plate. The optimization will be performed to reliability analysis of the flutter instability. The aeroelastic model is first described, and then the RBDO strategy is applied for the aeroelastic optimization of a composite plate subjected to airflow (see Figure 4.9). The dimension and material properties are shown in Table 4.2. The fluid parameters are presented in Table 4.4.

4.4.1 Model description

This subsection introduces the structural model, the applied loads, and the notions of aeroelastic dynamic instability flutter. The finite element software MSC NASTRAN (noa, 2014) was chosen as a solver due to its wide acceptance in the aircraft industry, its capability to handle aero-structural analysis, and to compute the required sensitivities efficiently for a large variety of predefined design variables and responses.

4.4.1.1 Finite Element Model

The structural model is solved with the Finite Element (FE) method. The model consists of a rectangular plate with 8 chordwise and 30 spanwise elements (see Figure 4.10a). The elements employed for the discretization are 4-node 2D linear elements with a shell kinematic model. The stiffness properties are defined with the stiffness bending matrix $\boldsymbol{D}$.

Fluid Parameters	Value
Density of airflow ρ_f (kg/m^3)	1.225
Angle of attack (AoA) (°)	5
Velocity V^{des} (m/s)	135

Table 4.4: Fluid properties.

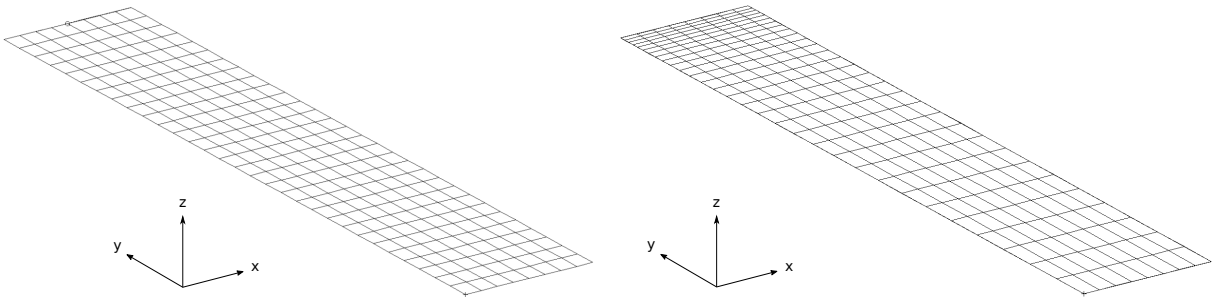

(a) Structural mesh. (b) Aerodynamic mesh.

Figure 4.10: Mesh of the plate.

4.4.1.2 Double Lattice Model

One reason for using Nastran is the availability of aerodynamic tools that, along with the finite element model, allow for coupled aeroelastic calculations. Depending on the Mach number, different aerodynamic methods can be applied. The doublet lattice subsonic lifting surface theory (DLM) (Albano and Rodden, 1969), is chosen for our application. It belongs to the potential theory methods, where singularities like sources, vortices, or doublets are superimposed with the undisturbed free stream.

The aerodynamic mesh is discretized with the same number of elements as the structural one. In the spanwise direction, the mesh refinement is smaller towards the plate tip to better describe the distribution of forces which presents large gradients at the plate tip using the function f_d (see Figure 4.10b):

$$f_d = \frac{1}{\pi}(1 - 1/4) * \sin(\pi * y). \tag{4.9}$$

4.4.1.3 Dynamic instability

Since critical flutter velocity is studied for reliability, dynamic aeroelastic analysis is performed. The coupling between the finite element model and the doublet lattice method is made with the surface spline method, available in Nastran, in order to interpolate motion and forces for the aeroelastic model.

The aeroelastic equations of motion are expressed in the classical form as:

$$\mathbf{M}\ddot{\mathbf{q}} + (\rho V \mathbf{E})\,\dot{\mathbf{q}} + \left(\rho V^2 \mathbf{C} + \mathbf{K}\right)\mathbf{q} = 0, \tag{4.10}$$

where:

- $\mathbf{M}$ is the mass matrix ,
- $\mathbf{K}$ is the structural stiffness matrix,

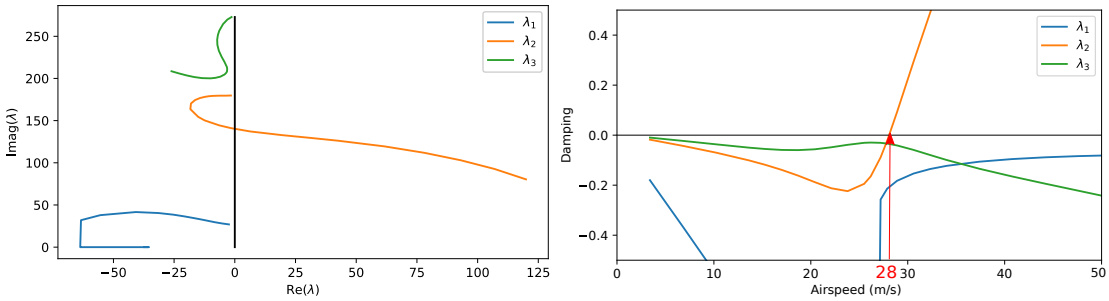

Figure 4.11: Flutter diagram for the experimental case coming from Hollowell and Dugundji (1982) obtained using the p-k method. The orange line represents the flutter mode with the critical flutter velocity $V_f = 28\text{m/s}$ given by the red arrow.

- $\mathbf{q}$ is the vector of the generalized displacements,
- $\mathbf{C}(k)$ is the aerodynamic stiffness matrix,
- $\mathbf{E}(k)$ is the aerodynamic damping matrix,
- $k = \frac{f_r c}{2V}$ is the reduced frequency, where f_r covers a range of frequencies between a small one (around 10^{-2}) and the frequencies of the modal basis studied c is the chord of the wing and V the velocities studied.

These can be reformulated as:

$$\begin{bmatrix} \dot{\mathbf{q}} \\ \ddot{\mathbf{q}} \end{bmatrix} - \begin{bmatrix} 0 & \mathbf{I} \\ -\mathbf{M}^{-1}(\rho V^2 \mathbf{C} + \mathbf{K}) & -\mathbf{M}^{-1}(\rho V^2 \mathbf{B}) \end{bmatrix} \begin{bmatrix} \mathbf{q} \\ \dot{\mathbf{q}} \end{bmatrix} = 0, \tag{4.11}$$

which is a polynomial eigenvalue problem of the general form $\dot{\mathbf{x}} - \mathbf{Q}\mathbf{x} = 0$.

The matrix $\mathbf{Q}(V, k)$ is a function of air-speed and the reduced frequency. The eigenvalues of this matrix may be computed to find the stability of the wing at a given air speed. Instability occurs when the real part of one of the eigenvalues is positive. This leads to flutter when the imaginary part is non-zero and is divergence otherwise. The aeroelastic instability speed is found by solving Eq.(4.11) at multiple air-speed with the p-k method Hassig (1971).

4.4.1.4 Validation

The aeroelastic model used in this thesis is validated against experimental and numerical studies throughout the literature. Experimental data are available in Hollowell and Dugundji (1982). The experimental investigation was conducted on a composite cantilevered plate with different stacking sequences. To describe the flutter phenomenon, in Figure 4.11, a set of the first three eigenvalues is shown for a composite plate following the properties in Hollowell and Dugundji (1982). The instability speed is given by the lowest velocity at which the damping reaches zero. The flutter velocities are compared in Table 4.5 between the experimental data and the numerical model. The latest presents a good representation of the dynamic instability. Moreover, our model was compared with the model in Stodieck et al. (2013), which uses Nastran and p-k method (see Figure 4.12). We assume that the model is accurate enough to perform the aeroelastic optimization under the reliability constraint for the flutter phenomenon.

Stacking sequence	Flutter Velocity (m/s)	
	Experimental	Numerical
$[0_2, 90]_s$	24	23.9
$[\pm 45, 0]_s$	> 32	45.5
$[45_2, 0]_s$	28	30.3
$[30_2, 0]_s$	27	28.0

Table 4.5: Flutter velocity of the experimental case in Hollowell and Dugundji (1982) compared with our numerical model.

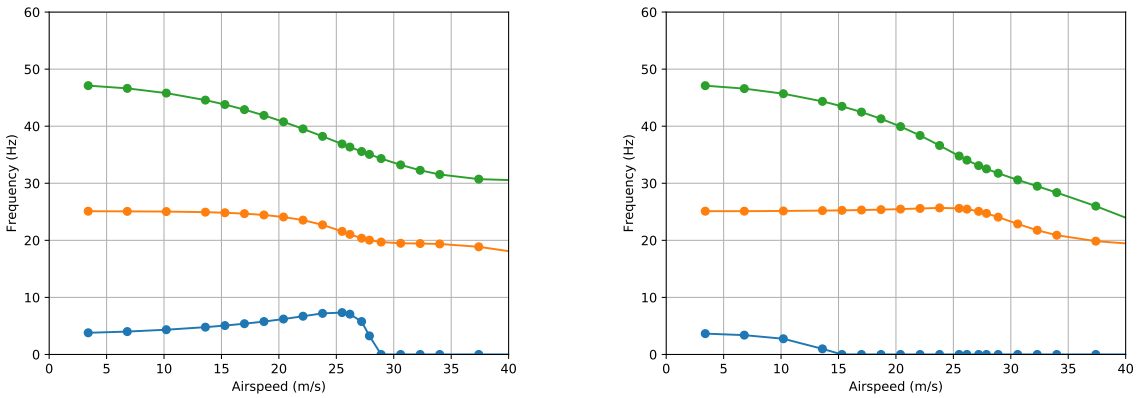

(a) $[90, -45, 45]_s$ (b) $[90, 45, -45]_s$

Figure 4.12: Vibration frequencies and damping ratios from FEM flutter analysis using pk-method for two different UD stacking sequences (case studied in Stodieck et al. (2013)).

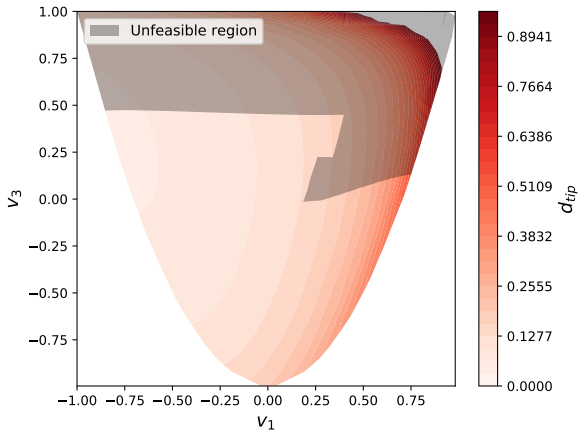

Figure 4.13: Response of the objective with the flutter failure domain in 2D space with $\mathrm{v}_2^D = \mathrm{v}_4^D = 0$.

4.4.2 Results of RBDO

The RBDO approach is applied to a composite flat plate subjected to a flow (see Figure 4.9). The dimensions, the material properties and the fluid parameters are recalled in Tables 4.2 and 4.4. The objective is to promote the flexibility of the wing by maximizing the displacement at the tip d_{tip} while remaining reliable with respect to the flutter constraint g. The formulation of the latter is described in the following form:

$$\min_{\boldsymbol{\mu}_{\boldsymbol{\Theta}}} -d_{\text{tip}}\left(\boldsymbol{\mu}_{\mathbf{v^D}(\boldsymbol{\Theta}|\boldsymbol{\mu}_{\boldsymbol{\Theta}})}\right) \quad \text{subject to:} \begin{cases} h_{LP}(\boldsymbol{\mu}_{\mathbf{v^D}(\boldsymbol{\Theta}|\boldsymbol{\mu}_{\boldsymbol{\Theta}})}) \leq 0 \\ \mathbb{P}\left(\tilde{g}(\mathbf{v^D} = H(\boldsymbol{\Theta})) \geqslant 0\right) \leq \mathbb{P}^{max} \end{cases}, \tag{4.12}$$

where $\tilde{g} = \tilde{V}_f - V^{\text{des}}$ is computed with the surrogate model strategy presented in Chapter 3 and $\mathbb{P}^{\text{max}} = 0.01$.

The objective and the failure domain are shown in the 2D projection $(\mathrm{v}_1^D, \mathrm{v}_3^D)$ with $\mathrm{v}_2^D = \mathrm{v}_4^D = 0$ in Figure 4.13. The displacement at the plate tip increases to the upper right side of the 2D design space, which represents composite laminate with only 0° plies. The color map in this region is not represented because the displacement explodes due to the static divergence instability that leads to higher deformation than the flutter. The limit-state function of the flutter constraint presents a discontinuity, already presented in Chapter 3.

Firstly, in Figure 4.14a, we could observe the optimization path of an aeroelastic RBDO using the global strategy with an initial guess taken far from the convergence region. The approach to compute the failure probability gradients is the hybrid one. In the same manner than for the previous application, the designs proposed by the MMA algorithm during the iterative process are shown as green points, and blue points represent the design points retrieved from the inverse problem solutions. The optimization goes through the boundary limit of the lamination parameters space (Figure 4.14a). This leads to slow convergence of the MMA because the LPs compatibility constraint is activated. Therefore, the MMA creates small bounds for each subproblem and moves forward with a small step. The convergence of the optimization is shown in Fig. 4.14c with the objective and the probability plotted through the 32 iterations. We notice that the failure probability is lower than the threshold, similarly to the first application. This is, in fact, due to the discrete nature of the ply orientations. Finally,

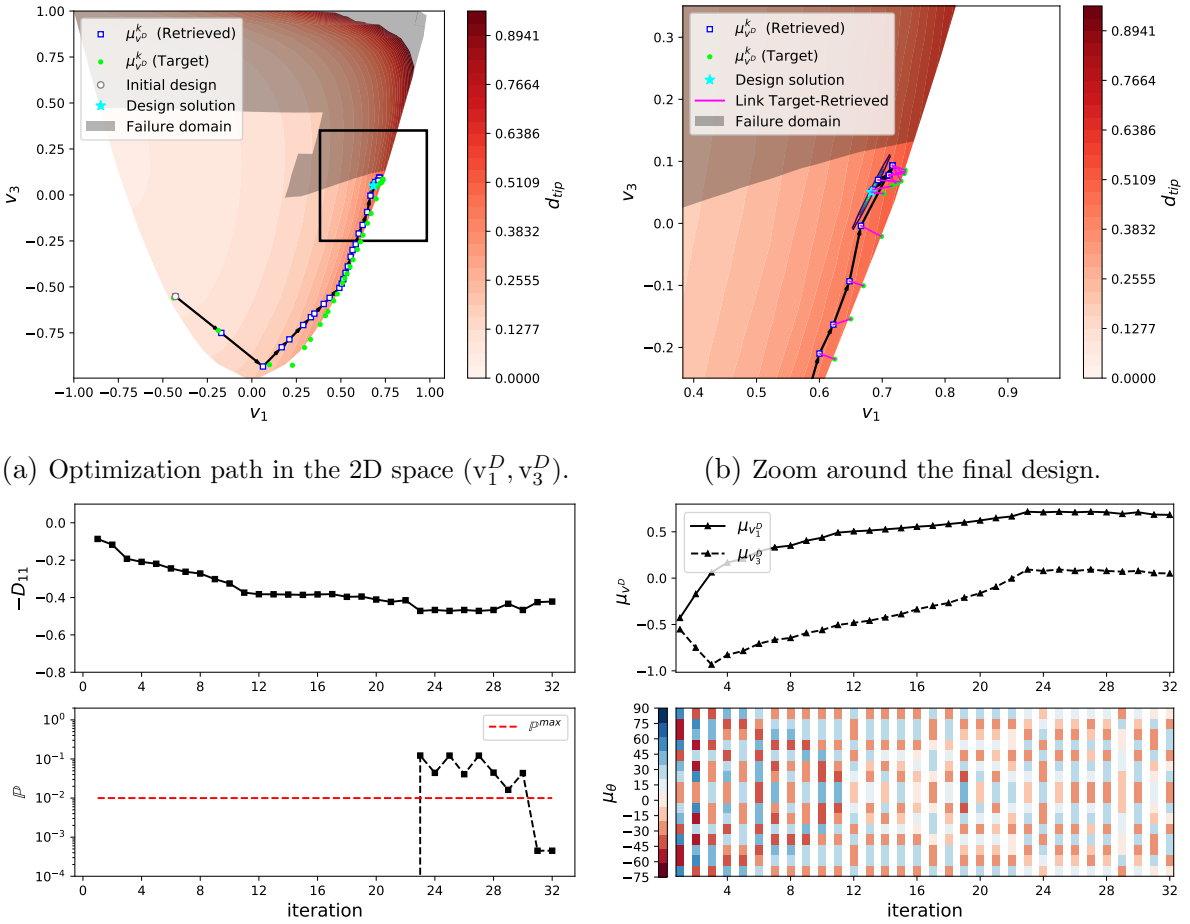

(a) Optimization path in the 2D space $(\mathrm{v}_1^D, \mathrm{v}_3^D)$.

(b) Zoom around the final design.

(c) Convergence of the objective f, failure probability $\mathbb{P}$.

(d) Convergence of the design variables represented in both design spaces.

Figure 4.14: Result of the aeroelastic RBDO with the probability sensitivity computed with the hybrid approach.

in Figure 4.14b, the probability density function around the final design point is shown in the 2D space, and we see the high correlation between v_1^D and v_3^D. This is because the design point is close to the limit of the LPs feasible domain. This leads to a decrease in Gaussian variability of the LPs. In this case, 33% of design points pass the Gaussian statistical test, which is 17% lower than the previous application. Moreover, the optimization using only the score function approach does not converge since it computes the wrong gradient values of the probability.

The critical flutter velocity PDFs corresponding to each of the RBDO and deterministic optimized designs are shown in Figure 4.15. The PDF for the deterministic case is obtained by uncertainty quantification around the stacking sequence design found after an inverse problem resolution. The flutter velocity of the retrieved stacking sequence of the deterministic case is represented as a star in Figure 4.15. This velocity does not respect the initial velocity constraint of 135m/s. This highlights a problem of the deterministic bi-level approach: at the end of the optimization in the homogenized space, when the inverse problem is solved to retrieve the design of the stacking sequence, it may lead to a solution layup that does not satisfy the constraint.

With our multi-scale approach for RBDO, when the optimizer converges, we do not need to perform an extra inverse problem since it is done at the beginning of each iteration and the

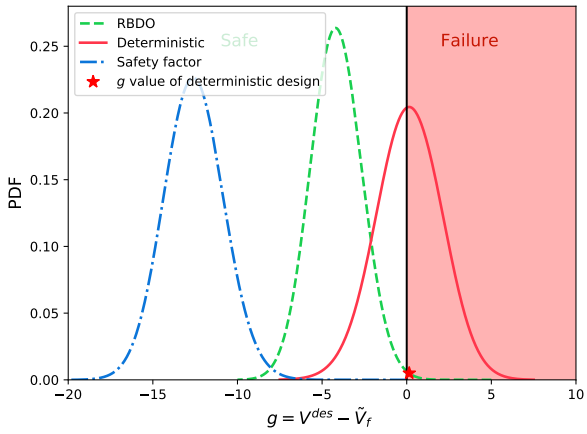

Figure 4.15: Critical flutter velocity PDFs for deterministic and reliability-based optimized designs.

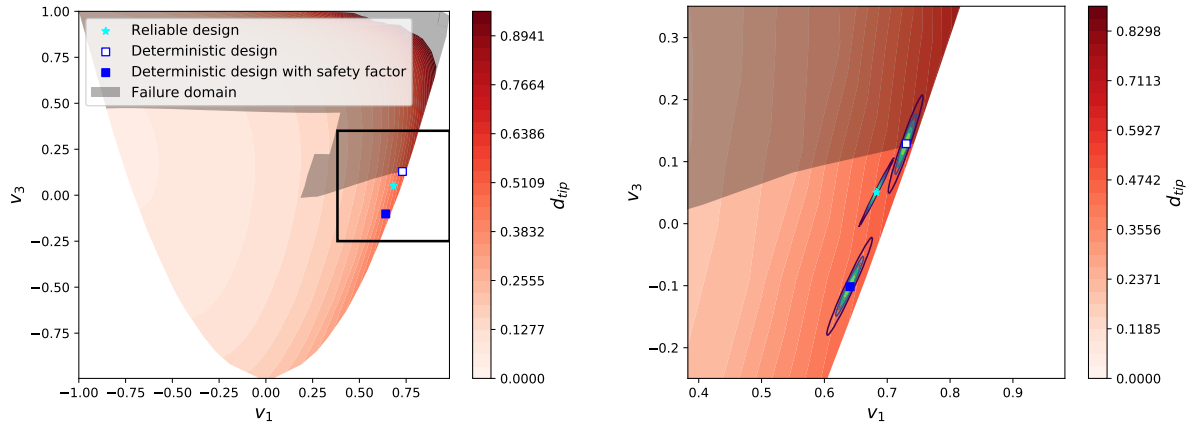

(a) 2D lamination parameters macroscopic space.

(b) Zoom around the final design with The joint PDF of the uncertainties associated to the different designs.

Figure 4.16: Comparison of the designs between RBDO and deterministic optimization with and without safety factor.

objective and constraints are evaluated according to a feasible stacking sequence.

In addition, we also impose a safety factor on the constraint for the deterministic case, such as the classical process of aeroelastic design. The different designs are shown in the 2D space in Figure 4.16 with the associated PDFs in Figure 4.15, the associated objectives, stacking sequences, and failure probabilities in Table 4.6. The reliable design outperforms the deterministic design with the safety factor showing the interest in going into RBDO process. Moreover, the variability of each design is represented in the 2D design in Figure 4.16b. The joint PDF of both deterministic designs are similar, whereas the one of the reliable design shows less variability but a higher correlation between v_1^D and v_3^D.

Type	Stacking sequence $\boldsymbol{\mu_\Theta}$	Objective d_{tip}	Failure probability
Deterministic	$[15, -15, 30, -30, -30, -15, 15, 30]_s$	0.54	0.52
Deterministic with safety factor	$[-30, 30, 15, -15, 15, -15, 45, -45]_s$	0.47	0
RBDO	$[0, -30, 30, 30, -30, 0, 30, -30]_s$	0.42	0.0005

Table 4.6: Results the different optimizations of the Figure 4.16.

4.5 Conclusion

In this chapter, the multi-scale approach, taking into account ply angle uncertainty, is applied to two problems: the composite plate optimization promoting the plate stiffness while remaining reliable to a buckling constraint and an aeroelastic optimization promoting the plate flexibility while remaining reliable with respect to the flutter phenomenon.

The proposed RBDO method has been tested and verified, compared to the direct RBDO using a genetic algorithm for the bucking analysis. In this first application, a computational time comparison can be made since the constraint is an analytical model. A computational gain is revealed, mostly when the score function approach is applied for the failure probability sensitivity. Additionally, the comparison of the methods to compute the probability gradients was performed (score function, centered finite differences, and the proposed hybrid approach). In the first application, the results converge to similar designs. However, for the aeroelastic application, the optimization path is close to the boundary limit of LP space, and the hybrid approach shows its efficiency since it converges, unlike the optimization using only the score function approach. The results shown an improvement in reliability compared to the deterministic optimized design for both cases. Furthermore, in the aeroelastic case, the results show enhanced performances with respect to a deterministic design where reliability is taken into account via a safety factor. However, the zone of convergence between the two types of optimization is similar.

In the end, we show the feasibility of our approach and illustrate it in test cases. The approach should stand out by considering a higher level of difficulty in the application case, where a reliability analysis throughout optimization will be of interest.

CONCLUSION AND PERSPECTIVES

Conclusion

In this work, reliability-based design optimization of composite laminates was performed with ply orientation uncertainty. The study of reliability during the optimization process focused on instabilities such as buckling and flutter. The main challenges were treating uncertainty on discrete design variables and dealing with the constraint response's discontinuity. Even if the strategy has been applied to academic test cases, the problems dealt with in this work are already representative of the ones encountered in more complex applications.

The new multi-scale approach developed in this manuscript is capable of taking into account the uncertainty of the ply orientations in a composite laminate RBDO framework. The benefit of the here-presented approach is that the optimization can converge faster to a reliable design compared to a direct method using a genetic algorithm. To achieve this, a gradient-based algorithm is exploited via the use of lamination parameters as design variables. However, the complex modeling of the uncertainties in the macroscopic lamination parameter's space motivated the process detailed in this work, inspired by the bi-level approach used in the deterministic framework. In fact, the new iterative methodology, which combines a macroscopic design space (with lamination parameters) and a mesoscopic design space (with ply angle), allows us to exploit the gradient information available analytically or provided by the simulation code (e.g., MSC Nastran). Nevertheless, one limit of this multi-scale approach concerns the inverse problem resolution step. This problem already poses difficulties in the deterministic case because of the multi-modal feature of this combinatorial optimization problem and the non-unicity of its solution. Moreover, since ply orientation follows some rules and can take only discrete values, a difference could present in the macroscopic response between the target and the retrieved stacking sequence. This error could be problematic for the convergence of our optimization. For example, if the difference in the lamination parameter space between the targeted LPs and the LPs of the retrieved stacking sequence is large enough to send the optimizer into the failure domain, the optimizer may struggle to come back to the safety domain.

However, in a variability framework, the inverse problem is solved as well as in the deterministic case, thanks to the use of Fourier Chaos Expansion metamodeling. With this metamodel, we have a precise description of LP statistics. Moreover, the computational cost to get the statistics is close to zero with the closed-form projection of the LP trigonometric functions into the basis. The advantage is that a database of expansion coefficients can be generated for each possible ply angle. The study made on the inverse problem in a variability

framework investigates on different possible formulations of the inverse problem. The variances and covariances of LPs can be exploited depending on the application. Considering the variances in the inverse problem may regularize the problem a bit more. In the end, the Fourier Chaos Expansion is a powerful tool to perform a more in-depth study on the inverse problem with ply orientation uncertainty.

The new multi-scale approach developed in this manuscript can also deal with a discontinuous instability constraint. The strategy proposed combining a classifier and classic surrogate models efficiently approximates the discontinuous quantity of interest. This is helpful in the reliability analysis of discontinuous constraint response with low computational time. However, the application of this strategy to approximate the flutter velocity of the plate shows some errors in the classifier. However, it is not impactful during the optimization since it is not a region of interest. For the sake of generality, this step should be improved. Active learning criteria could be used to enrich the classifier and the surrogate models in this critical area.

Concerning the probability sensitivity, the strategy of using a statistical test to know which method has to be used between the score function or the centered finite differences is quite suitable with lamination parameters since their variability cannot be modeled in all the design space. Depending on the application, the score function approach can be exploited instead of finite differences. For example, the study of a stacking sequence having a high number of plies tends to have a Gaussian distribution of the LPs (Kriegesmann, 2017). Therefore, the score function can be fully exploited, which could increase the interest in the methodology presented in this work regarding the computational time. However, in the aeroelastic case, we observe that we can struggle to compute the accurate probability sensitivity for the design points close to the compatibility constraint. Indeed, most of the time, the variability does not follow a gaussian shape, then the score function is cannot be used. Moreover, if the design point is very close to the limit of the domain, the perturbation made with the centered finite differences leads to inaccurate sensitivities. This is a limit of the approach if the optimizer passes through the limit of the LP domain.

The feasibility of the whole approach was conducted on two test cases with different objectives and constraints to analyze. The interest in going into the multi-scale strategy proposed in this work is shown in terms of computational time.

In a variable stiffness framework under uncertainty, we believe that a genetic algorithm is not suitable if design zones increase. However, this does not mean it will be straightforward with the multi-scale approach: the increase of LPs to design could be problematic in building the surrogate model for the reliability analysis since most of the surrogate models suffer from the curse of dimensionality.

In the aeroelastic application, we have performed deterministic optimization with a safety factor. The comparison shows interest in going into a reliability-based design optimization since optimization with a safety factor seems to oversize the design or lead the design to poor reliability, as mentioned in the introduction. With the RBDO approach, the impact of uncertainties is known through the optimization process with the information of the failure probability. However, in this case, the design converges in the same region that the deterministic design. Nevertheless, we believe that increasing the complexity of the application should lead to more distinguished designs between deterministic and reliability-based optimization.

In conclusion, this methodology handles the variability of LPs, which is quite complex. The global methodology could be applied to RBDO of other materials with different design scales, except the inverse problem with the FCE, which seems very specific to the LPs. But a classic

PCE could respond to the same objective for the inverse problem step.

However, better techniques could be exploited for some steps of this methodology. We detail some possible improvements below.

Perspectives

The first possible improvement, already mentioned above, which presents some limits, is the surrogate model for the reliability analysis. The classifier presents some errors around a high discontinuity area in the flutter velocity application (see Figure 3.10). Most of the surrogate techniques can not highlight this level of discontinuity. But a more deep comparison of the classification technique can be made. One promising technique that could improve our methodology is support vector machines (SVM). SVM constructs a hyperplane that separates data points into different classes and creates a so-called *margin* between the classes. This margin could be exploited when we have a *hump mode* in the flutter analysis. We could avoid the optimizer going toward this margin with a specific criterion to avoid the discontinuity region and a possible error on the actual flutter velocity value.

Another area of improvement is to exploit better the Kriging characteristic for reliability analysis. Some active learning criteria exploit the error given by the Kriging to enrich the design of experiments and the Kriging. It is applied to RBDO in Moustapha et al. (2016). However, this work explores the whole design during the optimization with a genetic algorithm. Therefore, the U-criterion of the active learning reliability method combining Kriging and Monte Carlo Simulation (AK-MCS) (Echard et al., 2011) was applied to the entire design space. In our case, the entire domain is not explored with the gradient-based algorithm used in the LP space. Therefore the surrogate model needs to be efficient only in the limit state function where the optimizer converges. Then, we could decrease the number of simulation calls to construct the surrogate with this kind of criteria. A surrogate model could be first built with a small DoE and, then, by using an AK-based criterion to enrich the surrogate model in the part of interest during the optimization.

Moreover, we first target a threshold failure probability of 1% for simplicity. In reality, we want to completely avoid the flutter phenomenon. In the future, a much smaller failure probability needs to be targeted around 10^{-6} or 10^{-7}. Therefore, Monte Carlo is no longer viable. The surrogate models need to be coupled with the importance sampling or subset sampling techniques to perform reliability analysis. Moreover, active learning criteria exist for small failure probabilities (Lelièvre et al., 2018; Xu et al., 2020).

In addition, we believe that considering a higher level of difficulty in the application case will further enhance the interest in the methodology. Increasing the complexity means going toward variable stiffness design with different design zones and the possibility of optimizing the thicknesses of each one, such as the Figure 4.17. This kind of application may lead to different local minimums and could further exhibit the advantage of applying our multi-scale RBDO approach. The variable stiffness formulation problem will increase the complexity for two points: the inverse problem resolution and the construction of the surrogate model for the reliability analysis. Firstly, the inverse problem resolution has to handle different zones and target thicknesses. The Stacking Sequence Table formulation already used in this work could handle this, considering design constraints coming from the manufacturer. Secondly, the surrogate model needs to bear the increase of dimension coming from the different design zones (i.e., input parameters). Moreover, the constraint response will now depend on the thickness, increasing the dimension of the surrogate model as well. If the dimension rises too much,

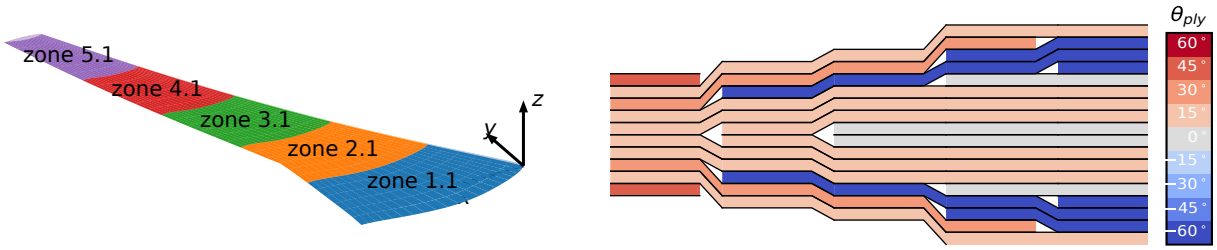

Figure 4.17: Structural test case of interest in a variable stiffness framework (Fabbiane et al., 2022).

another type of surrogate modeling or a technique that reduces the dimension of the problem for instance (Constantine et al., 2014).

Finally, the choice of the optimizer can be criticized. The MMA algorithm seems to have a slow convergence. Still, it has been chosen because, with the tuning of parameters, the subproblem created at each iteration tends to stay in the feasible region of the LPs (i.e., the inverse problem resolution does not make a huge error). One possible way to reduce the number of iterations and, therefore, the computational time is to investigate whether using another gradient-based algorithm, such as SQP, is compatible with our methodology.

APPENDIX A

ORTHONORMAL FOURIER BASIS

The objective of this appendix is to better detail the derivations of the Fourier basis used for Fourier Chaos Expansion for a Gaussian random variable.

A.1 Expectations of useful random trigonometric functions

Some useful expected expressions of trigonometric functions are recalled below. Given that $x \sim \mathcal{N}(\mu, \sigma^2)$ and using Mathematica, the integral corresponding to the expectation of $\sin(aX)$ and $\cos(aX)$ can be explicitly computed.

$$\mathbb{E}\left[\cos(aX)\right] = \cos(a\mu)w, \tag{A.1}$$
$$\mathbb{E}\left[\sin(aX)\right] = \sin(a\mu)w, \tag{A.2}$$

with $a \in \mathbb{R}$ and $w = \exp(-0.5a^2\sigma^2)$.
Since, $\cos(kx) = \frac{1}{2}\left(e^{ikx} + e^{-ikx}\right)$ and $\sin(lx) = \frac{1}{2}\left(ie^{-ilx} - ie^{ilx}\right)$, we can write the product of the trigonometric functions $\cos(kx)$ and $\sin(lx)$ as:

$$\cos(kx)\sin(lx) = \frac{1}{4}\left(ie^{i(k-l)x} + ie^{-i(k+l)x} - ie^{i(k+l)x} - ie^{i(l-k)x}\right). \tag{A.3}$$

Since the part of interest is only on the real part, the Eq.(A.3) can be written as the Eq.(A.5), and its expected value as the Eq.(A.5) using the Eq.(A.2) and Eq.(A.1).

$$\cos(kx)\sin(lx) = -0.5\ \sin((k-l)x) + 0.5\ \sin((k+l)X), \tag{A.4}$$
$$\mathbb{E}[\cos(kX)\sin(lX)] = -0.5\ \mathbb{E}[\sin((k-l)X)] + 0.5\ \mathbb{E}[\sin((k+l)X)]. \tag{A.5}$$

With the same idea:

$$\mathbb{E}[\cos(kX)\cos(lX)] = 0.5\ \mathbb{E}[\cos((l-k)X)] + 0.5\ \mathbb{E}[\cos((k+l)X)], \tag{A.6}$$
$$\mathbb{E}[\sin(kX)\sin(lX)] = 0.5\ \mathbb{E}[\cos((l-k)X)] - 0.5\ \mathbb{E}[\cos((k+l)X)]. \tag{A.7}$$

Moreover, given $\sin^2(x) = \frac{1-\cos(2x)}{2}$, $\cos^2(x) = \frac{1+\cos(2x)}{2}$, we can write:

$$\mathbb{E}\left[\sin^2(aX)\right] = 0.5 - 0.5\ \mathbb{E}\left[\cos(2aX)\right], \tag{A.8}$$
$$\mathbb{E}\left[\cos^2(aX)\right] = 0.5 + 0.5\ \mathbb{E}\left[\cos(2aX)\right]. \tag{A.9}$$

u_0	1
u_1	$\sin(X)$
u_2	$\cos(X)$
u_3	$\sin(2X)$
u_4	$\cos(2X)$
u_5	$\sin(3X)$
u_6	$\cos(3X)$

Table A.1: Set of Fourier polynomials to be orthogonalized

A.2 Fourier basis construction for a Gaussian random variable with zero mean

In the following, the one-dimensional Fourier chaos basis is constructed. A single random variable X is considered following a normal distribution, $X \sim \pi_X = \mathcal{N}(0, \sigma^2)$. We recall the Gram-Schmidt algorithm that calculates the coefficients of the polynomials using the inner product to ensure that each polynomial is orthogonal to all of its predecessors:

$$\begin{aligned} \psi_0(X) &= 1, \\ \psi_i(X) &= u_i(X) - \sum_{k=0}^{i-1} C_{ik}\psi_k(X), \end{aligned} \tag{A.10}$$

where u_i are the set of Fourier polynomials $(\cos(nX),\ \sin(nX))$ with $n \in \mathbb{N}$ and deterministic quantities C_{ik} must be computed as:

$$C_{ik} = \frac{\mathbb{E}\left[u_i(X)\psi_k(X)\right]}{\mathbb{E}\left[\psi_k(X)\psi_k(X)\right]}. \tag{A.11}$$

Now the orthonormal basis can be constructed using Eq.(A.10) and Eq.(A.11) with the set of Fourier polynomials in Table A.1. A zero mean in the random variable will vanish some terms during the derivation of the basis. Here is the detailed construction of the orthonormal basis function construction $\psi_i^{\mathrm{n}}(X)$:

The Fourier basis function $\psi_0^{\mathrm{n}}(X)$ is equal to:

$$\begin{aligned} \psi_0 &= u_0 = 1, \\ \psi_0^n &= 1. \end{aligned} \tag{A.12}$$

The Fourier basis function $\psi_1^{\mathrm{n}}(X)$ is computed as follows:

$$\psi_1(X) = u_1 - \frac{\mathbb{E}\left[u_1\psi_0\right]}{\mathbb{E}\left[\psi_0^2\right]}\psi_0 = \sin(X) - \mathbb{E}\left[\sin(X)\right]. \tag{A.13}$$

The expected value can be computed with Eq.(A.2). With a zero mean in the random variable, the expected value of the sinus function is equal to zero. Therefore:

$$\psi_1 = \sin(X), \tag{A.14}$$

and can be normalized as:

$$\psi_1^n = Z_{11}\sin(X), \quad \text{with} \quad Z_{11} = \frac{1}{\sqrt{\mathbb{E}\left[\sin(X)^2\right]}}, \tag{A.15}$$

which can be computed with the Eq.(A.8).
The Fourier basis function $\psi_2^{\mathrm{n}}(X)$ is computed as follows:

$$\begin{aligned}\psi_2 &= u_2 - \frac{\mathbb{E}\left[u_2\psi_0\right]}{\mathbb{E}\left[\psi_0^2\right]}\psi_0 - \frac{\mathbb{E}\left[u_2\psi_1\right]}{\mathbb{E}\left[\psi_1^2\right]}\psi_1 \\ &= \cos(X) - \mathbb{E}\left[\cos(X)\right] - \frac{\mathbb{E}\left[\cos(X)\sin(X)\right]}{\mathbb{E}\left[\sin(X)^2\right]}\psi_1 \\ &= \cos(X) - C_{20} - C_{21}\psi_1.\end{aligned} \tag{A.16}$$

The expected values can be computed with Eq.(A.1), Eq.(A.5), and Eq.(A.2). With a zero mean in the random variable, the expected value of the product between sinus and cosinus functions is equal to 0. Therefore:

$$\psi_2 = \cos(X) - C_{20}, \tag{A.17}$$

and can be normalized as:

$$\psi_2^{\mathrm{n}} = Z_{21}(\cos(X) - C_{20}), \quad \text{with} \quad Z_{21} = \frac{1}{\sqrt{\mathbb{E}\left[(\cos(X) - C_{20})^2\right]}}, \tag{A.18}$$

which can be computed with Eq.(A.9) and Eq.(A.1).

The Fourier basis function $\psi_3^{\mathrm{n}}(X)$ is computed as follows:

$$\begin{aligned}\psi_3 &= u_3 - \frac{\mathbb{E}\left[u_3\psi_0\right]}{\mathbb{E}\left[\psi_0^2\right]}\psi_0 - \frac{\mathbb{E}\left[u_3\psi_1\right]}{\mathbb{E}\left[\psi_1^2\right]}\psi_1 - \frac{\mathbb{E}\left[u_3\psi_2\right]}{\mathbb{E}\left[\psi_2^2\right]}\psi_2 \\ &= \sin(2X) - \mathbb{E}\left[\sin(2X)\right] - \frac{\mathbb{E}\left[\sin(2X)\sin(X)\right]}{\mathbb{E}\left[\sin(X)^2\right]}\psi_1 - \frac{\mathbb{E}\left[\sin(2X)(\cos(X) - C_{20})\right]}{\mathbb{E}\left[(\cos(X) - C_{20})^2\right]}\psi_2 \\ &= \sin(2X) - C_{30} - C_{31}\psi_1 - C_{32}\psi_2.\end{aligned} \tag{A.19}$$

C_{30} and C_{32} are equal to 0. Therefore:

$$\psi_3 = \sin(2X) - C_{31}\sin(X), \tag{A.20}$$

and can be normalized as:

$$\psi_3^{\mathrm{n}} = Z_{31}(\sin(2X) - C_{31}\sin(X)), \tag{A.21}$$

with:

$$\begin{aligned}\psi_3^2 &= C_{31}^2\sin^2(X) - 2C_{31}\sin(X)\sin(2X) + \sin^2(2X) \\ Z_{31} &= \frac{1}{\sqrt{\mathbb{E}\left[\psi_3^2\right]}} \\ \mathbb{E}\left[\psi_3^2\right] &= C_{31}^2\mathbb{E}\left[\sin^2(X)\right] - 2C_{31}\mathbb{E}\left[\sin(X)\sin(2X)\right] + \mathbb{E}\left[\sin^2(2X)\right].\end{aligned} \tag{A.22}$$

The Fourier basis function $\psi_4^{\mathrm{n}}(X)$ is computed as follows:

$$\begin{aligned}\psi_4 &= u_4 - \frac{\mathbb{E}\left[u_4\psi_0\right]}{\mathbb{E}\left[\psi_0^2\right]}\psi_0 - \frac{\mathbb{E}\left[u_4\psi_1\right]}{\mathbb{E}\left[\psi_1^2\right]}\psi_1 - \frac{\mathbb{E}\left[u_4\psi_2\right]}{\mathbb{E}\left[\psi_2^2\right]}\psi_2 - \frac{\mathbb{E}\left[u_4\psi_3\right]}{\mathbb{E}\left[\psi_3^2\right]}\psi_3 \\ &= \cos(2X) - \mathbb{E}\left[\cos(2X)\right] - \frac{\mathbb{E}\left[\cos(2X)\sin(X)\right]}{\mathbb{E}\left[\sin(X)^2\right]}\psi_1 - \frac{\mathbb{E}\left[\cos(2X)(\cos(X) - C_{20})\right]}{\mathbb{E}\left[(\cos(X) - C_{20})^2\right]}\psi_2 \\ &- \frac{\mathbb{E}\left[\cos(2X)(\sin(2X) - C_{31}\sin(X))\right]}{\mathbb{E}\left[(\sin(2X) - C_{31}\sin(X))^2\right]}\psi_3 \\ &= \cos(2X) - C_{40} - C_{41}\psi_1 - C_{42}\psi_2 - C_{43}\psi_3.\end{aligned} \tag{A.23}$$

C_{41} and C_{43} are equal to 0. Therefore:

$$\begin{aligned}\psi_4 &= \cos(2X) - C_{40} - C_{42}(\cos(X) - C_{20}) \\ \psi_4 &= \cos(2X) - C_{42}\cos(X) - \underbrace{C_{40} + C_{42}C_{20}}_{D_{43}},\end{aligned} \tag{A.24}$$

and can be normalized as:

$$\psi_4^{\mathrm{n}} = Z_{41}(\cos(2X) - C_{42}\cos(X) - D_{43}), \tag{A.25}$$

with:

$$\begin{aligned}\psi_4^2 &= C_{42}^2\cos^2(X) + 2C_{42}D_{43}\cos(X) - 2C_{42}\cos(X)\cos(2X) - 2D_{43}\cos(2X) \\ &\quad + \cos^2(2X) + D_{43}^2 \\ Z_{41} &= \frac{1}{\sqrt{\mathbb{E}\left[\psi_4^2\right]}} \\ \mathbb{E}\left[\psi_4^2\right] &= C_{42}^2\mathbb{E}\left[\cos^2(X)\right] + 2C_{42}D_{43}\mathbb{E}\left[\cos(X)\right] - 2C_{42}\mathbb{E}\left[\cos(X)\cos(2X)\right] \\ &\quad - 2D_{43}\mathbb{E}\left[\cos(2X)\right] + \mathbb{E}\left[\cos^2(2X)\right] + D_{43}^2.\end{aligned} \tag{A.26}$$

The Fourier basis function $\psi_5^{\mathrm{n}}(X)$ is computed as follows:

$$\begin{aligned}\psi_5 &= u_5 - \frac{\mathbb{E}\left[u_5\psi_0\right]}{\mathbb{E}\left[\psi_0^2\right]}\psi_0 - \frac{\mathbb{E}\left[u_5\psi_1\right]}{\mathbb{E}\left[\psi_1^2\right]}\psi_1 - \frac{\mathbb{E}\left[u_5\psi_2\right]}{\mathbb{E}\left[\psi_2^2\right]}\psi_2 - \frac{\mathbb{E}\left[u_5\psi_3\right]}{\mathbb{E}\left[\psi_3^2\right]}\psi_3 - \frac{\mathbb{E}\left[u_5\psi_4\right]}{\mathbb{E}\left[\psi_4^2\right]}\psi_4 \\ &= \sin(3X) - \mathbb{E}\left[\sin(3X)\right] - \frac{\mathbb{E}\left[\sin(3X)\sin(X)\right]}{\mathbb{E}\left[\sin(X)^2\right]}\psi_1 - \frac{\mathbb{E}\left[\sin(3X)(\cos(X) - C_{20})\right]}{\mathbb{E}\left[(\cos(X) - C_{20})^2\right]}\psi_2 \\ &- \frac{\mathbb{E}\left[\sin(3X)(\sin(3X) - C_{31}\sin(X))\right]}{\mathbb{E}\left[(\sin(2X) - C_{31}\sin(X))^2\right]}\psi_3 - \frac{\mathbb{E}\left[\sin(3X)(\cos(2X) - C_{42}\cos(X) - D_{43})\right]}{\mathbb{E}\left[(\cos(2X) - C_{42}\cos(X) - D_{43})^2\right]}\psi_4 \\ &= \sin(3X) - C_{50} - C_{51}\psi_1 - C_{52}\psi_2 - C_{53}\psi_3 - C_{54}\psi_4.\end{aligned} \tag{A.27}$$

C_{50}, C_{52} and C_{54} are equal to 0. Therefore:

$$\begin{aligned}\psi_5 &= \sin(3X) - C_{51}\sin(X) - C_{53}(\sin(2X) - C_{31}\sin(X)) \\ \psi_5 &= \sin(3X) - C_{53}\sin(2X) - \underbrace{(C_{proj15} - C_{proj35}C_{proj13})}_{D_{53}}\sin(X),\end{aligned} \tag{A.28}$$

and can be normalized as:

$$\psi_5^{\mathrm{n}} = Z_{51}(\sin(3X) - C_{53}\sin(2X) - D_{53}), \tag{A.29}$$

with:

$$\begin{aligned}\psi_5^2 &= C_{53}^2\sin^2(2X) + 2C_{53}D_{53}\sin(X)\sin(2X) - 2C_{35}\sin(2X)\sin(3X) + D_{53}^2\sin^2(X) \\ &\quad - 2D_{53}\sin(X)\sin(3X) + \sin^2(3X) \\ Z_{51} &= \frac{1}{\sqrt{\mathbb{E}\left[\psi_5^2\right]}} \\ \mathbb{E}\left[\psi_5^2\right] &= C_{53}^2\mathbb{E}\left[\sin^2(2X)\right] + 2C_{53}D_{53}\mathbb{E}\left[\sin(X)\sin(2X)\right] - 2C_{35}\mathbb{E}\left[\sin(2X)\sin(3X)\right] \\ &\quad + D_{53}^2\mathbb{E}\left[\sin^2(X)\right] - 2D_{53}\mathbb{E}\left[\sin(X)\sin(3X)\right] + \mathbb{E}\left[\sin^2(3X)\right].\end{aligned} \tag{A.30}$$

The Fourier basis function $\psi_6^{\mathrm{n}}(X)$ is computed as follows:

$$\begin{aligned}
\psi_6 &= u_6 - \frac{\mathbb{E}\left[u_6\psi_0\right]}{\mathbb{E}\left[\psi_0^2\right]}\psi_0 - \frac{\mathbb{E}\left[u_6\psi_1\right]}{\mathbb{E}\left[\psi_1^2\right]}\psi_1 - \frac{\mathbb{E}\left[u_6\psi_2\right]}{\mathbb{E}\left[\psi_2^2\right]}\psi_2 - \frac{\mathbb{E}\left[u_6\psi_3\right]}{\mathbb{E}\left[\psi_3^2\right]}\psi_3 - \frac{\mathbb{E}\left[u_6\psi_4\right]}{\mathbb{E}\left[\psi_4^2\right]}\psi_4 - \frac{\mathbb{E}\left[u_6\psi_5\right]}{\mathbb{E}\left[\psi_5^2\right]}\psi_5 \\
&= \cos(3X) - \mathbb{E}\left[\cos(3X)\right] - \frac{\mathbb{E}\left[\cos(3X)\sin(X)\right]}{\mathbb{E}\left[\sin(X)^2\right]}\psi_1 - \frac{\mathbb{E}\left[\cos(3X)(\cos(X) - C_{20})\right]}{\mathbb{E}\left[(\cos(X) - C_{20})^2\right]}\psi_2 \\
&- \frac{\mathbb{E}\left[\cos(3X)(\sin(3X) - C_{31}\sin(X))\right]}{\mathbb{E}\left[(\sin(2X) - C_{31}\sin(X))^2\right]}\psi_3 - \frac{\mathbb{E}\left[\cos(3X)(\cos(2X) - C_{42}\cos(X) - D_{43})\right]}{\mathbb{E}\left[(\cos(2X) - C_{42}\cos(X) - D_{43})^2\right]}\psi_4 \\
&- \frac{\mathbb{E}\left[\cos(3X)(\sin(3X) - C_{53}\sin(2X) - D_{53})\right]}{\mathbb{E}\left[(\sin(3X) - C_{53}\sin(2X) - D_{53})^2\right]}\psi_5 \\
&= \cos(3X) - C_{60} - C_{61}\psi_1 - C_{62}\psi_2 - C_{63}\psi_3 - C_{64}\psi_4 - C_{65}\psi_5.
\end{aligned} \tag{A.31}$$

C_{61}, C_{63} and C_{65} are equal to 0. Therefore:

$$\begin{aligned}
\psi_6 &= \cos(3X) - C_{60} - C_{62}(\cos(X) - C_{20}) - C_{64}(\cos(2X) - C_{42}\cos(X) - D_{43}) \\
\psi_6 &= \cos(3X) - C_{64}\cos(2X) - \underbrace{(C_{62} - C_{64}C_{42})}_{D_{63}}\cos(X) - \underbrace{C_{60} + C_{62}C_{20} + C_{64}D_{43}}_{D_{64}},
\end{aligned} \tag{A.32}$$

and can be normalized as:

$$\psi_6^{\mathrm{n}} = Z_{61}(\cos(3x) - C_{64}\cos(2x) - D_{63}\cos(x) - D_{64}), \tag{A.33}$$

with:

$$\begin{aligned}
\psi_6^2 &= C_{64}^2\cos^2(2X) + 2C_{64}D_{63}\cos(X)\cos(2X) + 2C_{64}D_{64}\cos(2X) \\
&- 2C_{64}\cos(2X)\cos(3X) + D_{63}^2\cos^2(X) + 2D_{63}D_{64}\cos(X) - 2D_{63}\cos(X)\cos(3X) \\
&+ D_{64}^2 - 2D_{64}\cos(3X) + \cos^2(3X) \\
Z_{61} &= \frac{1}{\sqrt{\mathbb{E}\left[\psi_6^2\right]}} \\
\mathbb{E}\left[\psi_6^2\right] &= C_{64}^2\mathbb{E}\left[\cos^2(2X)\right] + 2C_{64}D_{63}\mathbb{E}\left[\cos(X)\cos(2X)\right] + 2C_{64}D_{64}\mathbb{E}\left[\cos(2X)\right] \\
&- 2C_{64}\mathbb{E}\left[\cos(2X)\cos(3X)\right] + D_{63}^2\mathbb{E}\left[\cos^2(X)\right] + 2D_{63}D_{64}\mathbb{E}\left[\cos(X)\right] \\
&- 2D_{63}\mathbb{E}\left[\cos(X)\cos(3X)\right] + D_{64}^2 - 2D_{64}\mathbb{E}\left[\cos(3X)\right] + \mathbb{E}\left[\cos^2(3X)\right].
\end{aligned} \tag{A.34}$$

All the expected values including trigonometric functions can be computed with the formulas in Section A.1. An example of orthonormal basis is shown in Table A.2 for a Gaussian random variable $X \sim \pi_X = \mathcal{N}(0, 1)$.

Basis number	Fourier chaos polynomials $\psi_i^{\mathrm{n}}(X)$	
0	1	
1	1.520866623178815 $\sin(X)$	
2	2.2372529142129274 $\cos(X)$	-1.3569624860015785
3	1.8416989294907935 $\sin(2X)$	-1.2682227207889896 $\sin(X)$
4	2.1103613976186137 $\cos(2X)$	-2.394998456392556 $\cos(X)$
	$+1.167033636288187$	
5	1.939600268597864 $\sin(3X)$	-1.6893282147139512 $\sin(2X)$
	$+0.8604687025094444$ $\sin(X)$	
6	2.038695558018769 $\cos(3X)$	-2.110329605605427 $\cos(2X)$
	$+1.7715068841454853$ $\cos(X)$	-0.8115190461255738

Table A.2: Example of an orthonormal Fourier basis with 6 functions for a Gaussian random variable.

BIBLIOGRAPHY

(2014). MSC nastran - aeroelastic analysis user's guide.

Abouhamze, M. and Shakeri, M. (2007). Multi-objective stacking sequence optimization of laminated cylindrical panels using a genetic algorithm and neural networks. *Composite Structures*, 81(2):253–263.

Acar, E., Bayrak, G., Jung, Y., Lee, I., Ramu, P., and Ravichandran, S. S. (2021). Modeling, analysis, and optimization under uncertainties: a review. *Structural and Multidisciplinary Optimization*, 64(5):2909–2945.

Adali, S., Lene, F., Duvaut, G., and Chiaruttini, V. (2003). Optimization of laminated composites subject to uncertain buckling loads. *Composite Structures*, 62(3):261–269.

Adams, D. B., Watson, L. T., Gürdal, Z., and Anderson-Cook, C. M. (2004). Genetic algorithm optimization and blending of composite laminates by locally reducing laminate thickness. *Advances in Engineering Software*, 35(1):35–43.

Administration, F. A. (2014). Aeroelastic stability substantiation of transport category airplanes. advisory circular 25.629-1b.

Albano, E. and Rodden, W. P. (1969). A doublet-lattice method for calculating lift distributions on oscillating surfaces in subsonic flows. *AIAA Journal*, 7(2):279–285.

Albazzan, M. A., Harik, R., Tatting, B. F., and Gürdal, Z. (2019). Efficient design optimization of nonconventional laminated composites using lamination parameters: A state of the art. *Composite Structures*, 209:362–374.

Allemang, R. J. (2003). The modal assurance criterion – twenty years of use and abuse. *SOUND AND VIBRATION*, page 8.

Alpu, O. and Yuksek, D. (2016). Comparison of some multivariate normality tests: A simulation study. *International Journal of Advanced and Applied Sciences*, 3(12):73–85.

Andrieu, C. and Andrieu, C. (2003). An introduction to MCMC for machine learning. page 39.

António, C. A. C., Marques, A. T., and Gonçalves, J. F. (1996). Reliability based design with a degradation model of laminated composite structures. *Structural Optimization*, 12(1):16–28.

António, C. C. and Hoffbauer, L. N. (2009). An approach for reliability-based robust design optimisation of angle-ply composites. *Composite Structures*, 90(1):53–59.

Aoues, Y. and Chateauneuf, A. (2010). Benchmark study of numerical methods for reliability-based design optimization. *Structural and Multidisciplinary Optimization*, 41(2):277–294.

Asmussen, S. and Glynn, P. W. (2007). *Stochastic simulation: algorithms and analysis*. Number 57 in Stochastic modelling and applied probability. Springer.

Au, S.-K. and Beck, J. L. (2001). Estimation of small failure probabilities in high dimensions by subset simulation. *Probabilistic Engineering Mechanics*, 16(4):263–277.

Bailie, J. A., Ley, R. P., and Pasricha, A. (1997). A summary and review of composite lamiante design guidelines.

Balabanov, V., Weckner, O., Epton, M., Mabson, G., Cregger, S., and Blom, A. (2012). Optimal design of a composite sandwich structure using lamination parameters. In *53rd AIAA/ASME/ASCE/AHS/ASC Structures, Structural Dynamics and Materials Conference*, Structures, Structural Dynamics, and Materials and Co-located Conferences. American Institute of Aeronautics and Astronautics.

Balesdent, M., Morio, J., and Marzat, J. (2013). Kriging-based adaptive importance sampling algorithms for rare event estimation. *Structural Safety*, 44:1–10.

Baudin, M., Dutfoy, A., Iooss, B., and Popelin, A.-L. (2016). OpenTURNS: An industrial software for uncertainty quantification in simulation. In Ghanem, R., Higdon, D., and Owhadi, H., editors, *Handbook of Uncertainty Quantification*, pages 1–38. Springer International Publishing.

Beck, A. T. and Gomes, W. J. d. S. (2012). A comparison of deterministic, reliability-based and risk-based structural optimization under uncertainty. *Probabilistic Engineering Mechanics*, 28:18–29.

Beran, P., Stanford, B., and Schrock, C. (2017). Uncertainty quantification in aeroelasticity. *Annual Review of Fluid Mechanics*, 49(1):361–386.

Bichon, B. J., Eldred, M. S., Swiler, L. P., Mahadevan, S., and McFarland, J. M. (2008). Efficient global reliability analysis for nonlinear implicit performance functions. *AIAA Journal*, 46(10):2459–2468.

Bjerager Peter and Krenk Steen (1989). Parametric sensitivity in first order reliability theory. *Journal of Engineering Mechanics*, 115(7):1577–1582.

Blatman, G. and Sudret, B. (2010). An adaptive algorithm to build up sparse polynomial chaos expansions for stochastic finite element analysis. *Probabilistic Engineering Mechanics*, 25(2):183–197.

Blatman, G., Sudret, B., and Division, D. (2008). Adaptive sparse polynomial chaos expansions - application to structural reliability.

Bloomfield, M., Diaconu, C., and Weaver, P. (2009). On feasible regions of lamination parameters for lay-up optimization of laminated composites. *Proceedings of the Royal Society A: Mathematical, Physical and Engineering Sciences*, 465(2104):1123–1143.

Bloomfield, M., Herencia, J., and Weaver, P. (2008). Optimisation of anisotropic composite plates incorporating non-conventional ply orientations. In *49th AIAA/ASME/ASCE/AHS/ASC Structures, Structural Dynamics, and Materials Conference
 16th AIAA/ASME/AHS Adaptive Structures Conference
 10t.* American Institute of Aeronautics and Astronautics.

Bompard, M. (2011). Modèles de substitution pour l'optimisation globale de forme en aérodynamique et méthode locale sans pramétrisation. page 176.

Bordogna, M. T., Lancelot, P., Bettebghor, D., and De Breuker, R. (2020). Static and dynamic aeroelastic tailoring with composite blending and manoeuvre load alleviation. *Structural and Multidisciplinary Optimization*, 61(5):2193–2216.

Bourinet, J.-M. (2016). Rare-event probability estimation with adaptive support vector regression surrogates. *Reliability Engineering & System Safety*, 150:210–221.

Bourinet, J.-M., Deheeger, F., and Lemaire, M. (2011). Assessing small failure probabilities by combined subset simulation and support vector machines. *Structural Safety*, 33(6):343–353.

Boyer, C. (1997). Design of a composite structure to achieve a specified reliability level. *Reliability Engineering and System Safety*, page 11.

Breitung, K. (1989). Asymptotic approximations for probability integrals. *Prob. Eng. Mech*, 4:187–190.

Bucher, C. and Bourgund, U. (1990). A fast and efficient response surface approach for structural reliability problems. *Structural Safety*, 7(1):57–66.

C. K. I. Williams and D. Barber (1998). Bayesian classification with gaussian processes. *IEEE Transactions on Pattern Analysis and Machine Intelligence*, 20(12):1342–1351.

Callahan, K. J. and Weeks, G. E. (1992). Optimum design of composite laminates using genetic algorithms. *Composites Engineering*, 2(3):149–160.

Catapano, A., Desmorat, B., and Vannucci, P. (2015). Stiffness and strength optimization of the anisotropy distribution for laminated structures. *Journal of Optimization Theory and Applications*, 167(1):118–146.

Chabridon, V. (2018). Reliability-oriented sensitivity analysis under probabilistic model uncertainty – application to aerospace systems.

Chassaing, J.-C., Lucor, D., and Trégon, J. (2012). Stochastic nonlinear aeroelastic analysis of a supersonic lifting surface using an adaptive spectral method. *Journal of Sound and Vibration*, 331(2):394–411.

Chassaing, J.-C., Nitschke, C., Vincenti, A., Cinnella, P., and Lucor, D. (2018). Advances in parametric and model-form uncertainty quantification in canonical aeroelastic systems. *AerospaceLab Journal*, Issue 14:19 pages.

Chen, X., Hasselman, T., Neill, D., Chen, X., Hasselman, T., and Neill, D. (1997). Reliability based structural design optimization for practical applications. In *38th Structures, Structural Dynamics, and Materials Conference*, Structures, Structural Dynamics, and Materials and Co-located Conferences. American Institute of Aeronautics and Astronautics.

Chiachio, M., Chiachio, J., and Rus, G. (2012). Reliability in composites – a selective review and survey of current development. *Composites Part B: Engineering*, 43(3):902–913.

Chun, J. (2021). Reliability-based design optimization of structures using complex-step approximation with sensitivity analysis. *Applied Sciences*, 11(10):4708.

Conceição António, C. (2001). A hierarchical genetic algorithm for reliability based design of geometrically non-linear composite structures. *Composite Structures*, 54(1):37–47.

Conceição António, C. and Hoffbauer, L. N. (2017). Reliability-based design optimization and uncertainty quantification for optimal conditions of composite structures with non-linear behavior. *Engineering Structures*, 153:479–490.

Constantine, P. G., Dow, E., and Wang, Q. (2014). Active subspace methods in theory and practice: applications to kriging surfaces. *SIAM Journal on Scientific Computing*, 36(4):A1500–A1524.

Der Kiureghian, A. and Dakessian, T. (1998). Multiple design points in first and second-order reliability. *Structural Safety*, 20(1):37–49.

Di Sciuva, M., Gherlone, M., and Lomario, D. (2003). Multiconstrained optimization of laminated and sandwich plates using evolutionary algorithms and higher-order plate theories. *Composite Structures*, 59(1):149–154.

Diaconu, C. G. and Sekine, H. (2004). Layup optimization for buckling of laminated composite shells with restricted layer angles. *AIAA Journal*, 42(10):2153–2163.

Ditlevsen, O. and Madsen, H. O. (2007). *Structural reliability methods*. Wiley.

Doh, J., Kim, Y., and Lee, J. (2018). Reliability-based robust design optimization of gap size of annular nuclear fuels using kriging and inverse distance weighting methods. *Engineering Optimization*, 50(12):2161–2176.

Du, X. and Chen, W. (2004). Sequential optimization and reliability assessment method for efficient probabilistic design. *Journal of Mechanical Design*, 126(2):225–233.

Dubourg, V. (2011). Adaptive surrogate models for reliability analysis and reliability-based design optimization. page 309.

Dubourg, V., Sudret, B., and Bourinet, J.-M. (2011). Reliability-based design optimization using kriging surrogates and subset simulation. *Structural and Multidisciplinary Optimization*, 44(5):673–690.

Díaz, J., Cid Montoya, M., and Hernández, S. (2016). Efficient methodologies for reliability-based design optimization of composite panels. *Advances in Engineering Software*, 93:9–21.

Echard, B., Gayton, N., and Lemaire, M. (2011). AK-MCS: An active learning reliability method combining kriging and monte carlo simulation. *Structural Safety*, 33(2):145–154.

Erdal, O. and Sonmez, F. O. (2005). Optimum design of composite laminates for maximum buckling load capacity using simulated annealing. *Composite Structures*, 71(1):45–52.

Fabbiane, N., Irisarri, F.-X., Dillinger, J., and Lepage, A. (2022). Aeroelastic-tailoring of a wind-tunnel model for passive alleviation of static and dynamic loads. *CEAS Aeronautical Journal*.

Fukunaga, H. and Sekine, H. (1992). Stiffness design method of symmetric laminates using lamination parameters. *AIAA Journal*, 30(11):2791–2793.

Gantovnik, V. B. and Gu, Z. (2002). A genetic algorithm with memory for optimal design of laminated sandwich composite panels. *Composite Structures*, page 8.

Gautschi, W. (2004). *Orthogonal polynomials: computation and approximation*. Numerical mathematics and scientific computation. Oxford University Press.

Gayton, N., Bourinet, J., and Lemaire, M. (2003). CQ2rs: a new statistical approach to the response surface method for reliability analysis. *Structural Safety*, 25(1):99–121.

Genovese, K., Lamberti, L., and Pappalettere, C. (2005). Improved global–local simulated annealing formulation for solving non-smooth engineering optimization problems. *International Journal of Solids and Structures*, 42(1):203–237.

Gentle, J. (2003). *Random number generation and Monte Carlo methods*. Springer Science+Business Media, second ed. statistics and computing edition.

Ghasemi, H., Rafiee, R., Zhuang, X., Muthu, J., and Rabczuk, T. (2014). Uncertainties propagation in metamodel-based probabilistic optimization of CNT/polymer composite structure using stochastic multi-scale modeling. *Computational Materials Science*, 85:295–305.

Ghiasi, H., Fayazbakhsh, K., Pasini, D., and Lessard, L. (2010). Optimum stacking sequence design of composite materials part II: Variable stiffness design. *Composite Structures*, 93(1):1–13.

Ghiasi, H., Pasini, D., and Lessard, L. (2009). Optimum stacking sequence design of composite materials part i: Constant stiffness design. *Composite Structures*, 90(1):1–11.

Grenestedt, J. and Gudmundson, P. (1993). Layup optimization of composite material structures. In PEDERSEN, P., editor, *Optimal Design with Advanced Materials*, pages 311–336. Elsevier.

Hasofer Abraham M. and Lind Niels C. (1974). Exact and invariant second-moment code format. *Journal of the Engineering Mechanics Division*, 100(1):111–121.

Hassig, H. J. (1971). An approximate true damping solution of the flutter equation by determinant iteration. *Journal of Aircraft*, 8(11):885–889.

Herencia, J. E., Weaver, P. M., and Friswell, M. I. (2007). Optimization of long anisotropic laminated fiber composite panels with t-shaped stiffeners. *AIAA Journal*, 45(10):2497–2509.

Hollowell, S. and Dugundji, J. (1982). Aeroelastic flutter and divergence of stiffness coupled, graphite/epoxy, cantilevered plates. In *23rd Structures, Structural Dynamics and Materials Conference*. American Institute of Aeronautics and Astronautics.

Huang, X., Chen, J., and Zhu, H. (2016). Assessing small failure probabilities by AK–SS: An active learning method combining kriging and subset simulation. *Structural Safety*, 59:86–95.

IJsselmuiden, S. T., Abdalla, M. M., and Gürdal, Z. (2008). Implementation of strength-based failure criteria in the lamination parameter design space. *AIAA Journal*, 46(7):1826–1834.

Irisarri, F.-X., Abdalla, M. M., and Gürdal, Z. (2011). Improved shepard's method for the optimization of composite structures. *AIAA Journal*, 49(12):2726–2736.

Irisarri, F.-X., Julien, C., Bettebghor, D., Lavelle, F., Guerin, Y., and Mathis, K. (2021). A general optimization strategy for composite sandwich structures. *Structural and Multidisciplinary Optimization*, 63(6):3027–3044.

Irisarri, F.-X., Lasseigne, A., Leroy, F.-H., and Le Riche, R. (2014). Optimal design of laminated composite structures with ply drops using stacking sequence tables. *Composite Structures*, 107:559–569.

Jibawy, A., Julien, C., Desmorat, B., Vincenti, A., and Léné, F. (2011). Hierarchical structural optimization of laminated plates using polar representation. *International Journal of Solids and Structures*, 48(18):2576–2584.

Jonsson, E., Riso, C., Lupp, C. A., Cesnik, C. E., Martins, J. R., and Epureanu, B. I. (2019). Flutter and post-flutter constraints in aircraft design optimization. *Progress in Aerospace Sciences*, 109:100537.

Kang, F., Xu, Q., and Li, J. (2016). Slope reliability analysis using surrogate models via new support vector machines with swarm intelligence. *Applied Mathematical Modelling*, 40(11):6105–6120.

Kirkpatrick, S. (1984). Optimization by simulated annealing: Quantitative studies. *Journal of Statistical Physics*, 34(5):975–986.

Kogiso, N., Watson, L. T., Gürdal, Z., and Haftka, R. T. (1994). Genetic algorithms with local improvement for composite laminate design. *Structural Optimization*, 7(4):207–218.

Kradinov, V., Madenci, E., and Ambur, D. (2007). Application of genetic algorithm for optimum design of bolted composite lap joints. *Composite Structures*, 77(2):148–159.

Kriegesmann, B. (2017). Closed-form probabilistic analysis of lamination parameters for composite structures. *AIAA Journal*, 55(6):2074–2085.

Krige, D. G. (1951). A statistical approach to some basic mine valuation problems on the witwatersrand, by d.g. krige, published in the journal, december 1951 : introduction by the author. *Journal of The South African Institute of Mining and Metallurgy*, 52:201–203.

Kristinsdottir, B. P., Zabinsky, Z. B., Tuttle, M. E., and Neogi, S. (2001). Optimal design of large composite panels with varying loads. *Composite Structures*, page 10.

Kuschel, N. and Rackwitz, R. (1997). Two basic problems in reliability-based structural optimization. *Mathematical Methods of Operations Research*, 46(3):309–333.

Lebrun, R. and Dutfoy, A. (2009). Do rosenblatt and nataf isoprobabilistic transformations really differ? *Probabilistic Engineering Mechanics*, 24(4):577–584.

Lelièvre, N., Beaurepaire, P., Mattrand, C., and Gayton, N. (2018). AK-MCSi: A kriging-based method to deal with small failure probabilities and time-consuming models. *Structural Safety*, 73:1–11.

Lelièvre, N., Beaurepaire, P., Mattrand, C., Gayton, N., and Otsmane, A. (2016). On the consideration of uncertainty in design: optimization - reliability - robustness. *Structural and Multidisciplinary Optimization*, 54(6):1423–1437.

Lemaire, M. (2009). *Structural Reliability*. Wiley edition.

Li, X., Gong, C., Gu, L., Gao, W., Jing, Z., and Su, H. (2018). A sequential surrogate method for reliability analysis based on radial basis function. *Structural Safety*, 73:42–53.

Li, X., Qiu, H., Chen, Z., Gao, L., and Shao, X. (2016). A local kriging approximation method using MPP for reliability-based design optimization. *Computers & Structures*, 162:102–115.

Lilliefors, H. W. (1967). On the kolmogorov-smirnov test for normality with mean and variance unknown. *Journal of the American Statistical Association*, 62(318):399–402.

Lin, C.-C. and Lee, Y.-J. (2004). Stacking sequence optimization of laminated composite structures using genetic algorithm with local improvement. *Composite Structures*, 63(3):339–345.

Lobato, F. S., da Silva, M. A., Cavalini Jr, A. A., and Steffen Jr, V. (2020). Reliability-based robust multi-objective optimization applied to engineering system design. *Engineering Optimization*, 52(1):1–21.

Lozano, G. G., Tiwari, A., Turner, C., and Astwood, S. (2016). A review on design for manufacture of variable stiffness composite laminates. *Proceedings of the Institution of Mechanical Engineers, Part B: Journal of Engineering Manufacture*, 230(6):981–992.

Luo, Y., Li, A., and Kang, Z. (2011). Reliability-based design optimization of adhesive bonded steel–concrete composite beams with probabilistic and non-probabilistic uncertainties. *Engineering Structures*, 33(7):2110–2119.

López, C., Bacarreza, O., Baldomir, A., Hernández, S., and H. Ferri Aliabadi, M. (2017). Reliability-based design optimization of composite stiffened panels in post-buckling regime. *Structural and Multidisciplinary Optimization*, 55(3):1121–1141.

Macquart, T., Bordogna, M. T., Lancelot, P., and De Breuker, R. (2016). Derivation and application of blending constraints in lamination parameter space for composite optimisation. *Composite Structures*, 135:224–235.

Macquart, T., Werter, N., and De Breuker, R. (2017). Aeroelastic design of blended composite structures using lamination parameters. *Journal of Aircraft*, 54(2):561–571.

Manan, A. and Cooper, J. (2009). Design of composite wings including uncertainties: A probabilistic approach. *Journal of Aircraft*, 46(2):601–607.

Matheron, G. (1962). *Traité de géostatistique appliquée*. Editions Technip.

Metropolis, N., Rosenbluth, A. W., Rosenbluth, M. N., Teller, A. H., and Teller, E. (1953). Equation of state calculations by fast computing machines. *The Journal of Chemical Physics*, 21(6):1087–1092.

Metropolis, N. and Ulam, S. (1949). The monte carlo method. *Journal of the American Statistical Association*, 44(247):335–341.

Miki, M. and Sugiyama, Y. (1991). Optimum design of laminated composite plates using lamination parameters. page 9.

MIL-HDBK-17 (2002). Composite materials handbook.

Millman, D. R., King, P. I., and Beran, P. S. (2005). Airfoil pitch-and-plunge bifurcation behavior with fourier chaos expansions. *Journal of Aircraft*, 42(2):376–384.

Minka, T. P. (2001). A family of algorithms for approximate bayesian inference.

Mohamed, S., Rosca, M., Figurnov, M., and Mnih, A. (2020). Monte carlo gradient estimation in machine learning.

Montemurro, M., Catapano, A., and Doroszewski, D. (2016). A multi-scale approach for the simultaneous shape and material optimisation of sandwich panels with cellular core. *Composites Part B: Engineering*, 91:458–472.

Montemurro, M., Pagani, A., Fiordilino, G. A., Pailhès, J., and Carrera, E. (2018). A general multi-scale two-level optimisation strategy for designing composite stiffened panels. *Composite Structures*, 201:968–979.

Montemurro, M., Vincenti, A., and Vannucci, P. (2012a). A two-level procedure for the global optimum design of composite modular structures—application to the design of an aircraft wing: Part 1: Theoretical formulation. *Journal of Optimization Theory and Applications*, 155(1):1–23.

Montemurro, M., Vincenti, A., and Vannucci, P. (2012b). A two-level procedure for the global optimum design of composite modular structures—application to the design of an aircraft wing: Part 2: Numerical aspects and examples. *Journal of Optimization Theory and Applications*, 155(1):24–53.

Morio, J., Balesdent, M., Jacquemart, D., and Vergé, C. (2014). A survey of rare event simulation methods for static input–output models. *Simulation Modelling Practice and Theory*, 49:287–304.

Moustapha, M. and Sudret, B. (2019). Surrogate-assisted reliability-based design optimization: a survey and a unified modular framework. *Structural and Multidisciplinary Optimization*, 60(5):2157–2176.

Moustapha, M., Sudret, B., Bourinet, J.-M., and Guillaume, B. (2016). Quantile-based optimization under uncertainties using adaptive kriging surrogate models. *Structural and Multidisciplinary Optimization*, 54(6):1403–1421.

Murray Rosenblatt (1952). Remarks on a multivariate transformation. *The Annals of Mathematical Statistics*, 23(3):470–472.

Murugan, S., Ganguli, R., and Harursampath, D. (2008). Aeroelastic response of composite helicopter rotor with random material properties. *Journal of Aircraft*, 45(1):306–322.

Nagendra, S., Haftka, R. T., and Gurdal, Z. (1992). Stacking sequence optimization of simply supported laminates with stability and strain constraints. *AIAA Journal*, 30(8):2132–2137.

Nagendra, S., Jestin, D., Gürdal, Z., Haftka, R., and Watson, L. (1996). Improved genetic algorithm for the design of stiffened composite panels. *Computers & Structures*, 58(3):543–555.

Narayana Naik, G., Gopalakrishnan, S., and Ganguli, R. (2008). Design optimization of composites using genetic algorithms and failure mechanism based failure criterion. *Composite Structures*, 83(4):354–367.

Nataf, A. (1962). Determination des distributions dont les marges sont données. *Comptes Rendus de l'Académie des Science*, 225:42–43.

Navarro, M., Witteveen, J., and Blom, J. (2014). Polynomial chaos expansion for general multivariate distributions with correlated variables. *arXiv:1406.5483 [math]*.

Nikolaidis, E. and Burdisso, R. (1988). Reliability based optimization: A safety index approach. *Computers & Structures*, 28(6):781–788.

Nitschke, C., Vincenti, A., and Chassaing, J.-C. (2019). Influence of stochastic perturbations of composite laminate layups on the aeroelastic flutter of a cantilevered plate wing. *Composite Structures*, 220:809–826.

Omairey, S. L., Dunning, P. D., and Sriramula, S. (2019). Multiscale surrogate-based framework for reliability analysis of unidirectional FRP composites. *Composites Part B: Engineering*, 173:106925.

Omairey, S. L., Dunning, P. D., and Sriramula, S. (2021). Multi-scale reliability-based design optimisation framework for fibre-reinforced composite laminates. *Engineering Computations*, 38(3):1241–1262.

Pagani, A. and Sanchez-Majano, A. R. (2022). Influence of fiber misalignments on buckling performance of variable stiffness composites using layerwise models and random fields. *Mechanics of Advanced Materials and Structures*, 29(3):384–399.

Pai, N., Kaw, A., and Weng, M. (2003). Optimization of laminate stacking sequence for failure load maximization using tabu search. *Composites Part B: Engineering*, 34(4):405–413.

Panettieri, E., Montemurro, M., and Catapano, A. (2019). Blending constraints for composite laminates in polar parameters space. *Composites Part B: Engineering*, 168:448–457.

Pedregosa, F., Varoquaux, G., Gramfort, A., Michel, V., Thirion, B., Grisel, O., Blondel, M., Prettenhofer, P., Weiss, R., Dubourg, V., Vanderplas, J., Passos, A., Cournapeau, D., Brucher, M., Perrot, M., and Duchesnay, E. (2011). Scikit-learn: Machine learning in python. *Journal of Machine Learning Research*, 12:2825–2830.

Petit, C. L. (2004). Uncertainty quantification in aeroelasticity: Recent results and research challenges. *Journal of Aircraft*, 41(5):1217–1229.

Picchi Scardaoni, M., Montemurro, M., Panettieri, E., and Catapano, A. (2021). New blending constraints and a stack-recovery strategy for the multi-scale design of composite laminates. *Structural and Multidisciplinary Optimization*, 63(2):741–766.

Picheny, V., Ginsbourger, D., Roustant, O., Haftka, R. T., and Kim, N.-H. (2010). Adaptive designs of experiments for accurate approximation of a target region. *Journal of Mechanical Design*, 132(7):071008.

Potgieter, E. and Stander, N. (1998). The genetic algorithm applied to stiffness maximization of laminated plates: review and comparison. *Structural Optimization*, 15(3):221–229.

Rais-Rohani, M. and Singh, M. N. (2004). Comparison of global and local response surface techniques in reliability-based optimization of composite structures. *Structural and Multidisciplinary Optimization*, page 13.

Rama Mohan Rao, A. and Arvind, N. (2005). A scatter search algorithm for stacking sequence optimisation of laminate composites. *Composite Structures*, 70(4):383–402.

Rao, A. M., Ratnam, C., Srinivas, J., and Premkumar, A. (2002). Optimum design of multilayer composite plates using simulated annealing. 216:5.

Rasmussen, C. E. and Williams, C. K. I. (2006). *Gaussian processes for machine learning*. Adaptive computation and machine learning. MIT Press.

Razaaly, N. and Congedo, P. M. (2020). Extension of AK-MCS for the efficient computation of very small failure probabilities. *Reliability Engineering & System Safety*, 203:107084.

Reddy, J. N. (2003). *Mechanics of Laminated Composite Plates and Shells: Theory and Analysis*. Second edition (2nd ed.). CRC press edition.

Riche, R. L. and Haftka, R. T. (1993). Optimization of laminate stacking sequence for buckling load maximization by genetic algorithm. *AIAA Journal*, 31(5):951–956.

Rivier, M. and Congedo, P. (2022). Surrogate-assisted bounding-box approach applied to constrained multi-objective optimisation under uncertainty. *Reliability Engineering & System Safety*, 217:108039.

Romeijn, H. E., Zabinsky, Z. B., Graesser, D. L., and Neogi, S. (1999). New reflection generator for simulated annealing in mixed-integer/continuous global optimization. *Journal of Optimization Theory and Applications*, 101(2):403–427.

Royset, J. and Polak, E. (2004a). Reliability-based optimal design using sample average approximations. *Probabilistic Engineering Mechanics*, 19(4):331–343.

Royset, J. O. and Polak, E. (2004b). Implementable algorithm for stochastic optimization using sample average approximations. *Journal of Optimization Theory and Applications*, 122(1):157–184.

Rubinstein, R. Y. (1986). The score function approach for sensitivity analysis of computer simulation models. *Mathematics and Computers in Simulation*, 28(5):351–379.

Rubinstein, R. Y. and Kroese, D. P. (2004). *The Cross-Entropy Method: A Unified Approach to Combinatorial Optimization, Monte-Carlo Simulation and Machine Learning*. Springer-Verlag New York, information science and statistics edition.

Sacks, J., Welch, W. J., Mitchell, T. J., and Wynn, H. P. (1989). Design and analysis of computer experiments. *Statistical Science*, 4(4):409–423.

Salas, P. and Venkataraman, S. (2009). Laminate optimization incorporating analysis and model parameter uncertainties for predictable failure. *Structural and Multidisciplinary Optimization*, 37(6):541–555.

Saraygord Afshari, S., Enayatollahi, F., Xu, X., and Liang, X. (2022). Machine learning-based methods in structural reliability analysis: A review. *Reliability Engineering & System Safety*, 219:108223.

Sargent, P. M., Ige, D. O., and Ball, N. R. (1995). Design of laminate composite layups using genetic algorithms. *Engineering with Computers*, 11(2):59–69.

Savine, F. (2022). Simultaneous optimization of unconventional stiffener layouts and composite layups applied to large cylindrical shell structures. page 211.

Scarth, C. and Adhikari, S. (2017). Modeling spatially varying uncertainty in composite structures using lamination parameters. *AIAA Journal*, 55(11):3951–3965.

Scarth, C. and Cooper, J. E. (2018). Reliability-based aeroelastic design of composite plate wings using a stability margin. *Structural and Multidisciplinary Optimization*, 57(4):1695–1709.

Scarth, C., Cooper, J. E., Weaver, P. M., and Silva, G. H. (2014). Uncertainty quantification of aeroelastic stability of composite plate wings using lamination parameters. *Composite Structures*, 116:84–93.

Schöbi, R. and Sudret, B. (2014). PC-kriging: A new meta-modelling method and its application to quantile estimation. page 8 p.

Schöbi, R., Sudret, B., and Marelli, S. (2017). Rare event estimation using polynomial-chaos kriging. *ASCE-ASME Journal of Risk and Uncertainty in Engineering Systems, Part A: Civil Engineering*, 3(2).

Setoodeh, S., Abdalla, M., and Gurdal, Z. (2006). Approximate feasible regions for lamination parameters. In *11th AIAA/ISSMO Multidisciplinary Analysis and Optimization Conference*, Multidisciplinary Analysis Optimization Conferences. American Institute of Aeronautics and Astronautics.

Shapiro, S. S. and Wilk, M. B. (1965). An analysis of variance test for normality (complete samples). *Biometrika*, 52(3):591–611.

Stanford, B., Beran, P., and Bhatia, M. (2014). Aeroelastic topology optimization of blade-stiffened panels. *Journal of Aircraft*, 51(3):938–944.

Stanford, B., Wieseman, C. D., and Jutte, C. (2015). Aeroelastic tailoring of transport wings including transonic flutter constraints. In *56th AIAA/ASCE/AHS/ASC Structures, Structural Dynamics, and Materials Conference*. American Institute of Aeronautics and Astronautics.

Stephens, M. A. (1974). EDF statistics for goodness of fit and some comparisons. *Journal of the American Statistical Association*, 69(347):730–737.

Stodieck, O., Cooper, J. E., Weaver, P. M., and Kealy, P. (2013). Improved aeroelastic tailoring using tow-steered composites. *Composite Structures*, 106:703–715.

Suresh, S., Sujit, P., and Rao, A. (2007). Particle swarm optimization approach for multi-objective composite box-beam design. *Composite Structures*, 81(4):598–605.

Suryawanshi, A. and Ghosh, D. (2016). Reliability based optimization in aeroelastic stability problems using polynomial chaos based metamodels. *Structural and Multidisciplinary Optimization*, 53(5):1069–1080.

Svanberg, K. (1987). The method of moving asymptotes—a new method for structural optimization. *International Journal for Numerical Methods in Engineering*, 24(2):359–373.

Svanberg, K. (2002). A class of globally convergent optimization methods based on conservative convex separable approximations. *SIAM Journal on Optimization*, 12(2):555–573.

Székely, G. J. and Rizzo, M. L. (2005). A new test for multivariate normality. *Journal of Multivariate Analysis*, 93(1):58–80.

Taflanidis, A. (2007). Stochastic system design and applications to stochastically robust structural control.

Todoroki, A. and Ishikawa, T. (2004). Design of experiments for stacking sequence optimizations with genetic algorithm using response surface approximation. *Composite Structures*, 64(3):349–357.

Tsai, S. W. and Hahn, H. T. (1980). *Introduction to composite materials*.

Tu, J., Choi, K. K., and Park, Y. H. (1999). A new study on reliability-based design optimization. *Journal of Mechanical Design*, 121(4):557–564.

Vallat, R. (2018). Pingouin: statistics in python. *Journal of Open Source Software*, 3(31):1026.

Van Campen, J. and Gürdal, Z. (2009). Retrieving variable stiffness laminates from lamination parameters distribution. In *50th AIAA/ASME/ASCE/AHS/ASC Structures, Structural Dynamics, and Materials Conference*. American Institute of Aeronautics and Astronautics.

Vannucci, P. (2013). A note on the elastic and geometric bounds for composite laminates. *Journal of Elasticity*, 112(2):199–215.

Vannucci, P. and Verchery, G. (2001). Stiffness design of laminates using the polar method. *International Journal of Solids and Structures*, page 14.

Vannucci, P. a. r. r. (2018). *Anisotropic Elasticity*. Springer, 1st ed. 2018. edition.

Venkataraman, S. and Haftka, R. T. (1999). Optimization of composite panels – a review. page 11.

Verchery, G. (1982). Les invariants des tenseurs d'ordre 4 du type de l'Élasticité. In Boehler, J.-P., editor, *Mechanical Behavior of Anisotropic Solids / Comportment Méchanique des Solides Anisotropes*, pages 93–104. Springer Netherlands.

Vicente, F. (2019). Stacking sequence retrieval of large com- posite structures in bi-step optimization strategies using mechanical constraints.

Vincenti, A. (2002). Conception et optimisation des composites stratifiés par méthode polaire et algorithme génétique.

Vincenti, A., Ahmadian, M. R., and Vannucci, P. (2010). BIANCA: a genetic algorithm to solve hard combinatorial optimisation problems in engineering. *Journal of Global Optimization*, 48(3):399–421.

Vincenti, A., Verchery, G., and Vannucci, P. (2001). Anisotropy and symmetry for elastic properties of laminates reinforced by balanced fabrics. *Composites Part A: Applied Science and Manufacturing*, 32(10):1525–1532.

Walker, M. and Smith, R. (2003). A technique for the multiobjective optimisation of laminated composite structures using genetic algorithms and finite element analysis. *Composite Structures*, 62(1):123–128.

Wang, H., Chen, L., Ye, F., and Chen, L. (2017). Global sensitivity analysis for fiber reinforced composite fiber path based on d-MORPH-HDMR algorithm. *Structural and Multidisciplinary Optimization*, 56(3):697–712.

Wang, J., Sun, Z., Cao, R., and Yan, Y. (2020). An efficient and robust adaptive kriging for structural reliability analysis. *Structural and Multidisciplinary Optimization*, 62(6):3189–3204.

Wang, Z. and Sobey, A. (2020). A comparative review between genetic algorithm use in composite optimisation and the state-of-the-art in evolutionary computation. *Composite Structures*, 233:111739.

Wiener, N. (1938). The homogeneous chaos. *American Journal of Mathematics*, 60(4):897–936.

Wu, Y.-T. (1994). Computational methods for efficient structural reliability and reliability sensitivity analysis. *AIAA Journal*, 32(8):1717–1723.

Wu, Z., Raju, G., and Weaver, P. M. (2015). Framework for the buckling optimization of variable-angle tow composite plates. *AIAA Journal*, 53(12):3788–3804.

Xiu, D. and Karniadakis, G. E. (2002). The wiener–askey polynomial chaos for stochastic differential equations. *SIAM Journal on Scientific Computing*, 24(2):619–644.

Xu, C., Chen, W., Ma, J., Shi, Y., and Lu, S. (2020). AK-MSS: An adaptation of the AK-MCS method for small failure probabilities. *Structural Safety*, 86:101971.

Xu, Y., Zhu, J., Wu, Z., Cao, Y., Zhao, Y., and Zhang, W. (2018). A review on the design of laminated composite structures: constant and variable stiffness design and topology optimization. *Advanced Composites and Hybrid Materials*, 1(3):460–477.

Yamazaki, K. (1996). Two-level optimization technique of composite laminate panels by genetic algorithms. In *37th Structure, Structural Dynamics and Materials Conference*, Structures, Structural Dynamics, and Materials and Co-located Conferences. American Institute of Aeronautics and Astronautics.

Yao, W., Chen, X., Luo, W., van Tooren, M., and Guo, J. (2011). Review of uncertainty-based multidisciplinary design optimization methods for aerospace vehicles. *Progress in Aerospace Sciences*, 47(6):450–479.

Zehnder, N. and Ermanni, P. (2006). A methodology for the global optimization of laminated composite structures. *Composite Structures*, 72(3):311–320.

Zehnder, N. and Ermanni, P. (2007). Optimizing the shape and placement of patches of reinforcement fibers. *Composite Structures*, 77(1):1–9.

Zhu, P., Shi, L., Yang, R.-J., and Lin, S.-P. (2015). A new sampling-based RBDO method via score function with reweighting scheme and application to vehicle designs. *Applied Mathematical Modelling*, 39(15):4243–4256.

Zio, E. (2013). *The Monte Carlo Simulation Method for System Reliability and Risk Analysis*. Springer Series in Reliability Engineering. Springer London.

Zuniga, M. M. (2011). Méthodes stochastiques pour l'estimation contrôlée de faibles probabilités sur des modèles physiques complexes : application au domaine nucléaire.

RÉSUMÉ DE SYNTHÈSE (IN FRENCH)

Contexte et objectifs

L'un des principaux défis dans le domaine de l'optimisation des structures composites est d'exploiter leur plein potentiel. Les matériaux composites permettent d'adapter les propriétés élastiques d'une structure. Le processus de conception des structures composites aboutit souvent à un problème d'optimisation où la performance structurelle est maximisée, ou la masse est minimisée soumise à un ensemble de contraintes imposées par les matériaux et le comportement général de la structure.

En raison de la complexité de ces matériaux, la variabilité des performances structurales provient principalement de la variabilité provenant du processus de fabrication, comme les propriétés mécaniques du matériau, l'orientation des fibres, mais aussi des conditions de chargement. De telles incertitudes peuvent affecter la réponse mécanique d'une structure et conduire à sa défaillance.

Dans le cadre de l'optimisation déterministe, ces incertitudes sont souvent traitées à travers des hypothèses simplificatrices, telles que l'utilisation de facteurs de sécurité ou la prise en compte de valeurs moyennes ou extrêmes. Cependant, ces approches peuvent conduire à des conceptions conservatrices et inefficaces ou à des conceptions optimistes avec une fiabilité médiocre (Beck and Gomes, 2012). Pour mieux exploiter les matériaux composites, l'ambition est d'étendre ces stratégies dans un cadre stochastique prenant en compte des incertitudes des matériaux composites.

L'optimisation des structures composites est un vaste domaine de recherche. Dans un cadre stochastique il existe plusieurs travaux prenant en compte des incertitudes sur les propriétés matériaux ou les chargements. Ces travaux sont appliqués à principalement deux types d'optimisation sous incertitudes: l'optimisation robuste (RDO) qui est généralement associée à la prise en compte des incertitudes dans la fonction objective minimisant donc la moyenne et la variance de la fonction objective et l'optimisation sous contrainte(s) fiabiliste(s) (RBDO) où les incertitudes sont prises en comptes dans les contraintes visant un seuil limite sur la probabilité de défaillance pour chaque contrainte. Il est possible de combiner les deux approches.

Néanmoins peu de travaux prennent en compte les incertitudes sur les variables de conception, telles que l'orientation ou les épaisseurs des plis composite alors que certains travaux montrent une certaine sensibilité des instabilités mécaniques, tels que le flambage ou le flottement, liée à l'incertitude des orientations des plis (Scarth et al., 2014; Nitschke et al., 2019; Pagani and Sanchez-Majano, 2022). Récemment, une stratégie, résolvant une optimisation

mono-objectif prenant en compte l'incertitude des orientations des plis, a permis d'obtenir des conceptions fiables vis-à-vis du phénomène de flottement pour l'optimisation aéroélastique (Scarth and Cooper, 2018). Néanmoins, la formulation proposée pourrait être plus complète si l'on souhaite passer à une application plus réaliste.

Dans ce contexte, le travail de thèse vise à développer une stratégie pour l'optimisation de stratifiés composites sous contrainte fiabiliste avec la prise en compte de l'incertitude des orientations de plis pour des applications aéroélastiques. L'idée est de proposer une stratégie qui pourrait être potentiellement appliqué à des cas aéroélastiques complexes. Le travail de recherche s'articule autour de quelques axes de développement : l'optimisation des stratifiés composites, la métamodélisation et l'optimisation sous contrainte fiabiliste. Chaque chapitre du manuscrit comprend un ou deux axes de développement couplés avec un état de l'art de chaque domaine.

Démarche

À travers le Chapitre 1, l'enjeu est de formuler le problème d'optimisation et de présenter la méthodologie globale. Néanmoins, dans un cadre stochastique, le temps de calcul pour résoudre l'optimisation peut être conséquent. Pour ce faire, deux stratégies de métamodélisation ont été développées pour différentes étapes de la procédure d'optimisation afin de réduire le temps de calcul. La première stratégie consiste à métamodéliser le passage d'échelle du matériau composite, nécessaire dans la méthodologie proposée. Ceci correspond au Chapitre 2. La deuxième stratégie, détaillée dans le Chapitre 3, permet d'effectuer une analyse de fiabilité pour un coût de calcul limité en métamodélisant la réponse mécanique. Enfin la méthodologie globale est appliquée sur deux cas d'application: un cas favorisant la rigidité de la plaque avec une contrainte analytique de flambage et un ensuite un cas aéroélastique favorisant la flexibilité de la structure en restant fiable vis-à-vis du flottement aéroélastique. Un résumé des contributions de chaque chapitre est donné par la suite.

Stratégie multi-échelle pour l'optimisation de stratifiés composites sous incertitudes des variables de design

Le premier Chapitre consiste à présenter les principales étapes de la nouvelle méthodologie d'optimisation de stratifiés composites sous contrainte fiabiliste. Dans cette thèse, on utilise la théorie classique des stratifiés (CLT) pour modéliser le comportement des composites. La littérature montre qu'ils existent plusieurs familles de méthode (directe, bi-niveaux, hybride) d'optimisation de structure composite et qu'elles sont assez matures dans le cadre déterministe. Cependant, dans un cadre stochastique, il est très difficile d'optimiser une géométrie complexe en présence d'incertitudes avec un temps de calcul raisonnable. C'est pourquoi la plupart des applications visent des géométries plus simples. C'est encore plus complexe lorsque l'incertitude porte sur des variables de conception telles que l'orientation des plis où l'utilisation de méthodes directes via un algorithme métaheuristique est privilégiée pour optimiser les séquences d'empilement.

Dans cette thèse, une nouvelle méthodologie est proposée, s'inspirant de l'approche bi-niveaux utilisée dans le cadre déterministe. Dans l'approche bi-niveaux, le matériau composite est considéré, dans un premier temps, comme un matériau homogène équivalent. La rigidité est caractérisée par les paramètres de stratification (*lamination parameters*) ou les paramètres po-

laires, et l'optimisation est effectuée par un algorithme à gradient. Dans un deuxième temps, la séquence d'empilement est reconstituée en résolvant un problème inverse fortement multimodal avec une solution non unique via un algorithme génétique.

La volonté est d'utiliser l'espace de design homogénéisé, utilisant ici les paramètres de stratification, afin d'exploiter les algorithmes à gradient pouvant accélérer la convergence de l'optimisation. Pour ce faire, il serait nécessaire de modéliser l'incertitude de ces paramètres dans un cadre fiabiliste. Cependant l'étude de la quantification d'incertitudes des paramètres de stratification montre que la modélisation de l'incertitude de ces variables est complexe et nous oblige à utiliser l'espace de conception des orientations de pli où l'incertitude est connue et modélisée.

Nous avons donc proposé d'effectuer l'approche bi-niveaux à chaque itération de l'optimisation. L'approche muli-échelle développée utilise deux espaces de conception : l'espace homogénéisé avec les paramètres de stratification et l'espace mésoscopique avec les orientations des plis. Le premier est utilisé pour le processus d'optimisation global afin d'utiliser un algorithme à gradient. La fonction objective et les contraintes sont définies dans cet espace avec l'optimiseur qui améliore le design dans l'espace macroscopique (la ligne rouge dans la Figure 4.1). Le second espace est utilisé pour évaluer la probabilité de défaillance car la dispersion des orientations de plis est connue. Néanmoins, le passage des variables homogénéisées aux variables mésoscopiques nécessité la résolution du problème inverse (la ligne rose en pointillé dans la Figure 4.1) à l'aide d'un algorithme génétique. Une fois le problème inverse résolu, il est simple de propager l'incertitude vers l'espace homogénéisé et donc vers le modèle pour calculer la probabilité de défaillance par la méthode de Monte Carlo. Ensuite, l'optimiseur à gradient peut proposer un autre point de design, dans l'espace homogénéisé, jusqu'à convergence.

Dans un cadre de variabilité, la résolution du problème inverse doit être appliquée aux moments statistiques. Il est donc important de propager efficacement les incertitudes de la séquence d'empilement aux paramètres de stratification pour afin de *matcher* les statistiques des paramètres de stratification. Pour réduire le coût de calcul de cette procédure, nous proposons donc de construire un métamodèle permettant d'accéder rapidement aux statistiques nécessaires des paramètres de stratification sachant l'incertitude des orientations. Les détails techniques sont présentés au Chapitre 2. De plus, les contraintes mécaniques, soumises à l'analyse de fiabilité, pourraient être coûteuses ; par conséquent, une stratégie est proposée pour approximer efficacement la quantité d'intérêt à l'aide d'une stratégie de modèles de substitution pour calculer efficacement et rapidement la probabilité de défaillance et son gradient. Les détails techniques sont présentés au Chapitre 3.

Reconstruction d'une séquence d'empilement dans un cadre stochastique

Une quantification d'incertitudes des paramètres de stratification est nécessaire pour identifier correctement une séquence d'empilement optimisée en termes de correspondance sur les statistiques des paramètres de stratification sachant l'incertitude sur les orientations de pli. Cette étape doit être rapide et efficace. Avec l'incertitude prise en compte dans les orientations des plis à l'échelle mésoscopique, il est facile de propager l'incertitude dans les paramètres de stratification en utilisant l'équation des paramètres de stratification. Cependant, même si la formulation est analytique, il pourrait être coûteux d'utiliser des méthodes de simulation telles que Monte Carlo à chaque itération du processus d'optimisation globale.

Dans le Chapitre 2, un métamodèle non intrusif a donc été développé pour accéder

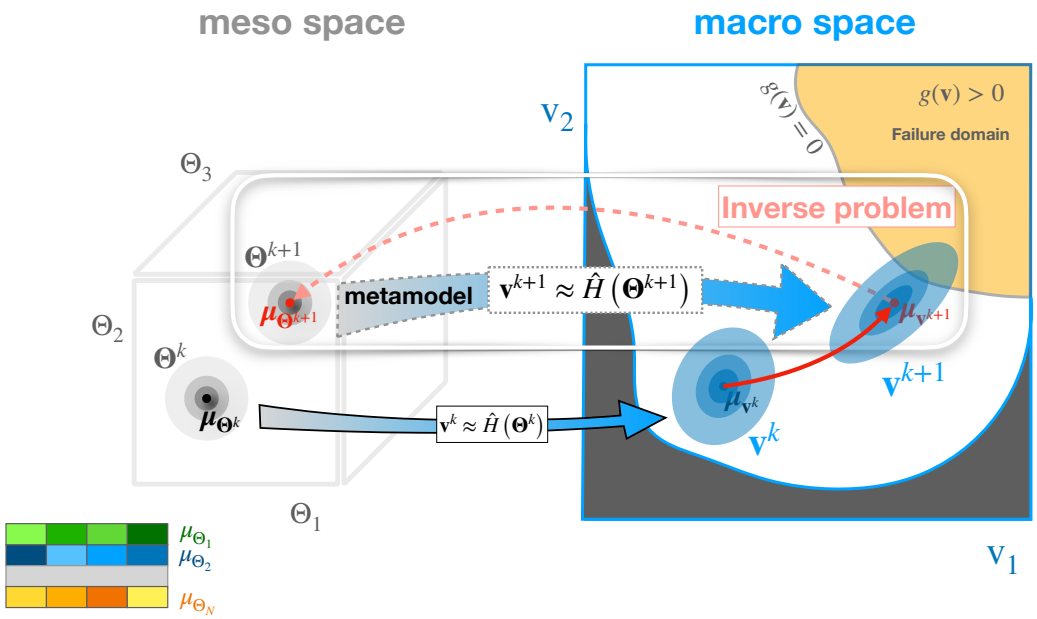

Figure 4.1: The proposed sequential multi-scale RBDO approach.

rapidement aux statistiques nécessaires des paramètres de stratification. La décomposition du chaos de Fourier est développée permettant d'approximer les fonctions trigonométriques de la formulation des paramètres de stratification. Pour ce faire, une base orthonormale de Fourier a été construite via l'algorithme de Gram-Schmidt. La base orthonormée de Fourier, faisant intervenir des fonctions trigonométriques, permet d'avoir une formulation analytique des coefficients déterministes de l'expansion. Ces coefficients permettent d'avoir accès aux statistiques des paramètres de stratification grâce à la propriété orthonormale de la base. Ce métamodèle a été validé et ensuite testé pour la résolution du problème inverse montrant son efficacité en termes de temps de calcul par rapport à la méthode de Monte Carlo. Pour la comparaison des temps de calcul, la formulation du problème inverse est basée sur la moyenne des paramètres de stratification. Néanmoins dans ce Chapitre 2, la question se pose de prendre en compte les écarts-type dans la formulation du problème inverse. Cela peut servir à réduire la variabilité des paramètres de stratification ou bien de limiter la déviation de certaines hypothèses, comme l'orthotropie du matériau composite. Une étude prenant en compte les écarts-type a été menée. Sur un ensemble très limité de points cibles, la prise en compte des écarts-type, en plus de la moyenne, peut régulariser le problème inverse. Pour la suite des travaux, la formulation avec seulement la moyenne statistique est choisie.

En somme, étant donné un jeu de paramètres de stratification, une séquence d'empilement est récupérée pour correspondre aux statistiques dans un temps de calcul négligeable. Grâce à cela, l'incertitude de l'orientation peut être modélisée de manière appropriée puis propagée dans l'espace de conception des paramètres de stratification. Une fois qu'un échantillon de paramètres de stratification est disponible, l'analyse de fiabilité nécessaire pour l'optimisation peut être effectuée. Cependant, le modèle aéroélastique utilisé dans cette thèse est coûteux, et une stratégie doit être mise en place pour effectuer l'analyse de fiabilité dans un temps de calcul acceptable par le biais d'une autre stratégie de modèle de substitution.

Stratégie de métamodélisation pour la fiabilité d'instabilité mécanique

La quantité d'intérêt visée pour l'analyse de fiabilité est la vitesse critique de flottement. Le flottement est une instabilité aéroélastique dynamique. Dans ces travaux, l'analyse aéroélastique est faites par le couplage entre le modèle d'éléments finis, pour la structure, et la méthode des doublets, pour l'aérodynamique. Ce couplage est réalisé avec la méthode des splines, disponible dans Nastran, afin d'interpoler les déplacements et les forces pour le modèle aéroélastique. Ensuite le calcul de flottement s'appuie sur une analyse modale. La réponse de la vitesse critique de flottement peut donc connaître des discontinuités dans l'espace de design homogénéisé, ce qui peut poser problème pour la construction d'un métamodèle.

Différents types de discontinuité sont possibles dans l'espace de conception pour le phénomène de flottement. Outre le changement de mode, il existe un mode particulier qui peut devenir soudainement le mode critique entre deux design proches : il s'agit d'un *hump mode*. On pourrait penser que la vitesse critique peut être régulière si chaque mode est étudié indépendamment et donc faciliter la construction d'un métamodèle mode par mode. Cependant, avec ce phénomène physique lié au *hump mode*, des discontinuités peuvent exister pour un mode étudié.

La volonté est de construire un métamodèle de la vitesse critique de flottement pour chaque mode étudié. Cependant, une stratégie doit être proposée pour traiter une éventuelle discontinuité d'un *hump mode*. Dans ces travaux, nous avons recours à des techniques de classification. De plus, pour traiter un éventuel changement de mode sur la quantité d'intérêt globale, le couplage de modèles de substitution classiques et de la classification est privilégié et présenté dans le Chapitre 3.

La stratégie proposée pour traiter un éventuel *hump mode* consiste à entrainer une classification pour savoir si le point de design est instable ou non dans l'espace de design. Pour ce faire, un plan d'expérience est construit dans l'espace de design homogénéisé, avec une certaine stratégie décrite dans le Chapitre 3. Comme indiqué précédemment, deux états de stabilité sont possibles : instable lorsque le flottement se produit ou stable lorsqu'il n'y a pas d'instabilité aéroélastique. Nous considérons donc un problème de classification binaire. Dans ce travail, un classificateur est entraîné avec la classification par processus gaussien (GPC) pour identifier une frontière entre les deux régions de stabilité. Cette classification présente une précision de 97% avec trois cents points testés autour de cette frontière.

Maintenant les métamodèles de la vitesse critique de flottement peuvent être construits mode par mode à l'aide de processus gaussiens par régression (ou aussi appelé *Krigeage*). Dans le cas d'un *hump mode*, seuls les points de conception qui présentent une instabilité sont utilisés pour construire le modèle de substitution. Après validation des métamodèles, il est possible de les coupler à la classification. En effet, le métamodèle du *hump mode* peut conduire à une mauvaise estimation de la vitesse critique de flottement si les paramètres d'entrée se trouvent dans la région stable. La vitesse critique globale est définie comme le minimum des vitesses des modes calculés. Par conséquent, la classification est exploitée pour savoir quel modèle de substitution de flottement utiliser.

Des éléments de validation sont présentés où la vitesse critique globale est comparée entre le vrai modèle et la réponse du couplage métamodèles et classification. La réponse de la vitesse de flottement couplant la classification avec les modèles de substitution classiques conduit à une certaine erreur autour d'une petite partie de la discontinuité. Parmi les 500 points de la base de données utilisés pour la validation, les estimations de la vitesse de flottement de cinq points

sont complètement inexactes. Cela provient de l'erreur commise par la classification qui n'a pas une précision exacte pour délimiter les régions stables et instables du *hump mode*. La stratégie pourrait donc être améliorée, notamment avec l'utilisation de critère d'enrichissement actif.

Néanmoins tous les ingrédients sont maintenant disponibles pour réaliser une optimisation aéroélastique de stratifiés composites sous contrainte fiabiliste.

Optimisation fiabiliste d'une plaque composite

Dans le Chapitre 4, l'approche multi-échelle, prenant en compte l'incertitude de l'angle des plis, est appliquée à deux problèmes : l'optimisation d'une plaque composite favorisant la rigidité de la plaque tout en restant fiable par rapport à une contrainte de flambage et une optimisation aéroélastique favorisant la flexibilité de la plaque tout en restant fiable par rapport au phénomène de flottement.

La méthode RBDO proposée a été testée et vérifiée, comparée à la méthode RBDO directe utilisant un algorithme génétique pour l'analyse du flambage. Dans cette première application, une comparaison du temps de calcul peut être effectuée puisque la contrainte est un modèle analytique. Un gain de calcul est révélé. La comparaison des méthodes de calcul des gradients de probabilité a également été effectuée (*score function*, différences finies centrées et l'approche hybride proposée qui utilisent les différences finies ou la *score function*). Dans la première application, les résultats convergent vers des conceptions similaires. Cependant, pour l'application aéroélastique, le chemin d'optimisation est proche de la limite de l'espace LP, et l'approche hybride montre son efficacité puisqu'elle converge, contrairement à l'optimisation utilisant uniquement l'approche par *score function*. Les résultats montrent une amélioration de la fiabilité par rapport à la conception optimisée déterministe dans les deux cas. De plus, dans le cas aéroélastique, les résultats montrent des performances accrues par rapport à une conception déterministe où la fiabilité est prise en compte par le biais d'un facteur de sécurité. Cependant, la zone de convergence entre les deux types d'optimisation est similaire.

Conclusion et perspectives

Dans ce travail, l'optimisation de stratifiés composites sous contrainte fiabiliste a été réalisée avec l'incertitude de l'orientation des plis. L'étude de la fiabilité au cours du processus d'optimisation s'est concentrée sur les instabilités telles que le flambage et le flottement aéroélastique. Les principaux défis consistaient à traiter l'incertitude sur les variables de conception discrètes et à gérer la discontinuité des contraintes pouvant exister dans l'espace de design. Même si la stratégie a été appliquée à des cas académiques, les problèmes traités dans ce travail sont déjà représentatifs de ceux rencontrés dans des applications plus complexes.

La nouvelle approche multi-échelle développée dans ce manuscrit est capable de prendre en compte l'incertitude des orientations des plis dans un cadre d'optimisation fiabiliste de stratifiés composites. L'avantage de l'approche présentée ici est que l'optimisation peut converger plus rapidement vers une conception fiable par rapport à une méthode directe utilisant un algorithme génétique. Néanmoins, l'une des limites de cette approche multi-échelle concerne l'étape de résolution du problème inverse. Ce problème pose déjà des difficultés dans le cas déterministe en raison de la caractéristique multimodale de ce problème combinatoire et de la non-unicité de sa solution. De plus, comme l'orientation des plis suit certaines règles et ne peut prendre que

des valeurs discrètes, une différence pourrait apparaître dans la réponse macroscopique entre la cible et la séquence d'empilement récupérée. Cette erreur pourrait être problématique pour la convergence de notre optimisation.

Concernant ce problème inverse, la construction et l'utilisation de l'expansion de Fourier pour calculer les statistiques des paramètres de stratification est très efficace en termes de précision et de temps de calcul. La nouvelle approche multi-échelle développée dans ce manuscrit peut également traiter une contrainte d'instabilité discontinue. La stratégie proposée, qui combine une classification et des modèles de substitution classiques, permet d'obtenir une approximation efficace de la quantité discontinue en question. Ceci est utile dans l'analyse de la fiabilité de la contrainte discontinue avec un faible temps de calcul. Cependant, l'application de cette stratégie à l'approximation de la vitesse de flottement de la plaque montre quelques erreurs dans la classification. Cependant, cela n'a pas d'impact sur l'optimisation puisqu'il ne s'agit pas d'une région d'intérêt. Cette étape devrait être améliorée pour un cas plus général. Des critères d'apprentissage actif pourraient être utilisés pour enrichir le classificateur et les modèles de substitution comme la méthode AK-MCS (Echard et al., 2011). De plus, dans notre cas, l'ensemble du domaine n'est pas exploré avec l'algorithme à gradient utilisé dans l'espace des paramètres de stratification. Par conséquent, le modèle de substitution doit être efficace uniquement dans la fonction d'état limite où l'optimiseur converge. Dans ce cas, nous pourrions réduire le nombre d'appels de simulation pour construire le métamodèle avec ce type de critères.

Enfin, nous montrons la faisabilité de notre approche et l'illustrons par des cas tests. L'approche devrait se distinguer en considérant un niveau de difficulté plus élevé dans le cas d'application, où une analyse de fiabilité tout au long de l'optimisation sera intéressante. Dans l'application aéroélastique, nous avons effectué une optimisation déterministe avec un facteur de sécurité. La comparaison montre l'intérêt de passer à une optimisation fiabiliste puisque l'optimisation avec un facteur de sécurité semble sur-dimensionner la conception comme mentionné dans l'introduction. Avec l'approche RBDO, l'impact des incertitudes est connu à travers le processus d'optimisation grâce aux informations sur la probabilité de défaillance. Cependant, dans ce cas, la conception converge dans la même région que la conception déterministe. Néanmoins, nous pensons que l'augmentation de la complexité de l'application devrait conduire à des conceptions plus distinctes entre les conceptions déterministes et les conceptions de l'application. Augmenter la complexité signifie aller vers une conception à rigidité variable avec différentes zones de conception et la possibilité d'optimiser les épaisseurs de chacune d'entre elles. Ce type d'application peut conduire à différents minimums locaux et pourrait mettre en évidence l'avantage de l'application de notre approche RBDO multi-échelle. Le problème de l'optimisation de la rigidité variable augmentera la complexité sur deux points : la résolution du problème inverse et la construction du modèle de substitution pour l'analyse de fiabilité. Tout d'abord, la résolution du problème inverse doit prendre en compte différentes zones et épaisseurs cibles. La formulation utilisant les tables de drapage déjà utilisée dans ce travail pourrait traiter cette question, en tenant compte des contraintes de conception imposées par le fabricant. Deuxièmement, le modèle de substitution doit supporter l'augmentation des dimensions provenant des différentes zones de conception (c'est-à-dire les paramètres d'entrée). En outre, la réponse des contraintes dépendra désormais de l'épaisseur, ce qui augmentera également la dimension du modèle de substitution. Si la dimension augmente trop, un autre type de modèle de substitution ou une technique qui réduit la dimension du problème, par exemple, peuvent être utilisés.

université PARIS-SACLAY

ÉCOLE DOCTORALE
Sciences mécaniques et énergétiques, matériaux et géosciences (SMEMAG)

Titre : Optimisation de stratifiés composites sous contrainte fiabiliste pour des applications aéroélastiques

Mots clés : optimisation sous incertitudes, matériau composite, multi-échelle, paramètres de stratification, métamodèles, flottement

Résumé : L'optimisation de stratifiés composites sous contrainte fiabiliste a été réalisée avec la prise en compte de l'incertitude des orientations de plis. Ce travail propose une nouvelle méthodologie itérative qui lie deux espaces d'analyse. Dans le premier espace est gérée la conception macroscopique à faible dimension (en utilisant les paramètres de stratification) avec des informations de gradient pour effectuer une optimisation rapide. Dans le deuxième espace, mésoscopique à haute dimension, les incertitudes des variables de conception sont modélisées et ensuite transportées à l'échelle macroscopique. Avec cette méthodologie, un problème inverse doit être résolu à chaque itération pour pouvoir propager l'incertitude de l'espace mésoscopique à l'espace de conception macroscopique et calculer la probabilité de défaillance nécessaire. Pour cela, une quantification de l'incertitude est nécessaire pour identifier correctement une séquence d'empilement correspondant à la description statistique des paramètres de stratification. Une base orthonormale de Fourier a donc été développée. L'approche d'optimisation présentée est appliquée à différents problèmes : d'abord, l'optimisation d'une plaque composite favorisant la rigidité de la plaque avec une contrainte analytique de flambage et ensuite une optimisation aéroélastique favorisant la flexibilité de la plaque tout en restant fiable vis-à-vis du phénomène de flottement. En raison de la nature modale de la vitesse de flottement, une stratégie combinant une classification et un modèle de substitution classique est proposée pour approximer la quantité d'intérêt et effectuer une analyse de fiabilité rapide. Les résultats obtenus démontrent une amélioration de la fiabilité par rapport à la conception optimisée déterministe et un gain de calcul significatif par rapport à l'approche consistant à optimiser directement les orientations des plis via un algorithme génétique.

Title: Reliability-based design optimization of composite laminates for aeroelastic applications

Keywords: optimization under uncertainty, composite material, multi-scale, lamination parameters, surrogate models, flutter

Abstract: Reliability-based design optimization of composite laminates was performed with uncertainty in ply orientation. This work proposes a new iterative methodology that links two analysis spaces. In the first space, the low-dimensional macroscopic design is managed (using lamination parameters) with gradient information to perform rapid optimization. In the second, a high-dimensional mesoscopic scale, uncertainties in the design variables are modeled and then propagated to the macroscopic scale. With this methodology, an inverse problem must be solved at each iteration to propagate the uncertainty from the mesoscopic space to the macroscopic design space and calculate the required failure probability. For this purpose, uncertainty quantification is necessary to correctly identify a stacking sequence corresponding to the statistical description of the lamination parameters. To this end, a Fourier orthonormal basis has been developed. The optimization methodology is applied to various problems, including instability constraint: (i) composite plate optimization promoting the plate stiffness with an analytic buckling constraint and (ii) aeroelastic tailoring promoting the plate flexibility while remaining reliable with respect to the flutter phenomenon. Due to the modal nature of the flutter velocity, a strategy combining a classifier and classic surrogate models is proposed to approximate the quantity of interest and perform a fast reliability analysis. The results demonstrate an improvement in the reliability compared to the deterministic optimized design and a significant computational gain compared to the approach of directly optimizing ply orientations via a genetic algorithm.